Measurements and Simulations on Position Dependencies in the Response of Single PWO Crystals and a Prototype for the $\overline{P}$ANDA EMC

Dipl.-Phys. Daniel Andreas Bremer
aus Lohra-Kirchvers
Gießen, 2013

Contents

Zusammenfassung

Das $\overline{\text{P}}$ANDA Experiment, welches sich später an der Facility for Antiproton and Ion Research befinden wird, hat die Erforschung der starken Wechselwirkung im Charm-Sektor mittels Antiproton Proton Kollisionen zum Ziel. Ein essentieller Bestandteil des $\overline{\text{P}}$ANDA Detektors zum Erreichen der gesteckten physikalischen Ziele ist das Elektromagnetische Kalorimeter (EMC). Dies liegt vor allem in seiner hohen Nachweiseffizienz für Photonen und Elektronen begründet, da viele der erwarteten physikalischen Kanäle von Photonen im Endzustand begleitet werden. Das EMC basiert auf Szintillatorkristallen aus Bleiwolframat der zweiten Generation und besitzt deswegen ein äußerst kompaktes Design und eine verbesserte Performance. Um ein homogenes und präzises Ansprechverhalten bezüglich Energie und Impuls zu gewährleisten, ist eine exakte Kenntnis des Auftreffpunktes eines nachzuweisenden Teilchens unumgänglich.

Im Rahmen dieser Arbeit wurden Ungleichmäßigkeiten in der Lichtausbeute von einzelnen Bleiwolframatkristallen mit pyramidenstumpfförmiger Geometrie untersucht. Dieser Effekt wurde unter Zuhilfenahme des SLitrani Simulationspaketes im Vergleich zu speziell entwickelten Experimentaufbauten studiert. Der sog. Präzisionsaufbau ermöglichte eine vergleichende Messung mittels kosmischer Muonen und niederenergetischer Photonen. Weiterhin wurde eine analoge Messung mit einem 80 MeV Protonenstrahl durchgeführt. Sowohl Simulation als auch Experiment stimmen darin überein, dass im Falle der in $\overline{\text{P}}$ANDA vorhandenen Kristallgeometrien, die Lichtausbeute quadratisch mit dem Abstand der Energiedeposition zum Photosensor steigt. Ein klare Korrelation zum mittleren Neigungswinkel der Seitenflächen der jeweiligen Kristallgeometrie konnte bestimmt werden. Darüber hinaus konnte kein signifikanter Unterschied im Verhalten der beobachteten Ungleichmäßigkeiten zwischen den einzelnen Teilchensorten festgestellt werden. Aufgrund dessen können diese Ungleichmäßigkeiten als unabhängig vom Mechanismus der Energiedeposition betrachtet werden. Folglich ist der dominierende Effekt, der für die Ungleichmäßigkeiten in der Lichtausbeute verantwortlich ist, das Zusammenwirken des aus dem hohen Anteil von intern reflektiertem Szintillationslicht resultierenden Fokussierungseffekts und der dem Kristall eigenen intrinsischen Absorption. Verschiedene Techniken zur Reduktion der Ungleichmäßigkeiten, darunter Modifizierungen der Kristallumhüllung oder der Kristalloberfläche selbst, wurden untersucht. Von diesen erzielte eine Aufrauhung einer Kristallseitenfläche mittels Schmirgeln eine zumindest teilweise Reduktion bei

gleichzeitig geringem Lichtausbeuteverlust im Vergleich zu einem uniformen quader-förmigen Kristalltyp. Eine Evaluation des Einflusses auf eine Matrix von 60 Kristallen, basierend auf GEANT4 Simulationen, wurde durchgeführt. Obwohl diese zeigte, dass eine Reduktion zwar günstig im Falle von Energien über mehreren hundert MeV sein kann, macht der damit einhergehende Verlust an Szintillationslicht und der daraus resultierende Auflösungsverlust bei niedrigen Energien ein solches Verfahren nicht empfehlenswert für das $\overline{\text{P}}$ANDA Barrel EMC. Im Falle der Endcaps werden, bedingt durch die quaderähnliche Kristallgeometrie der verwendeten Kristalle, solche Maßnahmen nicht benötigt.

Das Positionsansprechverhalten des Prototyps PROTO60 wurde bei einem Test am CERN SPS mit einem $15\,\frac{\text{GeV}}{c}$ Positronenstrahl untersucht. Dieser stellt eine Untereinheit des $\overline{\text{P}}$ANDA Barrel EMCs dar und besteht aus 6×10 Bleiwolframatkristallen. Durch das Vorhandensein einer hochauflösenden Positionsreferenz konnten Linearität und Ortsauflösung des PROTO60 eingehend untersucht werden. Beide verwendeten Ortsrekonstruktionsmethoden basieren auf einem Schwerpunktsalgorithmus, welcher entweder mit einer logarithmischen Gewichtung oder einer linearen Gewichtung mit anschließender S-Kurven Korrektur verwendet wurde. Beide Techniken erzielten vergleichbare Resultate und erreichten insgesamt eine Ortsauflösung von $\sigma_{x,y} = 1,1\,\text{mm}$. Für Auftreffpunkte und den Kristallgrenzen wurde eine verbesserte Auflösung von bis zu $0,5\,\text{mm}$ gemessen werden. Diese Ergebnisse sind besser als die genannten Spezifikationen. Zusätzlich kann aus einem Vergleich mit früheren Messungen der oberen Ortsauflösungsgrenze, welche aus der Überlagerung von Photonenstrahlprofil und Detektorauflösung bei bis zu $1{,}5\,\text{GeV}$ extrahiert wurde, geschlossen werden, dass auch im niederenergetischen Bereich eine Auflösung erreicht werden kann, die die Spezifikationen übertrifft. Die erhaltenen $\overline{\text{P}}$ANDA EMC spezifischen Resultate werden mit jüngsten Erfahrungen und Messungen des Kalorimeters des CMS Experimentes verglichen, wobei viele Gemeinsamkeiten festzustellen sind.

Abstract

The $\overline{\mathrm{P}}$ANDA experiment, which will be located at the future Facility for Antiproton and Ion Research, aims at the study of strong interaction within the charm sector via antiproton proton collisions. An essential component of the $\overline{\mathrm{P}}$ANDA detector to achieve the ambitious physics goals is the Electromagnetic Calorimeter (EMC). Reason for this is particularly its high detection efficiency for photons and electrons over a large dynamic range, since most of the expected physics channels are accompanied by secondary photons. The EMC is based on second generation lead tungstate scintillator crystals and thus features a very compact design and improved performance. To guarantee a homogeneous and precise energy and momentum response, an exact knowledge on the incident particle position is mandatory.

In the scope of this work, non-uniformities in the light yield of single lead tungstate crystals with tapered geometry are investigated. This effect was studied with the SLitrani simulation package in comparison to a series of dedicated experimental setups. The so called precision setup allowed for a comparative measurement of the response to cosmic muons and low energetic photons. Furthermore, an analogous beam measurement was performed with 80 MeV protons. Both, simulation and experiments agree that, in case of the $\overline{\mathrm{P}}$ANDA crystal geometry types, the obtained light yield increases quadratically with the distance of the location of the energy deposition inside the crystal to the photo sensor. A clear correlation of the observed amount of non-uniformity to the mean tapering angle of the individual crystal geometry type could be determined. Furthermore, no significant difference in non-uniformity was observed for the three different particle species. Therefore, the observed non-uniformities can be regarded as independent of the exact mechanism of the energy deposition. Hence, the main effect governing the obtained non-uniformities is the interplay of the focussing caused by the high amount of internally reflected scintillation light and the intrinsic absorption in the crystal. Various techniques to achieve a light yield uniformisation, including wrapping and crystal surface modifications, have been investigated. Among these, emery polishing of one crystal surface succeeded in a partial uniformisation of the response to photons with an acceptable light yield loss compared to an intrinsically uniform untapered crystal type. However, an evaluation of the influence on a matrix of 60 crystals based on GEANT4 simulations showed that, in spite being beneficial for energies above several hundred MeV energy, due to the inherent light yield loss entailing a resolution loss in the low energy regime, a uniformisation is not recommendable

for the $\overline{\text{P}}$ANDA Barrel EMC. In case of the end caps, the straight geometry of the implemented crystals does not require uniformisation.

The position response of the prototype PROTO60, representing a subsection of the $\overline{\text{P}}$ANDA Barrel EMC comprised of 6×10 lead tungstate crystals, was investigated during a $15\,\frac{\text{GeV}}{c}$ positron beam test at CERN SPS. Due to the availability of a high resolution reference position provided by a tracking station based on two double-sided silicon strip detectors, linearity and resolution of the incident particle position reconstructed with PROTO60 could be investigated extensively. Both deployed reconstruction techniques, based on a centre of gravity algorithm with either logarithmic weighting or linear weighting with successive S-curve correction, yield comparable results. An overall position resolution of $\sigma_{x,y} = 1.1\,\text{mm}$ could be achieved. However, for incident positions located at the crystal junctions, an improved resolution down to $0.5\,\text{mm}$ is obtained. These results, which represent the high energy limit of the $\overline{\text{P}}$ANDA EMC, are superior to the stated specifications. In addition, a comparison of the achieved resolution to the upper limit deduced from the convolution of photon beam and detector resolution at energies up to $1.5\,\text{GeV}$ leads to the conclusion that also in the low energy regime a resolution superior to the specifications is achievable.

The achieved results specific for the $\overline{\text{P}}$ANDA EMC design are compared to recent experiences of the CMS electromagnetic calorimeter, showing many similarities.

4

Chapter 1

Introduction

The future Facility for Antiproton and Ion Research (FAIR) at the site of the present GSI Helmholtzzentrum für Schwerionenforschung GmbH (GSI) at Darmstadt will provide as an international project accelerator and experimental facilities for basic physics research and applied sciences. Heart of the FAIR accelerator complex, shown in Fig. 1.1, will be, in the first stage, the SchwerIonenSynchrotron 100 (SIS100)[1], which is able to handle a wide range of beam particles from protons to heavy ions. Existing GSI accelerators like the UNIversal Linear ACcelerator (UNILAC) and SchwerIonen-Synchrotron 18 (SIS18)[2] will provide SIS100 with already pre-accelerated particles but will retain their ability to provide beam for experiments at the present GSI. One major difference to existing facilities is the broad scope of research areas offered by FAIR, which scientifically rests on four main pillars, consisting of 14 diverse experiments:

- APPA: Atomic, Plasma Physics and Applications

- CBM: Compressed Baryonic Matter

- NuSTAR: Nuclear Structure, Astrophysics and Reactions

- $\overline{\text{P}}$ANDA: AntiProton ANnihilation at Darmstadt

To ensure an efficient parallel operation of such a large number of experiments with widely different requirements, the beam from SIS100 is converted into secondary beams and further enhanced by a system of cooling and storage rings. Most important for the $\overline{\text{P}}$ANDA experiment and hence for the subject of this thesis is the High Energy Storage Ring (HESR), shown in Fig. 1.2. It stores antiprotons produced at the antiproton production target and is able to provide beam momenta ranging from $1.55\,\text{GeV}/c$ to $15\,\text{GeV}/c$. Due to a system of both stochastic cooling as well as an electron cooler, the HESR achieves an excellent momentum resolution (RMS) of up to $\frac{\sigma_p}{p} \leq 4 \cdot 10^{-5}$ at a luminosity of $2 \cdot 10^{31}\,\frac{1}{\text{cm}^2 \cdot \text{s}}$ in high resolution mode and $\frac{\sigma_p}{p} \sim 10^{-4}$ at a luminosity of $2 \cdot 10^{32}\,\frac{1}{\text{cm}^2 \cdot \text{s}}$ in high luminosity mode, respectively.

---

[1] The number 100 representing its magnetic rigidity of $B\rho = 100\,\text{Tm}$

[2] Magnetic rigidity of $B\rho = 18\,\text{Tm}$
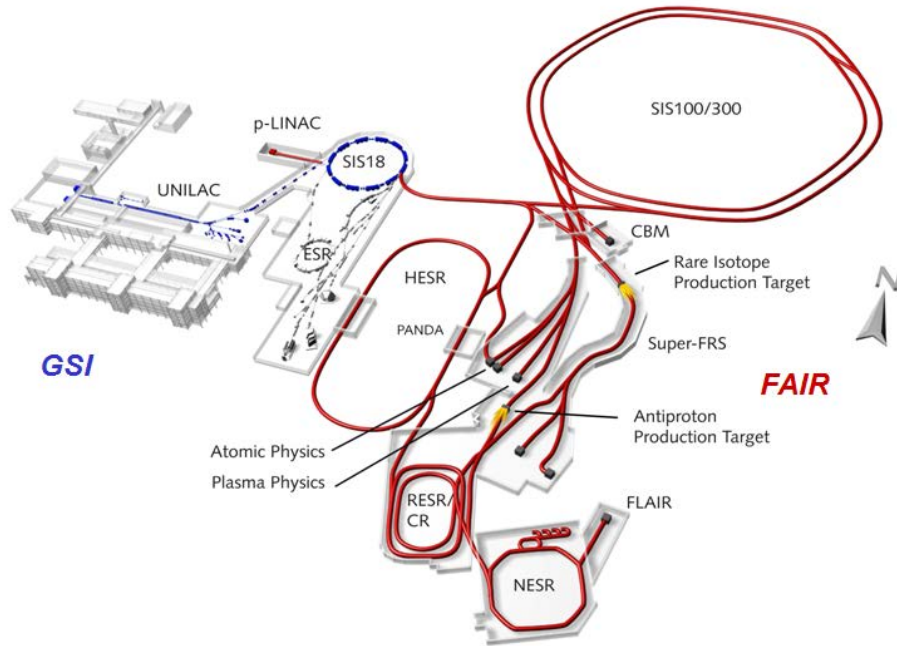
Figure 1.1: Artist's view of the planned FAIR facility (red) and the present GSI (blue). The $\overline{\mathrm{P}}$ANDA detector is located in the centre of one straight section of the HESR.
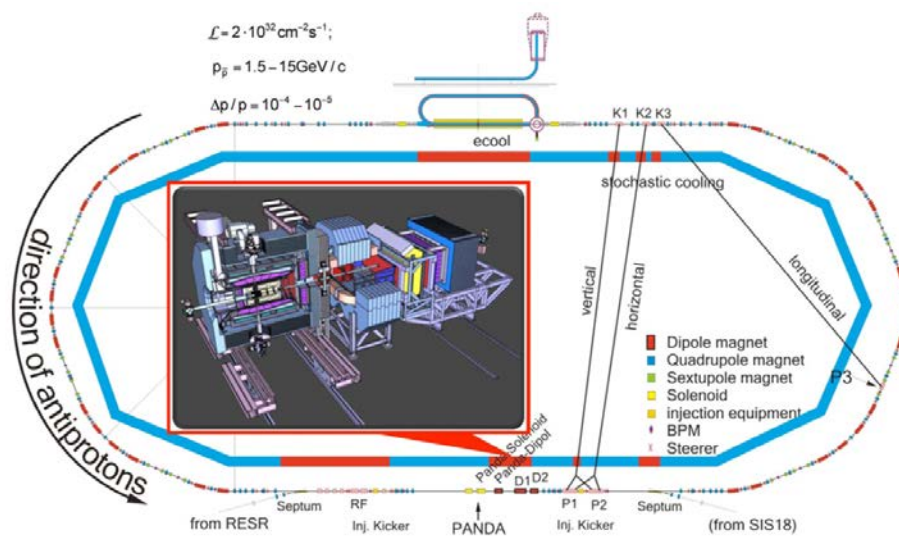
Figure 1.2: Schematic view of the HESR. The positions of electron cooler, stochastic cooling pickup (P1-P3) and kicker (K1-K3) as well as Rapid Frequency acceleration (RF) are indicated by red sections. The centre shows a schematic drawing of the PANDA detector [1].

1.1 Physics of the $\overline{\text{P}}$ANDA Experiment

High resolution antiproton beams as provided by the HESR enable the $\overline{\text{P}}$ANDA experiment to investigate the strong interaction and its corresponding fundamental theory, Quantum-Chromo-Dynamics (QCD). Whereas this theory is well understood at high centre of mass energies and corresponding short distances, where the strong coupling constant α_S is small, the low energy regime and large interaction distances do not allow appliance of perturbation theory, because the coupling constant rises strongly. In this region, the field of hadronic physics, calculations often rely on effective theories and are difficult, but also the experimental knowledge is limited. At $\overline{\text{P}}$ANDA the antiproton beam collides with the fixed target at centre of mass energies between 2.2 GeV and 5.5 GeV, which is located in the described non-perturbative region. Fig. 1.3 displays the accessible invariant mass range in comparison to the antiproton beam momentum. The physics program of $\overline{\text{P}}$ANDA can be divided in three major branches:
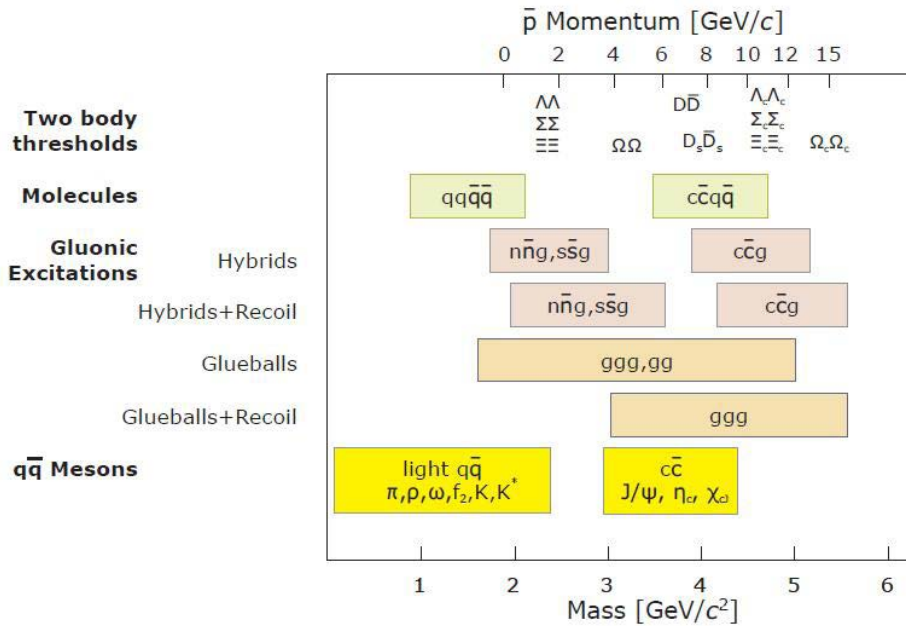
Figure 1.3: Invariant mass range (below) accessible to the $\overline{\text{P}}$ANDA experiment in comparison to the antiproton beam momentum (above). In Addition the producible particles and resonances are indicated.

spectroscopy of QCD bound states, hadron structure experiments and hadronic interaction experiments. In addition, not hadron specific experiments like CP-violation tests are possible. In the following, a selection of topics will be described in more detail:

1.1.1 Spectroscopy of QCD Bound States

Charmonium Spectroscopy   Despite charmonium was discovered experimentally already almost 40 years ago and many states in the charm region have been populated and identified, there are still plenty of theoretical issues which lack support by experimental precision data. Here the $\overline{\text{P}}$ANDA experiment can provide substantial support, because on the one hand antiproton-proton-annihilation is not restricted to the quantum numbers of the virtual photon $J^{PC} = 1^{--}$, like electron-positron-colliders. This allows to produce even rare or exotic states directly and with high abundance. On the other hand, the high precision provided by the HESR allows for a scanning of even narrow resonances, because the measured width only depends on the antiproton beam spread. Performing traditional charmonium spectroscopy with this direct access to the line shape of a resonance, one gets more sensitive to deviations from the expected charmonium potential shape and the comparison between theoretical models is much more effective. Furthermore, the widely unexplored region of open charm, meaning charmonium states decaying into charmed mesons, and charmonium decays near the $D\bar{D}$-threshold is accessible for $\overline{\text{P}}$ANDA. Here exists also the opportunity to study charmonium decays in the nuclear medium. An illustration of the charm system is shown in Fig. 1.4
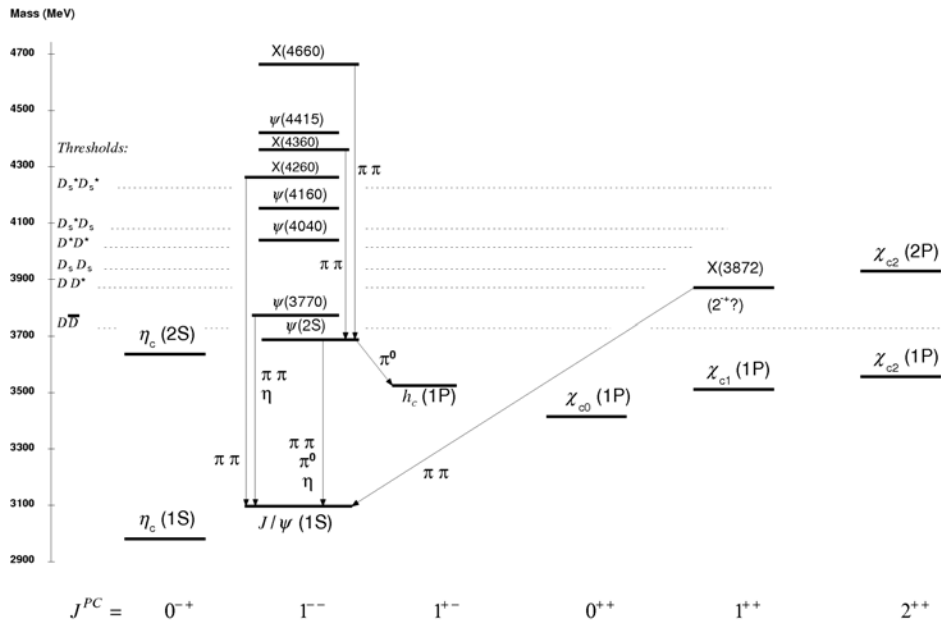

Figure 1.4: Level scheme of the charmonium system. On the ordinate the invariant mass energy equivalent is given. In addition, the different states are ordered by their quantum numbers J^{PC} (momentum J, parity P and charge conjugation C) [2].

Exotic Excitations Beside studies of the quark potential also the existence of gluonic excitations is a fundamental feature of QCD. In principle, two groups of gluonic excitations can be distinguished: bound $q\bar{q}$-states, where also the gluons, the exchange bosons of the strong interaction, themselves carry excitation degrees of freedom, or bound states consisting purely of gluons, so called glueballs. Due to the additional degrees of freedom added by the gluons, such excitations should be able to carry exotic quantum numbers not allowed for mesons, e.g. $J^{PC} = 0^{+-}, 1^{-+}, 2^{+-}$. Additionally, the decay of glueballs has to be flavour-blind, because they contain no valence quarks. Previous experiments with proton-antiproton-annihilations, like performed by the Crystal Barrel experiment at the Low Energy Antiproton Ring (LEAR), were able to find glueball candidates, but a non-ambiguous identification was not possible. As an example, the strong candidate state for the scalar glueball $f_0(1500)$ carries the non-exotic quantum numbers 0^{++} and has an width of $112\,\text{MeV}$. This allows a mixing with nearby light meson states like the $f_0(1370)$ and $f_0(1710)$ as closely described in [3], resulting in a non-flavour blind decay.

A comparison of recent theoretical studies of two-gluon glueballs using different theoretical approaches is shown in Fig. 1.5. It has to be stressed, that in the mass regime from $2 - 5\,\frac{\text{GeV}}{c^2}$ the differently calculated predictions agree on seven glueball states, four of these have exotic quantum numbers. Thus the above mentioned mixing, in this case with charmonium states, is excluded and $\overline{\text{P}}$ANDA should be able to give a clear experimental identification. Heavier Glueballs with masses near and above the $D\bar{D}$-threshold with up to now unknown width can decay in principle in any open channel, especially in D mesons and its excitations, are as well in the achievable mass region and can be investigated. The same holds for possibly existing multiquarks or mesic excitations of $q\bar{q}$-states. These are expected to be loosely bound and therefore possessing large widths. Such a candidate state is the $X(3872)$ with up to now unknown quantum numbers and only an upper limit to the width. As mentioned above, the resonance scan method deployed by $\overline{\text{P}}$ANDA is sensitive to the intrinsic line shape and therefore can unveil the nature of $X(3872)$. Benchmark channels in the search for exotics are:

$$\bar{p}p \to \tilde{\eta}_{c1}\eta \to \chi_{c1}\pi^0\pi^0\eta, \tag{1.1}$$

$$\tilde{\eta}_{c1}\eta \to D^0\bar{D}^{*0}\eta. \tag{1.2}$$

$\tilde{\eta}_{c1}$ represents a charmonium hybrid state with exotic quantum numbers 1^{-+}, decaying either via lower lying charmonium states (Eq. 1.1) or via open charm (Eq. 1.2). Especially for the open charm decay a large number of neutral mesons is produced, which can result in eight to twelve γ-particles in the final state, as illustrated in Fig. 1.6. This sets strong demands on the electromagnetic calorimeter of $\overline{\text{P}}$ANDA, the only subsystem capable of detecting photons.
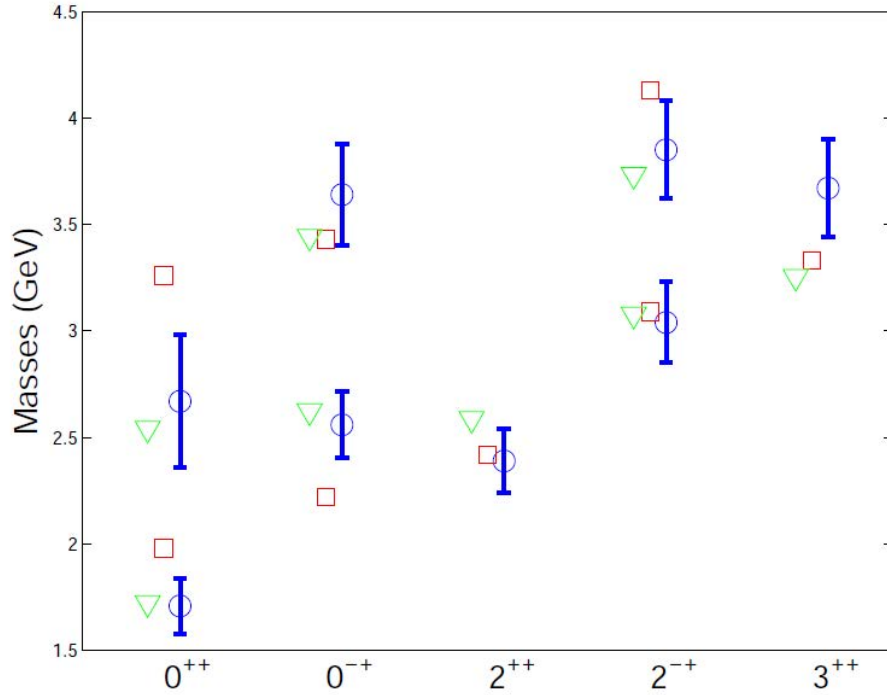
Figure 1.5: Comparison of theoretical predictions for two-gluon glueball states taken from [4]. The invariant mass energy equivalent is given for different quantum numbers determined by lattice QCD calculations [5] (circles) and constituent models from [6] (squares) and [7] (triangles).

$$\bar{p}p \to \bar{\eta}_{c1} + \eta$$
$$\hookrightarrow D^0 + \bar{D}^{*0}$$
$$\hookrightarrow D^0 + \pi^0$$
$$\hookrightarrow K^-\pi^+\pi^0$$
$$\hookrightarrow K^-\pi^+\pi^0$$
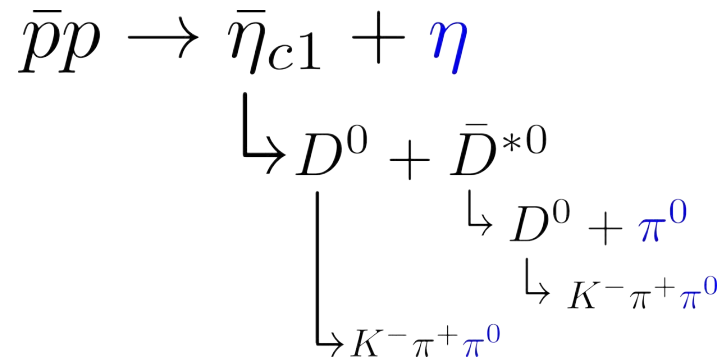
Figure 1.6: Possible decay scheme of hybrid state $\tilde{\eta}_{c1}$. The neutral mesons in the final state (blue) decay to a large fraction ($BR\left[\pi^0 \to 2\gamma\right] \approx 99\%$, $BR\left[\eta \to 2\gamma\right] \approx 39\%$) into 2γ, which yields 8 photons in the final state. For the other major decay branch of $\eta \to 3\pi^0$ ($BR \approx 33\%$), one ends up with 12 final state photons.

Charmed and Strange Baryons   One of the predominant goals of non-perturbative QCD is an understanding of the excitation spectra of baryons. While there is plenty of experimental data available for nucleons, the agreement to a still growing variety of different theoretical models is still unsatisfactory. On the contrary, the experimental efforts concerning excitation spectra of strange baryons is sparse and theoretical work on e.g. Ω and Ξ excitation spectra lack an experimental validation. $\overline{P}$ANDA can give a relevant contribution to the spectroscopy of strange, multi-strange and potentially even charmed baryons. Particularly for Ξ resonances, which can be produced in large abundance and are generally much narrower in width than nucleon or Δ resonances, the chance for experimental discoveries appears very promising. Also the reaction $\bar{p}p \to \Omega\bar{\Omega}$, on which no experimental data exists, will be a subject to study. Theoretical estimates for the cross section [8] amount to approximately $2\,\mathrm{nb}$, resulting in an event rate at full HESR luminosity of roughly 700 produced $\Omega\bar{\Omega}$ pairs per hour. This should be sufficient to measure excited states and their decay modes. Most important subdetectors for these investigations of strange baryons are the tracking detectors which pin down secondary vertices from weak decays.

1.1.2 Hadron Structure Experiments using Electromagnetic Processes

Several experimental concepts are envisaged to gain insight in the structure of hadrons and especially the nucleon. For example, in addition to the well explored space-like electromagnetic form factor of the nucleon with momentum transfer $q^2 \leq 0$, in antiproton-proton-annihilations it is possible to measure the time-like form factor ($q^2 \geq 0$) above the kinematic threshold of $q^2 = 4m_p^2c^2$. It represents the frequency spectrum of the electromagnetic response of the nucleon. The central reaction for the cross section measurement is $\bar{p}p \to e^+e^-$. Since the dominating background is given by the reaction $\bar{p}p \to \pi^+\pi^-$, an efficient separation between electrons and pions is mandatory. Here the Electromagnetic Calorimeter (EMC) can contribute especially in the high momentum range, where the efficiency of the other Particle Identification (PID) subdetectors decreases considerably. The transverse distribution of the partons included in the nucleon can be accessed by analysis of so called Drell-Yan processes, reactions where quark and antiquark annihilate to form a lepton pair via an virtual photon. Furthermore, the intermediate region between perturbative and non-perturbative QCD and the in recent years developed theoretical framework of generalised parton distributions can be studied via hard exclusive antiproton-proton-annihilation processes. Key channels of this research area at $\overline{P}$ANDA are:

$$\bar{p}p \to \gamma\gamma \tag{1.3}$$

$$\bar{p}p \to \pi^0\gamma. \tag{1.4}$$

Feasibility studies and simulations state that for the successful measurement of this processes in dependence of the Mandelstam variables s and t at $\overline{\text{P}}$ANDA, the performance of the electromagnetic calorimeter plays a significant role.

1.1.3 Hadronic Interaction Experiments

In-medium Modifications of Charmed Mesons   While the in-medium properties of light quark mesons have been studied in numerous experiments in proton-, photon- or nucleus-nucleus collisions, the antiproton-nucleus collisions available at $\overline{\text{P}}$ANDA are well suited to investigate this topic also for charmed hadrons. Like for the mass split observed for K and $\bar{K}$ mesons at normal nuclear matter density, one expects a splitting between D and $\bar{D}$ mesons of about $100\,\text{MeV}$ as well. An experimental approach to observe mass modifications of charmed mesons involves sub-threshold production, where a cross section enhancement should be visible. Also a shift of the $D\bar{D}$-threshold in the nuclear medium should distinctly increase the width of certain charmonium states, opening more possible decay channels. Nevertheless, taking the additional collisional width and rescattering of the D mesons on nucleons in account, the effect would be hard to observe.

Hypernuclear Physics   If one or more nucleons of a nucleus are replaced by hyperons[3], this system is called hypernucleus. Effectively, a third dimension is added to the nuclear chart. A hyperon in a nucleus is not bound by the Pauli principle and therefore able to access nuclear states not available to protons or neutrons. Hence they provide a unique and sensitive probe to the structure of nuclei. Furthermore, also the properties of the nuclei might change. Level schemes and decay spectra of hypernuclei or double hypernuclei can provide the experimental base for recently developed theoretical models in the fields of baryon-baryon interaction, weak decays, multi-strange atoms and form the doorway to exotic quark states.

1.2 The $\overline{\text{P}}$ANDA Detector

1.2.1 Overview

As described in the previous section, the $\overline{\text{P}}$ANDA experiment has a broad spectrum of research areas. Consequently, the $\overline{\text{P}}$ANDA detector is a multi-purpose detector able to detect a large variety of different particles from charged leptons and mesons to neutral particles like γ's and neutrons over nearly the complete solid angle. An

---

[3]Baryons containing strange quarks

overview of its layout is given in Fig. 1.7. As a fixed target experiment the detector has an asymmetric shape, taking into account the larger energy and multiplicity of particles kinematically boosted in beam direction. A Target Spectrometer covers the complete region near the interaction point excluding particles emitted at polar angles with respect to the beam axis smaller than 10° in horizontal and 5° in vertical direction, respectively. Particles escaping the Target Spectrometer in this direction will reach the Forward Spectrometer. The first device in beam direction is a dipole magnet capable of achieving a magnetic field strength of up to 1 T, deflecting charged particles and hereby decreasing the track density. Located inside the magnetic field are mini drift chambers for tracking. More tracking detectors are distributed at different distances from the target throughout the Forward Spectrometer. Also an Ring Imaging CHerenkov (RICH) detector for charged particle identification is foreseen and will be placed between the dipole magnet and an Shashlyk type Forward EMC. This calorimeter consists of sandwiches of lead and plastic scintillator plates. The light produced in the scintillator plates, e.g. by an electromagnetic shower, is guided to the photomultiplier tube sensor by wavelength shifting plastic fibres, as displayed in Fig. 1.8. These match the wavelength of the generated scintillation light to the range of highest sensitivity of the sensor's photo cathode. Such Shashlyk EMC modules with similar design have already been in use at other experiments and are known to attain an energy resolution of approximately $\frac{3\%}{\sqrt{E[\text{GeV}]}}$ [9], at least in the GeV range. Since the energy of most particles will be determined in the Shashlyk EMC, where they also will be absorbed, the last detector station in the Forward Spectrometer is the Forward Range System (FRS), effectively consisting of alternating layers of so called Mini Drift Tubes (MDTs) and iron. It is also part of the MUOn Detection System (MUO). The purpose of this device is to track and identify muons and efficiently separate them from charged pions due to their different penetration depth in the FRS. The $\overline{P}ANDA$ Target Spectrometer shown in Fig. 1.9 is designed in a way that the different subdetectors surround the interaction region like onion skins. In the following the detector systems are described subsequently according to their distance to the target.

Target System   Because the $\overline{P}ANDA$ Detector is located inside of a storage ring, it is desirable that beam particles not taking part in a reaction are kept inside the ring to maintain the high luminosity antiproton beam quality for as many revolutions as possible. Therefore, a target has to be minimum obtrusive. Three different target designs are envisaged, which mutually complement each other: cluster jet target, pellet target and wire target. The cluster jet target uses an convergent-divergent nozzle to expand a pre-cooled gas which cools down further and forms a beam faster than the speed of sound. Under the proper condition the gas condensates and forms so called nanoparticle clusters. The high mass of the nanoparticles compared to gas molecules leads to a negligible scattering of the beam particles on residual gas in the target region and enables high target densities even several meters away from the nozzle. Thanks to
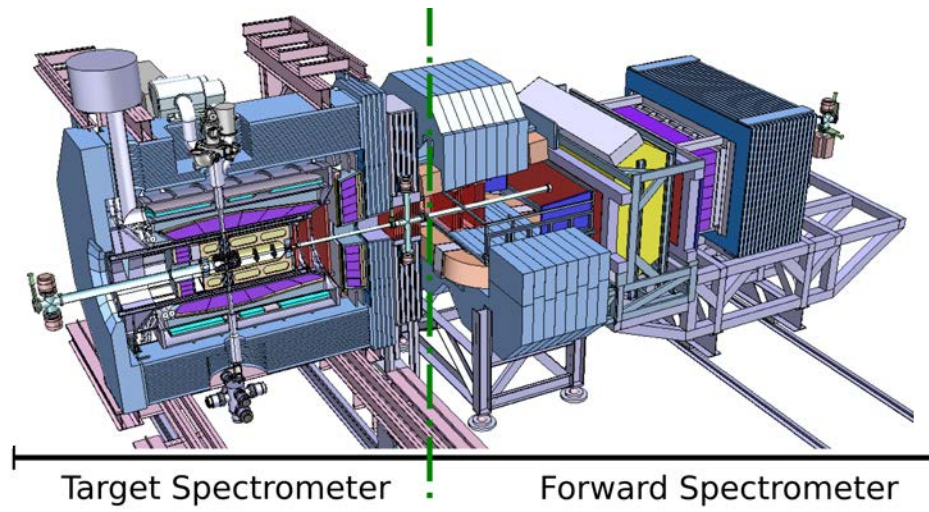
Figure 1.7: Layout of the $\overline{\mathrm{P}}$ANDA Detector.
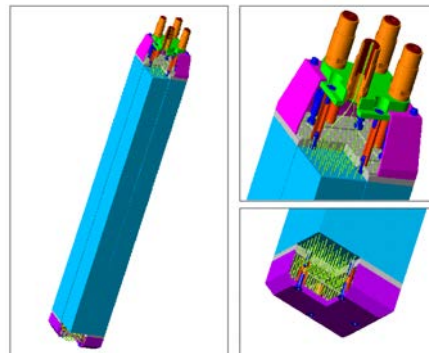
(a) CAD of a Shashlyk module
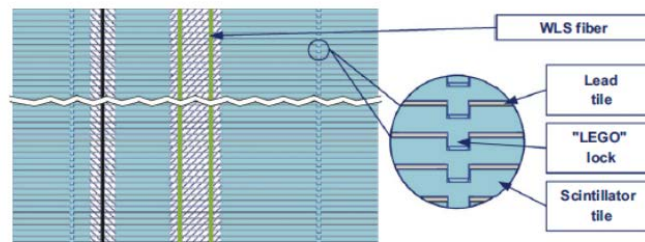
(b) Longitudinal cross section

Figure 1.8: Schematics of the Shashlyk type Forward Calorimeter [9].
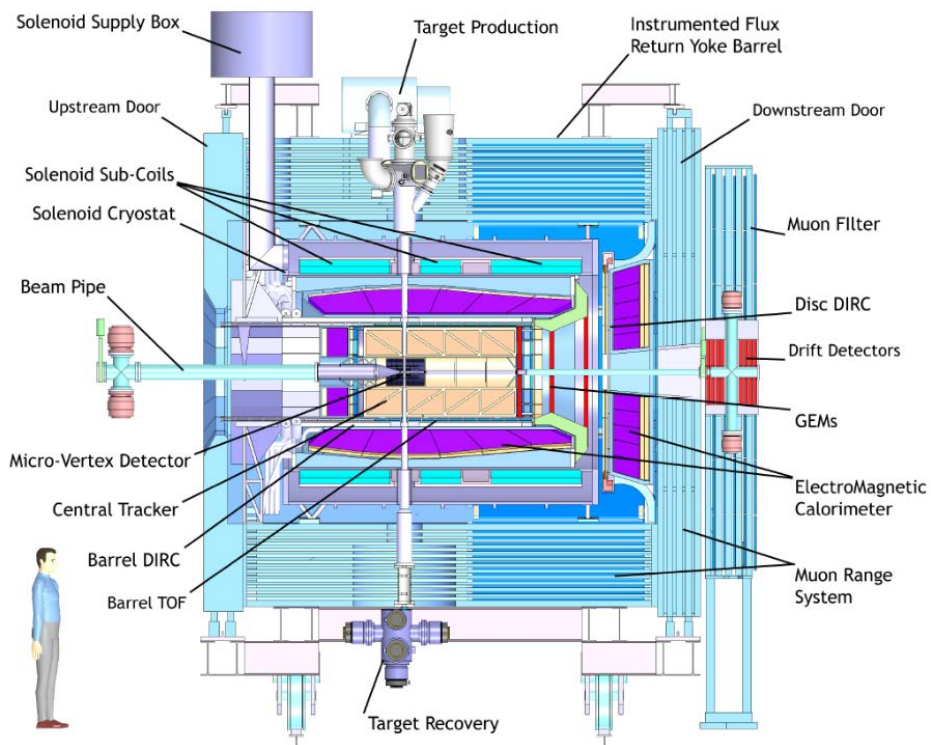
Figure 1.9: Layout of the $\overline{\text{P}}$ANDA Target Spectrometer.

this fact, most of the machinery needed for target preparation can be placed outside the solenoid and only a small diameter target pipe perpendicular to the beam direction passes through the detector, minimising space not occupied by detectors. One main advantage of the cluster jet is the homogeneous target density distribution, which avoids time structures in the luminosity as well. The target material can be varied from the standard H_2 as proton and D_2 as neutron target to additionally prepare cluster jets consisting of heavier gases like O_2, N_2, Ne, Ar, Kr and Xe. The pellet target follows a compact design, too. Here an axially symmetric jet of liquid is injected in a triple point chamber trough a periodically excited oscillating nozzle at which the jet disintegrates into droplets. These droplets are then injected into vacuum where they freeze out to form pellets. Pellet size can be varied to enable either an accurate tracking of single large sized pellets or a high number of small pellets to achieve high luminosity. In another phase of the measurement programme, it is envisaged to replace cluster jet and pellet target by solid target materials in the form of thin wires, which enables the investigation of research areas not possible with the former target material, e.g. in-medium modifications of hadrons.
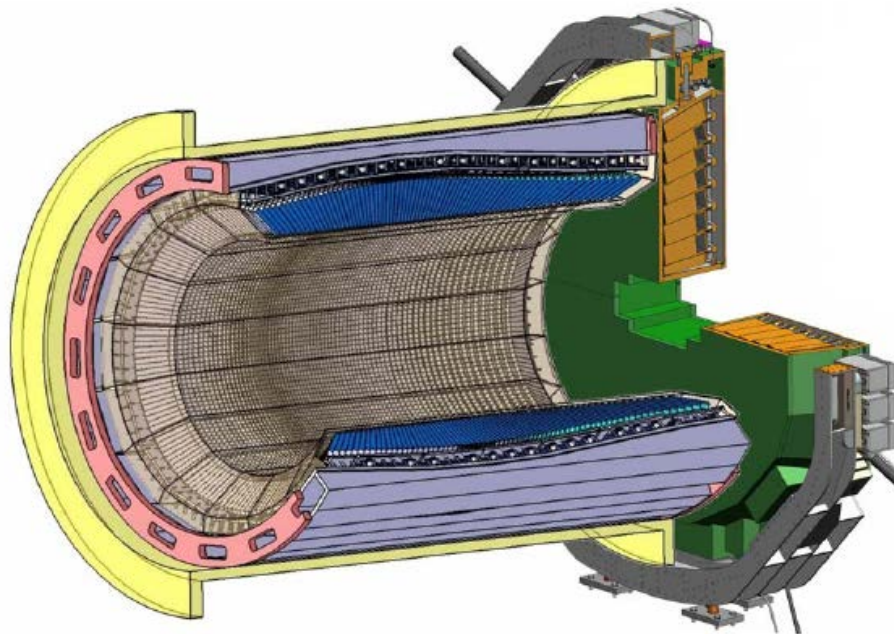

Figure 1.10: Layout of the electromagnetic calorimeter located in the Target Spectrometer.

Micro Vertex Detector   Directly surrounding the interaction point and the beam pipe, the Micro Vertex Detector (MVD) is the first detector hit by particles produced in a reaction. Its task is to measure the track of charged particles with high precision

close to the target, which is needed to define the initial reaction vertex and a starting reference for the later tracking in the straw tubes. Moreover it is mandatory for the reconstruction of secondary vertices from weak decays of charmed and strange hadrons, e.g. D-Mesons or hyperons. The design concept of the MVD is pictured in Fig. 1.11 and features a four layer barrel shaped part axially symmetric around the beam direction together with six disks in forward direction. The two inner barrel layers as well as all disks will consist of so called hybrid pixel detectors, whereas the outer barrel layers feature double-sided silicon microstrip detectors. The detection principle of these silicon detectors is basically to collect the number of electron-hole-pairs created in the silicon by ionisation due to a traversing charged particle. The produced charge is collected either on pixelated electrodes or anode / cathode strips placed on each side of the silicon, oriented in perpendicular direction. Since the energy loss $\frac{dE}{dx}$ of a charged particle in the silicon follows Bethe's energy loss equation (see Eq. 1.5), which will be briefly discussed later, it strongly depends on the velocity of the traversing particle. Together with a momentum or kinetic energy measurement of the same particle by another subdetector, it is possible to calculate the mass of the particle and therefore identify it.

Straw Tube Tracker and Gas Electron Multiplier Stations Enclosing the MVD is the Straw Tube Tracker (STT), consisting of 4636 individual straw tube modules [11]. In principle, an individual straw tube consists of an aluminised Mylar[4] cylinder with 10 mm inner diameter acting as cathode and a gold-plated tungsten-rhenium anode wire mounted in the cylinder axis. The 1500 mm long cylinder volume is filled with overpressured $\mathrm{Ar} + 10\,\% \,\mathrm{CO}_2$ gas mixture which provides stability and allows to operate the straw tube as a proportional counter. Hence, the energy loss of charged particles traversing the gas volume and the charge produced by secondary ionisation due to the high electric field near the anode wire are proportional. Accordingly, a single standalone straw tube gives information on the energy loss and in addition on its position along the anode wire, determined by the signal delay. For most of tubes this position reflects directly the position on the z-axis of the $\overline{\mathrm{P}}$ANDA detector (compare coordinate system in Fig. 1.11). All straw tubes are stacked together in two similar half shells. The position of a responding straw in the x-y-plane of the STT then directly relates to the corresponding particle position. However, to achieve a more stereoscopic view of a particle track, a fraction of straw tubes is skewed slightly with respect to the z-axis. With the described design, a polar angle coverage from 10° to 140° at an average material budget of only 1.23% of a radiation length X_0 (see Section 1.3) can be achieved, while simulations show that it is feasible to deduce the momentum from particle trajectories measured with the STT with a resolution of about $\frac{\sigma_p}{p} \approx 1 - 2\%$. Charged particle tracking for polar angles between 3° and 20°, after the MVD forward

---

[4]Brand name of biaxially-oriented polyethylene terephthalate (boPET) foil
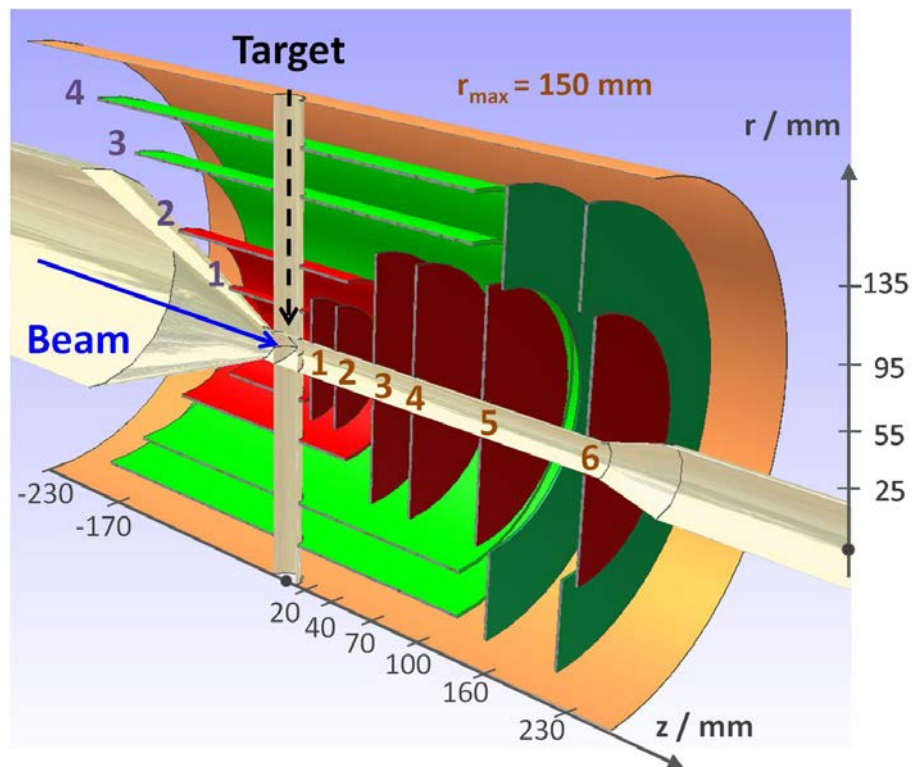
Figure 1.11: Proportionate schematics of the MVD, shown together with beam and target pipe. Red areas represent silicon hybrid pixel detectors, while the green areas indicate double-sided silicon strip detectors. The orange plane marks the inner radius of the central tracker [10].

discs, is performed by so called Gas Electron Multipliers (GEMs) [12]. Currently 3 to 4 GEM-Discs are envisaged in distances of 360 mm from each other. The centre of each gas filled GEM-Disc features a segmented double-sided readout pad plane for charge collection. Like a sandwich, it is enclosed on each side by 2 to 3 micro-perforated isolating foils, thinly coated from both sides with electrically conducting material. These are the actual GEMs. A voltage applied to the opposite sides of a foil generates large electric field strength inside and at the edges of the perforations. This field is strong enough to lead to secondary ionisations and therefore multiplying an initial primary ionisation. The outermost layers are drift electrodes, usually at lower electrical potential than the readout pads. In principle, a GEM-Disc is an ionisation chamber, where the GEMs, like a magnifying glass, project an amplified picture of the primary charge on the readout pad. Advantages of GEM detectors compared to conventional Multi Wire Proportional Chambers (MWPCs) or drift chambers are the easier production together with more flexible geometry, especially of the readout pads, and higher rate capability due to faster collection of the inert positive ions.

DIRC Detetectors Both, charged particle identification in the barrel part as well as in forward direction are based on the Detection of Internally Reflected Cherenkov light (DIRC) technique illustrated in Fig. 1.12b. Basically it relies on the detection of the Cherenkov light (see Sec. 1.3.1) produced in a fused silica radiator which is propagated to the sensor at the radiator rim via total internal reflection. This light is guided out of the radiator into an expansion volume with lower index of refraction than the radiator. Its task is to widen initially small angular differences while projecting the light onto the photo sensor. Thus, spatial coordinates where the single Cherenkov photon is detected on the position sensitive photo sensor, combined with the charged particle trajectory from other tracking detectors, translates to the initial Cherenkov angle ϑ_c. According to Eq. 1.17, it is equivalent to the particle velocity and identifies at known momentum the particle. Main advantage of DIRC is on the one hand the compactness due to the higher photon yield of a solid state radiator and on the other hand the larger Cherenkov angles and lower threshold momentum induced by the higher index of refraction compared to conventional gas-filled RICH detectors. Nevertheless these advantages can be outweighed by high photon absorption. Hence, a radiator of high quality is mandatory. In $\overline{P}ANDA$ two subdetectors with different radiator geometry are foreseen. For large polar angles the Barrel DIRC design envisages a set of flat cuboid shaped fused silica bars. An appropriate focusing optics allows an expansion volume and photo sensors to be placed only at the upstream radiator side. Its design goal is to allow a 3σ pion-kaon separation for particle momenta from $0.5\,\mathrm{GeV}/c$ to $4.0\,\mathrm{GeV}/c$. Low polar angles in forward direction will be covered by a Disc-DIRC, consisting of four identical trapezoidal fused silica plates. Readout is performed on the longest trapezoid side, while the three remaining edges are mirror coated to minimise reflection losses.

(a)

(b)
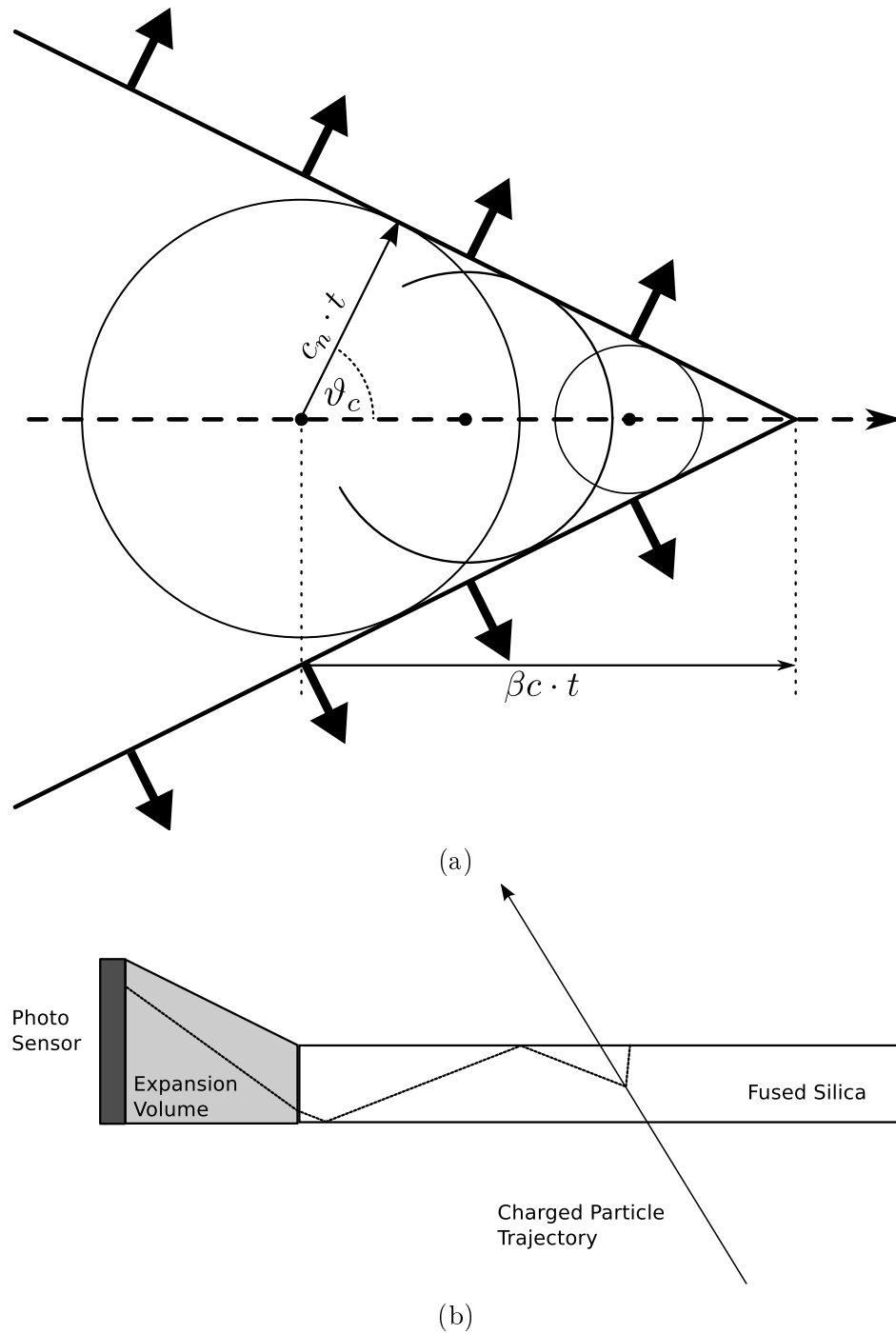
Figure 1.12: Formation of the Cherenkov cone in a radiator due to a traversing par-
ticle with velocity βc (a) and sketch of the DIRC technique (b). The
Cherenkov light is emitted in the fused silica radiator at a characteristic
Cherenkov angle. Like indicated, the fraction of the light which is totally
reflected inside the radiator enters an expansion volume with lower index
of refraction, effectively scaling the emission angle to higher values. The
position where the Cherenkov photon is detected by the position sensitive
photo sensor directly relates to the emission angle.

Electromagnetic Calorimeter   Next to the DIRC detectors is the EMC which is divided into three parts: Barrel EMC, Forward and Backward Endcap, named accordingly to their position with respect to the beam direction. A detailed description of the EMC, depicted in Fig. 1.10, can be found in Section 1.4.

Magnet   All previously described detector systems of the Target Spectrometer are enclosed by a superconducting solenoid with the beam pipe as symmetry axis. The streamlines of the magnetic field are parallel to the beam direction and it is able to provide a central magnetic flux density of $2\,\mathrm{T}$ with a homogeneity of $2\,\%$. Due to its superconducting nature, the solenoid is mounted inside a cryostat, which in turn serves as mounting structure for the inner detectors. Supporting the cryostat, as well as other inner detectors like e.g. the EMC Forward Endcap, is an octagonal barrel shaped iron yoke. It returns the magnetic flux produced by the solenoid and enhances the quality of the magnetic field, but also, due to its large amount of iron, serves as shielding to the area outside of the detector. To enable access to the inner detector systems, both ends of the yoke are designed as opening doors.

Muon Detection System   The iron yoke and the upstream opening doors are laminated into several layers to house the MUO. It operates as a so called Range System (RS). Between the iron samples serving as absorber, multi-layered MDTs perform a tracking of muons traversing the iron yoke or stopped by the absorber. In the latter case, the range in the absorber even allows an estimation of the muon energy at known momentum. Reflecting the fixed target kinematics, the iron sample thickness is increased from $3\,\mathrm{cm}$ in the yoke barrel to $6\,\mathrm{cm}$ in the upstream door. To increase the absorber depth even further for low polar angles and enhance the magnetical shielding, an additional Muon Filter (MF) with similar mechanical structure as the MUO-Endcap is inserted between it and the dipole magnet of the Forward Spectrometer.

1.3 Calorimeter Physics

1.3.1 Radiation interaction with matter

Detection of radiation and the the measurement of its energy with an electromagnetic calorimeter requires a basic understanding of the processes occurring in the detector material. In principle, these processes split in two categories, those triggered by charged particles and those triggered by photons, respectively. In the following both will be briefly discussed.

	ELECTRON SCATTERING	BREMS-STRAHLUNG	CHERENKOV RADIATION	ELASTIC NUCLEAR SCATTERING	NUCLEAR REACTIONS
	I	II	III	IV	V
Energy loss contribution	**main contribution** → Bethe Eq.	dominant for e^- if $E > E_c$	usually $< 10^{-3}$ of I	relevant for $\beta < 10^{-3}$	relevant for $E > 100\,\mathrm{MeV}$
Effect in Medium	Ionisation	EM shower	Coherent visible EM radiation	Nuclear recoil	Hadronic shower
Measured Quantity	Energy E	Energy E	Velocity β		Energy E

Table 1.1: Overview of the different processes contributing to the energy loss of charged particles in matter. A qualitative statement of the relative strength of the contribution to the total energy loss is given as well as the usual effect observed in a detector medium and the measured quantity.

Charged particles

The total energy loss per distance of a charged particle in an absorber or detector material is given by a combination of five processes:

   I Inelastic Scattering on atomic electrons

  II Bremsstrahlung

 III Cherenkov radiation

 IV Elastic scattering on nuclei

  V Nuclear reactions

Tab. 1.1 presents an overview over these processes. The dominating process with the main contribution to the total energy loss is inelastic electron scattering. The energy loss per distance of a particle with charge number z and velocity $v = \beta c$ in a homogeneous material with electron density n due to collisions with atomic electrons is given by Bethe's energy loss equation:

$$-\frac{dE}{dx} = \left(\frac{e^2}{4\pi\epsilon_0}\right)^2 \frac{2\pi n z^2}{m_e \beta^2} \left[\ln\left(\frac{2m_e c^2 \beta^2 W_m}{I^2(1-\beta^2)}\right) - 2\beta^2 - \delta - 2U\right] \tag{1.5}$$

$$n = \frac{Z \cdot \rho}{A_r \cdot u} \tag{1.6}$$

In this notation ϵ_0 is the vacuum permittivity, e the elementary charge and m_e the electron mass. The quantity W_m represents the maximum energy transfer from incoming particles to an absorber electron, while I is the average ionisation potential of the absorber. δ is a correction for the density-effect, especially important at very large energies, while U is related to the non-participation of electrons in inner shells to the ionisation process at very low energies. Except I, all properties of the absorber material are included in the electron density n given by 1.6, which depends mainly on the absorber density ρ, since the ratio of atomic number Z and relative atomic mass (atomic weight) A_r is nearly constant for all elements and u represents the constant unified atomic mass unit. Fig. 1.13 shows the ionisation energy loss in different materials over a large range of $\beta\gamma = \beta \cdot \frac{1}{\sqrt{1-\beta^2}}$, representing the particle velocity in a relativistic manner. One recognises that in the region around $\beta\gamma \approx 3$ the energy loss is minimal and varies only slightly. Particles kinematically located in this region are called Minimum Ionising Particles (MIPs). For most materials their energy loss amounts to $\sim 1 - 2 \, \frac{\text{MeV} \cdot \text{cm}^2}{\text{g}}$. This leads to the fact that usually large absorbers with high density are needed to stop MIPs. A prominent example for MIPs are cosmic muons, which are able to penetrate even several hundreds of meters of rock. The emission of Bremsstrahlung gives another contribution to the energy loss. Fundamentally, the radiation emitted per unit of time by a particle with charge number z and mass m due to acceleration in the coulomb field of an absorber with atomic number Z, is given by Eq. 1.7

$$\frac{dE}{dt} \propto \frac{z^2 Z^2}{m^2}. \tag{1.7}$$

Hence for light charged particles, in particular electrons and positrons, the emission of Bremsstrahlung gives a significant contribution to the energy loss, while heavy charged particles mostly lose their energy by collisions according to Eq. 1.5, which is independent of the particle mass m. For this reason, the following observations focus on the energy loss of electrons and positrons. Their energy loss per distance due to radiation emission at a given initial total energy E_0 is expressed in Eq. 1.8:

$$-\frac{dE}{dx} = \frac{\rho}{A_r \cdot u} E_0 \Phi_{rad}, \tag{1.8}$$

$$\Phi_{rad} = 4Z^2 r_e^2 \alpha \left[\ln\left(\frac{183}{\sqrt[3]{Z}}\right) + \frac{1}{18} - f(Z) \right], \tag{1.9}$$

$$r_e = \frac{e^2}{4\pi\epsilon_0 m_e c^2}. \tag{1.10}$$

This expression of Φ_{rad} (Eq. 1.9) is valid for high energies $E_0 \gg 137 m_e c^2 Z^{-\frac{1}{3}}$, where the electric field of the nucleus is completely screened by the surrounding bound electrons. The constant r_e is the classical electron radius, while $f(Z)$ represents a higher order correction to the Born approximation which is used to derive Eq. 1.8 and 1.9.
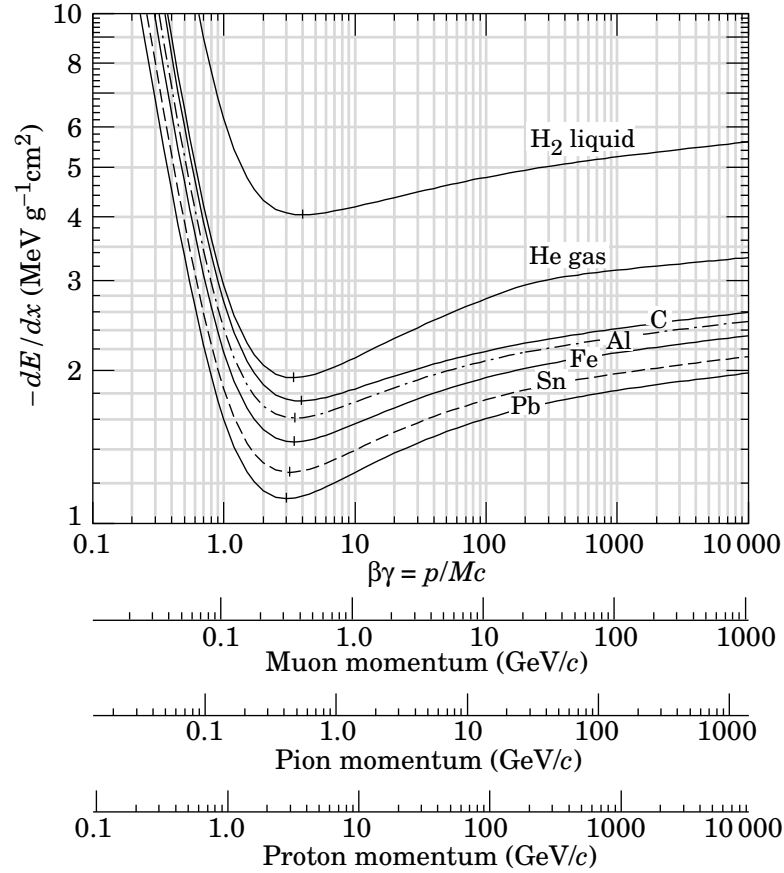
Figure 1.13: Energy loss due to collisions with atomic electrons in different absorber materials as a function of $\beta\gamma$. Additionally, the momentum for a muon, pion and proton is given [13].

Eq. 1.9 takes only radiative energy loss due to the absorber nuclei into account. To accommodate also Bremstrahlung on atomic electrons, the term Z^2 has to be replaced by $Z(Z+1)$. A more convenient form of Eq. 1.8 is

$$-\frac{dE}{dx} = \frac{E}{X_0}, \tag{1.11}$$

which is solved by

$$E(x) = E_0 \cdot e^{-\frac{x}{X_0}}, \tag{1.12}$$

$$X_0 = \frac{A_r \cdot u}{4Z(Z+1)\rho\alpha r_e^2[\ln(183Z^{-\frac{1}{3}}) - f(Z)]}. \tag{1.13}$$

The quantity X_0 is called radiation length and depends solely on the absorber material. Its is defined as the mean pathlength in a given absorber material after which

the energy $E(x)$ of an electron amounts to $\frac{1}{e}$ of its initial energy E_0. A common approximation of Eq. 1.13 is

$$X_0 = \frac{716.4 A_r}{Z(Z+1)\ln(\frac{287}{\sqrt{Z}})} \left[\frac{\text{g}}{\text{cm}^2}\right],\tag{1.14}$$

which is accurate within 2.5 % for most materials [14]. X_0 can be regarded as the natural unit of absorber thickness. If expressed in terms of radiation length, the radiation energy loss becomes nearly independent of the material properties. For mixtures and compounds like most scintillator materials, an effective value of the radiation length can be approximated by

$$\frac{1}{X_0} = \sum \frac{w_i}{X_i},\tag{1.15}$$

with the radiation length of the ith element X_i and its mass fraction w_i. Comparing Eq. 1.11 to Eq. 1.5, it is evident that at high energies the linear rise of the radiative energy loss exceeds the logarithmically rising ionisation loss. This is much more pronounced for absorbers with high atomic number Z, which contributes quadratically to radiative losses. Generally, the energy at which both energy losses per distance due to ionisation and due to Bremsstrahlung are equal is called the critical energy E_c. However, there is also a popular alternate calculus introduced in [15], which defines E_c as the energy, at which the energy loss per radiation length due to ionisation is equal to the electron energy. A convenient approximation for solids and liquids is given by

$$E_c \approx \frac{610\,\text{MeV}}{Z + 1.24}.\tag{1.16}$$

Emission of coherent Cherenkov light in a radiator with index of refraction n is caused by a particle with velocity $v = \beta c$ larger than the speed of light in this medium $c_n = \frac{c}{n}$. Due to formation of a electromagnetic shock wave (compare Fig. 1.12a), analogue to a sonic shock wave created by a supersonic aircraft, the Cherenkov light wave front is conical and travels at an characteristic Cherenkov angle ϑ_c relatively to the charged particle trajectory, given by the relation:

$$\cos\vartheta_c = \frac{1}{\beta n(\omega)}.\tag{1.17}$$

It has to be stressed that in dispersive media like fused silica, the index of refraction $n(\omega)$ is dependent on the frequency ω of the generated light, leading to a smearing of the Cherenkov cone. The amount of photons emitted per distance as a particle with charge ze passes a radiating medium can be calculated by Eq. 1.18.

$$\frac{dN}{dx} = 2\pi z^2 \alpha \sin^2\vartheta_c \int\limits_{\lambda_1}^{\lambda_2} \frac{1}{\lambda^2}\,d\lambda \tag{1.18}$$

To evaluate the number of photons per cm available at maximum, the integration over the typical range of sensitivity of a PhotoMultiplier Tube (PMT) and Avalanche Photo Diode (APD) is performed in Eq. 1.19 and 1.20, respectively.

$$\left.\frac{dN}{dx}\right|_{350\,\text{nm}}^{550\,\text{nm}} = 475 \cdot z^2 \sin^2 \vartheta_c \, \frac{\text{photons}}{\text{cm}} \tag{1.19}$$

$$\left.\frac{dN}{dx}\right|_{350\,\text{nm}}^{850\,\text{nm}} = 771 \cdot z^2 \sin^2 \vartheta_c \, \frac{\text{photons}}{\text{cm}} \tag{1.20}$$

This results in several hundred generated Cherenkov photons per cm which is not a large number. However, compared to the scintillation light yield of lead tungstate at room temperature (Tab. 1.3), for a minimum ionising particle which would amount to approximately $1836 \, \frac{\text{photons}}{\text{cm}}$, one recognises that roughly a fifth of this light collected with a PMT is Cherenkov light. This consideration is in agreement with the measurements presented in [16]. Although there is Cherenkov light emitted by charged particles in an material, the fact that the photons are near to the visible range entails that the energy loss per distance is small compared to ionisation losses. For instance, in condensed materials the energy radiated is of the order of $\approx 10^{-3} \, \frac{\text{MeV} \cdot \text{cm}^2}{\text{g}}$ while the MIP energy loss amounts to $\approx 2 \, \frac{\text{MeV} \cdot \text{cm}^2}{\text{g}}$. Therefore, in most cases where solid absorbers are concerned, energy loss due to Cherenkov radiation is negligible. The same holds true for elastic scattering on nuclei, since the involved absorber atoms have a considerably higher mass than the incoming particle leading to low momentum transfers and hence low energy loss. Cross sections for nuclear reactions are usually small compared to electromagnetic cross sections. The mean free pathlength Λ_I is defined as the distance after which the number of charged particles is reduced by $\frac{1}{e}$ due to inelastic nuclear reactions. As a general rule Λ_I is much larger than the electromagnetic radiation length X_0 and the energy losses due to electromagnetic processes are dominant. For neutral hadrons, especially neutrons, Λ_I is generally the main parameter governing the energy loss.

Photons

The interaction of photons with matter differs drastically from that of charged particles. Here the the main processes are:

   I Photoelectric effect

  II Compton scattering

III Electron-positron pair production

The photoelectric effect is understood as the absorption of a photon with energy E_γ by an atomic electron, which results in an ejection of this electron from the atom. Its kinetic energy E_e is then

$$E_e = E_\gamma - E_B \tag{1.21}$$

where E_B represents the electrons binding energy. Because of the discrete nature of E_e, the photoelectric effect provides a direct information about the photon energy. Due to the inclusion of different atomic shell effects, an exact cross section formula, valid for all photon energies, is difficult to derive. For energies above the K-Edge though, the photoelectric cross section per absorber atom, σ_p, follows the general dependence

$$\sigma_p \propto \frac{Z^{4-5}}{E^{\frac{7}{2}}}. \tag{1.22}$$

Accordingly, an absorber with high atomic number Z is advantageous to achieve a compact and efficient absorption of photons. Compton scattering represents the scattering of a photon on a free electron. This condition is also met by an atomic electron, if the condition $E_\gamma \gg E_B$ is fulfilled. Following the laws of momentum and energy conservation, the incoming photon transfers part of its energy as recoil energy E_e to the electron during the scattering process, resulting in a photon with lower energy $E_\gamma\prime$, depending on the scattering angle ϑ like displayed in Eq. 1.23.

$$E_e = E_\gamma \cdot \frac{\epsilon(1 - \cos\vartheta)}{1 + \epsilon(1 - \cos\vartheta)} \tag{1.23}$$

$$\epsilon = \frac{E_\gamma}{m_e c^2} \tag{1.24}$$

In contrast to the photoelectric effect, this is a continuous distribution of E_e up to a maximum value of $E_{e,max} = E_\gamma \frac{2\epsilon}{1+2\epsilon}$ at an scattering angle of 180°, which is usually referred to as the Compton edge. Because of this, Compton scattering is usually regarded as undesirable for a photon energy measurement, since it generates a continuous background. Furthermore, scattered photons may escape the detector material which leads to energy leakage effects. The cross section for the Compton scattering on a free electron, σ_c, can be calculated via quantum electrodynamics and is given by the Klein-Nishina formula. The general dependence under the condition $E_\gamma \gg m_e c^2$ follows

$$\sigma_c \propto \frac{Z}{E}. \tag{1.25}$$

For one absorber atom, this has to be multiplied by the number of its electrons Z. Beside Compton scattering, which leads to scattered photons with reduced energy, there are also the processes of Thompson scattering and Rayleigh or coherent scattering ($E_\gamma \ll E_B$). The former can be regarded as the low energy limit of scattering of

photons on free electrons, where $E_\gamma \ll m_e c^2$ and therefore no recoil energy is transferred, while the latter takes place under the condition $E_\gamma \ll E_B$ and is performed on all electrons of an atom in a coherent manner. Both are elastic processes not resulting in photons with reduced energy, but changing the direction of the incoming photons. In most cases, they can be neglected for higher energies. If the energy of a photon exceeds the limit of $2m_e c^2$, also electron-positron pair production is a possible reaction channel. Here the photon is converted into an electron-positron pair and its energy, reduced by their rest energy, is shared between the two. Because of momentum conservation, a third body, usually a nucleus of the absorber material, has to participate in the process, but also pair production in the field of atomic electrons is possible. The mechanism of pair production is similar to that of the Bremsstrahlung process discussed in Sec. 1.3.1. For $m_e c^2 \ll E_\gamma \ll 137 m_e c^2 Z^{-\frac{1}{3}}$, where screening effects can be excluded, the cross section σ_{pair} has the dependence

$$\sigma_{pair} \propto Z^2 \ln E_\gamma. \tag{1.26}$$

In the case of $E_\gamma \gg 137 m_e c^2 Z^{-\frac{1}{3}}$ (complete screening), the cross section σ_{pair}, taking into account nucleus and atomic electrons, is given by Eq. 1.27.

$$\sigma_{pair} \approx \frac{7}{9} \cdot 4Z(Z+1)\alpha r_e^2 [\ln(183 Z^{-\frac{1}{3}}) - f(Z)] \tag{1.27}$$

$$= \frac{7}{9} \frac{A_r \cdot u}{\rho \cdot X_0} \tag{1.28}$$

If one converts this into the mean free path Λ_{pair} a photon can travel before undergoing pair production, another definition of the Radiation length becomes evident:

$$\Lambda_{pair} = \frac{9}{7} \cdot X_0. \tag{1.29}$$

Thus, after an absorber thickness of one radiation length X_0 the number of photons is reduced by a factor $\frac{1}{e^{\frac{7}{9}}} \approx 46\%$. All three of the previously described effects have in common that the initial photon either is absorbed if the effect takes place or traverses the absorber unchanged. This has on the one hand the consequence, that, in contrast to charged particles, the energy of photons is not degraded as they pass through matter. On the other hand it is only possible to make a statistical statement about the fraction of photons passing an absorber material of given thickness x (see Eq. 1.30). The fraction of passing intensity $I(x)$ to the incident intensity I_0 can for one photon be regarded as its probability to survive the absorber thickness x:

$$\frac{I(x)}{I_0} = e^{-\mu x}. \tag{1.30}$$

The quantity μ is known as (total) attenuation coefficient. It is absorber material specific and obtained from the total photon absorption cross section σ, including photoelectric effect, Compton effect and pair production:

$$\mu = \frac{\rho}{A_r \cdot u} \cdot \sigma = \frac{\rho}{A_r \cdot u} \cdot \left(\sigma_p + Z\sigma_c + \sigma_{pair} \right). \tag{1.31}$$

Because all individual cross sections are functions of the initial photon energy E_γ, the attenuation coefficient has a strong dependence on E_γ. Often also the mass attenuation coefficient $\frac{\mu}{\rho}$ is used, which allows to evaluate the photon absorption properties of different materials more effectively, since it is independent of the material's density. As an example, the mass attenuation coefficient of lead tungstate is plotted in Fig. 1.14. Notable is that in the low energy region the photoelectric effect is the dominating process, while at high energy pair production is clearly the main process. The impact of Compton scattering is mostly recognised in the region around a few MeV.

Electromagnetic Shower

The first electromagnetic showers were observed in 1933 and induced by cosmic rays. Nowadays particles of sufficiently large energy are frequently produced in hadron and particle physics experiments and the reconstruction of electromagnetic showers has become a common task of electromagnetic calorimeters. In most cases, an electromagnetic shower is initiated by a high energetic photon or electron. As presented in the previous sections, a photon entering a detector material at sufficient energy, usually more than a few MeV, with high probability produces an electron positron pair. Both lose energy due to ionisation of the surrounding medium and, under the condition that their energy exceeds the critical energy E_c of the material, in turn radiate Bremsstrahlung and thereby produce new high energetic photons. These again are converted in secondary reactions in electrons or positrons, which leads to the development of a cascade of electromagnetic reactions, which usually is called electromagnetic shower. The shower development ends if the secondary photon energy is insufficient for pair production or the lepton energy is considerably smaller than E_c. A schematic view of the shower development and the involved threshold gives Fig. 1.15. The propagation of an electromagnetic shower is usually described separately in longitudinal development in direction of the initial particle and into lateral or transversal development. In both cases it is advantageous to define natural units, which parametrise the relevant quantities in a manner independent of the concrete absorber material. For longitudinal direction, the parameters $y = \frac{E}{E_c}$ and $t = \frac{x}{X_0}$ are the natural units for the energy of the initial particle and penetration depth into the detector medium, respectively. Consequently, the longitudinal centre of gravity of the shower energy profile t_{cg} and its maximum t_{max} can be calculated according to Tab. 1.2. Both scale with the logarithm of y, but are not identical, because the profile has a pronounced tail to
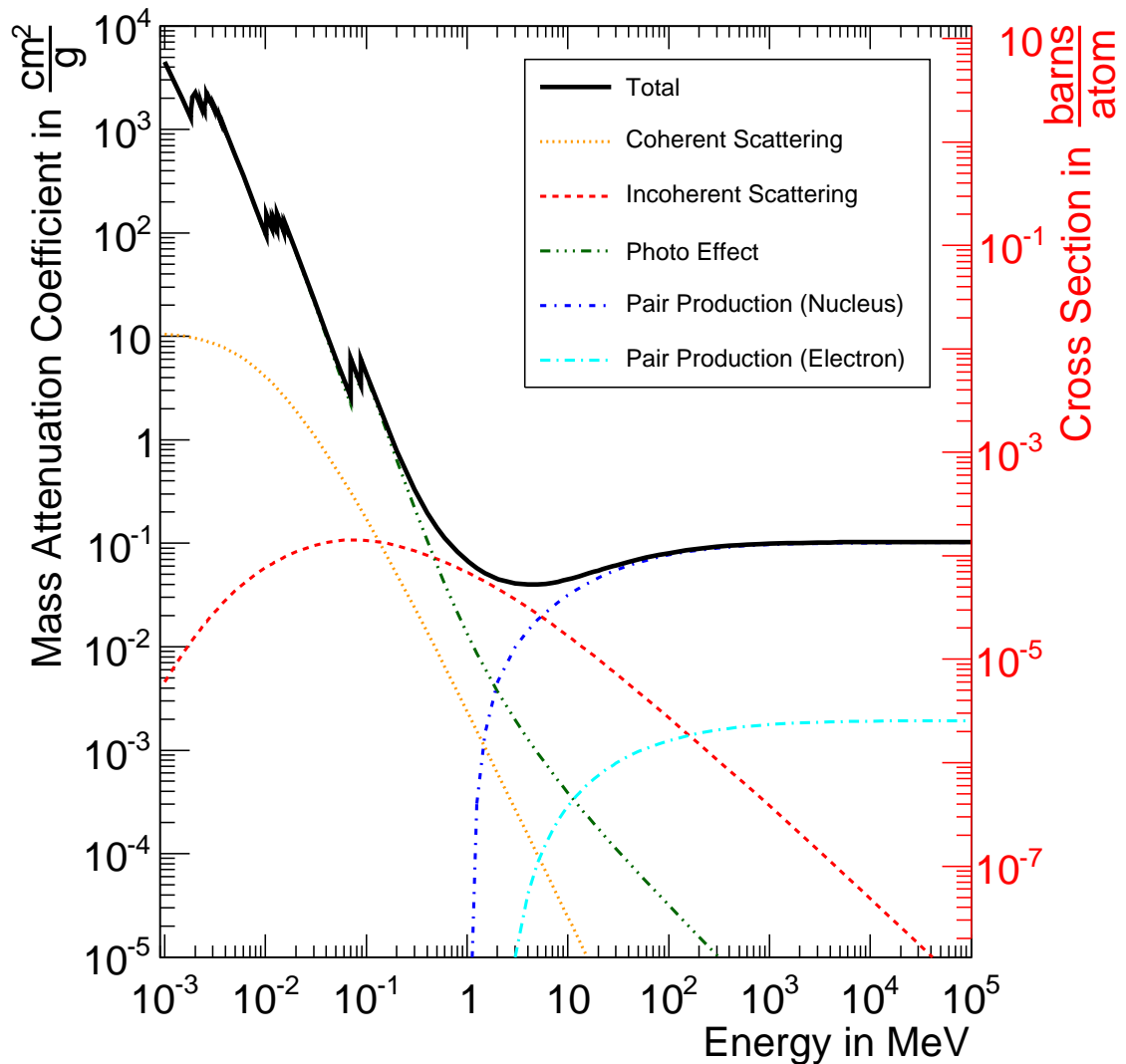
Figure 1.14: Mass Attenuation Coefficient of lead tungstate and corresponding photon absorption cross section as a function of the incident photon energy. Plotted data taken from [17].

	INITIAL PHOTON	INITIAL ELECTRON
t_{max}	$1.01[\ln y - 0.5]$	$1.01[\ln y - 1]$
t_{cg}	$t_{max} + 1.7$	$t_{max} + 1.4$

Table 1.2: Determination of the longitudinal shower energy profile maximum t_{max} and centre of gravity t_{cg} [18].
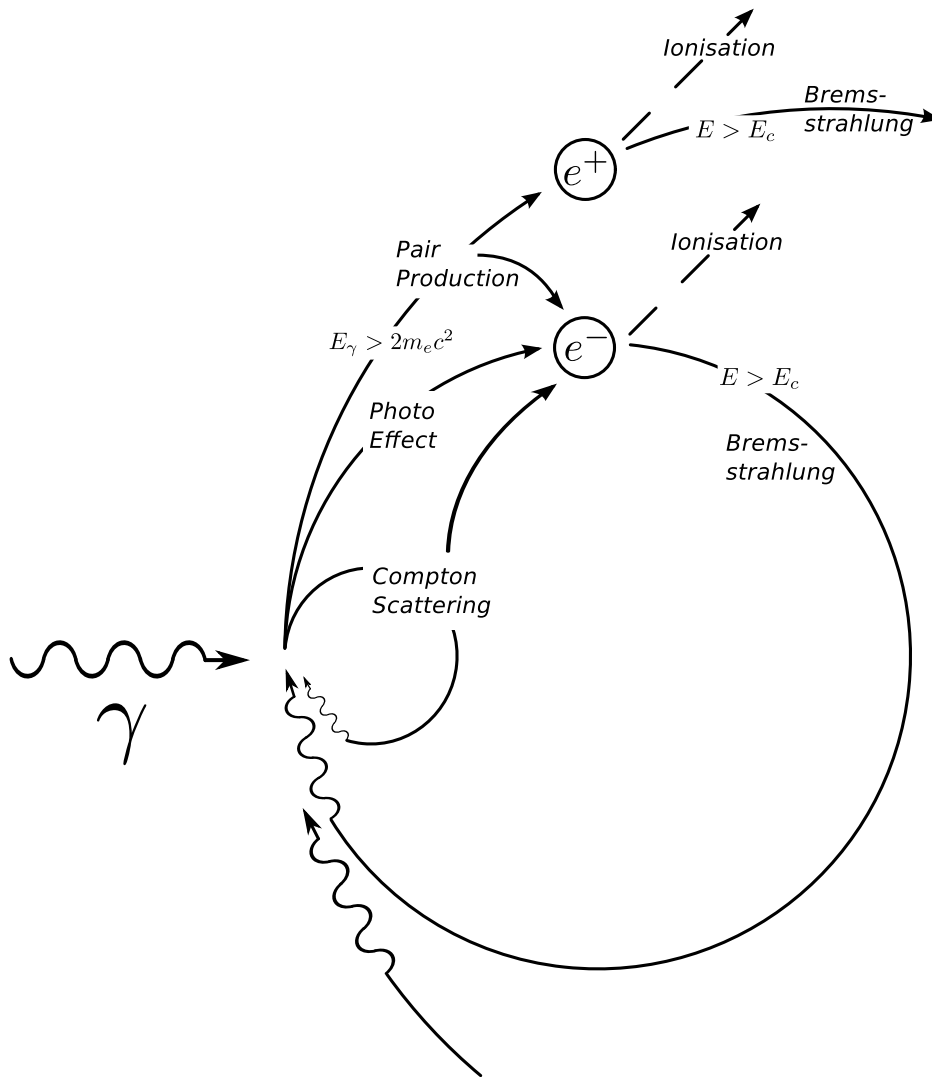
Figure 1.15: Schematic view of the development of an electromagnetic shower.
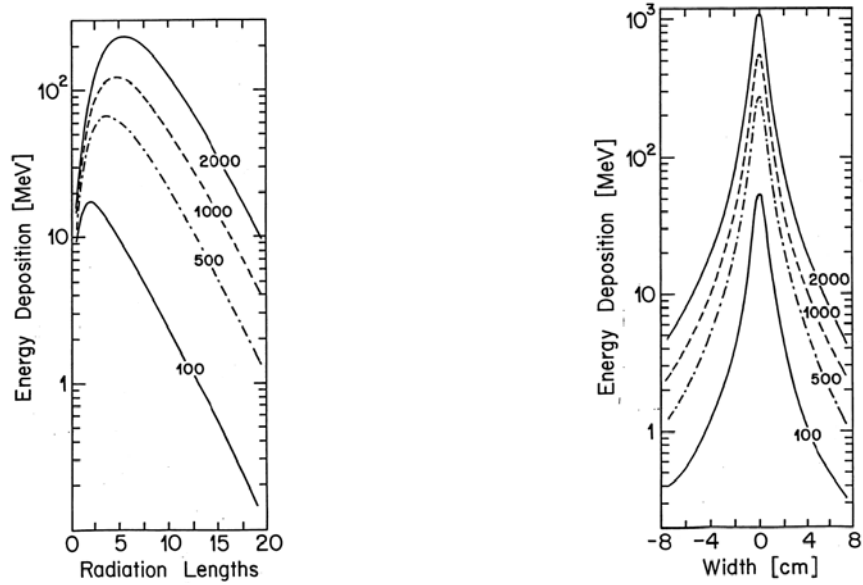
(a) Longitudinal shower energy profile

(b) Lateral shower energy profile

Figure 1.16: Shower energy profiles for incident photon energies of 100 MeV, 500 MeV 1000 MeV and 2000 MeV in CsI(Tl), which has a radiation length $X_0 = 1.85\,\text{cm}$ and Molière radius $R_M = 3.8\,\text{cm}$ [19].

higher values of t, as seen in Fig. 1.16a for thallium doped caesium iodide $(\text{CsI}(Tl))$. A rough approximation for the longitudinal energy containment of an electromagnetic shower is that 98% of the incoming particle energy is deposited in a depth of

$$L(98\%) \approx 3t_{cg}. \tag{1.32}$$

A lateral spread of the electromagnetic shower is caused mainly by the angular distribution of Bremsstrahlung and the multiple scattering of electrons and positrons, but also Compton scattering and photoelectric effect contribute and are even able to emit particles in backward direction. The mean transverse deflection scales with the so called Molière radius R_M of the absorber material given by

$$R_M = \frac{21.2\,\text{MeV}}{E_c} \cdot X_0. \tag{1.33}$$

On average, 95% of the total energy of the shower is contained in a cylinder with radius

$$R(95\%) = 2R_M, \tag{1.34}$$

centred around the track of the incident particle. As indicated exemplarily in Fig. 1.16b for CsI(Tl), the lateral energy loss profile of the shower generally decreases

32

exponentially. A common parametrisation for the energy deposited in distance r from the shower axis is [20]

$$E(r) = a_1 \cdot e^{-\frac{r}{b_1}} + a_2 \cdot e^{-\frac{r}{b_2}}, \tag{1.35}$$

where the parameters a_i and b_i have to be determined experimentally for a specific detector. However, the exact parametrisation depends on geometry and material budget of absorber or detector and may differ from Eq. 1.35. In calorimetry, detectors are often laterally segmented which enables the determination of the point of impact of the incident particle. It is deduced from the energy distribution in the individual responding segments. Nevertheless, this segmentation makes an detector also prone to lateral energy leakage, which in turn deteriorates the energy response. A width of a single segment of $1R_M$ has been proven to represent a good compromise between lateral spatial sensitivity and a preferably complete energy containment.

1.4 The Electromagnetic Calorimeter

The diverse physics programme of $\overline{\text{P}}$ANDA sets several requirements for the design of the EMC. First of all, there are the spatial constraints given by the limited size of the superconducting solenoid, inside which the EMC has to be placed. Therefore, it has to be compact and operational in a strong magnetic field. Secondly, the energy response of the calorimeter has to be very precise over the large energy range reaching from 10 MeV to 15 GeV. Moreover, the high antiproton-proton-annihilation rate at the HESR demands a high count rate capability which entails a fast detector response. Timing information with a resolution σ_t below 1 ns is needed, due to the envisaged triggerless Data AcQuisition (DAQ) system. To guarantee long operation periods with a minimum of degradation in performance, the radiation hardness of the detector should also be sufficient.

Scintillation Material

To meet the stated requirements, a design based on homogeneous crystals consisting of the inorganic scintillator lead tungstate ($PbWO_4$, PWO) was chosen. A collection of its properties is listed in Tab. 1.3. It has a short radiation length X_0 and a small Molière radius R_M which allows for the required compactness of the detector. The mean wavelength of the Gaussian-like scintillation light emission spectrum amounts to $\lambda_{mean} = 420$ nm, while the distribution has a Full Width Half Maximum (FWHM) of 40 nm. Based on the exploration of lead tungstate as a scintillator for the high energy physics Compact Muon Solenoid (CMS) experiment and the experiences gained in the production of a large number of samples, research efforts were made to improve

the scintillation material even further, culminating in the development of PWO-II. Due to a reduction of defects in the crystal lattice achieved by an enhanced control of stoichiometry during the growing process, a lower required concentration of rare earth (La, Y, etc.) dopants was required to achieve sufficient radiation hardness. In turn, this lead to an increase of scintillation light of $\sim 80\%$ compared to the quality of the Electromagnetic CALorimeter of the CMS experiment (CMS-ECAL) [21]. Nevertheless, for lower energies, an additional increase in scintillation light yield is desirable to improve the achievable relative energy resolution according to Poisson statistics. In $\overline{\text{P}}$ANDA, this is solved by cooling down the scintillator material to a temperature of $T = -25\,°\text{C}$. Then, because of a reduced temperature quenching of the light emission, the light yield can be increased by another factor 3.5 compared to room temperature. A drawback of this cooling is a raise of the scintillation light's emission decay constant τ_{decay}. At room temperature it amounts only to 6 ns and therefore enables a fast collection of the scintillation light. At $T = -25\,°\text{C}$ this scintillation kinetics is significantly slower. Despite this effect, it is still possible to collect 97% of the light within a time gate of 100 ns width.

Layout

As illustrated in Fig. 1.10 the $\overline{\text{P}}$ANDA EMC consists of three parts, which are named according to their position with respect to the beam direction: Barrel EMC, Forward EndCap (FEC) and Backward EndCap (BEC). Tab. 1.4 presents an overview of the three subsections, detailing the covered polar angle range. By exploitation of symmetries it is possible to assemble the EMC out of 15552 Second generation lead tungstate (PWO-II) crystals with 13 different geometries. The exact numbers are 11360 crystals for the Barrel EMC, 3864 crystals for the FEC and 592 crystals for the BEC, respectively. Accounting for the fixed target kinematics, the Forward Endcap possesses a higher granularity, visible in the polar angle ϑ covered by a single crystal. All are of type EC, featuring a tapered parallelepipedal shape, which in average is equivalent to 1° of polar angle in contrast to 4° for the crystal types used in the other detector parts. This reduces the hit occupancy of a single crystal. The geometrical arrangement of crystals in the Barrel EMC can be observed in Fig. 1.17a. It is divided into 16 similar slices consisting of six modules each with altogether 710 individual crystals, as shown in further detail in Fig. 1.17b. To avoid the passing of secondary particles in between adjacent crystals, all of them are tilted by a polar and azimuthal angle of 4° with respect to the target. For a uniform energy and position response of the barrel, it is important that all crystals cover the same solid angle. Therefore it is necessary to deploy 11 different crystal types. All feature a tapered parallelepipedal shape, but the individual dimensions, especially the tapering angles (compare Fig. 2.2), vary. Moreover, each type is represented by two longitudinally mirror-inverted designs. As can be seen in Fig. 1.18, a crystal is defined by the dimensions of the

Quantity	Value	Unit	Comment	Value	Unit	Comment
Effective atomic number Z_{eff}	75.6					
Mean $\left\langle \frac{Z}{A} \right\rangle$	0.41315					
Density ρ	8.30	$\frac{g}{cm^3}$				
Mean excitation energy	600.7	eV				
MIP energy loss	1.229	$\frac{MeV \cdot cm^2}{g}$		10.20	$\frac{MeV}{cm}$	
Radiation length X_0	8.30	$\frac{g}{cm^2}$		0.8903	cm	
Critical Energy E_c	9.64	MeV	for e^-	9.31	MeV	for e^+
Molière radius R_M	16.26	$\frac{g}{cm^2}$		1.959	cm	
Nuclear interaction length λ_A	168.3	$\frac{g}{cm^2}$		20.27	cm	
Muon critical Energy	$160^{+5}_{-6} \pm 8$	GeV	[22]			
Index of refraction at 425 nm	2.35(2)		ordinary; [23]	2.2(36)		extra-ordinary; [23]
Mean scint. wavelength λ_{mean}	420	nm				
Mean scint. lifetime τ_{decay}	6	ns	at 18 °C			
Average light yield	180	$\frac{photons}{MeV}$	at 18 °C	630	$\frac{photons}{MeV}$	at -25 °C
Average light yield (PMT)	18	$\frac{phe}{MeV}$	at 18 °C	63	$\frac{phe}{MeV}$	at -25 °C

Table 1.3: Several Properties of lead tungstate. Except noted otherwise, values in the upper part are taken from [24], while the values below originate from [21].

DETECTOR SUBSECTION	POLAR ANGLE RANGE	SINGLE CRYSTAL			
		ϑ equiv.	Type	Shape	Readout
Forward Endcap	$5° \leq \vartheta < 22°$	$1°$	EC	tapered parallelepiped	2 LAAPDs or VPTT
Barrel EMC	$22° \leq \vartheta < 140°$	$4°$	1 - 11	tapered parallelepiped	2 LAAPDs
Backward Endcap	$140° \leq \vartheta$	$4°$	EC-R	cuboid	2 LAAPDs

Table 1.4: Overview of the polar angle range covered by each EMC subsection. In addition, crystal shape and foreseen readout are indicated.

(a) Division into 16 slices

(b) Layout of a single EMC slice
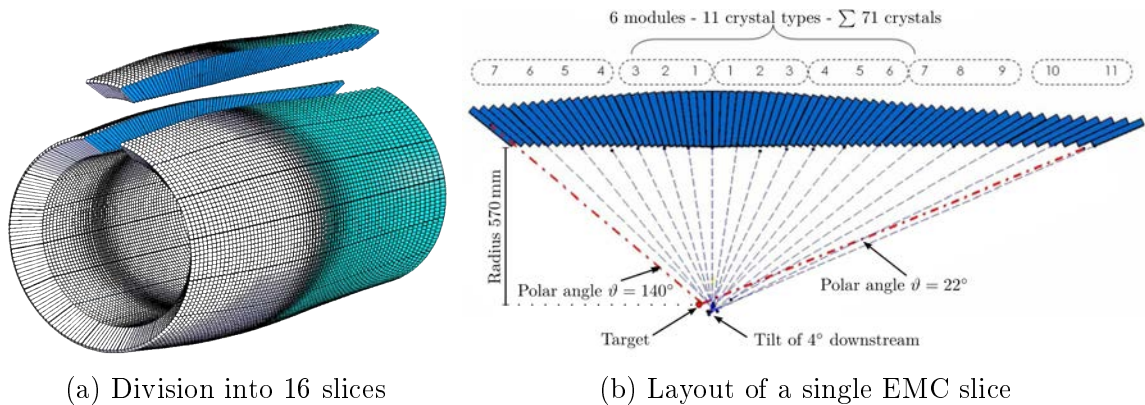
Figure 1.17: Crystal arrangement in the Barrel EMC.

Type	Volume cm^3	AF	BF	CF	AR	BR	CR
				mm			
1	126.86	21.21	21.28	21.27	29.04	28.75	29.12
2	126.56	21.18	21.28	21.39	28.78	28.75	29.07
3	125.79	21.17	21.28	21.51	28.36	28.75	28.81
4	120.85	21.17	21.28	21.60	27.90	27.22	28.45
5	119.69	21.17	21.28	21.69	27.35	27.22	28.01
6	118.35	21.19	21.28	21.78	26.72	27.22	27.47
7	112.90	21.22	21.28	21.86	26.23	25.47	26.99
8	111.75	21.23	21.28	21.91	25.70	25.47	26.51
9	110.52	21.23	21.28	21.95	25.14	25.47	26.00
10	107.01	21.25	21.28	22.00	24.70	24.42	25.56
11	106.25	21.25	21.28	22.02	24.35	24.42	25.23
EC (12)	126.88	24.38	24.38	24.38	26.00	26.00	26.00
EC-R (13)	118.58	24.35	24.35	24.35	24.35	24.35	24.35

Table 1.5: Definition of the geometrical parameters of the lead tungstate crystals. The EC and EC-R geometry corresponds to crystals for the FEC and the BEC, respectively.

trapezoidal rear face AR, BR, CR and of its front face AF, BF, CF, respectively. In each case, the sides AR and CR (AF and CF) stand perpendicular on the side BR (BF). The exact values for the side lengths are tabulated in Tab. 1.5, including BEC and FEC crystals. All crystals feature the same distance of the parallel back and front face, which amounts to 200 mm.

Photo Sensors

Another peculiarity of the FEC is that the photo sensor readout of a portion of crystals at low polar angles, where highest rates are expected, is performed by single Vacuum Photo Tetrodes (VPTTs), which, due to the faster response, possess a higher rate capability than the LAAPDs envisaged for Barrel EMC, BEC, and FEC's outer rim. A VPTT can be described as a simplified version of a PMT. Similarly, it consists of an evacuated cylindrical glass tube featuring on one end face an entrance window with photo sensitive bialkali coating, for the conversion of visible photons into electrons via photoelectric effect, while the other end face usually holds connectors for signal output and the voltage supply of the internal electrodes. In a VPTT these are represented by the bialkali layer serving as photo cathode, a metal grid anode and two dynodes at gradually lower electrical potential. The nominal signal amplification factor achieved by a VPTT is around 20, which is significantly lower than for a conventional PMT,
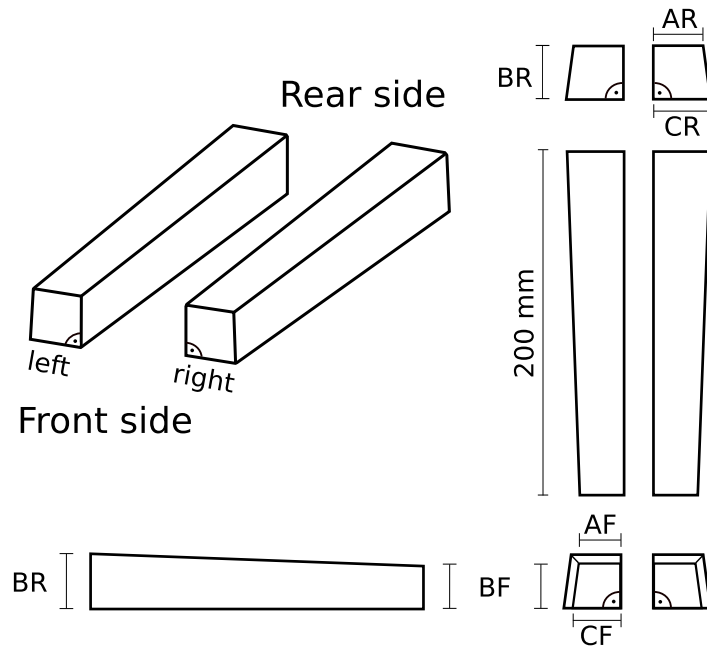
Figure 1.18: Drawing of the crystal geometry (from [21], slightly changed). The individual dimensions of the front face AF, BF, CF and the rear face AR, BR, CF are given in Tab. 1.5.
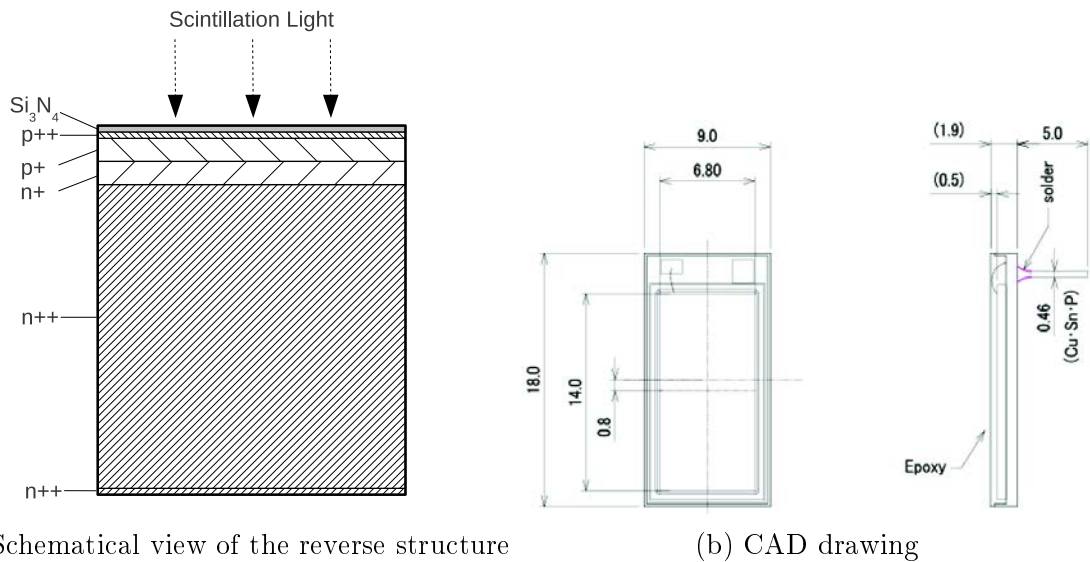

(a) Schematical view of the reverse structure   (b) CAD drawing

Figure 1.19: Layout of the rectangular $\overline{\text{P}}$ANDA LAAPDs.

but unlike it, a VPTT is able to operate in a strong magnetic field. However, depending on the alignment relative to the magnetic streamlines, a moderate decrease in amplification has to be accepted.

On the contrary, the aforementioned LAAPDs are hardly influenced by a magnetic environment and feature a very compact design, which makes them an ideal choice as photo sensor for the less occupied Barrel and BEC. Like a conventional Si-photodiode, LAAPDs are principally based on a p-n-junction operated under reverse bias voltage. Other than these, LAAPDs operate at a significantly higher voltage resulting in large electric field strength at the p-n-junction, able to lead to an avalanche of secondary ionisations, induced by the primarily generated electron hole pairs. Like in a proportional counter, the amount of secondary charge is proportional to the primary charge and an effective charge multiplication (gain) up to a factor of several hundred can be achieved depending on the bias voltage. Due to the random nature of the avalanche multiplication, the number of generated electron hole pairs is subject to fluctuations. The relative width σ of the distribution of the number of the collected electron hole pairs N at a given gain M is characterised by the so called excess noise factor F,

$$\sigma \approx \sqrt{\frac{F}{N}} \tag{1.36}$$

which in general itself depends on the gain. One distinctive feature of the LAAPDs for $\overline{\text{P}}$ANDA, which are in principle a further development of the ones used in the CMS-ECAL, is a reverse structure, as depicted in Fig. 1.19a. After traversing the impassive protective Si_3N_4 coating and the more positively doped p^{++}-anode, the light is converted into electron-hole-pairs in the thin p^+-layer, which is directly adjacent to the p-n-junction, where the charge multiplication takes place. Afterwards, the electrons drift through the n^{++}-substrate to the n^{++}-doped cathode. This design ensures a suppression of the nuclear counter effect, because charge produced in the effectively much larger drift region is not multiplied and therefore negligible in comparison to the primary charge produced by the scintillation light and amplified afterwards. Furthermore, in a first step the active area of the quadratic LAAPDs could be increased to $1\,cm^2$. This type is used in the first prototype for the Barrel EMC. However, to enable the opportunity to fit two LAAPDs on the end face, in a second step a rectangular version with the same active area, but the edge lengths of $0.7\,cm \times 1.4\,cm$ was developed, which is envisaged to be used in the final Barrel design. In the best case, this doubles the amount of collected scintillation light, which should improve the achievable energy resolution, especially at lower energies.

Front End Electronics and Data Aquisition

In the Barrel EMC, the signals generated by both LAAPDs are individually shaped and amplified further by the so called ASIC for $\overline{\text{P}}$ANDA Front End Electronics (APFEL).

This dedicated Application Specific Integrated Circuit (ASIC) features two independent channels, one for each LAAPD. Each channel possesses a digital dynamic range of 10000 and a maximum input charge of 7 pC. Additionally, a dual gain output, whose relative gain can be programmed to amount to either a factor of 16 or 32, is implemented. By this design one becomes more sensitive to low energies in the high gain branch, whereas it is still possible to observe the complete energy range with the low gain branch. Digitisation is to be performed with Sampling Analogue to Digital Converters (SADCs). This has the advantage, that no additional timing branch in the readout chain is necessary. A sampling frequency of 50 MHz has been proven sufficient to achieve a timing resolution σ_t below 1 ns at deposited energies above 100 MeV [25]. For the FEC, the readout has to be varied, due to the mixed choice of photo sensors and the higher count rates in a single unit. Both, LAAPD as well as VPTT signals will be amplified by different versions of the Low Power Low Noise charge Preamplifier (LNP) developed at Basel University (SP883 preamplifier family, [25, 26]). In contrast to the Barrel EMC, there is only one preamplifier channel per photo detector and an additional shaper board is introduced, which, together with the envisaged sampling frequency of ~ 80 MHz of the currently developed SADC, guarantees high rate capability.

As indicated in the DAQ schematics in Fig. 1.20, the preamplified and shaped signals are routed to digitiser modules containing in addition to the actual SADC chip also a Field Programmable Gate Array (FPGA) able to execute online pulse data processing. This is performed in two stages: At first, the continuously digitised signal baseline is monitored and pulses are identified, while a time stamp is set to the pulse maximum. Moreover, possible pile-up in the pulse is recognised and marked, before in the second stage the precise time and pulse height are determined. With this information, a hit is built and sent via optical link to the data concentrator, which is responsible for building EMC events, including time ordering and pile up recovery together with communicating clock information from the global time distribution system and slow control information to the digitiser modules. Completely processed EMC events are then sent to the Compute Node, where online physics event reconstruction under consideration of the information from all $\overline{P}$ANDA subdetectors takes place. Only events which satisfy the flexible software trigger conditions are then stored to hard disk, avoiding the accumulation of undesired data. Moreover, this allows to collect data of different physics channels and reactions with similar initial kinematical conditions in parallel, as the decision if an event is desirable takes place at a level where all physics information of an event is in principle available. This is not possible with most hardware triggers, which usually rely on very basic trigger conditions tuned to a specific reaction channel, while most other channels are suppressed. Therefore, beam time can be used more efficiently at $\overline{P}$ANDA, which is especially worthwhile for rare reactions. However, the amount of collected data is still limited by the dead times of the individual subdetectors and the available compute node buffer size.
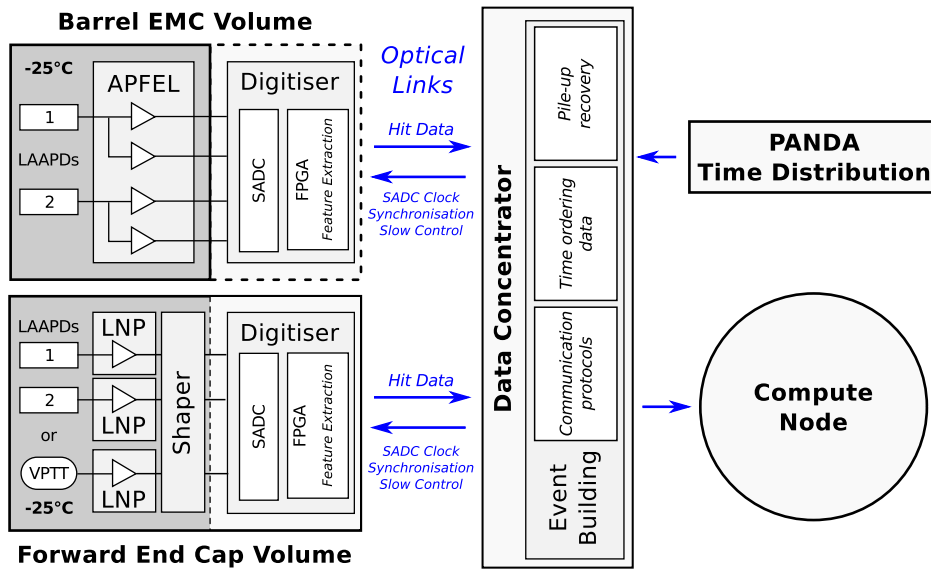
Figure 1.20: Schematic view of the EMC DAQ. The preamplified and shaped signals coming from individual detectors are sent to the Digitiser for digitisation. An on-board FPGA performs feature extraction and hit building. Hit data of several digitiser modules is then transmitted via optical links to the Data Concentrator where the EMC event building takes places. A processed event is then forwarded to the Compute Node where online event reconstruction with data from all subdetectors takes place.

Chapter 2

Scintillation Light Collection Non-Uniformities

2.1 Origin and Description

2.1.1 Nature of the Scintillation Light Collection Non-Uniformity

As introduced in Section 1.4, most of the PWO-II crystals for the $\overline{\text{P}}$ANDA EMC are of a tapered parallelepipedal shape. For use as scintillation detector, the photo sensors are attached at the rear face, indicated in Fig. 1.18. In consequence, of the complete amount of scintillation light produced in the crystal, only the fraction which arrives at the photo sensor within a given time gate contributes to the measured signal. Furthermore, the efficiency of the sensor, as well as losses at the transition between crystal and sensor entrance window, has to be taken into account. Usually the Light Yield (LY), in terms of photoelectrons (phe) generated at the bialkali photo cathode of a PMT divided by the energy deposited inside the scintillator material, is used to quantify the amount of scintillation light available as signal, independent of the deposited energy. For quality control, the LY is calculated according to Eq. 2.1. The response P_{Cs} of a crystal to a ^{137}Cs-source with known photon energy E_γ is normalised to the pulse height P_{SEP} generated by a single photoelectron emitted by the photo cathode due to thermal excitation.

$$LY \left[\frac{\text{phe}}{\text{MeV}} \right] = \frac{P_{\text{Cs}} - P_{Ped}}{P_{SEP} - P_{Ped}} \cdot \frac{1}{E_\gamma[\text{MeV}]} \qquad (2.1)$$

Both pulse heights have to be corrected for the pedestal P_{Ped}, defining the zero position of a digital readout. Although independent of the deposited energy, the amount of light collected at the photo sensor can depend on the position in the crystal, where the scintillation light is produced, especially at which distance to the photo sensor, like

43
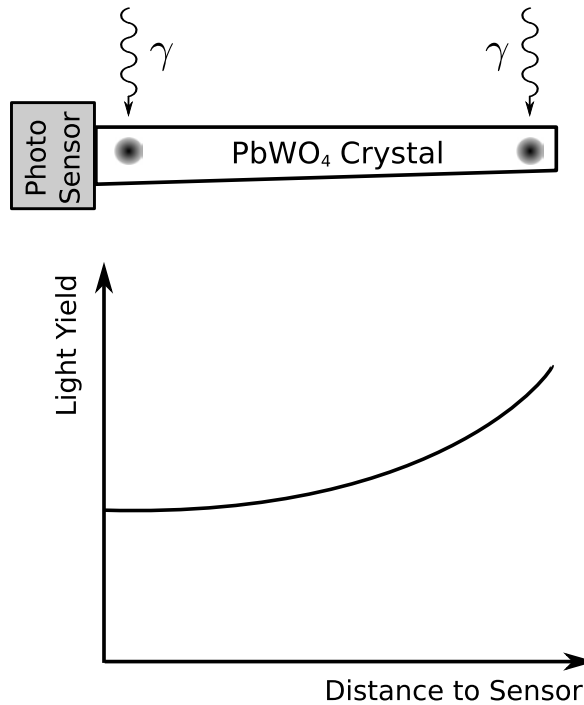
Figure 2.1: Schematic example for a case of light collection NUFs.

indicated schematically in Fig. 2.1. This NUF is caused by the interplay of absorption and focusing effect, influencing the amount of scintillation light reaching the readout end face. In the following sections, the origin and characterisation of the NUFs will be investigated, utilising basic geometrical calculations, Super LITRANI (SLitrani) simulations and dedicated experimental setups.

2.1.2 Geometrical Considerations

The level of tapering for each of the 13 different geometries (for comparison see Fig. 1.18 and Tab. 1.5) can be parametrised by three tapering angles named α, β and γ, respectively. As depicted schematically in Fig. 2.2, these angles originate from the length difference of the edges $AR-AF$, $BR-BF$ and $CR-CF$. For all crystal shapes, the edges AF and CF are perpendicular to BF, while AR and CR are perpendicular to BR as well. In the special case of the geometry EC-R, all three tapering angles are equal to zero, resulting in a cuboid shape. Using the crystal dimensions as given in Tab. 1.5, the tapering angles α, β and γ in degrees have been calculated for each geometry and are shown in Fig. 2.3a. A comparison to the tapering angles calculated from the geometry measurements for quality control, briefly described in Section 2.3.1, is displayed in Fig 2.3b. Both diagrams show a similar behaviour with only minor deviations. α and γ amount to roughly the same value and show the same progression
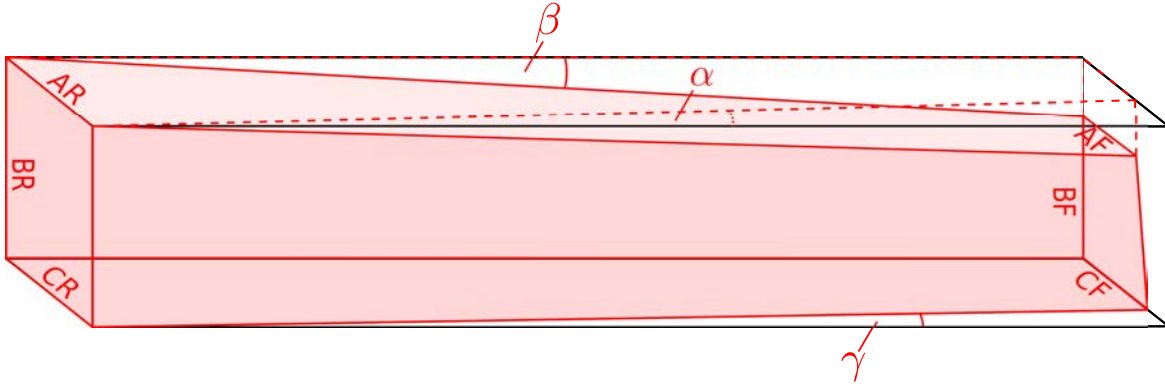
Figure 2.2: Definition of the three tapering angles α, β, and γ originating from the length difference of the sides $AR - AF$, $BR - BF$ and $CR - CF$, respectively. For all crystal shapes the relations $AX \perp BX$, $BX \perp CX$ and $AX \parallel CX$ are valid.

with a strong dependence on the geometry type. For β however, six sub-groups can be observed, because it does not vary between some of the types belonging to the Barrel EMC. As a measure for the overall level of tapering, the mean tapering angle μ is defined as

$$\mu = \frac{\frac{\alpha+\gamma}{2} + \beta}{2} = \frac{\alpha + \gamma + 2\beta}{4}. \tag{2.2}$$

Since α and γ are tilting the same crystal face, their average is calculated before determination of the overall mean tapering angle. Therefore, their weight in the mean calculation is half as large as the weight of tapering angle β. The μ values for each crystal type are shown in Fig. 2.4a.

In a first approach to understand the NUFs by basic geometrical optical calculations, it is assumed that scintillation light originating at distance z from the rear face, is only transported there, if either a direct illumination exists or it is transported there via total internal reflection. For calculation of its threshold angle θ_{thr}, the ordinary refractive index n_{ord}, given in Tab. 1.3, was used for lead tungstate, while the surrounding medium was assumed to be air with refractive index $n_{Air} \approx 1$. Under these conditions, the incident angle θ_0 under which a scintillation photon is emitted from the source located at coordinates z and y (as illustrated in Fig. 2.5), determines if the photon propagates successfully to the sensor. In general, scintillation light is emitted isotropically. Therefore, the width of the angular range, under which a successful propagation is possible, should give a rough estimation of the detectable light fraction. As also indicated in Fig. 2.5, there are several angular regions, which can be defined: If θ_0 lies within ζ_0, the light is able to travel directly to the rear face. Consequently, ζ_1 in addition includes light which gets extracted after a maximum of one reflection.
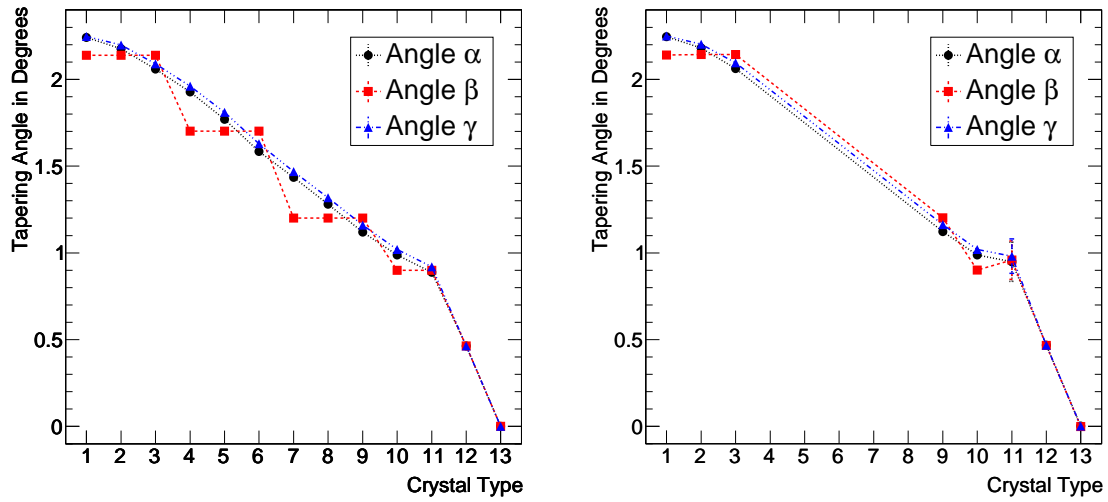
(a) Tapering angles calculated from the geometry specifications given in Tab. 1.5. A clear correlation between all three angles and geometry type is visible.

(b) Actual tapering angles calculated from the averaged geometry measurement of the quality control at CERN. Because crystal production is not yet finished, only data for selected geometries is available.

Figure 2.3: Tapering angles α, β, and γ for the 13 different crystal geometries.

(a)

(b)
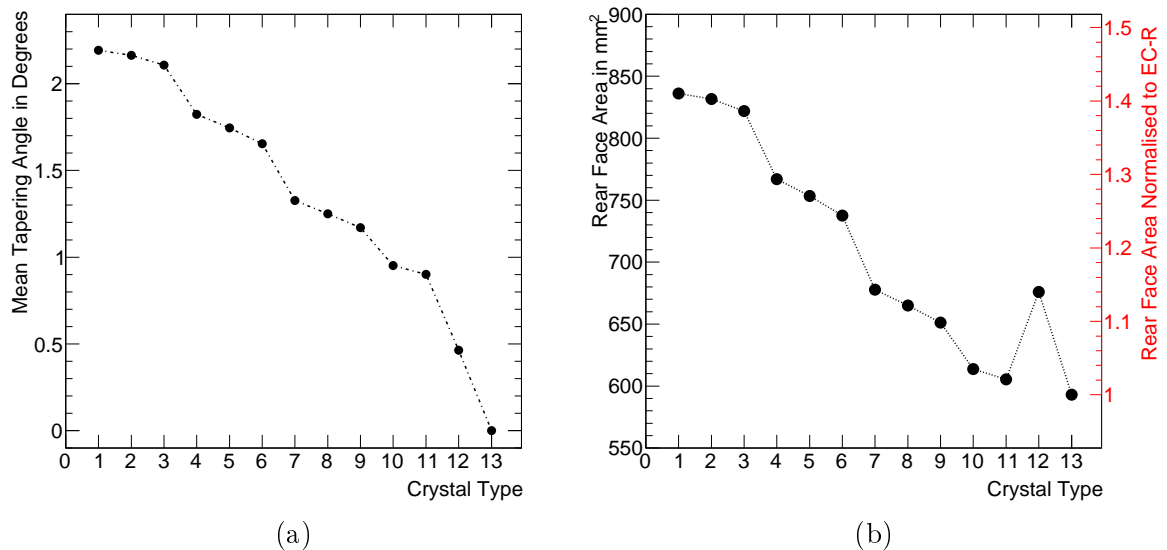
Figure 2.4: Mean tapering angle calculated according to Eq. 2.2 (a) and area of the rear face in mm^2 and relatively to type EC-R (b).
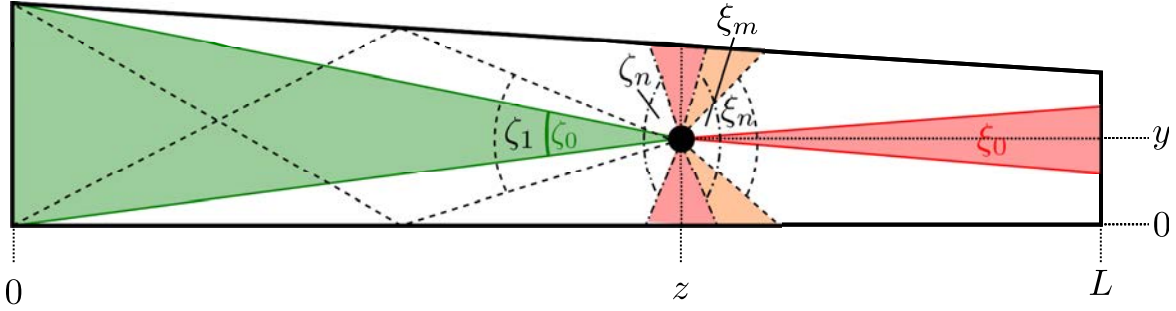
Figure 2.5: Opening angles ζ and ξ for forward and backward scintillation light propagation, respectively. Green colour indicates that light emitted within this angular range is reaching the photo sensor, while red or orange colour represent that light is lost during propagation or not propagated there at all. In these considerations, only total internal reflection is taken into account.

Both opening angles have been calculated and are plotted in Fig. 2.6 as a function of the distance to the rear face. The coordinate y has been set to $\frac{BF}{2}$ for each geometry, whereas for the purpose of this calculation the upper side is tapered by angle β. One observes that ζ_0, and therefore the amount of direct light, is larger for the more strongly tapered crystal types. This effect is more pronounced for ζ_1, including the light reflected once. Additionally, one recognises that at $z \geq 70\,\text{mm}$ ζ_0 is lower than $5\,\%$ of the full circular angle, which means most of the light reaching the photo sensor has to be internally reflected light. Calculations for different y coordinates of the point of origin showed similar behaviour.

To also take into account higher orders of reflection, discrete geometrical calculations are necessary. For a simplified description of the scintillation light propagation, the problem was split into two cases, as illustrated in Fig. 2.7: Scintillation light emitted in direction of the photo sensor (backward direction) or in direction of the crystal front face (forward propagation). In each case the following recursive equations for the coordinate z_n of the nth total internal reflection on a crystal side face can be derived from Fig. 2.7:

$$e(z) = BR - \frac{BR - BF}{L} \cdot z. \tag{2.3}$$

Forward propagation:

$$\theta_n = \theta_0 - n\beta, \tag{2.4}$$

$$z_1(\theta_0) = \frac{e(z_0) - y_0}{\cot \theta_0 + \tan \beta} + z_0, \tag{2.5}$$
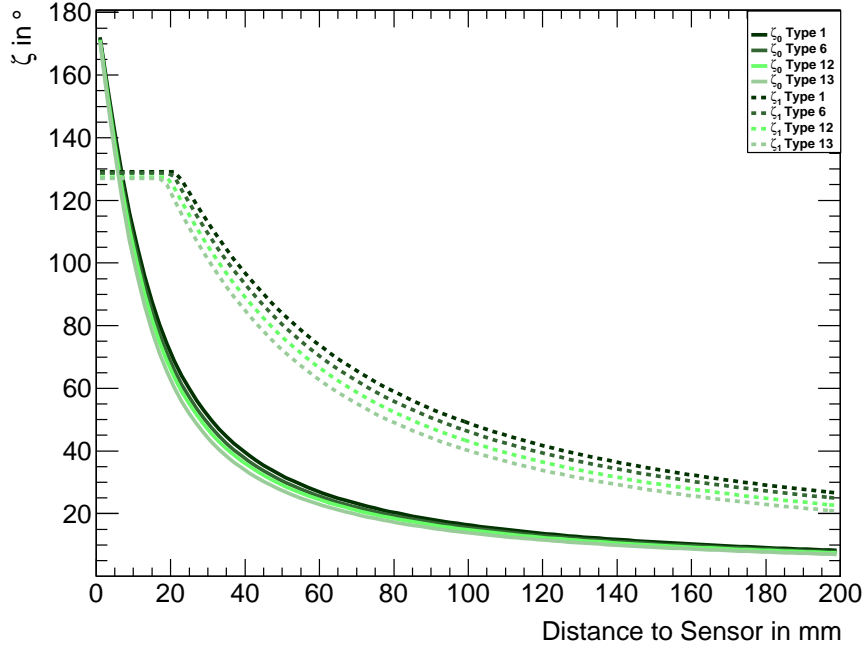
Figure 2.6: Opening Angles ζ for scintillation light originating at distance z and reaching the photo sensor directly (ζ_0) or after one reflection (ζ_1). One recognises that for more tapered crystals ζ becomes significantly larger. At low distances, ζ_1 is limited due to the threshold angle θ_{thr} for total internal reflection.
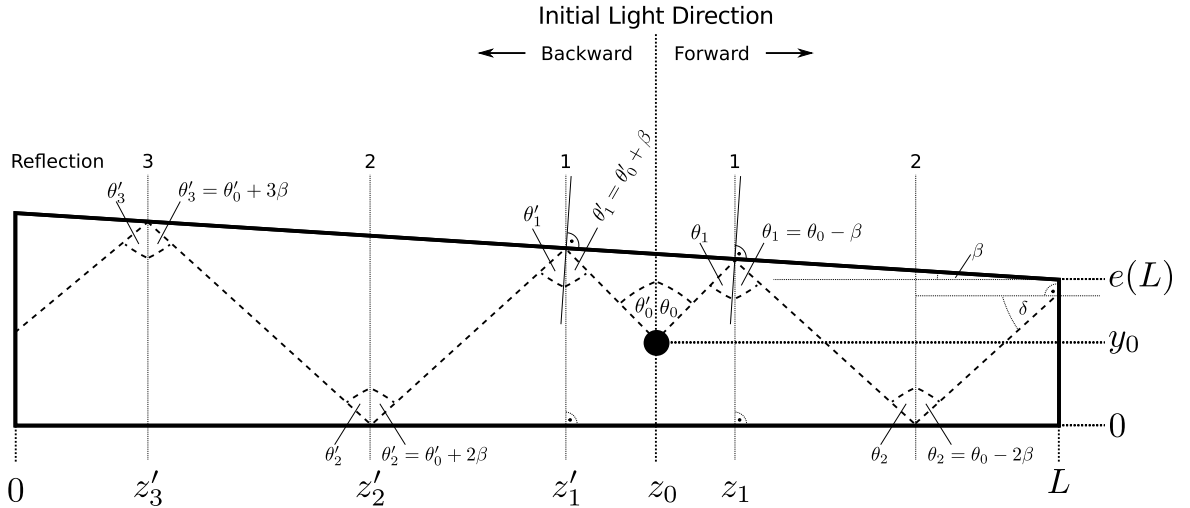

Figure 2.7: Schematic two dimensional view of a tapered crystal used to derive Eq. 2.3 to 2.11.

n even:

$$z_n(\theta_n) = e(z_{n-1}) \cdot \tan\theta_n + z_{n-1}, \tag{2.6}$$

n odd:

$$z_n(\theta_{n-1}) = \frac{e(z_{n-1})}{\cot\theta_{n-1} + \tan\beta} + z_{n-1}. \tag{2.7}$$

Backward propagation:

$$\theta'_n = \theta'_0 + n\beta, \tag{2.8}$$

$$z'_1(\theta_0) = z_0 - \frac{e(z_0) - y_0}{\cot\theta'_0 - \tan\beta}, \tag{2.9}$$

n even:

$$z'_n(\theta'_n) = z'_{n-1} - e(z'_{n-1}) \cdot \tan\theta'_n, \tag{2.10}$$

n odd:

$$z'_n(\theta'_{n-1}) = z'_{n-1} - \frac{e(z'_{n-1})}{\cot\theta'_{n-1} - \tan\beta}. \tag{2.11}$$

Eq. 2.3 represents the height of a crystal $e(z)$ depending on the coordinate z and is well defined by the dimensions of the crystal. By using the set of Eqs. 2.4 to 2.7, the reflection angle θ_n and the corresponding coordinate z_n can be calculated in the forward propagation case, while Eqs. 2.8 to 2.11 are used for backward propagation. For simplicity, and to avoid ambiguities in angle calculations, the range of θ_0 has been limited to

$$0\,^\circ \le \theta_0 \le 90\,^\circ, \tag{2.12}$$

effectively meaning that only light initially emitted in the upper half of a crystal is regarded. This does not result in an information deficit, since the lower half of each crystal geometry is in principle identical. Optical differences only can arise due to the influence of the tapered side, which in the following 2-dimensional calculations will be always the side tapered by angle β. In this basic consideration, again, only total internal reflection is taken into account. Therefore, whether the generated light reaches the back face, is dependent solely on the initial emission angle θ_0. Nevertheless, for different coordinates (z_0, y_0) of the scintillation light's point of origin, the angular range of allowed θ_0 angles is varying. Figs. 2.8a to 2.8d show reflection maps for the most tapered geometry type 1 and the untapered type EC-R. For six given initial angles θ_0,

(a) Crystal type 1, forward emission.

(b) Crystal type EC-R, forward emission.

(c) Crystal type 1, backward emission.

(d) Crystal type EC-R, backward emission.
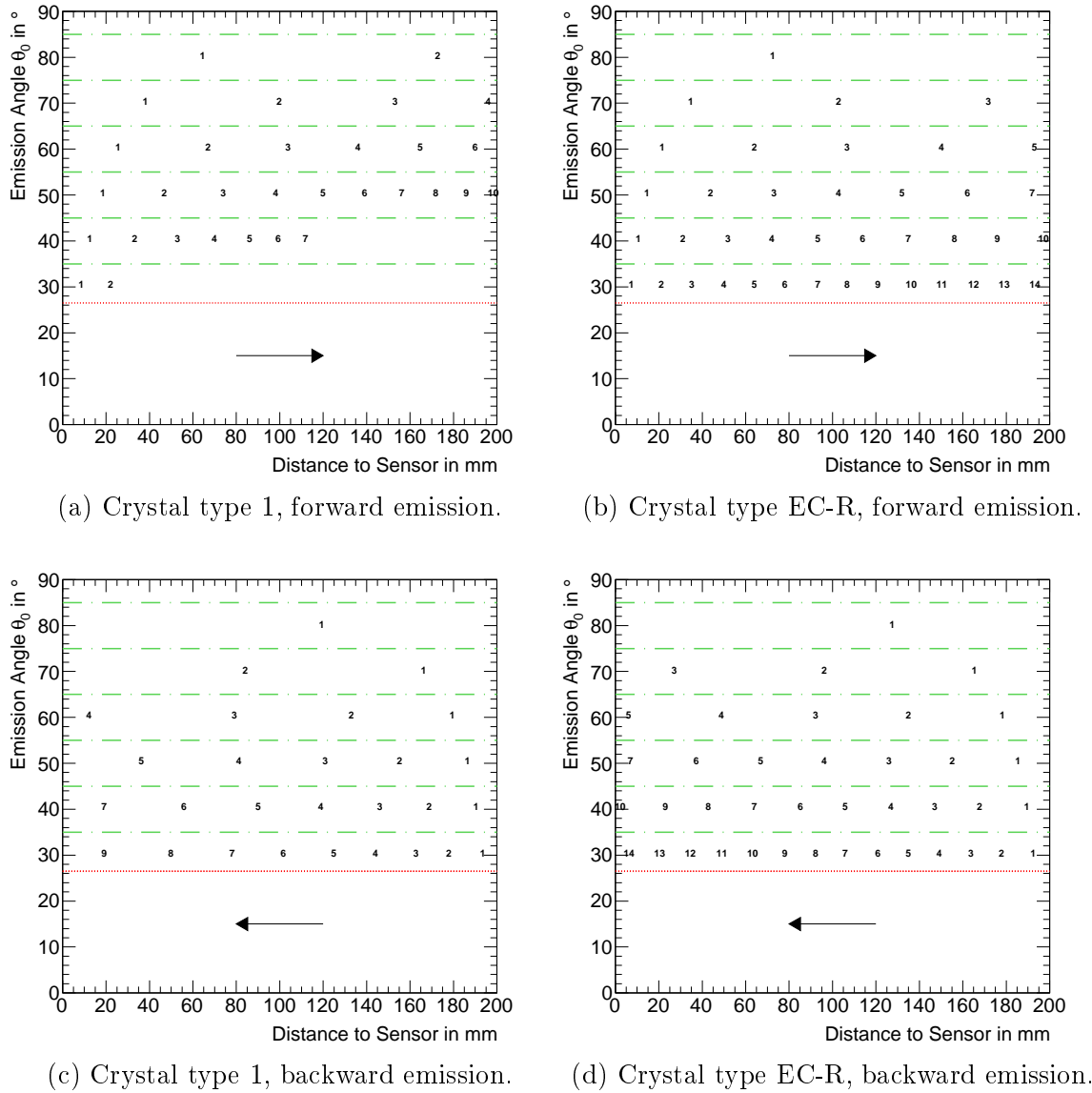
Figure 2.8: Reflection map of the two extreme crystal geometry types 1 and EC-R for forward and backward scintillation light emission under six different angles θ_0. Displayed is the reflection number in the plane created by its distance to the sensor z_n and θ_0. The red line indicates the threshold angle for total internal reflection, while the green lines separate the reflection sequences belonging to different θ_0.

amounting to $30°$, $40°$, $50°$, $60°$, $70°$ and $80°$, the reflection sequences are plotted, with number n of the individual reflection appearing at its position z_n. Comparing type 1 (Fig. 2.8a) to type EC-R (Fig. 2.8b), in the case of light propagating to the front face, one recognises on the one hand that distances between reflections decrease with increasing reflection number, if the crystal is tapered (type 1). On the other hand, Fig. 2.8a also shows aborted propagation in case of low emission angles θ_0. This is connected to the fact that, according to Eq. 2.4, the reflection angle decreases, which entails that light, which is totally reflected during the first reflections, may be lost later. Therefore, light which is produced at larger z is more likely to propagate successfully to the front face and back than light produced at lower z. In contrast to this, Fig. 2.8b shows a more uniform picture for different θ_0. Also the lower number of reflections for a fixed θ_0 has to be noted, because it means that the integral path length for a photon travelling to the front face is lower, which in reality leads to lower absorption probability.

The situation is different if one regards backward propagation. By comparing Fig. 2.8c to 2.8a, severe differences become visible. First, in Fig. 2.8c, no abortion of reflection sequences is visible. Secondly, the distances between reflections now become larger with increasing number of reflection, which is mirrored in Eq. 2.8. This also leads to a significantly lower number of reflections for the tapered crystal type 1. On the contrary, type EC-R, whose reflection map for backward propagation is depicted in Fig. 2.8d, shows the same number of reflections and the same uniform behaviour as in the forward propagation case shown in Fig. 2.8b. A conclusion from these observations is that, for untapered geometries, forward and backward propagation of light is more or less similar, while for tapered geometries, the propagation in backward direction needs much less reflections than in forward direction, where light emitted at low θ_0 can get lost after a few reflections.

To get an impression of the overall amount of light reaching the back face of the crystal for a given position (y_0, z_0), the integral range of emission angles θ_0 enabling a successful propagation, has to be determined. In the following, if the initial emission is forward, this integral is called ξ_n. If the initial emission is backward, it is called ζ_n. Because only light at the back face is recognised, the calculation of ξ_n includes the condition that the angle δ (compare Fig. 2.7), at which the scintillation light impinges on the front face is above θ_{thr}. The requirement, that in turn the new angle θ_0 for backward propagation, derived form δ, is larger than θ_{thr}, is included as well. Because photo sensors are usually coupled to the crystal by optical grease, these conditions have been omitted in case of ζ_0. If scintillation light is emitted isotropically in the $y - z$-plane, the sum of ξ_n and ζ_n is a measure for the light yield available for detection on the end face. $\xi_n + \zeta_n$, as well as ξ_n and ζ_n individually have been calculated for different z_0 distributed over the whole crystal length of $200\,\text{mm}$. For a fixed y_0 amounting to $\frac{BF}{2}$, these values are displayed in Fig. 2.9. Like concluded before, the comparison of both integral angle sums shows that in contrast to the untapered geometry, the
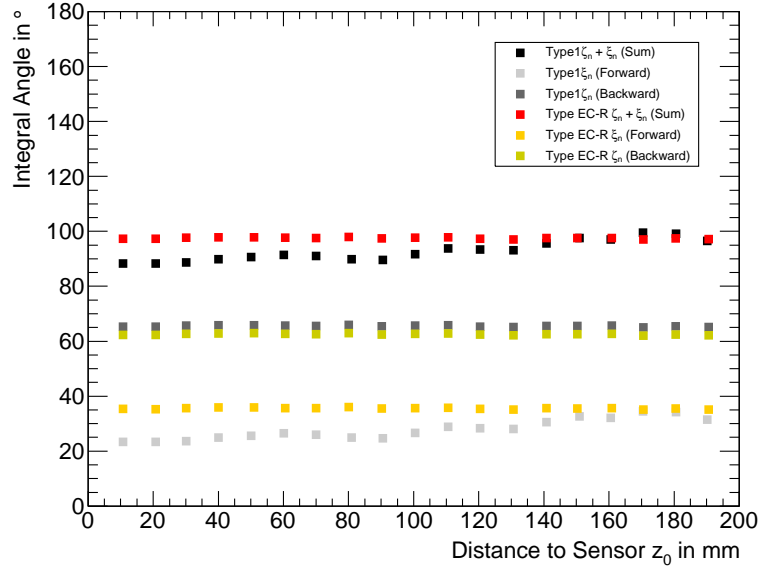
Figure 2.9: Integral emission angle range in dependence of the z-coordinate of the scintillation light's point of origin.

light yield for type 1 geometry depends on the coordinate of its point of origin z_0. For low z_0, less light is propagated through the crystal. Investigating the individual contributions of ζ_n and ξ_n, one recognises that the former gives a constant amount of light over the whole z_0 range, which is slightly higher for type one because of the higher opening angle for direct light and the more favourable reflection angle for backward propagation. In contrast to this, ξ_n for type one shows a strong non-uniformity in its z_0 dependence, because light is lost due to reasons discussed in context of Fig. 2.8a.

2.2 SLitrani Simulations

2.2.1 Implementation

To study NUF effects in a more sophisticated approach, also the more complex mechanisms affecting light propagation, which were neglected in the previous section, have to be taken into account. The SLitrani simulation package [27] is dedicated to perform simulations on light transportation in anisotropic and birefringent media, like Lead Tungstate (PWO). A complete description of the physics behind and included in SLitrani is given in [28]. A 3-dimensional model of a particular crystal shape can
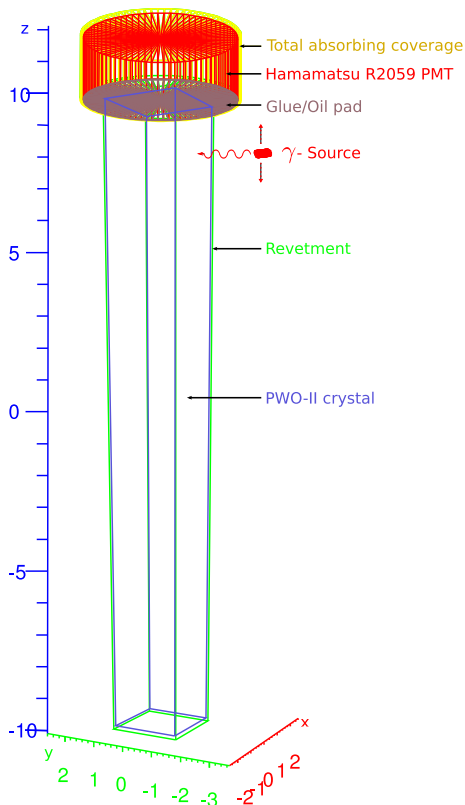
Figure 2.10: Setup as implemented in the performed SLitrani simulations. A PWO-II-crystal of variable geometry type is coupled to a PMT with the properties of a Hamamatsu R2059 by a glue pad. Between the crystal and its revetment, an air gap exists. In each simulation event, a photon of 511 keV energy is emitted in transverse direction to the crystal by the source, which can be moved to different positions along the longitudinal crystal axis. The total absorbing coverage serves the purpose to absorb photons escaping the setup at the rear side.

be implemented by using the class `TGeoTrap` included in the ROOT[1] framework [29]. For each crystal geometry `TGeoTrap` is invoked with different initialisation parameters, which allows to perform the same simulation for different crystal types without changing any other input parameter. These are necessary to mimic the properties of PWO-II as realistic as possible in simulation. Fig. 2.10 shows the used simulation setup schematically. In the following, the implementation of each component and the related major input parameters will be described.

Scintillation light emission spectrum The scintillation light emission spectrum of PWO-II was obtained experimentally with radio-luminescence measurements with a ^{57}Co-source [21, 30]. To implement it into simulation, the superposition of two Gaussian distributions was fitted to the total emission line shape, as indicated in Fig. 2.11a. This was found to describe the line shape very accurately while enabling a robust generation of the desired line shape in simulation by composition of two Gaussian distributions with the extracted fit parameters. The number of photons produced per deposited energy was set to $180\,\frac{\text{photons}}{\text{MeV}}$, according to Tab. 1.3.

---

[1]See also: `http://root.cern.ch`

(a)   (b)
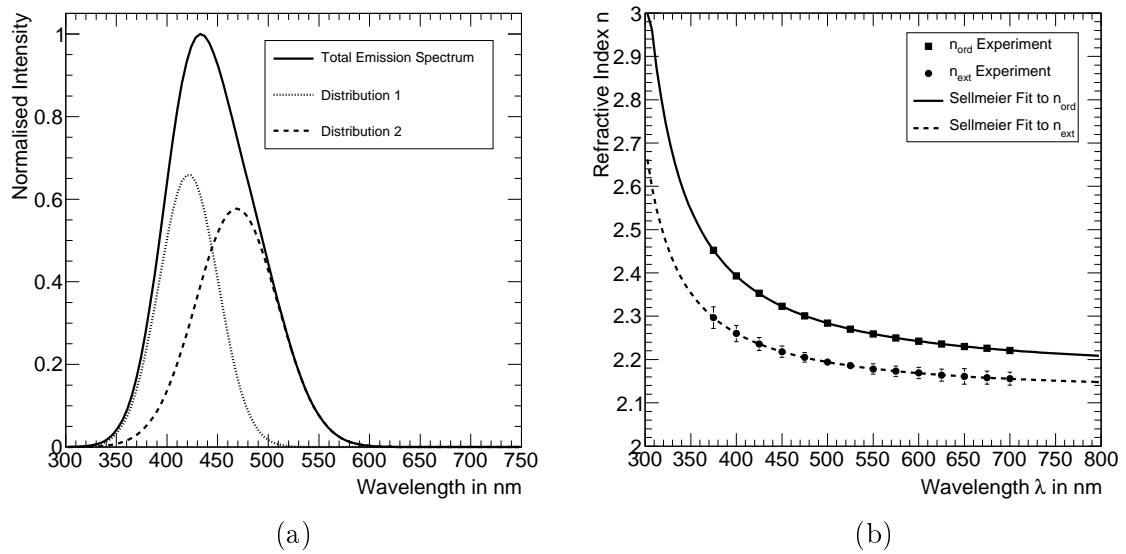
Figure 2.11: Input parameters for the SLitrani simulations. (a) Composition of the experimentally measured scintillation light spectrum out of two Gaussian distribution. (b) Plot of ordinary and extraordinary refractive index n_{ord} and n_{ext} given by [23]. Each is parametrised by an fit of the Sellmeier law for extrapolation over the whole wavelength range.

	FIT TO n_{ord}			FIT TO n_{ext}		
n_0	1.59	$\pm$	0.13	1.67	$\pm$	0.23
n_1	1.09	$\pm$	0.16	0.86	$\pm$	0.40
λ_1	270	$\pm$	19	267	$\pm$	61

Table 2.1: Parameters from Sellmeier fit to the discrete values of n_{ord} and n_{ext}.

Refractive indices and absorption length Because lead tungstate is an uniaxial negative birefringent optical medium, a correct implementation of two refractive indices is mandatory. Values for the real part of the ordinary and extraordinary refractive indices n_{ord} and n_{ext} of PWO for usage in the CMS-ECAL are given in [23] for several discrete wavelengths in the range from 375 nm to 700 nm. Because differences to PWO-II consist mainly in different dopant concentrations, the basic structure of the crystal lattice is hardly changed. Therefore, the refractive indices of both lead tungstate generations should be the same and can be regarded as valid also for $\overline{\text{P}}$ANDA. Since SLitrani needs continuous values over the complete wavelength range of the emission spectrum, the known discrete values of n_{ord} and n_{ext} were each parametrised by a fit according to the Sellmeier law (see Eq. 2.13), which describes empirically the usual wavelength dependence of the refractive index in a transparent medium.

$$n(\lambda) = \sqrt{1 + n_0^2 + \frac{n_1^2}{1 - \frac{\lambda_1^2}{\lambda^2}}} \tag{2.13}$$

The obtained free parameters n_0, n_1 and λ_1 are tabulated for both cases in Tab. 2.1. These can be directly transferred to SLitrani, which then calculates the refractive index n for the required wavelengths according to Eq. 2.13. Another input parameter which can be deduced from optical transmission measurements at known refractive index, is the absorption coefficient k of PWO-II. The measurement used here was performed along the longitudinal crystal axis, with a beam parallel to the extraordinary axis. In this case, only n_{ext} contributes to the measured transmission value. However, due to the high value of n_{ext}, one has to include multiple reflections on front and rear face of the crystal, which are oriented perpendicular to the light beam. Using the transmission t and reflectance r for one boundary of two media with refractive indices n_1, n_2, which are given by

$$t = 1 - r, \tag{2.14}$$

$$r = \left| \frac{n_2 - n_1}{n_2 + n_1} \right|^2, \tag{2.15}$$

the overall transmission T for an infinite number of reflections can be calculated. Light entering the crystal at the rear face and exiting at the front face comprises the main

contribution T_0 to the overall transmission, which amounts to

$$T_0 = t^2 e^{-kL}, \tag{2.16}$$

where k represents the absorption coefficient and L the crystal length. Light initially reflected back can exit at the front face again after two reflections, having traversed an additional length of $2L$, resulting in a further transmission contribution T_1, reduced by a factor

$$q = r^2 e^{-2kL} \tag{2.17}$$

in comparison to T_0. Also, each subsequent contribution T_i is then reduced by the same factor q. The overall transmission can be obtained by a summation of all transmission contributions T_i, resulting in a representation of the geometric series, the limit for which is well defined:

$$T = \sum_{i=0}^{\infty} T_i \tag{2.18}$$

$$= T_0 \cdot \sum_{i=0}^{\infty} q^i \tag{2.19}$$

$$= T_0 \cdot \frac{1}{1-q}. \tag{2.20}$$

Replacing T_0 and q by Eq. 2.16 and Eq. 2.17, the following expression for the overall transmission including multiple reflections and absorption is obtained:

$$T = \frac{t^2 e^{-kL}}{1 - r^2 e^{-2kL}}. \tag{2.21}$$

For the determination of the absorption coefficient k, Eq. 2.21 has to be rearranged, ending up with:

$$k = -\frac{1}{L} \cdot \ln\left(\frac{\sqrt{t^4 + 4T^2 r^2} - t^2}{2Tr^2} \right) \tag{2.22}$$

With the measured longitudinal transmission $T(\lambda)$, the relevant refractive index $n_{ext}(\lambda)$ of the PWO-II crystal, the surrounding air ($n_{Air} \approx 1$), and the well defined length of the crystal amounting to $L = 20\,\text{cm}$, the absorption coefficent can be calculated for a given wavelength. Using for example the mean transmission value from Quality Control (QC) at Justus-Liebig-Universität Gießen (JLU Gießen) of $T(420\,\text{nm}) = 70.96\,\%$, one obtains an absorption coefficient of $k(420\,\text{nm}) = 2.303 \cdot 10^{-3}\,\frac{1}{\text{cm}}$, corresponding to an absorption length of $l_{abs} = 434.22\,\text{cm}$, which amounts to more than 21 crystal lengths.
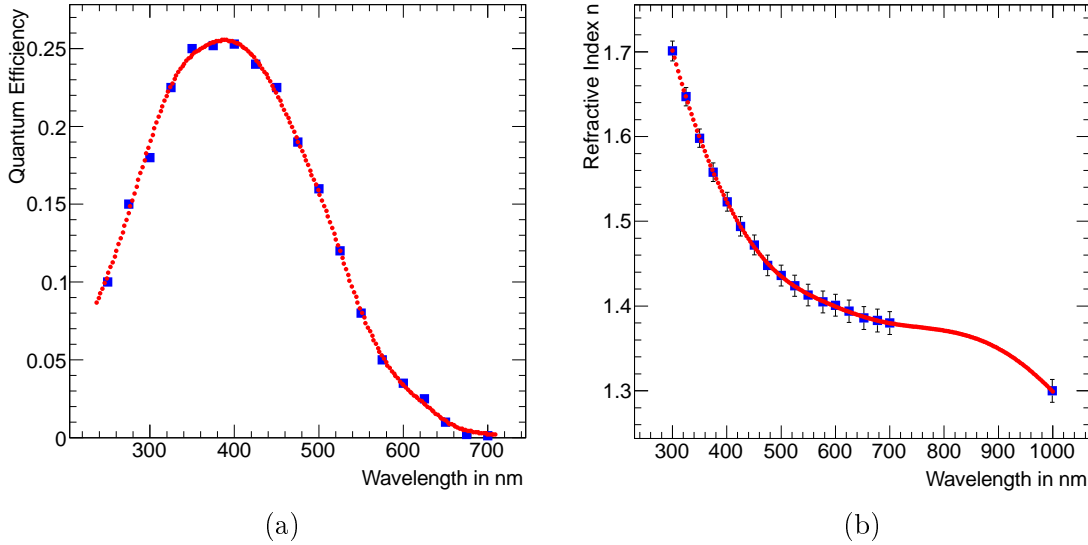
Figure 2.12: Spline fits for implementation of the optical properties of PMT quantum efficiency (a) and refractive index of the optical coupling material (b).

Photo sensor quantum efficiency and coupling Beside the properties of the scintillator material itself, also the optical properties of the photo sensor attached to the rear face of the crystal have to be defined properly. Due to reasons of comparability to the experiments described in Sec. 2.3, a PMT with 2" diameter, which covers the complete crystal rear face, was chosen. The quantum efficiency of the photo cathode was taken from the datasheet of the Hamamatsu R2059 [31], used in experiment. Known quantum efficiency values at given wavelengths were fitted with a spline[2], as indicated in Fig. 2.12a. The available datasheet of R2059 gives no information on the refractive index of the entrance window, which consists of fused silica. Therefore a spline fit to the refractive index of sodocalcic glass, another common material for PMT entrance windows, was used as simulation input to describe its optical properties. Since it shows only slight variations inside the relevant wavelength range and corresponds, within uncertainties, to the same value of the refractive index as commonly found in literature for fused silica, this should represent a good approximation. Optical properties of the coupling between crystal and entrance window is implemented into simulation by a spline fit to the refractive index of the Dow Corning 3145 RTV (DC3145) adhesive (see Fig. 2.12b). This glueing material was studied by the CMS-ECAL collaboration and is envisaged for optical coupling or glueing of LAAPDs and VPTTs to the PWO-II crystals in the $\overline{\text{P}}$ANDA EMC [32]. For these reasons, its optical properties are well known and implementation seems reasonable, despite the fact that for the experiments described in Sec. 2.3, coupling was performed non-permanently with silicone oil. The

---

[2]Piecewise-defined polynomial

thickness of the glue pad coupling crystal and entrance window was set to 0.1 mm.

Crystal wrapping As wrapping of the crystal, the VM2000 enhanced specular reflector film (VM2000)[3], foreseen for use in the EMC and already used in prototypes, is implemented as a specular reflector, which absorbs 10 % of the incoming intensity. However, there exists an air gap between crystal surface and wrapping, which has a thickness of 0.1 mm. Therefore the optical properties of the wrapping have a minor impact on light propagation compared to the influence generated by the large difference of the indices of refraction of crystal and air gap.

γ-Source Finally, an event is triggered by emission of a photon of 511 keV mean energy by a γ-source placed at coordinates

$$\vec{r}_{Source} = \left(\frac{CR}{2}, \frac{BR}{2} - 3.5\,\text{cm}, z_0\right). \tag{2.23}$$

For the sake of comparability to calculations and experiments in Sec. 2.1.2 and Sec. 2.3, in Eq. 2.23 the coordinate system has been defined according to Fig. 2.7. The coordinate origin is located at the intersection of the edges BR and CR. In contrast to that, the origin for the setup shown in Fig. 2.10 is located in the crystal centre, due to reasons of simplicity in construction of interlaced geometry objects. γ-quanta are emitted from a flat elliptical surface, whose semi-major is oriented along the crystal's x-axis and has a length of 0.2 cm. Its half as long semi-minor is parallel to the longitudinal crystal axis (z-axis). The energy distribution has a Gaussian shape with a σ of 20 keV, but no photon energy outside the 1σ-region is allowed.

2.2.2 Simulation Procedure

Using the setup and initial parameter settings as described above, SLitrani simulations can be performed for a specific crystal geometry type and chosen longitudinal γ-source position z_0. A simulation event is started by emission of exactly one γ-particle from the source emitted in direction of the PWO-II crystal. In the course of the simulation, first the interaction of the initial photon with the materials of the setup is calculated, resulting, if energy is deposited inside the scintillator by e.g. photo or Compton effect, in the generation of scintillation light. A map of the energy deposition inside the different media is shown in Fig. 2.13. As can be recognised, the complete energy is deposited in the crystal volume, with a clearly recognisable photo peak and Compton background. The generated scintillation photons are then further propagated until

---

[3]Manufactured by 3M. Now available under the brand name Vikuiti[TM] (ESR)
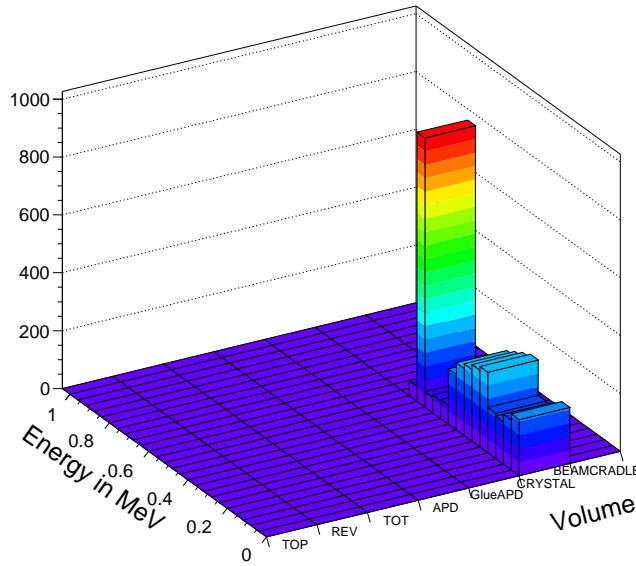
Figure 2.13: Energy deposited by the initial photon in different Volumes of the simulation setup.

absorbed or reaching the PMT's photo cathode, where they will be, with respect to the Quantum Efficiency (QE), detected or rejected. To obtain a realistic response comparable to the light yield measured in an experiment, as defined in Eq. 2.1, the number of scintillation photons N_{ph} registered by the PMT was determined for each event. Because each registered photon corresponds to a photoelectron emitted by the photo cathode, N_{ph} can also be regarded as the number of photoelectrons. To obtain the simulation light yield LY_{sim}, this has to be normalised by the mean γ-energy E_γ, as expressed in Eq. 2.24:

$$LY_{Sim} = \frac{N_{ph}}{E_\gamma}. \tag{2.24}$$

The individual LY_{Sim} is then histogrammed for all events of a specific simulation run and finally stored in a `.root`-file. As a typical run size, a number of 2000 events was chosen, which represents a good compromise between simulation duration and suppression of statistical fluctuations. For test purposes, also runs with sizes of 5000 events were performed without significant changes to the extracted information. After several test runs ensuring the correct implementation of all geometry objects and parameters as described, a simulation scheme was performed. For each geometry, runs were performed at nine different γ-source positions. Its z coordinate was varied in steps of 2 cm in the range $2\,\mathrm{cm} \leq z_0 \leq 18\,\mathrm{cm}$. Although for each geometry the same

amount of information is available, the analysis of the simulation data will concentrate on the geometry types which show the largest difference in the mean tapering angle. As can be seen in Fig. 2.4a, these are types 1, 4, 7, 10, EC(12) and EC-R(13), respectively. Additionally, type 6 is of importance, because of its use in the first prototype for the $\overline{\mathrm{P}}$ANDA Barrel EMC.

2.2.3 Simulation Data Analysis

An overview of the LY_{Sim} distribution for each γ-source position z_0 is displayed exemplarily for geometry type 1 in Fig. 2.14. The spectrum shows mainly a Gaussian shape with a background originating from events, where no scintillation photon was registered by the photo sensor. For this strongly tapered geometry type, a clear peak shift is observed at larger distances to the photo sensor.

Light Yield Position Dependence

To determine the exact mean of the LY_{Sim} distributions, each was fitted with a Gaussian distribution in the range of ± 2.5 Root Mean Square (RMS) around the histogram maximum. To exclude background events, it was additionally required that the lower bound of the fit range was $\geq 2\,\frac{\mathrm{phe}}{\mathrm{MeV}}$. All fits for geometry type 1 are displayed in Fig. 2.14 as well. The extracted mean values for the simulated light yield, together with the corresponding errors, are shown for selected geometries in Fig. 2.15a. A clear non-uniformity in the mean LY_{Sim} is observed, most strongly pronounced for geometry type 1, where the values range from approximately $9\,\frac{\mathrm{phe}}{\mathrm{MeV}}$ close to the sensor to roughly $18\,\frac{\mathrm{phe}}{\mathrm{MeV}}$ at 18 cm distance. In contrast to that, type EC-R shows a uniform response of approximately $7\,\frac{\mathrm{phe}}{\mathrm{MeV}}$ for all γ-source positions. These discrepancies between the geometry types become even more pronounced, if one regards the light yield normalised to the value at 2 cm distance, as displayed in Fig. 2.15b. Types 1 and EC-R represent the two extreme cases, while the other geometry types show an intermediate non-uniformity with a grouping similar to the tapering angle grouping observed in Fig. 2.4a.

Non-uniformity Characterisation

In order to achieve a characterisation of the level of non-uniformity depicted in Fig. 2.15a, the curve shape belonging to the individual geometry types has to be described adequately. If the same characterisation is applied to simulated data as well as measurement data, a decoupling of the curve's shape and the absolute LY level is desirable, because the latter will be influenced significantly by the intrinsic quality of the
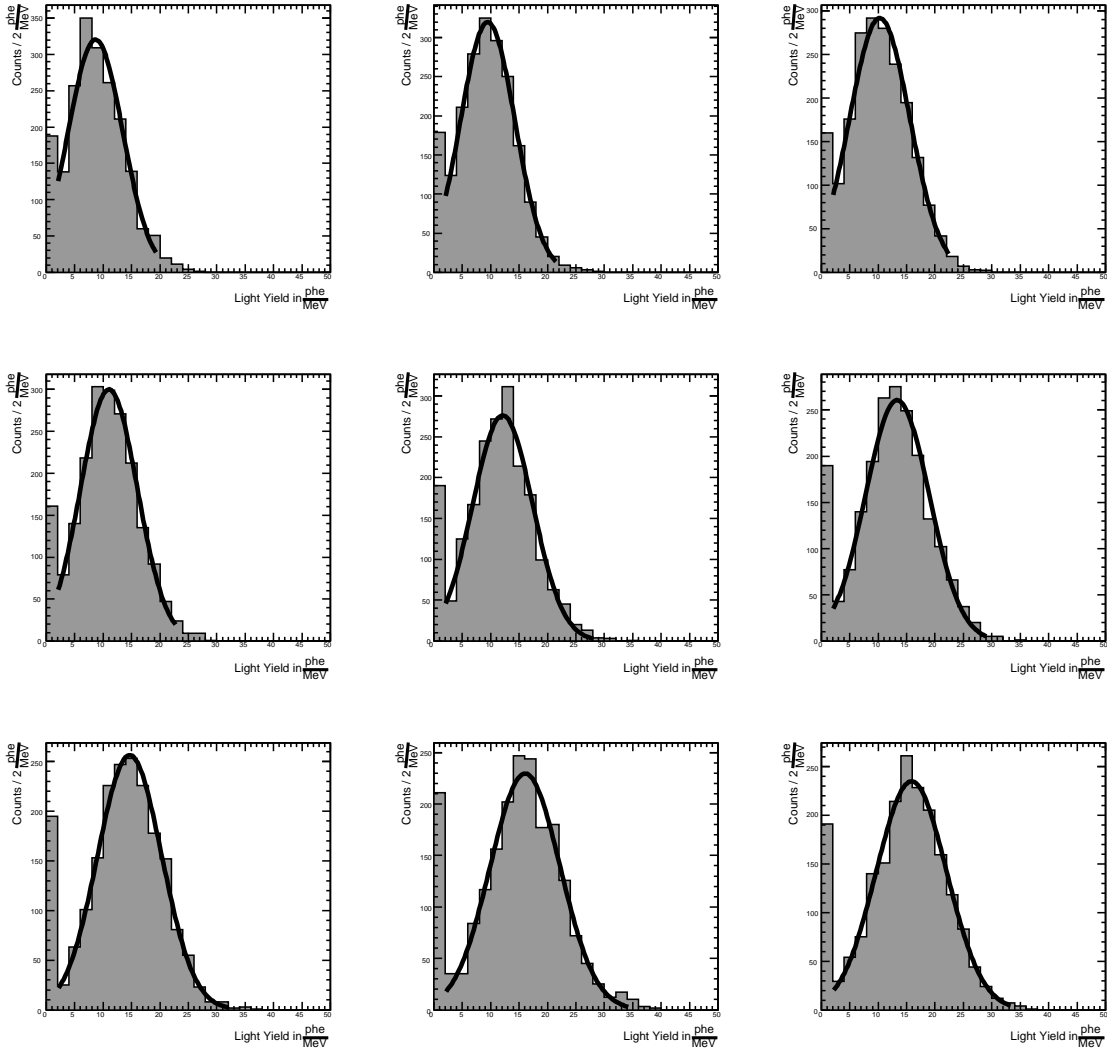
Figure 2.14: Light yield simulated for type 1 geometry at different distances from the photo sensor, fitted with a Gaussian function.

(a)   (b)
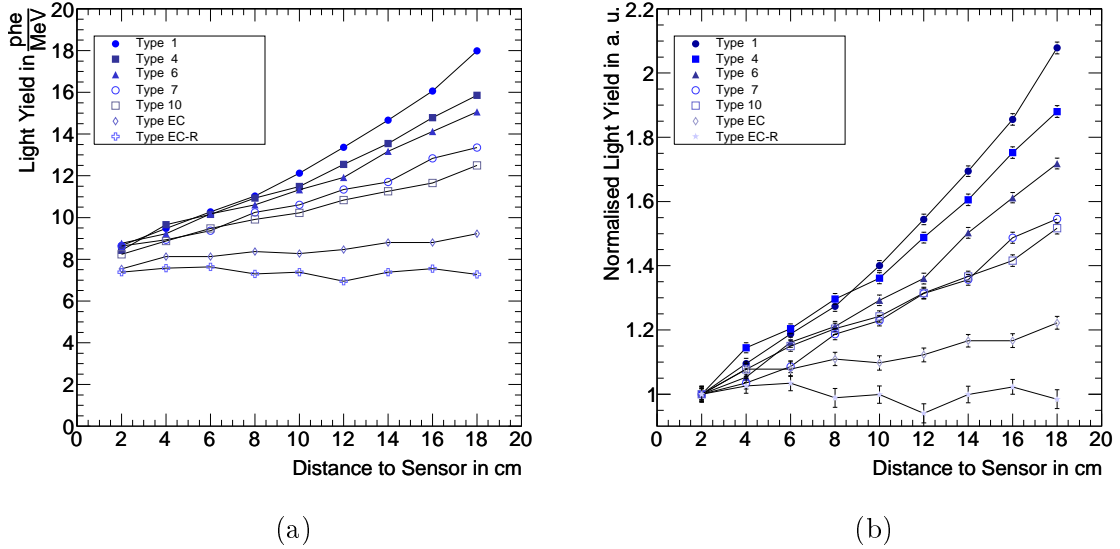
Figure 2.15: Simulated light yield for selected geometry types plotted in dependence
of the distance of the γ-source to the PMT in absolute values (a) and
normalised to the position closest to PMT (b).

scintillator material. This is subject to variations due to fluctuation in the crystal
production process. Furthermore, the light yield position dependence curve shape is
non-linear. A polynomial of second degree was chosen to parametrise the light yield
position dependence, as given in Eq. 2.25, representing a good compromise between
shape flexibility and the minimum amount of two parameters.

$$LY(z) = a + b \cdot z + c \cdot z^2 \tag{2.25}$$

The free parameter a represents the absolute position of the function, while b and c
contain the function shape information. All fits performed for the individual geome-
tries are visualised in Fig. 2.16a, while the corresponding extracted parameters for
each geometry type can be found in Figs. 2.16b, 2.16c and 2.16d, respectively. Appar-
ently, the absolute LY_{Sim} (parameter a) is hardly varying among crystal types. This is
understandable, since the material properties in all of the performed simulation runs
where exactly the same. The linear contribution to the function shape (parameter b)
is, within the error bars, the same for all crystal types belonging to the Barrel EMC,
while types EC and EC-R show decreased or no linear contribution. For the quadratic
contribution (parameter c), one observes the largest value for crystal type 1, which is
continuously decreasing for larger type numbers. Types 10, EC and EC-R show no
quadratic dependence at all within the uncertainties.
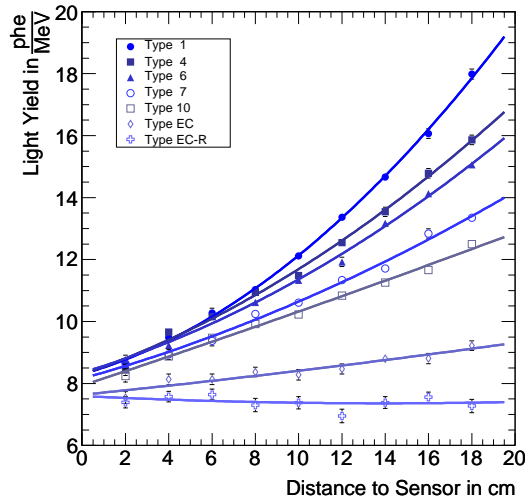
(a)
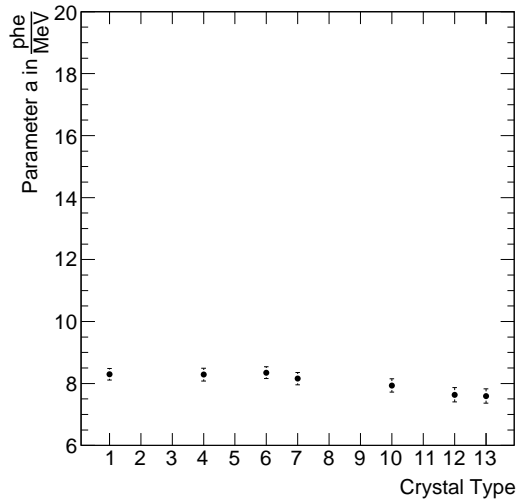
(b)
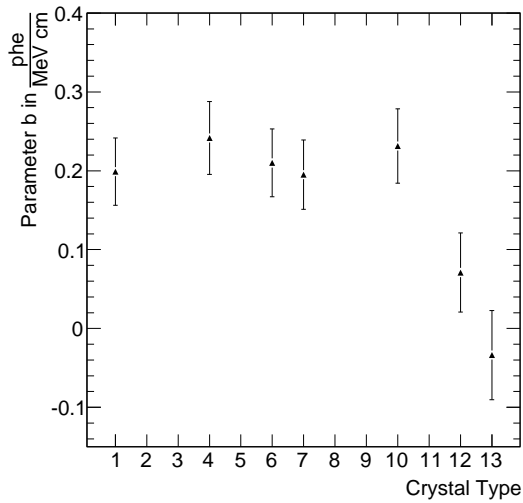
(c)
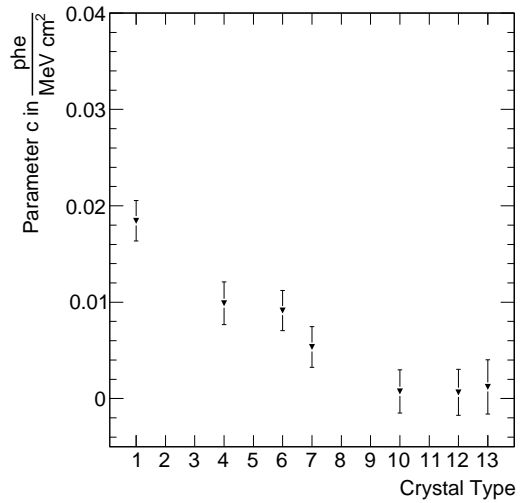
(d)

Figure 2.16: Simulated NUF for several types fitted with a second order polynomial (a). The extracted parameters a, b and c are shown in (b), (c) and (d), respectively.

An indicator for the local NUF at position z is the derivative of Eq. 2.25.

$$\frac{dLY(z)}{dz} = b + 2c \cdot z \tag{2.26}$$

For a characterisation of the global level of NUF of a crystal, the local NUFs for a whole range, reaching from point z_1 to point z_2, has to be evaluated. Therefore the integral of 2.26 within the given limits is calculated to be

$$\int_{z_1}^{z_2} \frac{dLY(z)}{dz}\, dz = b \cdot z + c \cdot z^2 \Big|_{z_1}^{z_2} \tag{2.27}$$

$$= b \cdot (z_2 - z_1) + c \cdot (z_2^2 - z_1^2). \tag{2.28}$$

By dividing Eq. 2.28 by $(z_2^2 - z_1^2)$, the strong range dependence is reduced. Finally the single parameter Π, characterizing the overall NUF, is obtained, which is expressed in Eq. 2.30.

$$\Pi = \frac{\int_{z_1}^{z_2} \frac{dLY(z)}{dz}\, dz}{z_2^2 - z_1^2} \tag{2.29}$$

$$= \frac{b}{z_2 - z_1} + c. \tag{2.30}$$

Accounting for both, linear and quadratic NUF contributions, represented by parameters b and c, Π reflects the situation pictured in Fig. 2.14 better than either of these alone. This is underlined by Fig. 2.17a, where Π values calculated for the range limits $[z_1, z_2] = [2\,\text{cm}, 18\,\text{cm}]$ are displayed for the selected crystal geometry types. The overall NUF is largest for crystal type 1 and decreases with increasing geometry type number, which is consistent with the previous considerations. Plotting Π versus the mean tapering angle μ (defined in Eq. 2.2), as depicted in Fig. 2.17b, a clear correlation is visible. A fit with a linear function yields an offset of $-0.0012 \pm 0.0027 \frac{\text{phe}}{\text{MeVcm}^2}$ and a slope of $0.0130 \pm 0.0018 \frac{\text{phe}}{\text{°MeVcm}^2}$. This leads to the conclusion that the NUF is directly proportional to the mean level of tapering of a crystal, which is in agreement with the considerations stated in Sec. 2.1.2.

Mean Travelled Distance and Absorption

To evaluate the influence of absorption effects on the NUF, the travelled distance of scintillation photons until detection by the PMT is plotted in Fig. 2.18a and Fig. 2.18b for each geometry type, if the γ-source is positioned at $z = 2\,\text{cm}$ or $z = 18\,\text{cm}$, respectively. Fig. 2.18a shows a gap of the order of two crystal lengths between
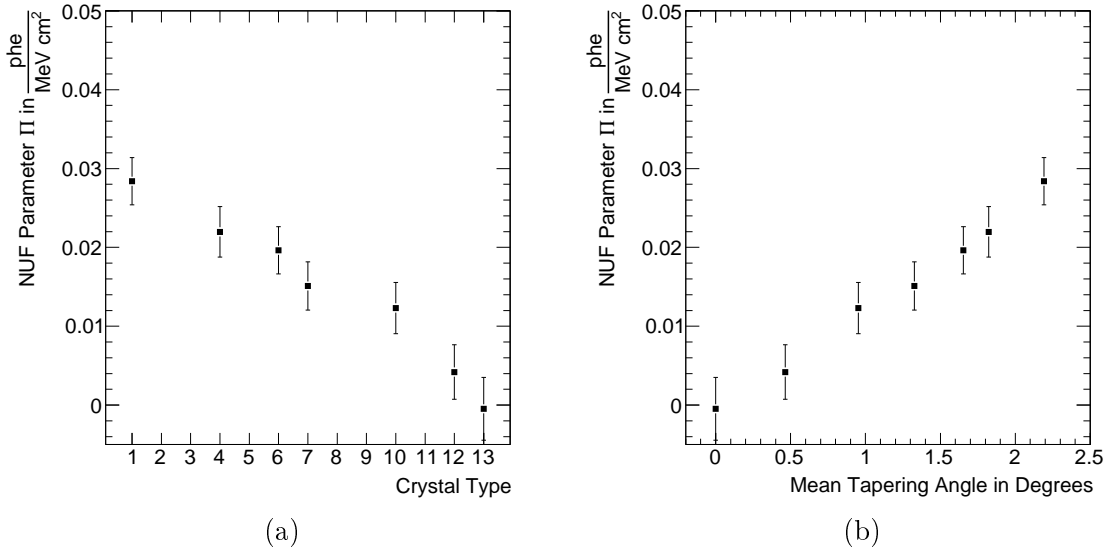
Figure 2.17: Non-uniformity parameter Π as obtained from fit to the simulated NUF curve for the selected crystal types (a) and in dependence of the mean tapering angle μ (b).

the peaks in the travelled distance distribution, representing light arriving directly and after propagating once through the crystal. As can be expected, this gap is smaller in Fig. 2.18b, due to the smaller path length difference between forward and backward propagating light. Another peculiarity is that this gap is still visible after several passages through the crystal in the case of the non-tapered type EC-R, while for increasing level of tapering the peaks become more smeared out, resulting in a disappearing gap after the second passage for type numbers smaller than 4. The described behaviour can be interpreted as the conservation of the initial scintillation light emission angle information for non- or less tapered crystals, while it is lost for more strongly tapered shapes. Figs. 2.19a and 2.19b use the same style of diagram to depict the distance travelled before scintillation photons are absorbed anywhere in the simulated setup. Here the characteristics attributed to the travelled distance distribution are quite inverse to the one observed previously. Strongly tapered shapes show peaks in the number of absorbed photons at distances fitting the arrival at the PMT, while less tapered types show a more or less uniform distribution. To evaluate the contributing absorption effects in more detail, Tab. 2.2 lists, for the two extreme geometries, the number of photons absorbed attributed to the place of absorption. Apparently, for type EC-R, most photons are absorbed in the crystal material, followed secondly by absorption in the wrapping and due to the quantum efficiency of the photo sensor. It has to be stressed that the latter amount scales directly with the amount of photons arriving at the sensor. As anticipated, no major differences are visible

(a) Scintillation light produced at 2 cm distance to photo sensor.

(b) Scintillation light produced at 18 cm distance to photo sensor.
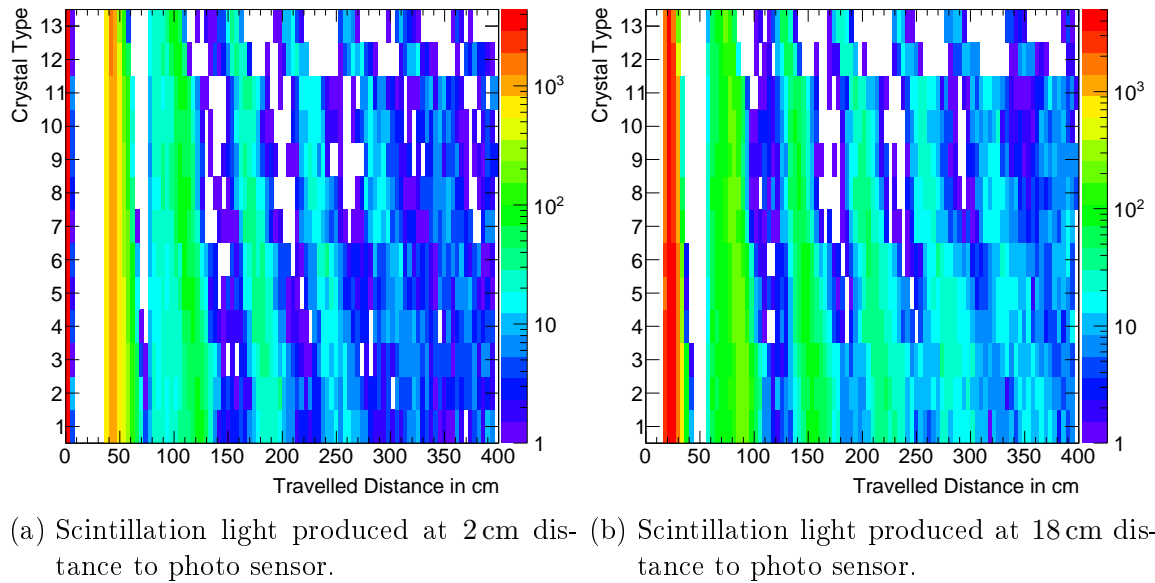
Figure 2.18: Distance travelled by scintillation photons inside a crystal before registration by the photo sensor, displayed for different crystal types.

(a) Scintillation light produced at 2 cm distance to photo sensor.

(b) Scintillation light produced at 18 cm distance to photo sensor.
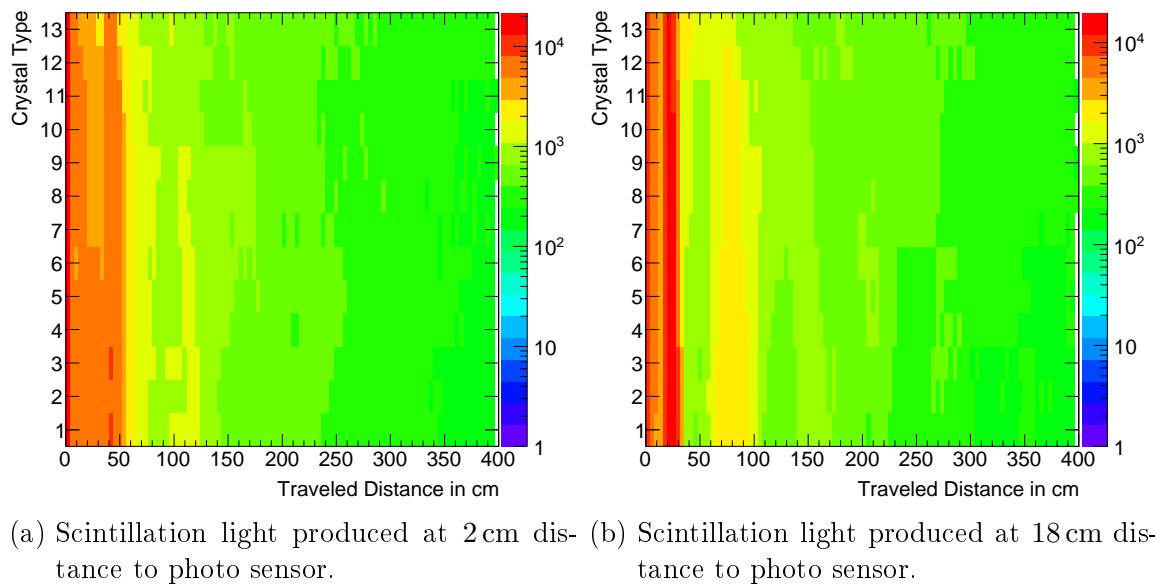
Figure 2.19: Distance travelled by scintillation photons inside a crystal before absorption, displayed for different crystal types.

Type	Posi-tion	Absorbed due to / in			
		PWO-II	Wrapping	Quantum Efficiency	Anywhere
1	2 cm	51197	75741	35257	162958
	10 cm	45076	63833	45191	154470
	18 cm	38031	42489	62819	143557
EC-R	2 cm	85714	37845	30467	159002
	10 cm	84595	37374	29856	156799
	18 cm	85032	38050	29930	158011

Table 2.2: Number of absorbed scintillation photons for a type 1 geometry at three different γ-source positions. Listed are the numbers for photons either absorbed in the PWO-II scintillator material, by the wrapping during reflection or not registered due to the quantum efficiency of the photo sensor. Additionally, the total amount of scintillation photons, lost anywhere in the setup, is given.

if comparing different γ-source positions. On the contrary, type 1 shows a strong position dependence. While for $z = 2\,\mathrm{cm}$ most photons are absorbed when reflected by the wrapping, followed secondly by the scintillation material, at $z = 18\,\mathrm{cm}$ the loss due to quantum efficiency provides the largest share, due to the large amount of photons impinging on the PMT. The dominance of the wrapping's absorbance can be attributed, in accordance to the considerations described in Sec. 2.1.2 and depicted in Fig. 2.9, to the reduced amount of totally reflected photons propagating in direction of the front face. For a further understanding of the discrepancies in Tab. 2.2, especially the amount of photons absorbed in the scintillator itself, Fig. 2.20 shows the total amount of photons absorbed and detected, if produced at $z = 18\,\mathrm{cm}$ for both types over an extended range. Although after the first passage through the crystal roughly the same amount of scintillation photons is absorbed and detected, for each passage after the first there are significantly more detected photons in case of type 1 geometry. This is mostly caused by the larger width of the peaks, which further enlarges after each passage, leading to a disappearance of the peak structure, denoting that the travelled distance is subject to large variations. On the contrary, the peak structure's width is conserved in case of EC-R geometry. This implies that, as mentioned above, also the information on the incident emission angle is conserved. Therefore, photons can, with a certain probability, be trapped inside a crystal or need at least a longer time and hence have to travel a larger distance in the scintillator material, until transmitted through the rear face to the PMT. As a result, the amount of photons absorbed is significantly larger than for type 1, as can be seen in Fig. 2.20, for travelled distances larger than 150 cm. The absorption peaks at lower distances
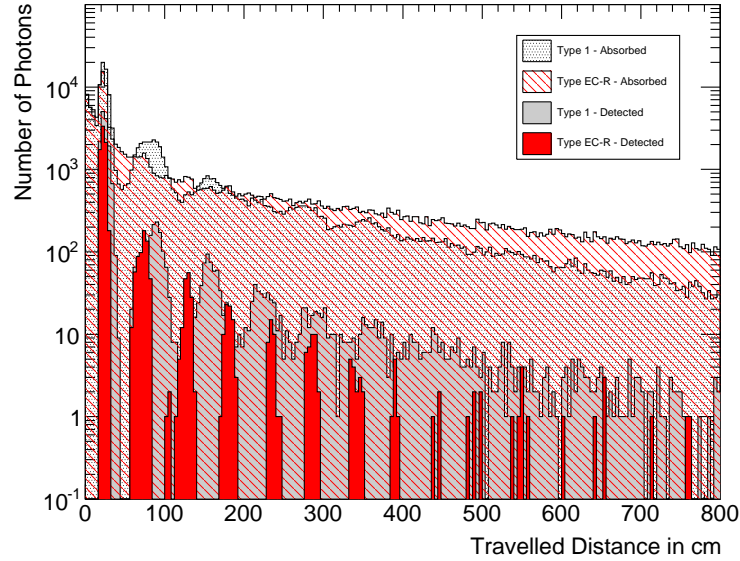
Figure 2.20: Comparison of the number of photons absorbed anywhere in the setup or detected by the PMT for type 1 and EC-R, if the source is at $z = 18\,\mathrm{cm}$.

represent the loss caused by the quantum efficiency of the photo sensor, correlated to the high amount of detected photons.

Point of Impact on Photo Sensor

Since the amount of scintillation photons detected at the crystal rear face varies with the production distance, also its distribution may be subject to such variations. Indeed, simulations show that for the two extreme cases of production at $z = 2\,\mathrm{cm}$ and $z = 18\,\mathrm{cm}$, the scintillation light is unequally distributed. Fig. 2.21a and Fig. 2.21b illustrate this for a type 1 geometry crystal, while Fig. 2.22a and Fig. 2.22b depict the same for type EC-R geometry. In both cases, for production close to the sensor, one observes a local maximum close to the side, where the initial γ enters the crystal. In case of the cuboid EC-R crystal (Fig. 2.22a), the maximum is more pronounced. If light is produced at larger distances, namely $z \gtrsim 4\,\mathrm{cm}$, the points of impact are equally distributed over the whole crystal rear face. This effect should not have a large impact on measurements with photo sensors possessing sufficiently large sensitive area to cover the whole crystal rear face. However, for the LAAPDs envisaged for the EMC, whose sensitive area is smaller than the crystal rear face, the non-uniform point of impact distribution can have a considerable influence on the detector response. On account of this, a coverage of the non-sensitive crystal rear face area with reflective material is desirable, to collect as much light as possible, regardless of the photo sensor's size.
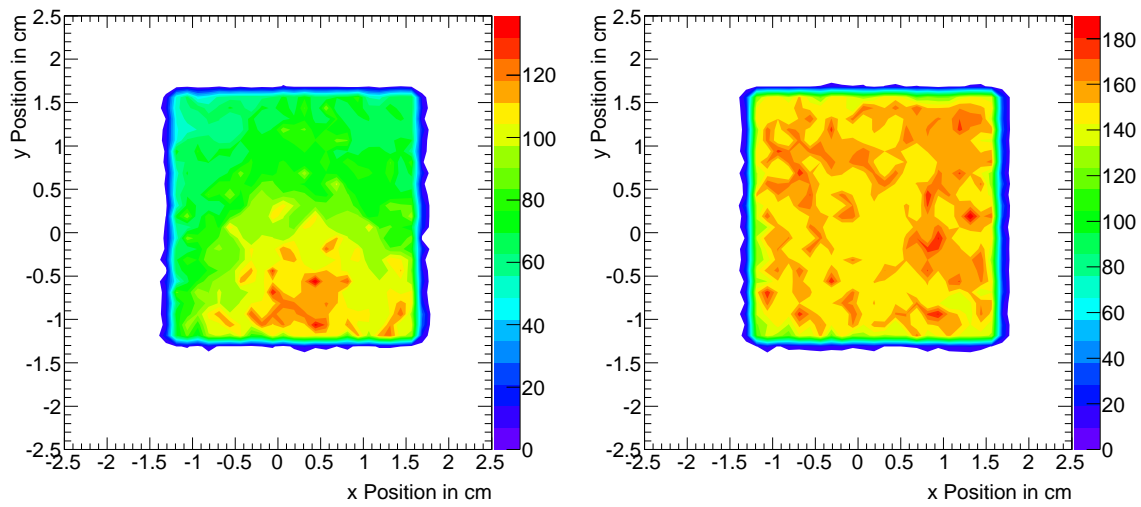
(a) Scintillation light produced at 2 cm distance to photo sensor.

(b) Scintillation light produced at 18 cm distance to photo sensor.

Figure 2.21: Point of impact of scintillation photons on PMT photo cathode in type 1 geometry crystals.

Nevertheless, in all these observations it has to be considered that the initial 511 keV photon is entering the crystal from the side and has, as can be derived from Fig. 1.14, a mean free path length of $x_e = 0.878$ cm. This means most of the scintillation light is produced at the crystal surface, whereas in calorimetry, where an electromagnetic shower is developing within the crystal and the production of scintillation light is less localised, a more homogeneous illumination of the crystal rear face can be expected.
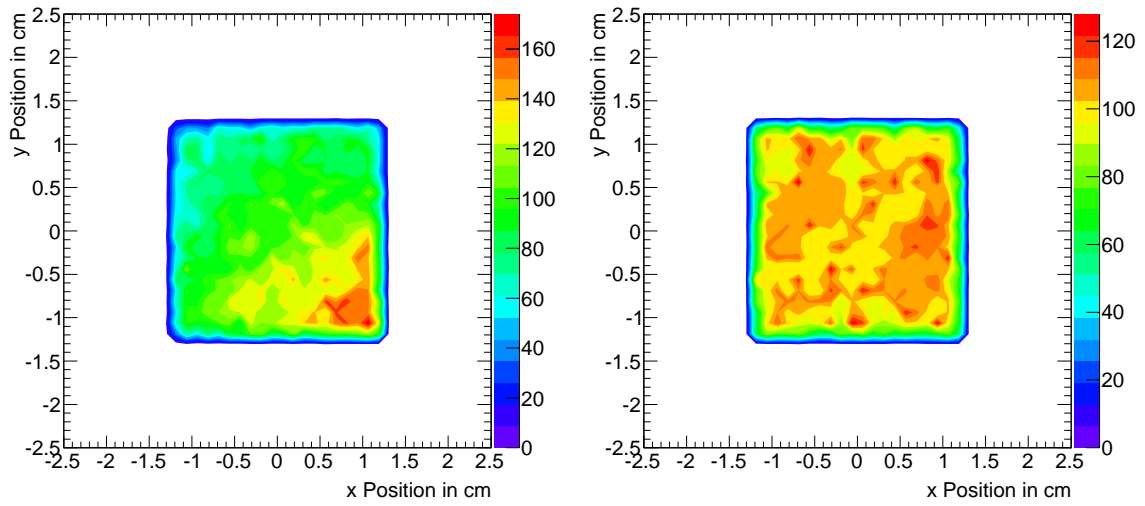
(a) Scintillation light produced at 2 cm dis-
tance to photo sensor.

(b) Scintillation light produced at 18 cm dis-
tance to photo sensor.

Figure 2.22: Point of impact of scintillation photons on the PMT photo cathode in
type EC-R geometry crystals.

2.3 Experiments

2.3.1 NUFs in Quality Control Measurements

Because during QC a large number of crystals has to be processed, LY is measured at CERN by an Automatic Crystal quality COntrol System (ACCOS) relatively to a reference crystal. The system was previously used for CMS-ECAL crystals and is described in detail in [33]. With only slight adaptations, due to the different geometry, ACCOS is also able to measure PWO-II crystals with $\overline{\text{P}}$ANDA geometry. To obtain the absolute LY of the crystals, the correlation of the relative values provided by ACCOS to the independently measured absolute LY of a sample of the same crystals remeasured at JLU Gießen was used. This procedure is discussed in detail in [34]. Fig. 2.23, shows the LY distributions of all PWO-II crystals delivered so far by the producer Bogoroditsk Techno Chemical Plant (BTCP), grouped according to the geometry type. One observes a different LY mean value for each shape. At maximum, a shift of approximately $8 \frac{\text{phe}}{\text{MeV}}$ is visible, which is far too large to be caused only by fluctuations in the scintillator material quality. Furthermore, although crystals are cut into different shapes after growth, the ingots, drawn from the melt applying the Czochralski method [21], are about the same size and shape. Consequently no major differences in dopant concentration and neither in the intrinsic LY are expected. As can be seen in Figs. 2.24a to 2.24d, there is a correlation between QC LY and the tapering angles α, β, γ and mean tapering angle μ. In turn, the latter is proportional too the NUF parameter Π, as described in Sec. 2.2.3, indicating that the LY indeed is caused by light collection NUFs.

This can be understood by a closer inspection of the LY calibration setup at JLU Gießen, illustrated in Fig. 2.25. The used ^{137}Cs-sources are placed approximately $2 - 5\,\text{cm}$ from the crystal front face. To avoid pileup, sources with high activity were placed at a larger distance. Nevertheless, this source positioning inflicts systematic bias on the measurement. The mean free path length for the given energy in lead tungstate amounts to $x_e = 1.13\,\text{cm}$, which means on average $\sim 95\%$ of the $662\,\text{keV}$ photons deposit energy at distances $z > 16.5\,\text{cm}$ from the PMT. In this region, the NUF's influence on the measured LY is strongest. Thus, a systematically higher LY can be expected for more tapered shapes and the pattern observed in Fig. 2.23 can be regarded as a first experimental prove of a light collection NUF in PWO-II crystals with $\overline{\text{P}}$ANDA EMC geometry. In an approach to measure the NUFs more precisely and investigate uniformisation methods, a series of experimental setups was developed, which are described in the following.
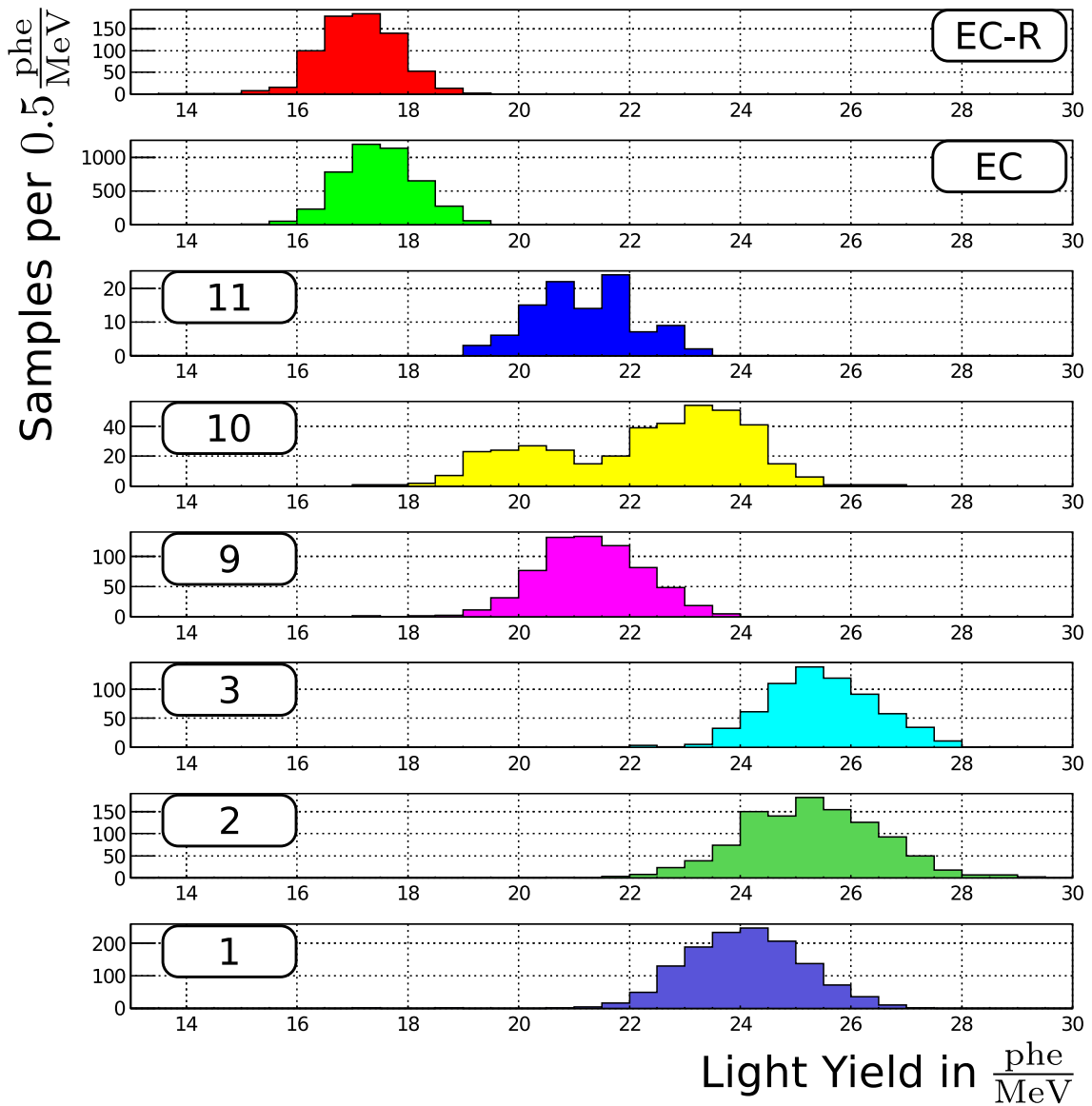
Figure 2.23: LY distributions measured relatively to a reference crystal by ACCOS [33] at CERN and calibrated to absolute values in units of $\frac{phe}{MeV}$ at JLU Gießen [34]. The LY is displayed separately for each geometry. One recognises an increase of the average LY for more strongly tapered shapes.

(a)

(b)

(c)

(d)
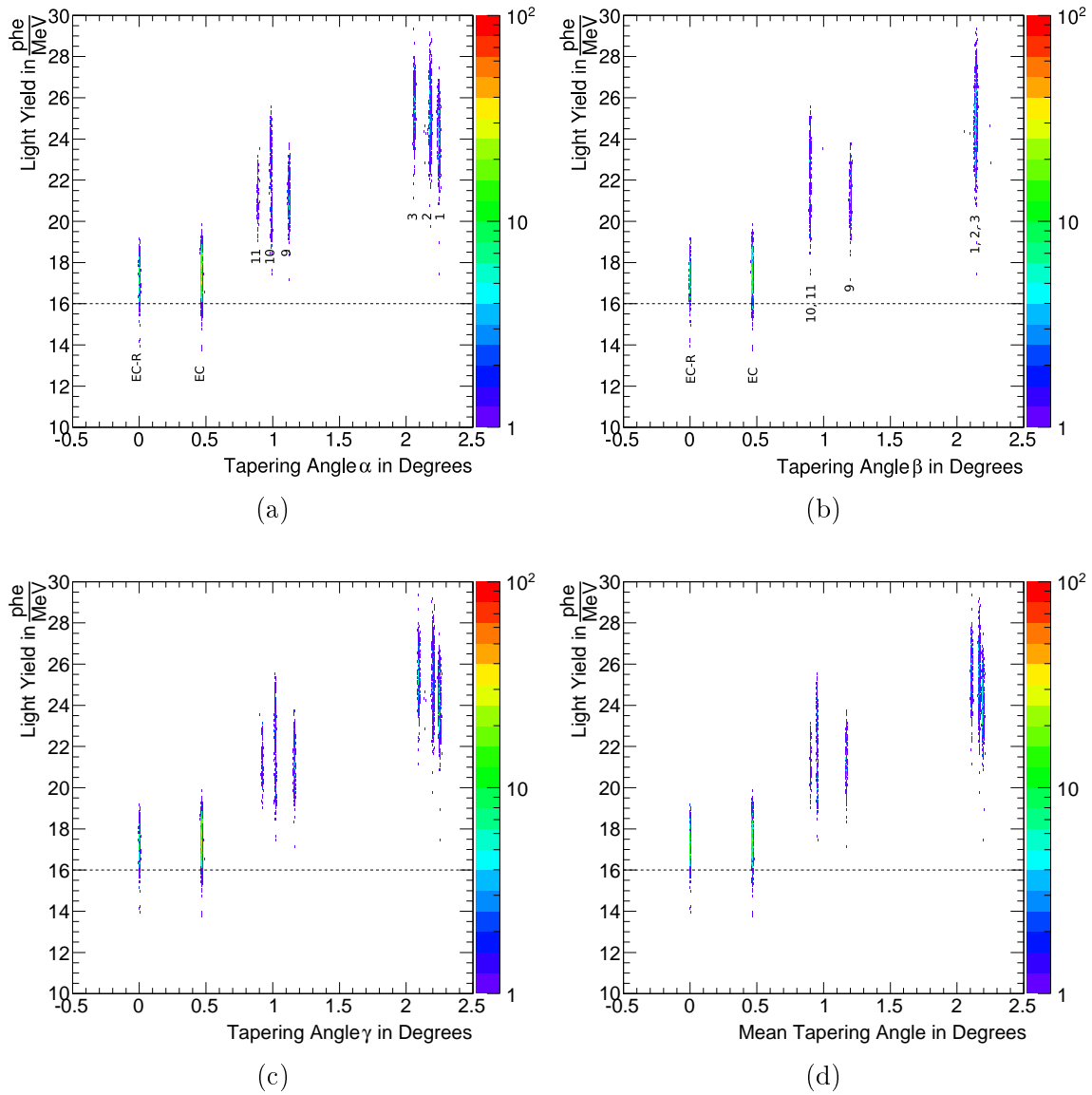
Figure 2.24: Correlations between LY and the tapering angles α (a), β (b), γ (c) and mean tapering angle μ (d). The LY specification limit is marked with a dashed line. A clear correlation of LY and tapering angle is visible.
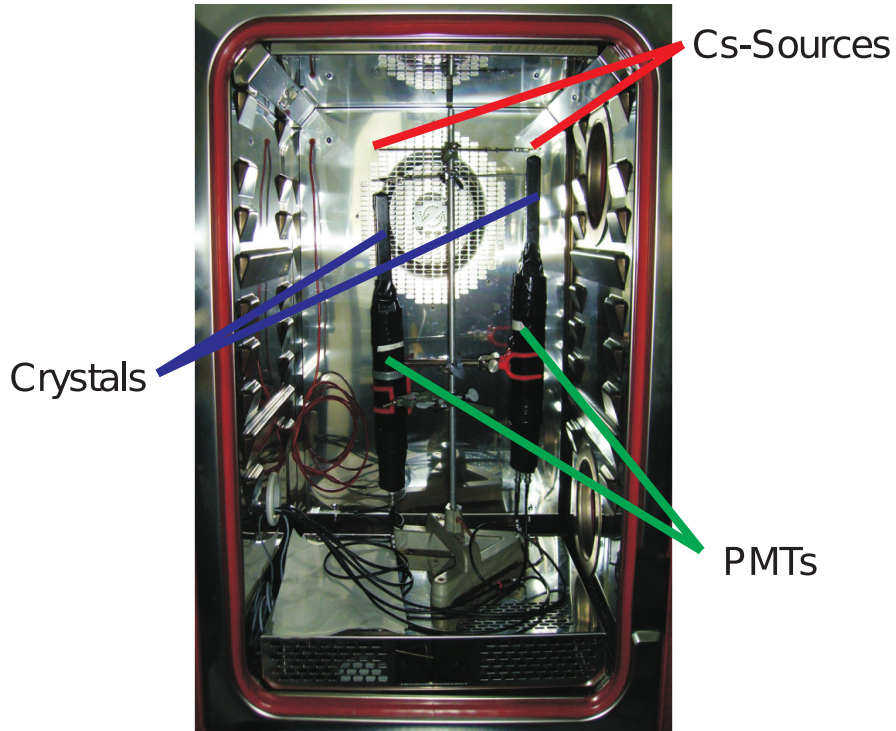
Figure 2.25: Measurement setup at JLU Gießen used for calibration of relative LY values provided by ACCOS at CERN [34].

CRYSTAL ID	PLANT NUMBER	TYPE	LOT	REL. LIGHT YIELD	LIGHT YIELD IN $\frac{\text{phe}}{\text{MeV}}$	COMMENT
451	878	1L	B-1	0.407	26.34	–
458	912	1L	B-1	0.356	23.02	–
647	1149	1L	B-1	0.356	23.05	–
6656	1691	EC-R	B-8	0.259	18.39	–
20635	678	6L	B-0	0.315	–	Preproduction
20646	689	6L	B-0	0.339	–	Preproduction

Table 2.3: Lead tungstate crystals of $\overline{\text{P}}$ANDA geometry used in the NUF Measurements
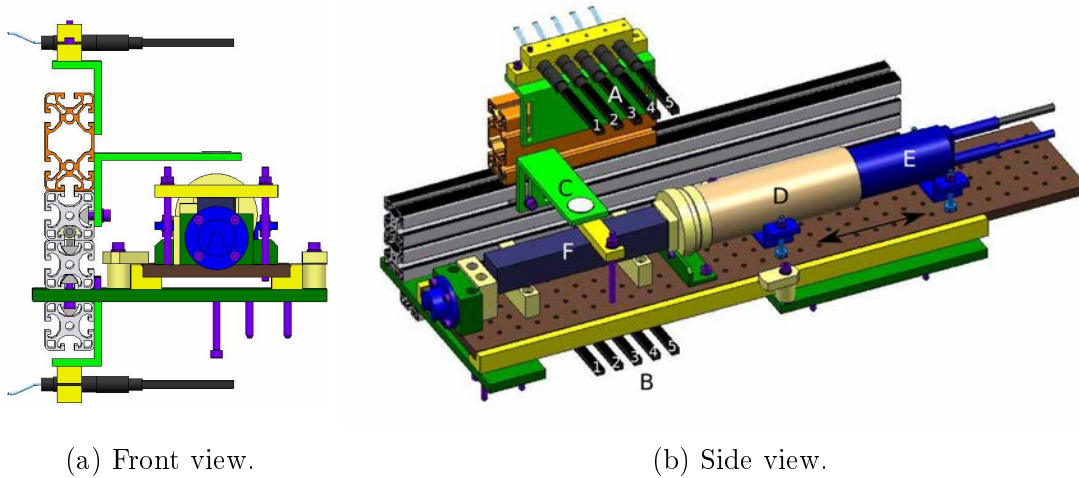
(a) Front view.   (b) Side view.

Figure 2.26: CAD of the precision setup for NUF measurements. For the individual modules, refer to Tab. 2.4. In cosmic measurement configuration, module C is removed. For 511 keV photon measurements, plastic scintillator detector A-1 is replaced by a BGO detector (module G) with significantly larger efficiency.

2.3.2 Precision Setup

Description

The first setup was designed to measure NUF in $\overline{\mathrm{P}}$ANDA geometry crystals with a precisely determined location of energy deposition. As further requirements, it had to be possible to use the same setup to measure the response of cosmic muons and low energetic γ-rays. Additionally, due to the low signal expected for low energy sources at room temperature, the setup has to be contained in an insulating volume for operation at $T = -25\,°\mathrm{C}$. A CAD of the developed setup is displayed in Figs. 2.26a and 2.26b. The essential modules are listed in Tab. 2.4, where also further details are given. The wrapped crystal sample (F) is coupled to a two inch diameter Hamamatsu R2059 PMT (D) with silicone oil[4]. Because the sensitive area of the photo cathode is larger than the crystal rear face, a specially formed mask is attached which serves the purpose of avoiding exposition to stray light. At the same time, the mask helps to fix the rear face position on the photo sensor, which is beneficial for optical coupling. The position of the lead tungstate crystal is defined by three bedstops against which the front face and the rectangular sides of the crystal are pressed. Two clamps fix the PMT and the attached passive voltage divider (E) to

---

[4]Type Baysilone M300000, manufactured by Bayer-Silicone

ID	MODULE	DETAILED
A	Upper array of five plastic scintillator detectors	$0.9\,\text{cm} \times 0.5\,\text{cm} \times 5\,\text{cm}$ $(w \times h \times d)$ each
B	Lower array of five plastic scintillator detectors	$0.9\,\text{cm} \times 0.5\,\text{cm} \times 5\,\text{cm}$ $(w \times h \times d)$ each
C	Radioactive source with lead collimator	Thickness $1.0\,\text{cm}$, bore diameter $3\,\text{mm}$; only in use for $511\,\text{keV}$ photon detection
D	PMT	Hamamatsu R2059, diameter $2\,\text{inch}$
E	Voltage divider	Passive
F	Lead tungstate crystal	Individual types see Tab. 2.3
G	BGO scintillation detector	$1.0\,\text{cm} \times 1.0\,\text{cm} \times 2.5\,\text{cm}$ $(w \times h \times d)$; replaces module A-1 for $511\,\text{keV}$ photon detection

Table 2.4: Collection of modules comprising the precision setup, depicted schematically in Fig. 2.26b
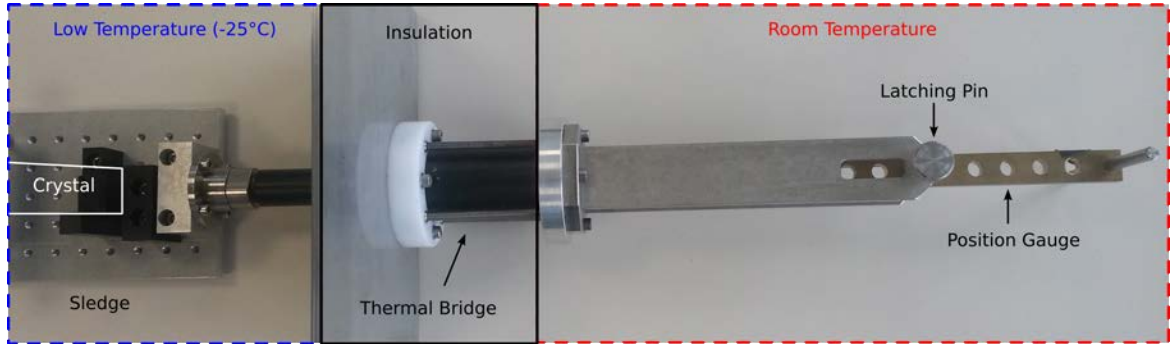
Figure 2.27: Detailed photograph of the sliding mechanism with positioning gauge.

an aluminium sledge. This sledge is rested on plastic rails and it can be slid in longitudinal direction, as indicated by the arrows in Fig. 2.26b, relatively to an array of five plastic scintillators placed at a fixed vertical distance above (A) and below (B). A coincident response of array A and B gives a clear definition of the path of a traversing charged particle. To fix the relative position of the plastic scintillators and crystal, a special positioning mechanism was designed. This sliding mechanism is shown in detail in Fig. 2.27. Although the movable sledge including the attached crystal is contained in an insulating volume cooled to $-25\,^{\circ}\text{C}$, the position has to be monitored and adjusted from the outside. To enable efficient cooling, the insulation feedthrough and shifting rod attached to the sledge in the low temperature region are manufactured out of plastics with low thermal conductivity. On the outside end of the shifting rod, a brass position gauge is attached, which can be exchanged easily if required.
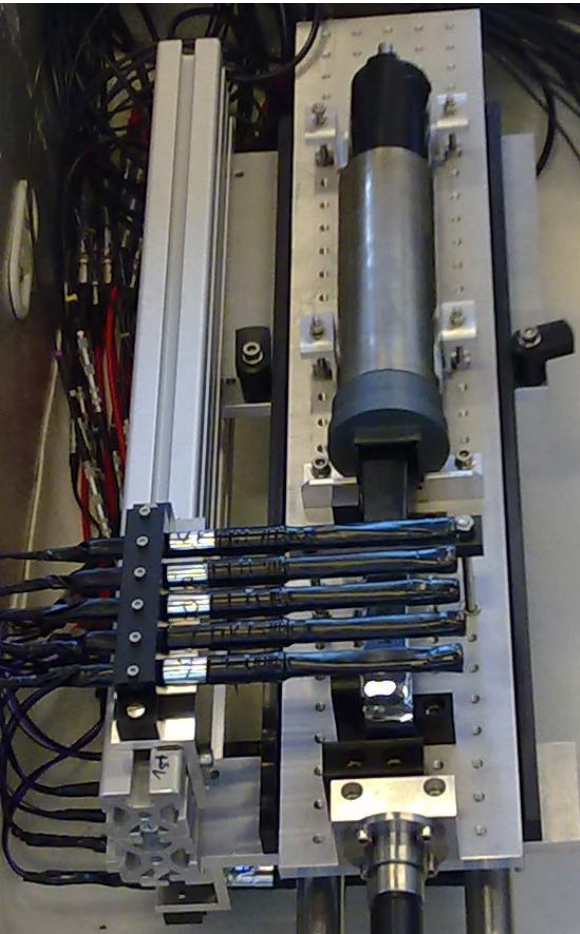
Figure 2.28: Photograph of the installed NUF measurement setup in cosmic ray configuration, contained in a large volume extension of the climate chamber. The upper array of five plastic scintillator detectors, mounted on an aluminium profile, is clearly visible. In the background, the crystal, covered with black shrinking tube and already attached to the PMT is shown. Below, the coupling of the sledge to the positioning gauge can be recognised.

Each hole of the gauge refers to a definite crystal or sledge position, respectively. In the experiments described, a gauge with 11 positions in 2.00 cm distance to each other are foreseen and realised by holes with 1.00 cm diameter. A given position can be selected by placement of a latching pin, which avoids further movement of the shifting rod. Due to the standard accuracy of 0.1 mm in the manufacturing of the metal parts of the setup, especially the brass gauge, a high positioning accuracy and reproducibility can be expected. Nevertheless, backlash in the coupling of sledge and shifting rod and material stress induced by cooling act as additional error sources. For the aluminium parts (coefficient of linear thermal expansion $\alpha_{Al} = 23.1 \cdot 10^{-6} \frac{1}{K}$, [35]), the relative length decrement at the given temperature difference of 45 K is about 0.1 %. For instance, at a sledge length of 65 cm this translates to maximum length deviation of 0.65 mm. Including the mentioned coupling backlash, an overall positioning error of 1 mm represents a reasonable estimation. A photograph of the NUF measurement precision setup installed in a large volume extension of the climate chamber[5], is shown in Fig. 2.28. Due to a special modification, the deployed climate chamber is able to climatise an additional external volume, guaranteeing a low air humidity to avoid ice formation on the setup, in especially on the PWO-II crystal, which disturbs the measurement profoundly. In all measurements performed with the described precision setup, the crystal wrapping was performed in two different ways, in the following abbreviated as Teflon[6] and VM2000 wrapping, respectively. An overview of the detailed layer sequence, as well as further information on the materials used is presented in Tab. 2.5. The Teflon wrapping also used in LY determination during QC and JLU Gießen, relies on the excellent diffusive reflection properties of a PTFE membrane commonly used for high performance filters. Light tightness is guaranteed by an additional outer layer of aluminium foil, while the outermost shrinking tube layer serves as mechanical fixation. On the other hand, the VM2000 wrapping only requires the VM2000 enhanced specular reflector film and shrinking tube for fixation and light tightness. However, the reflector foil has to be cut and moulded before assembly for each geometry. In prototypes as well as in the final EMC, the shrinking tube is dispensable due to the containment of the crystal in specially designed carbon alveoli.

Cosmic Ray Measurements

Readout In cosmic setup configuration, the key to determine the place of energy deposition inside the PWO-II crystal are the two arrays of plastic scintillators (A and B in Fig. 2.26b), consisting of five individual detectors each. These plastic scintillator detectors themselves are comprised of a plastic scintillator bar of the dimensions given in Tab. 2.4, which are coupled to a cylindrical Hamamatsu R1635 PMT (diameter

---

[5]Type: Weiss WT11 180

[6]Brand name for Polytetrafluoroethylene (PTFE) by DuPont Co.

Wrapping Acronym	Layer		Details
	#	Material	
Teflon	8	PTFE membrane	38.1 μm thickness; Donaldson Company, Inc.
	1	Aluminium foil	20 μm thickness;
	1	Shrinking tube	
VM2000	1	VM2000 enhanced specular reflector film	previously cut and moulded; 3M Company
	1	Shrinking tube	

Table 2.5: Overview of the applied crystal wrappings. Material layers are mentioned in sequence from inside to outside.
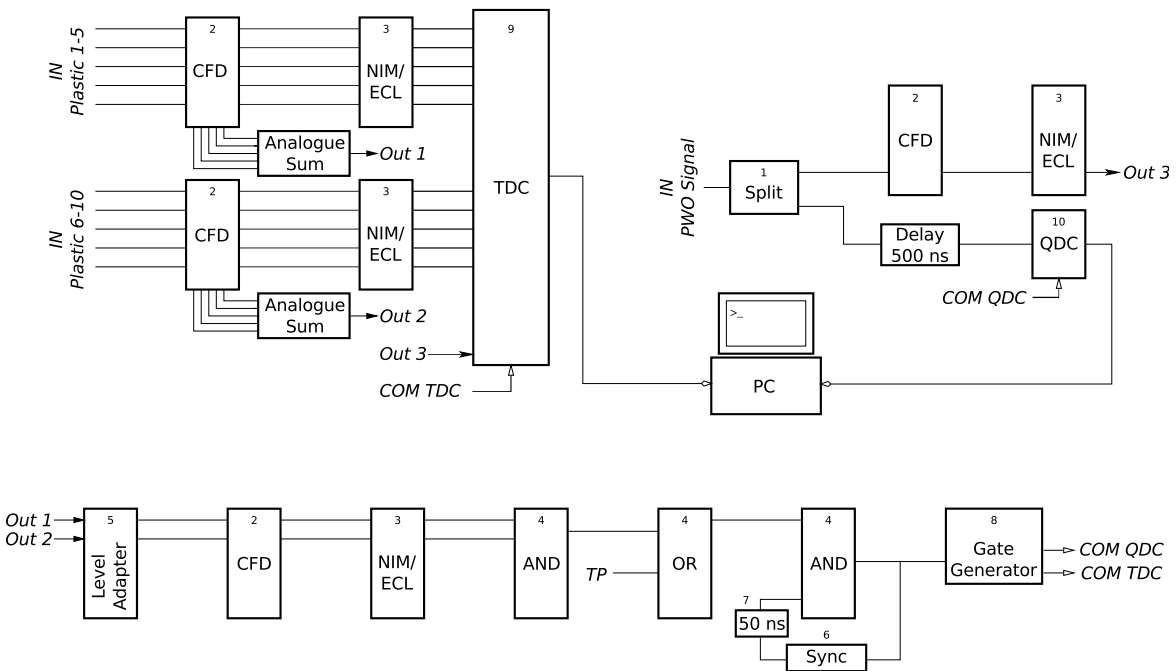
Figure 2.29: Precision setup readout scheme for cosmic measurements. The specific type of modules is listed in Tab. 2.6.

MODULE NUMBER	FUNCTION	TYPE	STANDARD
1	Split	16 Fold AS-04 Active Split	NIM
2	CFD	Ganelec FCC 8 Constant Fraction Discriminator (CFD)	CAMAC
3	ECL/NIM	16 Channel Emitter Coupled Logic (ECL) / Nuclear Instrumentation Module (NIM) Converter	NIM
4	OR or AND	LeCroy Model 622 Quad Coincidence	NIM
5	Level Adapter	LeCroy Model 428F Linear Fan-In / Fan-Out	NIM
6	Sync	Struck SIS 3320 Synchronisation Module	VME
7	Delay	DV 8000 Octal Variable Delay	NIM
8	Gate Generator	LeCroy Model 222 Dual Gate Generator	NIM
9	TDC	CAEN V775N 16 Channel Time to Digital Converter (TDC)	VME
10	QDC	CAEN V792N 16 Channel Charge integrating ADC (QDC)	VME

Table 2.6: Collection of electronics modules utilised for the NUF measurement setups displayed in Figs. 2.29, 2.31 and 2.38.

10 mm) by a special light guide. Bar and light guide are wrapped with Teflon, as indicated in Tab. 2.5. A coincident response of at least one plastic scintillator in the upper and one detector in the lower array defines the track of a traversing charged particle originating from cosmic radiation. Most likely these are minimum ionising muons. The readout of this setup was designed accordingly. A scheme of the deployed readout electronics is provided in Fig. 2.29. More specific information on the individual modules can be found in Tab. 2.6 under the corresponding module number. The signals originating from the upper and lower plastic scintillator array (*IN Plastic 1-5* or *IN Plastic 6-10*) are treated similarly in two separate branches. First, signals face a CFD, whose thresholds were individually adapted for each channel to be slightly above the noise level. The used CFD generates two kinds of output signals: An analogue sum of all five input channels, whose voltage level is proportional to the number of channels above threshold (*Out1* or *Out2*) and five logical differential ECL signals carrying the information if the individual channel is above threshold. The arrival times relatively to the trigger signal of the latter are, after conversion to a non-differential NIM signal, digitised by an TDC. To generate the trigger, the analogue sums of upper and lower branch are used. A level adapter serves the purpose of eliminating signal contortions, before another CFD, with a threshold corresponding to a number of at least one responding module, discriminates the analogue sum signal. Finally, the logical AND of both discriminated analogue sums defines an event trigger. Additionally, it is possible to generate a trigger with a test pulser, which is coupled in by a logical OR. If there is a TRUE event trigger, a gate generator provides a time gate of $\sim 1\,\mu$s length (*COM QDC*), during which the QDC accepts signals for digitisation. Moreover, a delayed NIM signal (*COM TDC*) is sent to the TDC, serving as a common stop for time digitisation, started individually by each responding detector. A synchronisation loop inhibits the acceptance of another trigger before the current event is fully digitised and stored. The PWO crystal's signal is split into a time and an energy branch. The energy branch is, after a delay of 500 ns, digitised by the QDC while the time branch is discriminated by a CFD and re-converted to a NIM signal before digitisation by the TDC. Accordingly, for each event, timing information is available for all plastic scintillator detectors and the PWO-II-detector, while pulse charge information is available solely for the PWO-II crystal. Digitised information for all events of a measurement run is routed to and stored on a Linux-PC.

Procedure   All crystals with $\overline{\text{P}}$ANDA geometry used in NUF experiment are listed in Tab. 2.3, together with QC information on the LY at $T = 18\,°$C. Cosmic ray measurements were performed with one crystal of geometry type 1L and one crystal of type EC-R. The setup was cooled down to $T = -25\,°$C to enhance the intrinsic LY, due to reduced temperature quenching, enabling a better distinction of response differences at separate positions. Five plastic scintillators with 2 cm spacing correspond to five measurement positions covering approximately the half length of a crystal. Therefore,

two measurement runs per crystal for distances z from the photo sensor, ranging from $2\,cm - 10\,cm$ and $12\,cm - 18\,cm$, respectively, were performed. Caused by the small sensitive area of one plastic scintillator bar of $4.5\,cm^2$ and the required coincidence of upper and lower array, the count rate was of the order of $10\,mHz$. Applied later offline in the readout software was the even sharper condition that only events are accepted, if only the two plastic scintillators in the upper and lower array, which were closest to each other (e.g. A-2 and B-2 in Fig. 2.26b), responded. This reduced the number of events by another factor $4 - 5$. Hence, one measurement run had a duration of 14 days, resulting in a measurement time of 1 month per crystal.

Sodium Source Measurements

In consequence of the long measurement time for the position dependent response to cosmic rays, which is not applicable for an extended series of measurements, the setup was modified to measure γ-rays instead. Plastic scintillator A-1 was replaced by a small BGO crystal (exact dimensions see entry G in Tab. 2.4), which has a significantly larger detection efficiency for photons. Furthermore, the distance to the crystal was increased to enable the placement of a ^{22}Na-source in between. Exploiting the coincident detection of back-to-back emitted $511\,keV$ photons after β^+ annihilation, in BGO and PWO-II, the photons' point of impact could be deduced. Furthermore, the crystal was shielded from direct irradiation by a lead collimator of $1\,cm$ thickness (corresponding to $83\,\%$ absorption at $511\,keV$ and $48\,\%$ at $1274\,keV$, respectively), leaving only a bore of $3\,mm$ diameter. As a consequence, a reduced amount of chance coincidences can be expected. From the distances of the source to the particular crystal, together with the size of the BGO crystal, the maximum area of incidence on the PWO-II crystal can be determined geometrically, as outlined in Fig. 2.30a. According to the intercept theorem, it is a scaled down projection of the BGO crystal shape on the PWO-II crystal surface. The maximum angle of incidence for the photons will vary from $\frac{\alpha}{2} = 4.76\,°$ to $\frac{\beta}{2} = 11.76\,°$, which is fairly small. Hence, the mean depth of energy deposition in the scintillator material varies scarcely. Nevertheless, due to the collimator, the real area of incidence is reduced in transversal direction. According to the schematic drawing in Fig. 2.30b, up to a minimum width of $1.35\,cm$ full source intensity can be expected, while up to the geometrically determined maximum width of $1.875\,cm$, intensity is reduced due to absorption in the collimator.

Readout   In this configuration, several changes were applied to the readout chain. As displayed in Fig. 2.31, the plastic scintillator branches are now replaced by a single branch, discriminating and digitising the time of the BGO signal relatively to the trigger. In this configuration, it is defined solely by the discriminated response of the PWO-II detector, i.e. it ran in self-triggered mode. Like in the cosmic configuration,

(a) Several perspectives ignoring collimator.   (b) Front view with collimator.
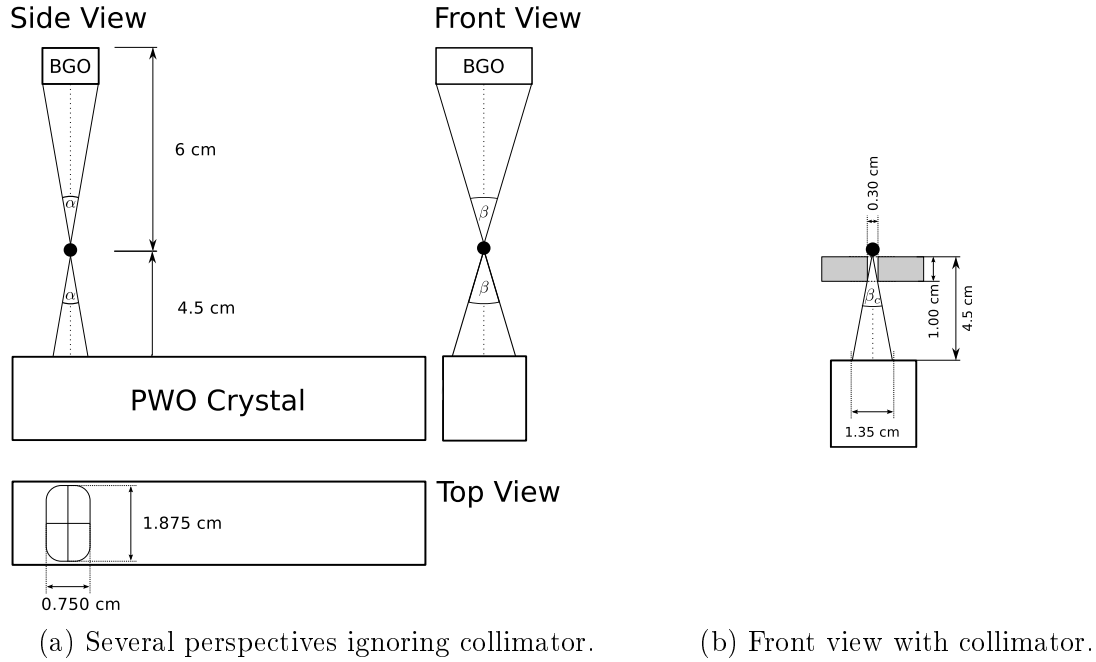
Figure 2.30: Schematic drawing illustrating the beam spot size determination.

the TDC was operated in common stop mode, the QDC in common start mode. For each event, the time of both crystals and the energy response of the PWO-II is recorded.

Procedure   Because the BGO crystal only covers one z position, a number of 10 runs has to be performed to obtain the same amount of information as in cosmic configuration. Nevertheless, due to the higher event rate, a measurement time of two days per crystal, including the cooling cycle, is sufficient. Fig. 2.32 shows exemplarily the raw spectrum of energy deposition inside the PWO-II crystal. Both γ peaks expected for a ^{22}Na-source, corresponding to 511 keV annihilation photons and the 1274 keV electric quadrupole (E2) transition, are clearly visible. In addition, Fig. 2.32 shows the spectrum after requiring a coincident response of the BGO crystal within a time window of 8.5 ns width. Background and 1274 keV peak are suppressed effectively. However, because of the self-triggered readout, the yield of favourable events is low. To extract the peak position, a Gaussian distribution was fitted to the line shape. The position of the single electron peak P_{SEP}, necessary for LY determination according to Eq. 2.1, was obtained in a separate run at 18 °C, while the pedestal was determined from a subgroup of events triggered by the test pulser.
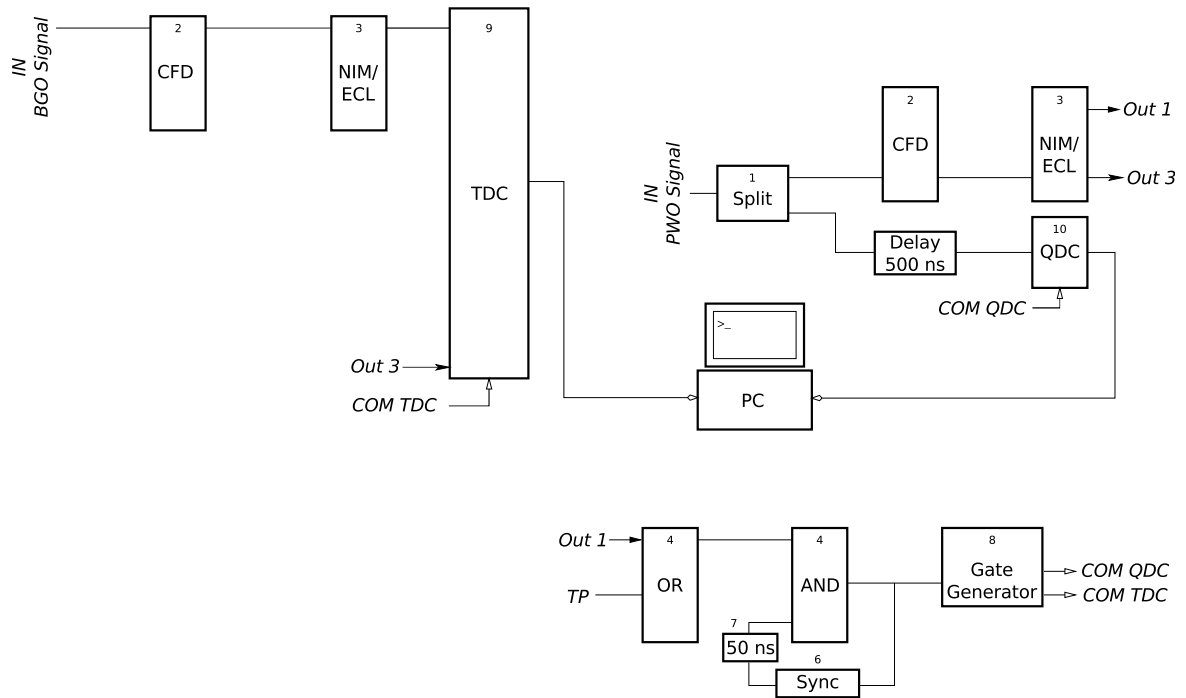
Figure 2.31: Precision setup readout scheme for 511 keV photon measurements. For the specific type of modules, compare to Tab. 2.6.

Results

Fig. 2.33 shows the position dependent response of a type 1 and type EC-R crystal to minimum ionising cosmic muons. The ordinate is scaled in units of the pedestal corrected Analogue to Digital Converter (ADC) channel number, divided by the most probable energy deposited inside the scintillator material. This was calculated from the expected energy loss in PWO, given in Tab. 1.3, and the mean pathlength of the particles through the crystal. Both curves show a similar shape with only a slight enhancement in the response at higher z for type 1 geometry. In addition, a shift of about $10 \frac{\text{ADC Channels}}{\text{MeV}}$ is observed over the whole range of measured distances z from the photo sensor. Nevertheless, in case of the tapered type 1 geometry, the real path length of the particles is dependent on the crystal height, given in Eq. 2.3. If one corrects for the pathlength at each corresponding z separately, a clear non-uniform behaviour of the response becomes visible. It also has to be noted that after correction, the response for both types at $z = 2$ cm is equal within the error bars, which suggests the same intrinsic quality of the scintillator material. Apparently, the uncorrected response is uniform because the light collection NUF leads to an overestimation of the deposited energy at large z and an underestimation at low z, respectively. This can have a significant impact on the calibration of larger detectors like EMC prototypes
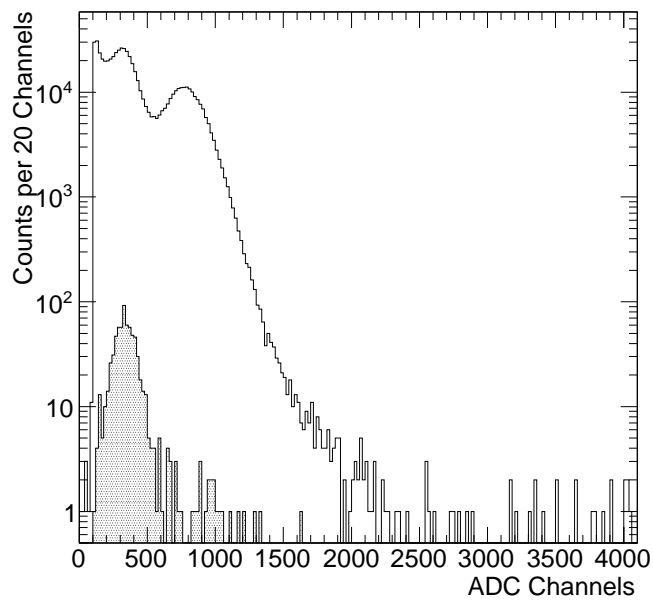
Figure 2.32: Energy deposition in the lead tungstate crystal without (unshaded) and
with (shaded) a required coincident response of the BGO crystal within
a time window of 8.5 ns. The selected spectrum was recorded for EC-R
geometry at $z = 10$ cm distance to the PMT entrance window.
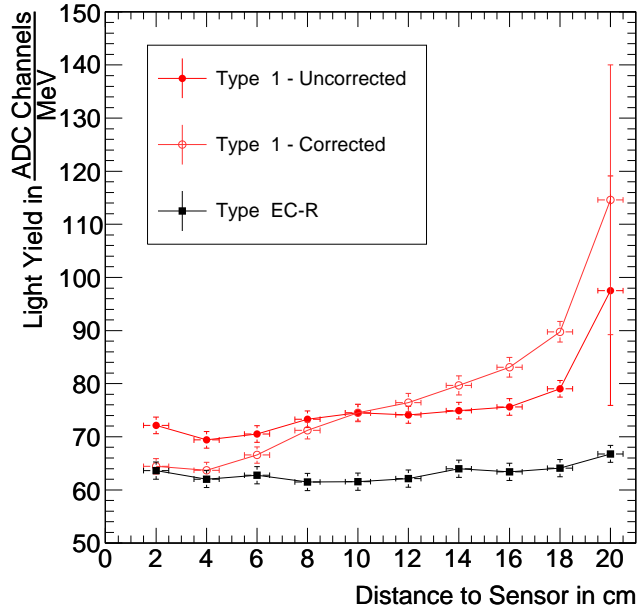
Figure 2.33: Position dependent response to minimum ionising cosmic muons at $-25\,°C$ for PWO-II crystals in type 1 and EC-R geometry. For the tapered shape, additionally the LY corrected for the most probable MIP energy deposition (see Tab. 1.3) for the corresponding pathlength $e(z)$ is shown.

with cosmic muons, which will be discussed later.

The measured LY for energy deposition by $511\,keV$ photons in dependence on z is shown in Fig. 2.34a for types 1, 6 and EC-R. The response of the latter is uniform, while for the other types a non uniform shape is observed, most pronounced for geometry type 1.

Also differences in the absolute values at $z = 2\,cm$ of up to $6\,\frac{phe}{MeV}$ are visible. This, together with the LY values, which are approximately $10\,\%$ to $30\,\%$ lower than expected for cooled operation, can be related to an imperfect coupling of crystal and PMT due to mechanical stresses and increased viscosity of the silicon oil. During QC at JLU Gießen this is usually avoided by a vertical setup, relying on the crystal weight to maintain optical coupling during the cooling cycle. Due to spatial constraints this was not applicable in case of the precision setup. Accounting for this issue, the high rate setup described in Sec. 2.3.3, again features a vertical design. A comparison regardless of the absolute values can be found in Fig. 2.34b. Here the response was normalised to the point closest to the PMT. Since a second order polynomial function describes the NUF curves obtained by simulation adequately (see Sec. 2.2.3), the same fit was
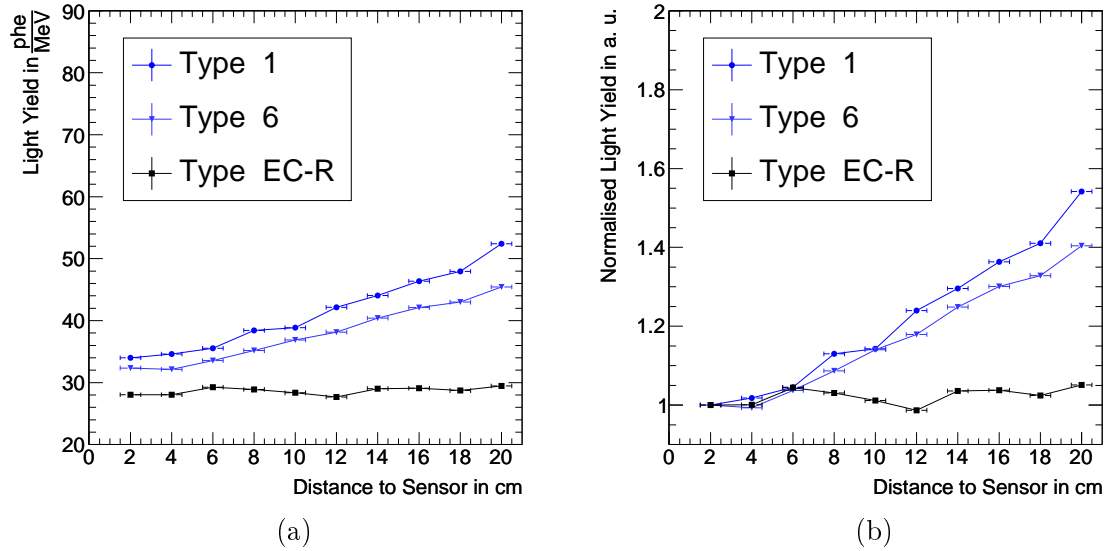
Figure 2.34: Measured LY response at $-25\,°C$ to $511\,keV$ photons in dependence on the distance to the PMT in absolute values (a) and normalised to the position closest to PMT (b).

TYPE	a IN $\frac{phe}{MeV}$		b IN $\frac{phe}{MeVcm}$		c IN $\frac{phe}{MeVcm^2}$		Π IN $\frac{phe}{MeVcm^2}$	
1	32.69	$\pm$ 0.10	0.417	$\pm$ 0.022	0.0272	$\pm$ 0.0010	0.0462	$\pm$ 0.0015
6	30.76	$\pm$ 0.12	0.437	$\pm$ 0.026	0.0153	$\pm$ 0.0012	0.0352	$\pm$ 0.0018
EC-R	28.28	$\pm$ 0.08	-0.005	$\pm$ 0.016	0.0027	$\pm$ 0.0007	0.0025	$\pm$ 0.0011

Table 2.7: Parameters obtained from a second order polynomial fit to the LY position dependence at $-25\,°C$, depicted in Fig. 2.35a.

also applied to the measured LY position dependences, as depicted in Fig. 2.35a. The extracted parameters are listed in Tab. 2.7. Plotting the NUF parameter Π versus the constant LY contribution, represented by parameter a, which is displayed in Fig. 2.35b, one recognises that type 1 has the largest NUF, while also the constant contribution is $2\,\frac{phe}{MeV}$ or $4\,\frac{phe}{MeV}$ larger than for type 6 or EC-R geometry, respectively. Fig. 2.36 features the same kind of normalisation as Fig. 2.34b, but includes in addition the normalised response to comsic muons. Within the uncertainties, the corrected response to cosmic muons for the individual geometry shows a similar relative NUF as the response to photons, although mechanism and lateral spatial distribution of the energy deposition inside the crystal differs distinctly. As a conclusion, since the long-term cosmic measurements contain no significant information surplus regarding the NUF, it is sufficient to perform the much faster photon measurement.

(a)

(b)
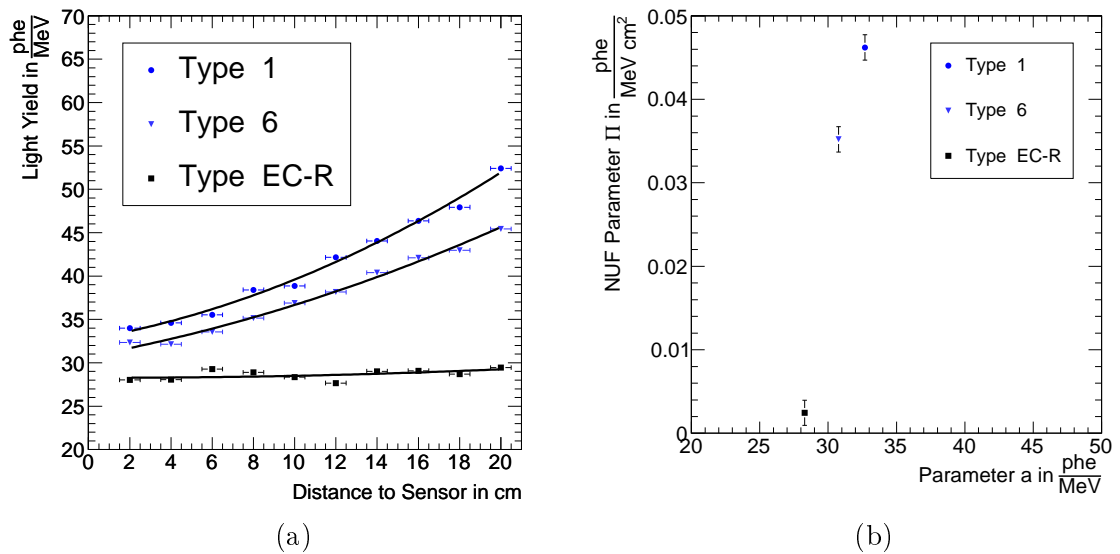
Figure 2.35: Measured LY response at $-25\,°\mathrm{C}$ to $511\,\mathrm{keV}$ photons in dependence on the distance to the PMT fitted by a second order polynomial (a). NUF parameter Π in dependence of the constant LY contribution represented by parameter a (b).

2.3.3 High Rate Setup

Description

To investigate the NUF in a series of more time efficient experiments, a new setup dedicated to $511\,\mathrm{keV}$ photon measurements was designed. To avoid issues due to insufficient coupling, as indicated before, a vertical setup was chosen. Moreover, the setup had to be sufficiently compact to be operated in the climate chamber itself, enabling a more efficient temperature and humidity control, resulting in shorter cooling cycles. To reduce the time necessary for measuring one specific crystal even more, the number of z-positions was reduced to five. These were measured in parallel due to the deployment of one ^{22}Na-source with varying activity at each position. A CAD of this so called high rate setup is shown in Fig. 2.37 in isometric and detailed top view, respectively. Main mechanical component is a vertically oriented aluminium profile with longitudinal grooves for fixation of the five aluminium source holders. Each of the five similar L-shaped source holders has a slot designed to hold a rectangular sodium source with rectangular shaped sealing, covered by a geometrically matching lead collimator on the side facing the PWO-II crystal during measurement. Since the source holders are fixed to the aluminium profile by toothed washer secured screws, the z-position of the holders, and thus the sources, can be chosen freely. The only
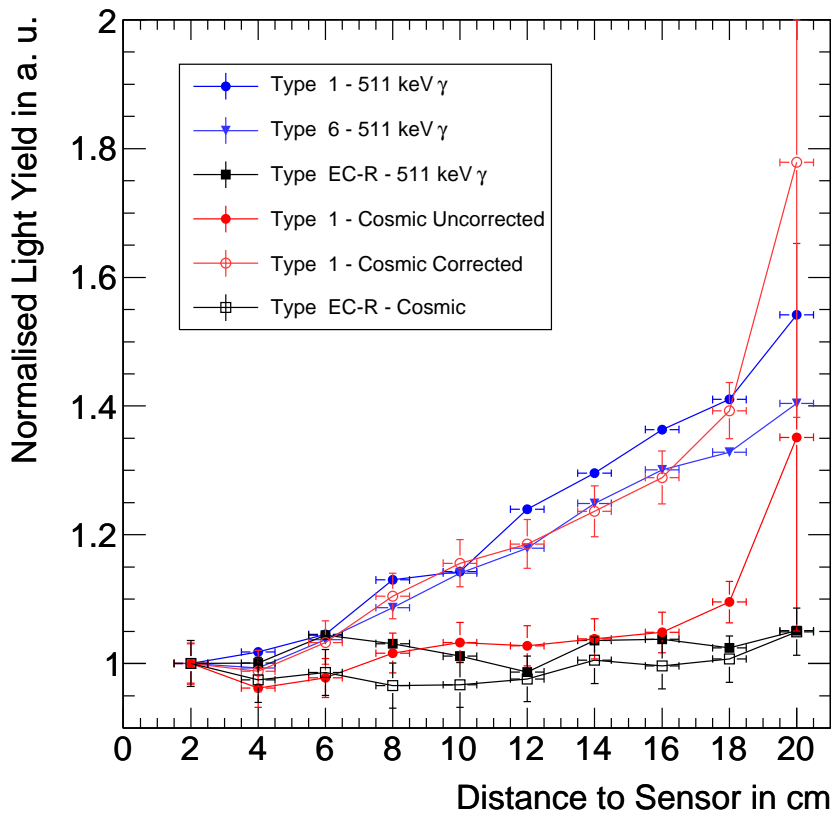
Figure 2.36: Comparison of the normalised response to cosmic muons and 511 keV photons, depending on the distance to the photo sensor.

(a) Isometric view.   (b) Detailed top view.
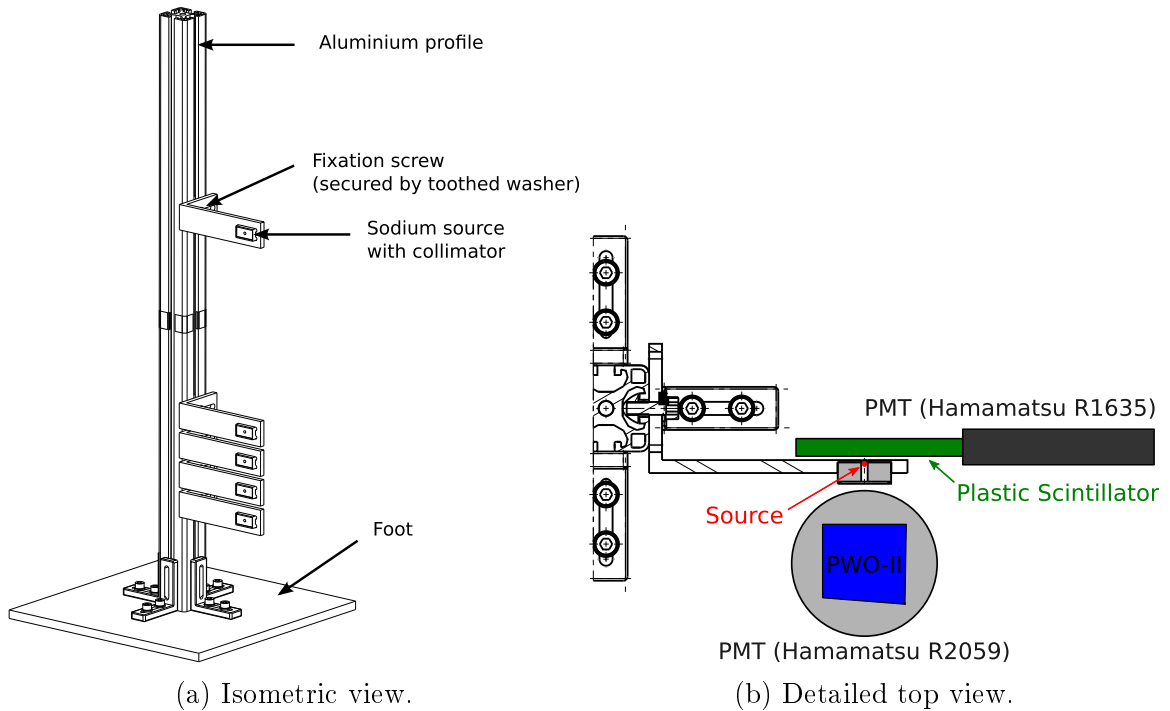
Figure 2.37: CAD of the high rate setup for NUF measurements.

constraint is a minimum spacing of $2\,cm$ dictated by the holder width. The lead collimators are of $1\,cm$ thickness and possess a bore of $3\,mm$ diameter. Crystals were placed in a distance of approximately $5\,cm$ to the sources, with the untapered side facing in their direction. On the opposite side of each γ-source, divided by the aluminium of the source holder with $2\,mm$ thickness and bore hole of $3\,mm$ diameter, matching the one in the collimator, a plastic scintillator, similar to the type used in the precision setup, was mounted. Again, the plastic scintillator served the purpose of coincident detection of backward emitted photons. However, because of the closeness to the γ-source, no geometrical limitation of the area of incidence on the PWO-II crystal due to the coincidence requirement can be expected. Thus, this area is solely determined by the lead collimator bore diameter, which is similar to the collimator used in the precision setup. Also the distance of source and crystal is approximately the same, which entails that the area of incidence can be determined analogically to Fig. 2.30b. This results in a circular area of incidence with approximately $1.5\,cm$ diameter. Based on this geometrical consideration, combined with the positioning error during the source mounting procedure, which amounts at maximum to $0.1\,cm$, an overall z position error of $0.8\,cm$ is a reasonable estimation.
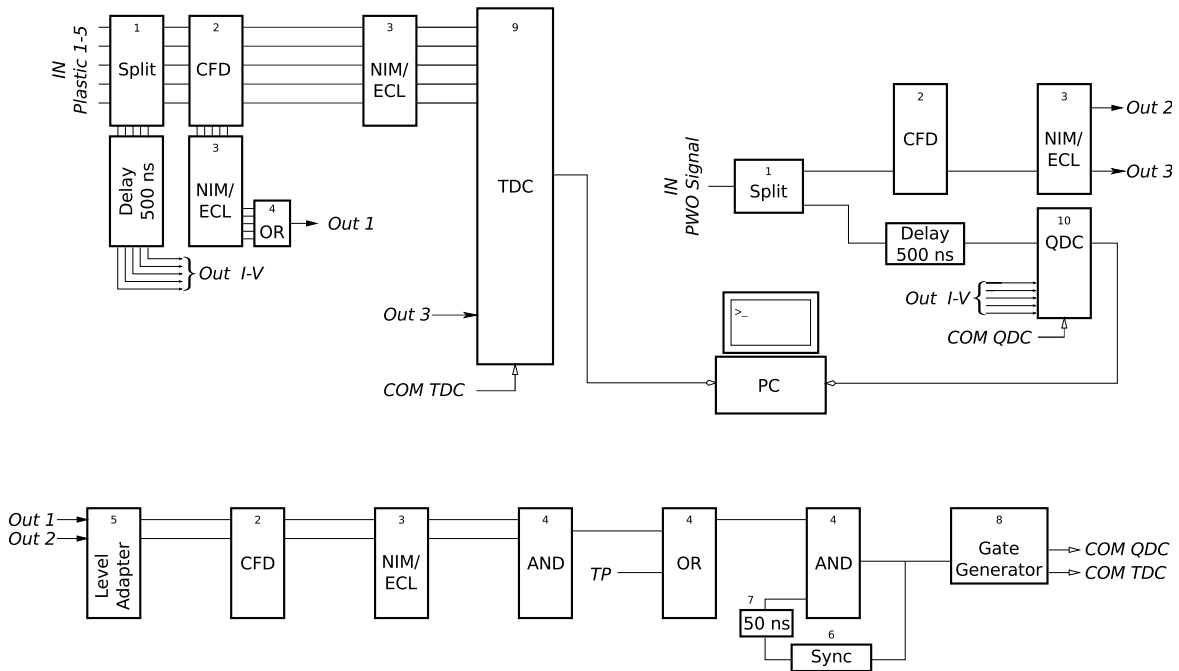
Figure 2.38: High rate setup readout scheme. For the specific type of modules, compare to Tab. 2.6.

Readout   For this setup, the trigger is built by a coincidence of the logical OR of the discriminated signals of all five plastic scintillators and the discriminated signal of the lead tungstate crystal. As in case of the precision setup, the opportunity to trigger via testpulser is available as well. After a trigger is successfully built, the response time of all five plastic scintillators is digitised by the TDC operated in common stop mode, while the QDC operated in common start mode integrates their signals within a time gate of 150 ns. A synchronisation module inhibits incoming triggers until the event is processed. Due to the usage of multiple ^{22}Na-sources, there is a high number of chance coincidences, which cannot be completely suppressed by the coincidence trigger. These can be divided into three classes: First the case of coincident detection of a 511 keV and a 1274 keV photon, which is in principle also present in case of the precision setup. As shown in Fig. 2.32, this type of chance coincidences can be efficiently suppressed. Also the second type, photons penetrating the collimator and firing the PWO-II crystal as well as a neighbouring plastic scintillator, can be regarded as a minor contribution to the background, because the solid angle region required for this scheme is small. Thirdly, if a photon is detected in the PWO-II crystal, while the according plastic scintillator is not responding due to inefficiency, the trigger condition can be fulfilled by the response of a plastic scintillator belonging to another source. This kind of chance coincidences, which occur with different probability depending on the source activity, were reduced offline by software requirements.

Procedure   As a measure to reduce the third kind of the chance coincidences mentioned above, a narrow cut was set on the response time of the individual plastic scintillator. Furthermore, a multiplicity of exactly one responding plastic scintillator per event was required. Despite this combination of software requirements, an effective suppression was not achieved, resulting in a still recognisable 1274 keV photo peak and a slight deformation of the 511 keV peak in the ^{22}Na pulse height spectrum for a single source. For analysis purposes, the former can be neglected, because it is clearly separated from the region of interest, namely the annihilation photon peak. On the contrary, its slight deformation by background from other sources has to be taken into account. This was done by assuming a systematic uncertainty of the LY derived from a Gaussian fit of the photo peak amounting to $1\,\frac{\text{phe}}{\text{MeV}}$, although the value due to error propagation of the peak position fit error is indeed much smaller. In order to have the same background for comparative measurements, it was taken care that the amount of collected events was roughly equal among individual measurements.

Uniformisation method investigations with $\overline{\text{P}}$ANDA geometry crystals

Main aim of the measurements performed with the high rate setup was the investigation of a method to achieve a uniformisation of the LY position response. In principle, there are three different approaches: Modifications on the crystal wrapping, deposits on the crystal surface or crystal surface modifications. Because the latter is not desirable because of its irreversible nature, the other two approaches were investigated first.

Different homogeneous wrappings   For an experimental comparison of the influence of the wrapping on the light collection, the type 1 crystal with ID 647 was measured successively with three different wrapping types: The specular reflecting VM2000, the diffuse reflecting Teflon and with no wrapping at all. Details on the wrapping can be found in Tab. 2.5. Operating temperature for each measurement was $-25\,°$C. Fig. 2.39a shows the measured absolute light yield depending on the position of the energy deposition with respect to the PMT, while Fig. 2.39b shows the values normalised to the position closest to the PMT.

Results   As expected, in the measurement without any wrapping, the lowest absolute LY values are obtained, while significantly more light is collected by applying a Teflon wrapping to the crystal. With VM2000, the absolute LY can be enhanced even further. Nevertheless, the curve shape and therefore the NUF, varies only slightly between the three measurements, which can be seen even more clearly in Fig. 2.39b. To summarise the outcome of this measurement, one can state that only the absolute amount of collected light in crystal 647 is influenced by the wrapping, whereas the NUF does

(a) (b)
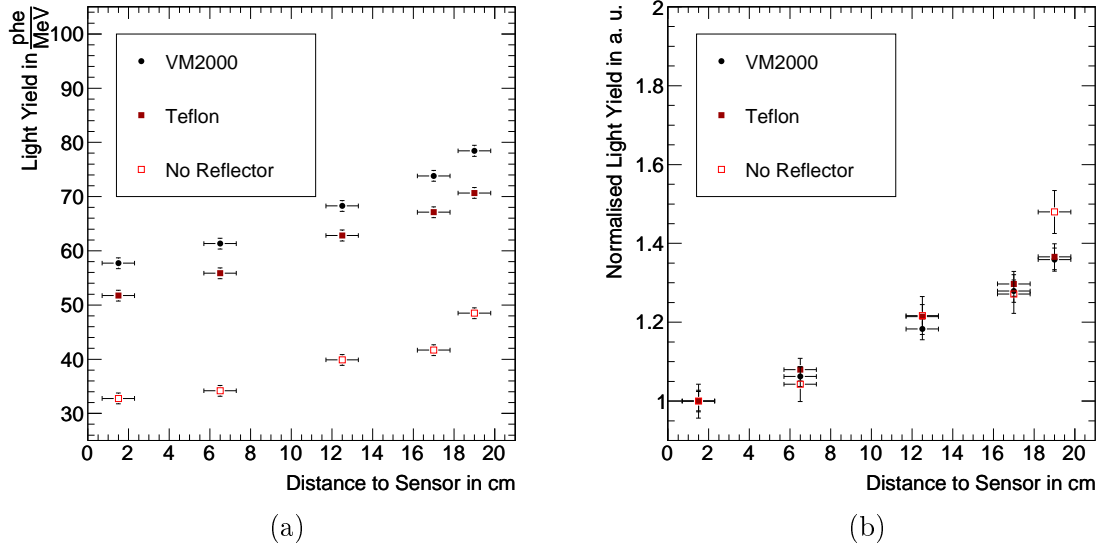
Figure 2.39: Light yield position dependence of crystal 647 (type 1L) for different wrappings in absolute values (a) and normalised to the position closest to the PMT (b).

not change. Additionally, it has to be stressed, that roughly half of the generated scintillation light is propagated to the photo sensor by internal reflection, requiring no wrapping at all.

Wrapping modifications Since a homogeneous wrapping did not show an influence on the NUF, in another approach the crystal wrapping was partially modified as depicted schematically in Fig. 2.40. Because the NUF is most uniform at large distances to the photo sensor, the objective is to reduce the amount of specular reflected light in the first half of the crystal. To achieve this, the following set of wrapping modifications was applied. As basic wrapping VM2000 was used (I). Then, on one side over a half crystal length beginning at the front, the wrapping was partially removed and replaced by VM2000 with a triangle cutout where no wrapping was applied (II). Representing the negative of this configuration, a black tape triangle was attached to the crystal surface (III). As fourth variation, the cutout was filled with Tyvek[7] paper of type L-3057M (IV).

Results The results of the NUF measurements are plotted in Fig. 2.41. Apparently the applied modifications to make the wrapping less homogeneous, also have only a

---

[7]Brand name of flashspun high-density polyethylene fibers, registered trademark of DuPont.
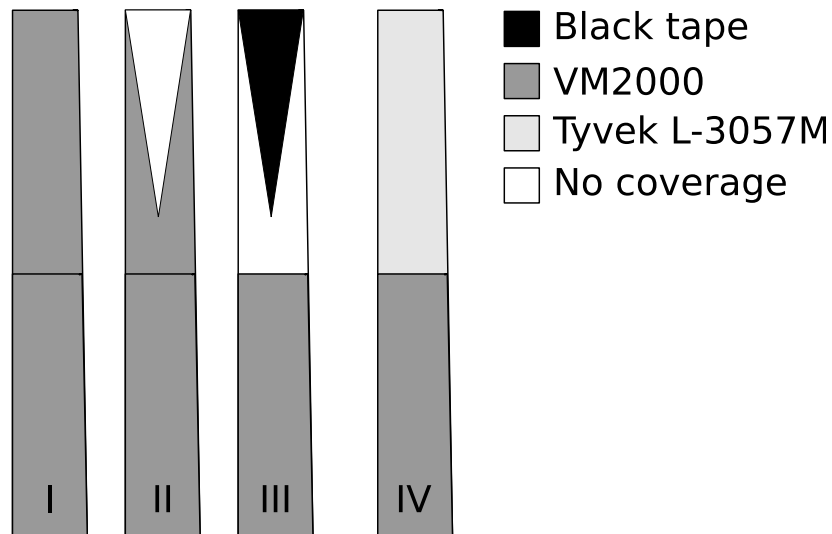
Figure 2.40: Schematical depiction of the wrapping modifications applied to crystal 458.

minor impact on the curve shape but lead to a shift the absolute LY to lower values. Nevertheless, for both measurements of crystal 647 as well as 458, one has to consider that the steps between the individual measurements, which include manual wrapping, renewal of the optical coupling, as well as the repeated cooling cycles, influence the reproducibility of the measurement.

Uniformisation method investigations with non-$\overline{P}$ANDA geometry crystals

Because surface modifications of crystals foreseen for use in the $\overline{P}$ANDA EMC are not desirable, the tests described in the following were performed with crystals used previously in prototype tests for the proposed Photon Ball at the Apparatus for Studies of Nucleon and Kaon Ejectiles (ANKE)/COoler SYnchrotron (COSY) located at Forschungszentrum Jülich (FZ Jülich) [36]. As they were produced by the same manufacturer as the PWO-II crystals for $\overline{P}$ANDA, the basic optical properties should be equal. Nevertheless, the geometry is slightly different. The Photon Ball crystals are a truncated pyramid with rear face dimensions of $31.0 \, \text{mm} \times 29.7 \, \text{mm}$ and front face dimensions of $20.0 \, \text{mm} \times 19.5 \, \text{mm}$ and a length of $120 \, \text{mm}$. Although front and rear face are parallel, in contrast to the $\overline{P}$ANDA crystals, the crystal is tapered on all four sides symmetrically, instead on two. The according overall tapering angle μ_{PB}, taking into account the angles of two opposite side faces, amounts to $4.76°$. This is roughly twice as much as for the most tapered $\overline{P}$ANDA geometry type. Between the two surface treatment methods available in the mechanics workshop, emery polishing and sandblasting, the former was chosen, since the latter cannot be sufficiently con-
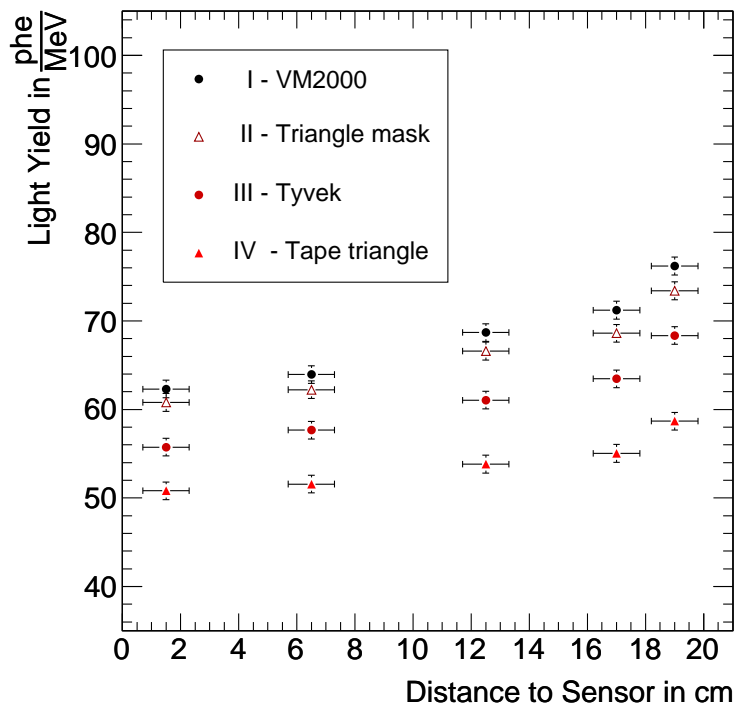
Figure 2.41: Light yield position dependence of crystal 458 (type 1L) for different wrapping modifications, as depicted in Fig 2.40.

Figure 2.42: Three small crystals with a fully or partly emerised surface.

trolled. One reason is the brittleness of lead tungstate, which leads to an uncontrolled splintering of shards with different sizes, especially on the crystal edges. Due to the fact that emery polishing was done manually, it is much more sensitive and ensures that no damage to the crystal occurs. Also the treatment area can be much more controlled. In a first sequence of measurements, three crystals were chosen, where one side face was emerised fully or partly. A photograph of the treatment result is shown in Fig. 2.42. For one crystal, the complete side face was emerised, while for the other two, the front third or rear third was emerised, respectively. To obtain an evaluation of the roughness achieved during the emery polishing process, the surface of a special small size sample of approximately $1\,cm^3$ volume, which received the same surface treatment, was measured in an Atomic Force Microscope (AFM). Due to the space restrictions and the required low inertia of the sample in this type of measurement, it was not possible to measure the full size crystals. The height profile for three different surface area sizes is shown in Figs. 2.43a, 2.43b and 2.43c. A statistical evaluation of the height profiles with the analysis software Gwyddion[8] yields the values given in Tab. 2.8. R_a and R_q, representing arithmetic average and RMS of the surface roughness after surface treatment with emery paper for the different areas, vary from approximately $0.05\,\mu m$ to $0.50\,\mu m$. Nevertheless, it is recognizable that partially large height gradients are present in the profile for the largest area (2.43c). For the smaller

---

[8]http://gwyddion.net/

(a) (b) (c)
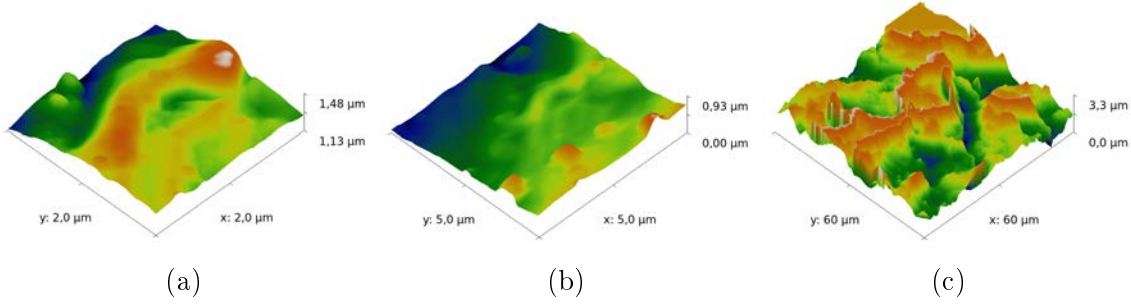
Figure 2.43: Height profiles of a small lead tungstate sample after surface treatment with emery paper. The area dimensions amount to $2\,\mu\text{m} \times 2\,\mu\text{m}$ (a), $5\,\mu\text{m} \times 5\,\mu\text{m}$ (b) and $60\,\mu\text{m} \times 60\,\mu\text{m}$ (c).

Quantity	(a)		(b)		(c)	
	Value	Unit	Value	Unit	Value	Unit
Projected area	4.000	μm^2	24.741	μm^2	3590.41	μm^2
Average height	187.5	nm	373.3	nm	1.829	μm
Minimum	0.0	nm	0.0	nm	0.0	μm
Maximum	351.3	nm	926.1	nm	3.274	μm
Median	197.2	nm	407.8	nm	1.846	μm
R_a	52.4	nm	133.4	nm	0.533	μm
R_q (RMS)	67.1	nm	160.9	nm	0.659	μm

Table 2.8: Statistical quantities derived from the height profiles obtained by AFM measurements (see Fig. 2.43).

(a)   (b)
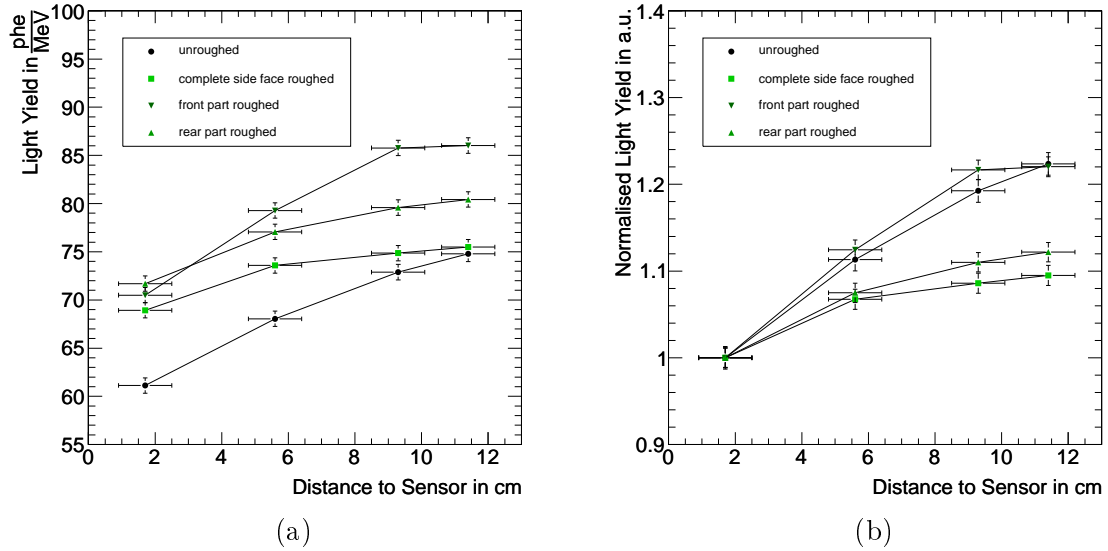
Figure 2.44: Light yield position dependence at $-25\,°C$ of four small crystals with different roughed side face areas in absolute values (a) and normalised to the position closest to the PMT (b).

areas measured, depending on the selected region, these sharp height peaks are only recognised partly and therefore the amplitude of the fluctuations can be underestimated. Hence, only the measured R_a values extracted from the height profiles of the two larger areas represent the situation reasonably. The obtained surface roughness achieved by emery polishing is between $0.1\,\mu m$ and $0.6\,\mu m$. With respect to the facts, that with an AFM measurement only a relatively small selected area is measured and that one can recognise visually small grooves in the direction of the polishing, the roughness value throughout the surface can be subject to variations. As a comparison, the maximum R_a for polished surfaces allowed in the specification is $R_a \leq 0.02\,\mu m$. For the measurements of these only $12\,cm$ long crystals in the high rate setup, one ^{22}Na-source had to be skipped, because the spatial restrictions, especially the source holder width allowed only the placement of four sources at the selected z positions $1.7\,cm$, $5.6\,cm$, $9.3\,cm$ and $11.4\,cm$. Despite this source rearrangement, the experiment was performed exactly as for $\overline{\mathrm{P}}$ANDA geometry crystals. During measurement, the crystals were wrapped with Teflon, with an exact layer arrangement as given in Tab. 2.5.

A comparison of the measured LY position dependence is shown in Fig. 2.44a in absolute values and in Fig. 2.44b normalised to the position closest to the PMT. Apparently a roughing of one complete side face, as well as a roughing of the rear third of one face succeed in making the response more uniform on a comparable level. For roughing of the front third, even a slight increase of NUF is observed. Nevertheless
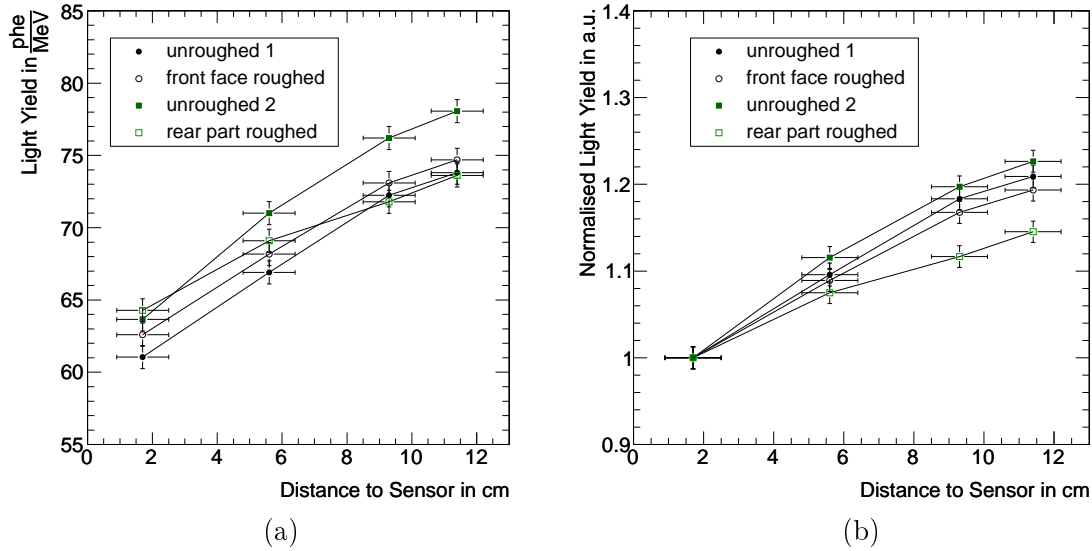
Figure 2.45: Light yield position dependence at $-25\,°C$ of two small crystals before and after surface treatment in absolute values (a) and normalised to the position closest to the PMT (b).

a direct comparison of the absolute values is misleading, since the initial overall light yield of a crystal before surface treatment is unknown. To solve this issue, a comparative measurement was performed with two other crystals, henceforth called sample 1 and 2, which were measured before and after surface treatment under the same conditions. The result is shown in absolute values in Fig. 2.45a, while Fig. 2.45b shows the curves normalised to the position closest to the PMT. Here, no significant change of NUF can be observed for sample 1 before and after surface treatment of the front third. Also the slight increase of the absolute values is within the typical fluctuation for repeated measurements after changing wrapping or coupling on the level of $1\,\frac{\text{phe}}{\text{MeV}}$, which is based on experience. For sample 2 however, a decrease of the NUF is achieved by surface treatment of the rear third, effectively halving the maximum deviation. At the same time no change in the absolute value at the position closest to the photo sensor is observed.

2.3.4 Proton Beam Measurements

Setup

To investigate the NUF with hadrons, an experiment was performed at the Accelerateur Groningen-ORsay (AGOR) cyclotron, located at Kernfysisch Versneller Instituut

Groningen (KVI)[37]. In the used beam line designed for proton irradiation, an energy degrader enables selection of proton energies between $10-184\,\mathrm{MeV}$. For the performed experiment, $80\,\mathrm{MeV}$ protons were chosen. To guarantee a localised energy deposition, a circular collimator with $2\,\mathrm{mm}$ bore diameter was placed in $1.2\,\mathrm{cm}$ distance to the crystal. For positioning, the crystal was mounted on an electronically movable $x-y$-table. The two $\overline{\mathrm{P}}\mathrm{ANDA}$ crystals measured were of the most strongly tapered type 1 geometry and type 6 geometry, used in the Barrel EMC prototype Proto60. The latter was equipped with a single quadratic APD[9] placed at the middle of the crystal rear face, while the former was equipped with two rectangular shaped LAAPDs[10], located adjacent to the sides BR and CR. In both cases, coupling was done with silicone oil. Readout was performed with one Basel LNP per LAAPD. Signals were digitised with a SIS3302 SADC, with already implemented feature extraction algorithms as described in [25]. Both crystals were wrapped with VM2000. Additionally, to ensure proper grounding and shielding of the readout electronics, some self-adhesive aluminium foil cover was applied on the outside.

The response to protons was measured for 19 beam positions along the longitudinal crystal axis, with protons entering either the crystal side bounded by edges BR/BF or the side bounded by CR/CF, henceforth named side 1 and 2, respectively. The beam was moved in steps of $1\,\mathrm{cm}$. Due to the length of the crystal, which was larger than the area shielded by the collimator, it was necessary to turn the crystal lengthwise, effectively switching the position of rear and front face. By this means, also the five outermost positions could be covered.

Results

The position dependent response of the type 1 crystal to $80\,\mathrm{MeV}$ protons impinging on 19 different positions of side 1 is shown in Fig. 2.46a in absolute values and in Fig. 2.46b normalised to the position closest to the LAAPDs, respectively. Due to the described collimator issue, for two positions, the proton signal shows a double peak structure. The affected points are marked with a red shaded area. Points left and right of it belong to opposite longitudinal crystal orientations. For each response curve, belonging to the two single LAAPDs and to the sum of both, a clear NUF is visible. For beam impinging onto side 2, the corresponding plots are shown in Figs. 2.46c and 2.46d. In addition, the response for a type 6 crystal equipped with one LAAPD is shown. Also here, the points derived from distorted proton spectra are marked by a shaded areas in the corresponding colour. Comparing the curves for single LAAPD and sum, the absolute location and hence the signal amplitude for the sum is roughly a factor two higher, which is in agreement with the expectations.

---

[9]Hamamatsu S8664-1010SPL, sensitive area $1\,\mathrm{cm}^2$.
[10]Hamamatsu S11048, sensitive area $1\,\mathrm{cm}^2$ each.

(a)

(b)

(c)

(d)
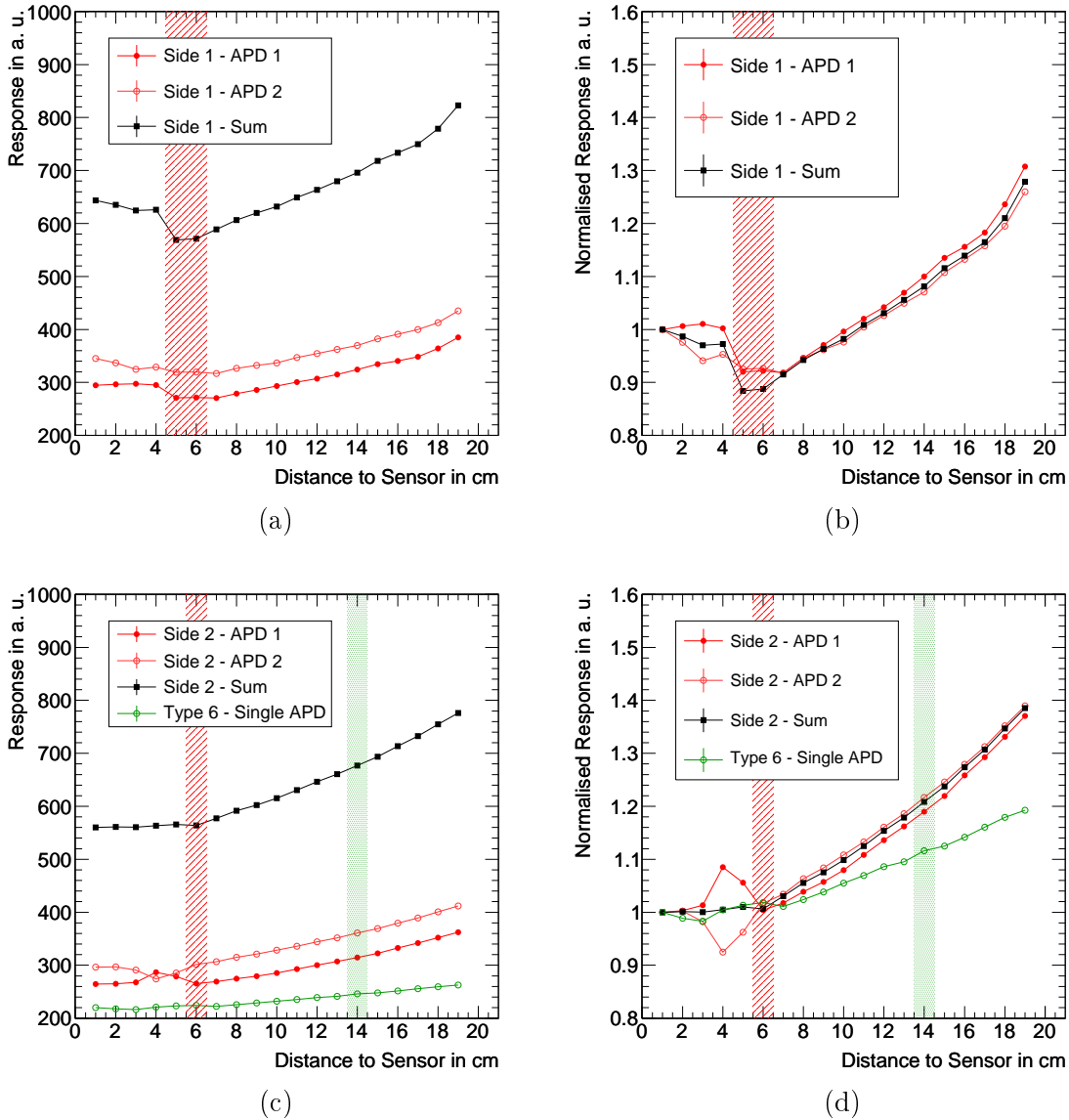
Figure 2.46: Position dependence of the response to 80 MeV protons for a type 1 crystal with beam entering side 1, shown in absolute values (a) and normalised to the position closest to the LAAPDs (b). The analogous plots for beam impinging onto side 2 are shown in (c) and (d), respectively. In addition, the spectra for a crystal of geometry type 6 equipped with a single LAAPD are shown. The shaded areas divide the two regions, where the crystal had to be turned in opposite direction. Points within the area are extracted from a slightly distorted line shape of the proton signal, caused by collimator leakage. All measurements were performed at room temperature.

Nevertheless, they show a similar shape and NUF, which is most apparent if comparing the normalised response (see Fig. 2.46b and 2.46d). For type 6 crystal, the absolute response is slightly smaller and the shape is more uniform. Although the used readout, as well as particle species and energy, differs distinctly from the experiments described in the previous sections, the measured NUF curves are in good agreement in shape and maximum deviation for both measured crystal types. This can be regarded as another indication, that the LY NUF is solely caused by light collection, regardless of the exact mechanism of energy deposition.

Chapter 3

Position Reconstruction

3.1 Position Reconstruction Algorithms

For reconstruction of the point of impact of photons or charged particles onto an laterally segmented scintillation detector like the $\overline{\text{P}}$ANDA EMC, usually a centre of gravity algorithm is used, as indicated in Eq. 3.1:

$$x_{cg} = \frac{\sum\limits_{i} w_i x_i}{\sum\limits_{i} w_i}. \tag{3.1}$$

Here, x_i represents the position of a lateral segment, i.e. the centre of an individual crystal, given either in Cartesian or spherical coordinates. w_i stands for the weight attributed to it. In the most simple case, the weight w_i is equal to the energy E_i deposited by the electromagnetic shower inside crystal i. Accordingly, the denominator in Eq. 3.1 is the total energy deposited in the complete detector or in a cluster with restricted size, respectively. However, as pointed out by [38], positions reconstructed with this weighting are systematically biased towards the centre of a crystal leading to an S-shaped correlation between reconstructed position x_{lin} and actual position x_{ref}. A common parametrisation which relates both positions is given in Eq. 3.2

$$x_{ref} = x_c + b \, \text{arcsinh} \left(\frac{x_{lin} - x_c}{\Delta} \sinh \frac{\Delta}{b} \right), \tag{3.2}$$

where x_c is the coordinate of the crystal centre and Δ its half-width. The parameter b is related to the transversal shower shape and has to be tuned to values fitting the scintillator properties. Because the Molière radius R_M, the relevant parameter describing the lateral spread of an electromagnetic shower inside a medium, is energy independent, also the shape of this so called S-curve is virtually independent of the incoming particle energy. Therefore, if an exact measurement of the S-curve is performed, the systematic bias can be corrected accordingly, delivering satisfactory position resolutions.

However, the $\overline{\text{P}}$ANDA EMC will consist of staggered crystals with 13 different geometries, entailing a multitude of S-curves. Hence an algorithm which naturally delivers a less biased position response is desirable. As proposed by [39], a logarithmic weighting of the energy fraction deposited in a given unit i, as given in Eq. 3.3, takes into account the exponential shape of the lateral electromagnetic shower distribution.

$$
w_i = \begin{cases} 0 & , W_0 + \ln\left(\frac{E_i}{E_T}\right) \leq 0; \\ W_0 + \ln\left(\frac{E_i}{E_T}\right) & , \text{else}; \end{cases} \tag{3.3}
$$

$$
E_T = \sum_i E_i. \tag{3.4}
$$

The weighting parameter W_0 serves on the one hand the purpose to set a threshold to the lowest energy fraction deposited inside a single module which is accepted for position reconstruction. On the other hand, W_0 influences the relative weight among several modules with different deposited energy. In general, a higher W_0 value leads to a more uniform relative weighting, while a low value is in favour of small fractions of deposited energy. Especially at low incident energies and consequently small cluster sizes, this is necessary to avoid systematic bias similar to the linear energy weighting case, originating from insufficiently weighted low energetic tails of the shower profile. Therefore, if large variations of incident photon or electron energy are expected, a non-constant value of $W_0(E_T)$, rising moderately with increasing cluster energy E_T, can have a beneficial influence on the position response linearity and resolution.

3.2 The Barrel EMC Prototype PROTO60

3.2.1 Mechanics

The first prototype for the $\overline{\text{P}}$ANDA Barrel EMC is the so called PROTO60. Geometrically it closely represents a subsection of a Barrel EMC slice, as schematically depicted in Fig. 3.1. It consists of 60 PWO-II crystals, which are solely of geometry type 6, arranged in a matrix with six rows times ten columns. In the final EMC geometry, two rows would be of geometry type 5. Reason for this discrepancy is a simplification in the manufacturing process of the carbon alveoli, serving as holding structure of the crystals, as well as in crystal production itself. The complete matrix is contained in a copper cladded aluminium box surrounded by a PolyVinyl Chloride (PVC) housing. The interspace is filled with insulating styrene foam, to enable standalone operation at a temperature of $-25\,^\circ\text{C}$. Merely the entrance window in front of the matrix is designed in a different way. Here, to achieve thermal shielding with minimum attenuation of incoming particles, the space between two thin aluminium
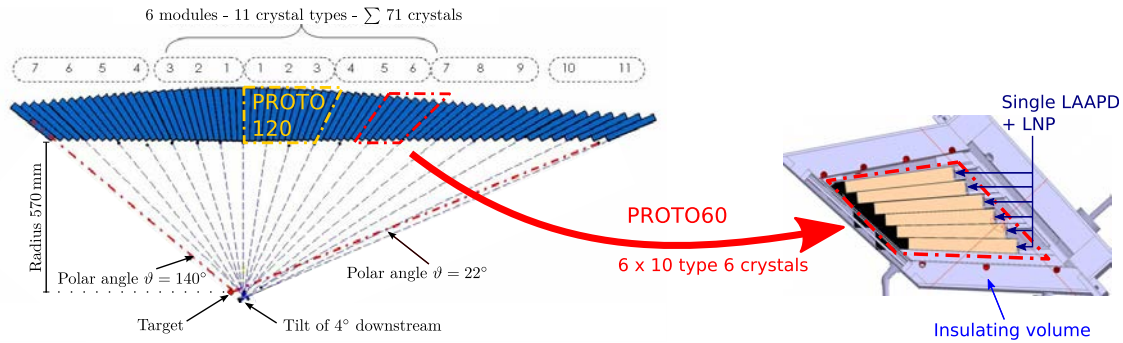
Figure 3.1: Schematic view of the Barrel EMC slice subsection represented by PROTO60, which is marked by the red box. The matrix, consisting of 6×10 PWO-II crystals of type 6 geometry, is contained in an insulating volume for standalone operation. Each crystal is read out by a single LAAPD coupled to a Basel LNP. Additionally the section represented by the future prototype PROTO120 is marked in yellow.

plates is evacuated. For cooling, a mixture of water and ethanol, circulating through meandering copper pipes attached to the inner box, is used. To avoid ice formation, the PROTO60 housing is sealed with silicon. Additionally, its interior is flooded with slightly overpressured dry nitrogen during cooled operation, significantly reducing the humidity.

Each crystal of PROTO60 is equipped with a single LAAPD[1], wrapped with VM2000 fixated by Mylar film and grouped together to packages of four crystals. To avoid optical crosstalk and homogenise the dead material, thin carbon sheets are placed between the crystals. Fig. 3.2a shows exemplary such a crystal quartette, before insertion into the alveole. Inside the protruding alveoli space at the crystal quartette's back, an aluminium insert is installed, serving as suspension for the alveoli. These overall 15 inserts (one per 4 crystals) are screwed to the backplane of the prototype housing. In addition, the SP883b Quad LNP is attached to the insert. One readout backplane per two columns, supplying three LNPs and connected LAAPDs, guides the signals to the outside of the PROTO60 housing. There, coaxial connectors enable flexible routing of signals to a test beam DAQ.

---

[1]Hamamatsu S8664-1010SPL, $1\,cm^2$ sensitive area.

<div align="center">(a)   (b)</div>
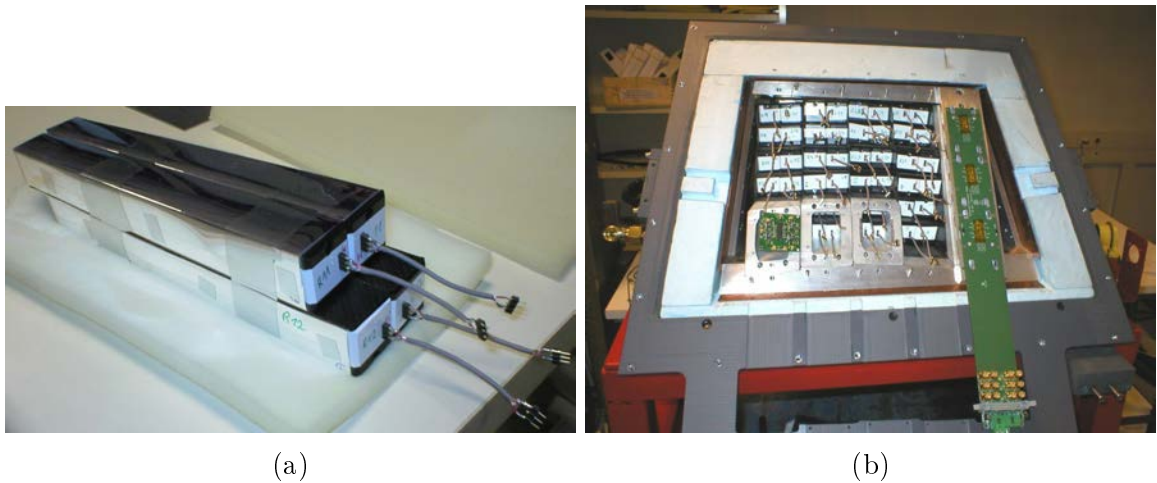
Figure 3.2: Photographs taken during the assembly of PROTO60. Crystals are wrapped with VM2000 and equipped with a single LAAPD and arranged in groups of four crystals (a). They are inserted through the opened back-plane (b). From there also aluminium inserts, LNP and readout backplanes are mounted.

3.3 Experiment at CERN SPS

3.3.1 Setup

The PROTO60 test measurement, covering the highest particle energy foreseen for detection in the later $\overline{\text{P}}$ANDA EMC, was performed at the H4 beamline located at the North Area of CERN, frequently used for detector tests. The primary beam was provided by the Super Proton Synchrotron (SPS), whose location in the CERN accelerator complex is shown schematically in Fig. 3.3. This synchrotron operates with conventional (non-superconducting) electromagnets and is able to accelerate a variety of particles, e.g. protons, electrons or even light nuclei, up to energies of $450\,\frac{\text{GeV}}{\text{A}}$. At the H4 beamline however, the primary proton beam was converted at a beryllium target into secondary beams. For the PROTO60 tests, mainly a beam of positrons with $15\,\frac{\text{GeV}}{c}$ momentum was selected. For calibration of the inner detectors though, a muon beam with $150\,\frac{\text{GeV}}{c}$ momentum was deployed, originating from the decay of charged pions produced at the Be-target. In addition to PROTO60, the so called Bonn Tracking Station, a modular detector for tracking of charged particles, was used in the experiment. A detailed description of the station, actually representing prototypes for the $\overline{\text{P}}$ANDA MVD, can be found in [41]. Main part of the station in the used configuration were two double sided silicon strip detectors, contained in an aluminium box with appropriate entrance window and placed at $758\,\text{cm}$ distance
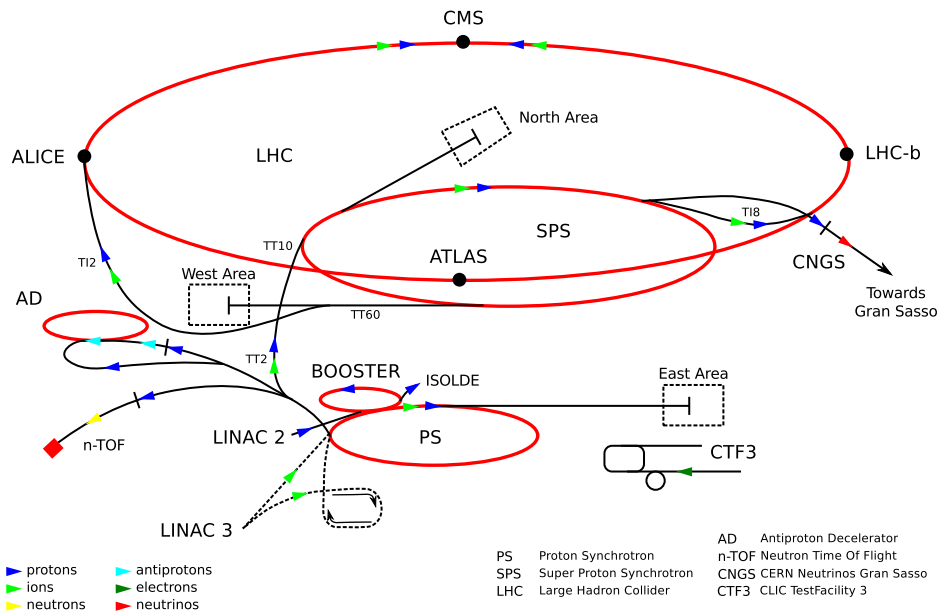
Figure 3.3: Schematic view of the CERN accelerator complex [40]. The experiment described in this work was performed at the H4 beamline located at the North Area. The primary proton beam provided by SPS was converted into secondary beams of either $15\,\frac{\text{GeV}}{c}$ momentum positrons or $150\,\frac{\text{GeV}}{c}$ momentum muons.

(a)   (b)

(c)
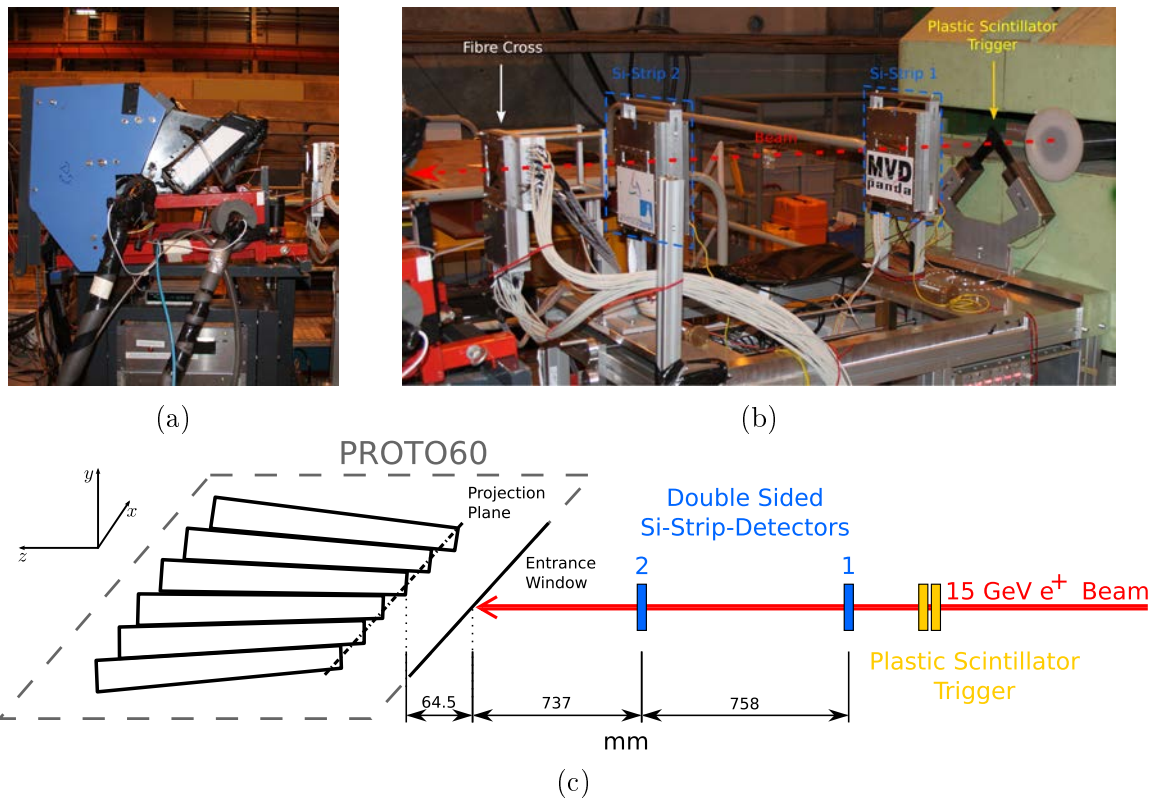
Figure 3.4: Photographs of PROTO60 (a) and tracking station during the test beam time at CERN SPS. In addition, the components and their respective distances essential for analysis are shown in a schematic view (c).

to each other. Each of these detectors has an active area of $1.92\,\mathrm{cm} \times 1.92\,\mathrm{cm}$, a thickness of $300\,\mu\mathrm{m}$ and strips with a pitch of $50\,\mu\mathrm{m}$. Strips at opposite sides are oriented perpendicular to each other. Therefore each detector is able to give a two dimensional position information of a traversing charged particle. In addition, to provide a trigger signal for DAQ, two overlapping plastic scintillator bars with PMT readout were mounted in front of both Si-strip detectors. Fig. 3.4a and Fig. 3.4b show photographs of PROTO60 and the Bonn Tracking Station set up at the experimental area. For orientation, Fig. 3.4c shows a schematic view of the components, as well as their relative distances relevant for the analysis described in the following sections. The relative position of beam and tracking detectors was fixed during the course of the experiment. The PROTO60 though was mounted on a positioning table, able to move the prototype in horizontal and vertical direction perpendicular to the beam. The table is operated by stepper motors, which are monitored by four digital measuring slides, enabling a positioning accuracy in the order of $0.1\,\mathrm{mm}$. The absolute positioning of PROTO60 and positioning table with respect to the beam direction was performed with a laser aided lead according to the positioning markers fixed on front and back

side of the PROTO60 housing. These represent the vertical symmetry axis of the crystal matrix and divide it horizontally into 3 crystal rows, each. This axis was adjusted parallel to the beam direction, as defined by markers at the experimental site. However, the precision of these adjustments is inferior to the precision of the positioning table. Therefore, the absolute value of the beam position relatively to the PROTO60 matrix bears a systematic uncertainty of about 2 mm. Despite the fact that intrinsically PROTO60 was moved relatively to beam and tracking station, for simplicity in position reconstruction, henceforth the PROTO60 position will be regarded as fixed, with the beam moving in its coordinate system.

3.3.2 Readout and DAQ

Data Acquisition

In contrast to previous beam times at lower energies, as described in [25], a large fraction of PROTO60 was read out with SADCs. Merely the outermost column on left and right side of the crystal matrix were omitted from the readout, because of the limited number of available ADC channels. Accordingly, 48 of 60 crystals were read out by LAAPDs and Quad-LNPs, whose pulses were routed to the six available SIS 3302 SADC modules (8 channels each) by coaxial cables and digitised without further shaping. The sampling frequency amounted to 50 MHz, resulting in one sample every 20 ns. Traces stored to hard disk had a length of 250 samples, corresponding to a time window of 5 μs. Fig. 3.5 shows schematically the design of the test experiment DAQ. Relevant units of the used modules are listed in Tab. 3.1. The six SADC modules of the PROTO60 readout were continuously taking samples of the pulses generated by the individual crystals. In case of a trigger signal, the 250 samples taken before were sent via Versa Module Eurocard (VME) bus to the Central Processing Unit (CPU) for further processing. The trigger was built by a coincidence of the plastic scintillator trigger mounted on the Tracking Station (see Fig. 3.4a) and the logical OR of all 48 channels of PROTO60. The threshold for each channel was set individually by software during SADC configuration. Additionally, a trigger could be generated by a testpulser integrated in the customised SIS 3320 synchronisation module, responsible for prohibiting additional trigger signals until complete processing of the previous event. Information on both Si-tracker modules, already processed by the standalone tracking station readout, was sent to a VME CPU via an Ethernet (Transmission Control Protocol / Internet Protocol (TCP/IP)) connection. A complete dataset for one event consists of one trace per PROTO60 channel and information on the response, which of the 2 × 384 strips, oriented in x and y direction, of each Si-tracker responded. Event datasets were stored after processing on a Network Access Storage (NAS), accessible via Ethernet connection, too. Due to the exponential falloff of the electromagnetic shower caused by the positron beam, for the crystal directly hit
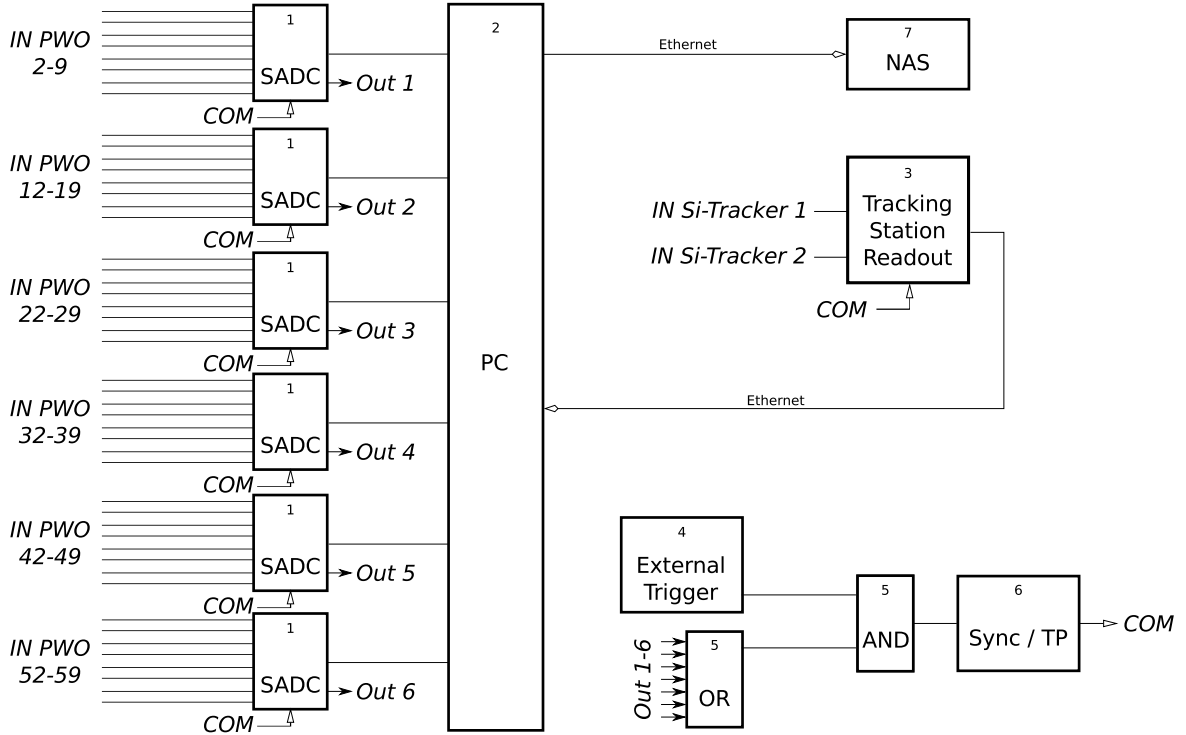
Figure 3.5: Schematic view of the prototype readout during the test beamtime at CERN SPS. For the individual module types, see Tab. 3.1.

Module Number	Function	Type	Standard / Connection
1	SADC	Struck SIS 3302 SADC	VME
2	PC	VME CPU with Tundra-II chipset	VME
3	Tracking	Bonn Tracking Station [41]	TCP/IP
4	External Trigger	Discriminated plastic scintillator paddle signal	NIM
5	AND or OR	LeCroy Model 622 Quad Coincidence	NIM
6	Sync / TP	Customised synchronisation module incl. test pulser (based on Struck SIS 3320)	VME
7	NAS	QNAP TS-659 Pro+ NAS	TCP/IP

Table 3.1: Collection of electronics modules utilised for the PROTO60 test beam setup at CERN, as displayed in Fig. 3.5.

110

DETECTOR REGION	LAAPD GAIN	NOISE σ IN MeV	DYNAMIC RANGE IN MeV
Centre	50	2.57	12500
Outer Rings	150	0.97	4500

Table 3.2: Estimated dynamic range and noise RMS for PROTO60 at CERN SPS.

by the incident positron and its direct neighbours large energy depositions are to be expected in comparison to the rest of the PROTO60 crystal matrix. Since the used version of the LNP is able to tolerate a maximum input charge of approximately 4 pC, the LAAPD gain for the inner detectors had to be reduced in comparison to previous measurements to comply with this constraint. As a consequence, the dynamic range of detector centre and outer rings differ. For an estimation of the respective gain of the previously unscreened LAAPDs and the dynamic range in terms of energy of both detector regions, see Tab. 3.2. A detailed description of the dynamic range calculation is given in [42].

Feature Extraction

To deduce energy and time information from the raw SADC traces, elaborate feature extraction algorithms are needed, which are simple enough to allow for a future implementation into the SADC FPGA. Studies concerning algorithms for application in the $\overline{\mathrm{P}}$ANDA EMC are described in detail in [43, 25]. Because thorough testing of these algorithms on experimental data is mandatory, they also served as basis for the analysis described in the following sections. Therefore, a brief summary of the implemented steps and their impact on the trace form is given. The complete feature extraction applied to a SADC trace consists of two successive steps, one of which is common for both, energy and time extraction. Figs. 3.6a to 3.6d show exemplary a trace after each feature extraction step.

The first step is the so called Moving Window Deconvolution algorithm (MWD), which serves the purpose to shape the raw LNP signal, which possesses a relatively slow trailing edge, into a much shorter, almost symmetric pulse. The used algorithm, displayed in Eq. 3.5,

$$x_{MWD}(n) = x(n) - x(n - M) + \frac{\ln 2}{\tau} \sum_{i=n-M}^{n-1} x(i), \qquad (3.5)$$

in principle takes the difference of the pulse height $x(n)$ of sample n and a previous sample and adds the Moving Average algorithm (MA) of the pulse heights in between. Window length M and decay constant τ serve as parameters which have to be fitted to

signal rise time and decay constant of the raw LNP signal, respectively. The values of $M = 240\,\text{ns}$ (12 samples) and $\tau = 25\,\mu\text{s}$ (1250 samples) represent a good compromise between energy and time response and were used during this analysis. For the purpose of energy extraction, in a second step, an MA filter is applied to the already shaped trace. The corresponding algorithm can be found in Eq. 3.6,

$$x_{MA}(n) = \sum_{i=n-L}^{n-1} x_{MWD}(i), \tag{3.6}$$

where L represents the smoothing length. Although the pulse shape is hardly changed (see Fig. 3.6c), signal fluctuations are suppressed, effectively resulting in a reduced noise contribution. This effect is especially important for low signal heights, where the application of the MA filter can improve the energy resolution distinctly. By choosing larger values of L this effect is even more pronounced, though at the cost of a longer signal rise time, which can be problematic at high event rates, increasing the probability for pileup events. Finally, for each pulse the baseline is deduced individually. In case of this analysis, the baseline was obtained as the average of samples 40 to 60, corresponding to a time window of $1.2\,\mu\text{s}$. The final signal amplitude is then given by the difference of pulse maximum and baseline, and proportional to the energy deposited inside the crystal. For time extraction, the MA filter is replaced by the Constant Fraction Timing algorithm (CFT) filter, mimicking the signal treatment as performed in a conventional analogue CFD. The shaped pulse after the MWD step is delayed and overlayed with the inverted pulse of reduced amplitude. The CFT algorithm is expressed in Eq. 3.7,

$$x_{CFT}(n) = x_{MWD}(n - D) - R \cdot x_{MWD}(n), \tag{3.7}$$

with the parameters D and R corresponding to signal delay and fraction of the inverted pulse height relatively to the original pulse, respectively. As time reference, the point of the baseline crossing is used. A delay of $D = 100\,\text{ns}$ (5 samples) and a ratio of $R = 0.45$ have been proven to deliver an appropriate time response. As shown in [34], despite limitations due to the comparatively large rise time of the APD and a sampling rate of $50\,\text{MHz}$, an acceptable resolution, distinctly better than the sample width, has been achieved.
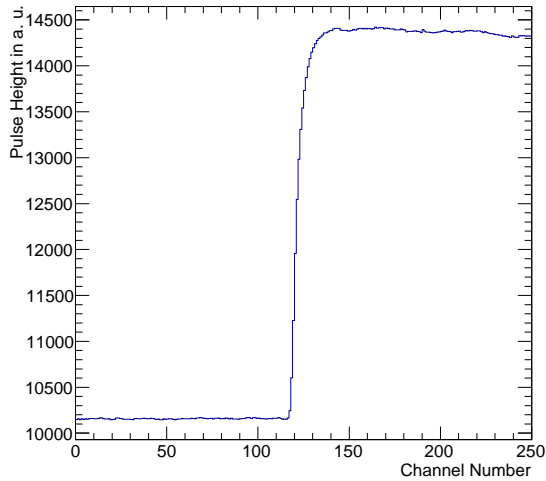
(a) Raw SADC trace.
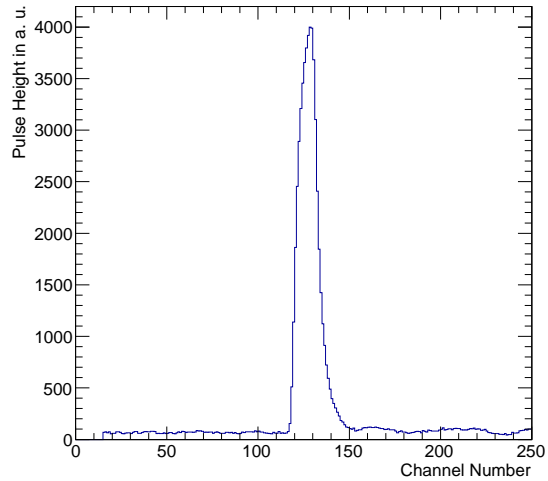
(b) Trace after MWD.
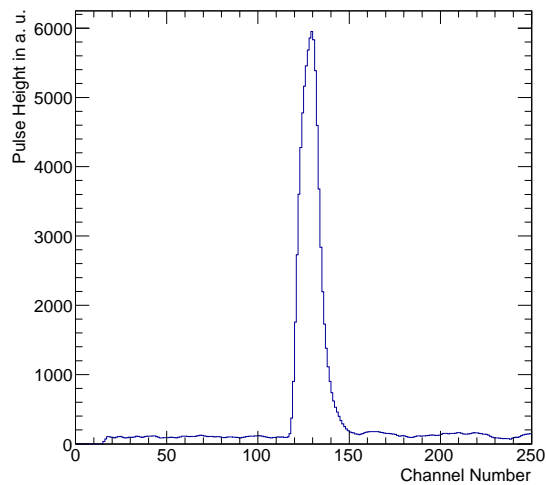
(c) Trace after MWD and MA.
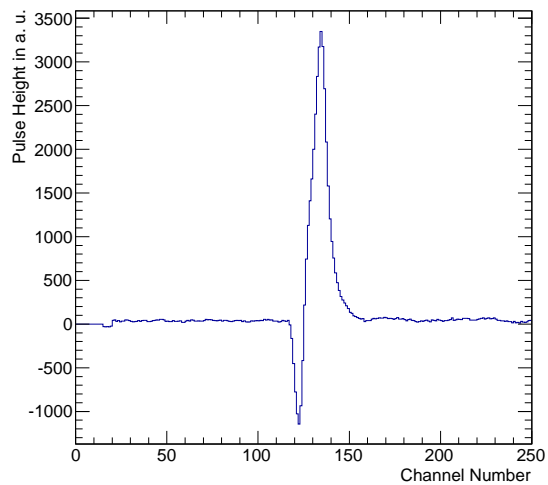
(d) Trace after MWD and CFT.

Figure 3.6: SADC traces of crystal 28 during the different steps of feature extraction. The final deposited energy for the selected event is derived from (c), while the time is extracted from (d).

3.4 Analysis

Both position reconstruction techniques presented in Sec. 3.1 rely on a centre of gravity algorithm, albeit with different weighting of the individual detector unit in comparison to the complete cluster. Hence, these synergies were exploited during analysis, resulting in basic prerequisites common for both reconstruction techniques. The calibration of the absolute position values however, has to be performed separately for each technique, as described in Sec. 3.4.2 and 3.4.3.

3.4.1 Common Prerequisites

Energy Calibration

A detailed description of relative and absolute energy calibration methods for the PROTO60 can be found in [42]. For the analysis presented in this work, which mainly concentrates on position reconstruction, an accurate relative calibration is mandatory. Therefore, a mixed approach was pursued, using different calibration methods for the inner crystals of the matrix, which are exposed to higher energy depositions, and the outermost crystals, respectively. For clarification, Fig. 3.7 presents a schematic view of the PROTO60 crystal matrix seen in beam direction, with crystals marked in different shades of grey according to their specific calibration method. Crystals marked with light grey were calibrated relatively to each other according to their individual response to a $150 \frac{\text{GeV}}{c}$ muon beam. The five crystals marked slightly darker, represent those with the above mentioned reduced LAAPD gain and consequently a lower uncalibrated response, but larger dynamic range. Due to the large muon beam diameter, several crystals could be covered at the same time. Nevertheless, the outer crystals, marked in white, were calibrated with cosmic MIPs. Reasons for this were on the one hand time constraints and on the other hand the expected low energy depositions, demanding no high energy calibration point. Since the energy of the muon beam used for calibration is relatively close to the critical energy of muons in lead tungstate (see Tab. 1.3), their energy deposition is not solely governed by ionisation. Therefore, to obtain a correct absolute energy calibration, GEANT4 simulations with settings similar to the experimental conditions were performed [42]. With the help of these, the peaks observed in the spectra used for calibration could be assigned to realistic energy values.

Coordinate System

As indicated in Sec. 3.3.1, the position of PROTO60 relatively to the fixed position of tracking station and positron beam, was changed between the two performed measure-
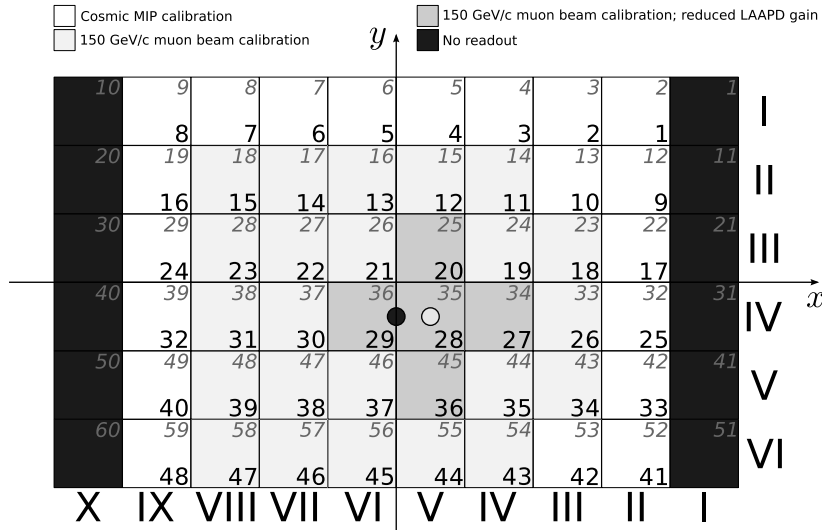
Figure 3.7: Scheme of the PROTO60 crystal matrix in beam direction. Grey italic numbers indicate the physical number of the crystals in the matrix, while black numbers are the crystal indices used in readout and analysis. The positron beam was either impinging on the centre of crystal 28 (run 1) or in between crystal 28 and 29, marked by an open and a filled circle, respectively. The schematics are not true to scale.
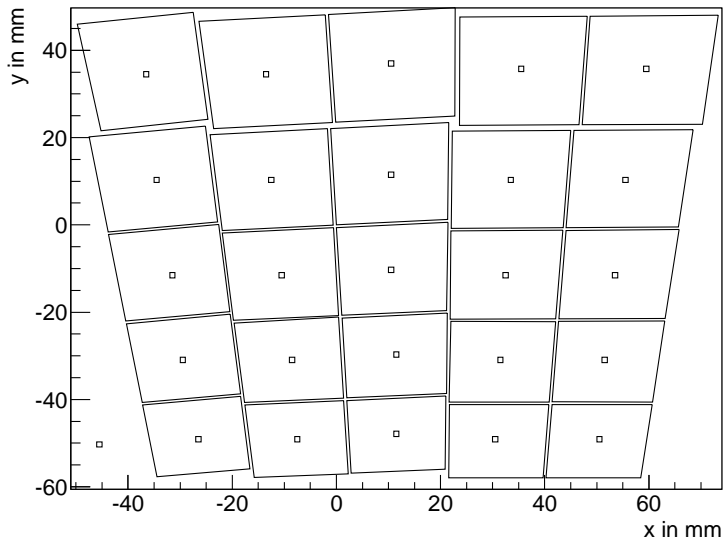
Figure 3.8: Crystal coordinates used in position reconstruction and front face projections of the 25 innermost crystals.

ment runs. For position reconstruction purposes however, the PROTO60 coordinate system will be regarded as resting, with the beam spot impinging on two different positions onto the crystal matrix. Another consequence is though that the position information provided by the tracking station has to be calibrated absolutely, twice for each reconstruction technique. An essential ingredient for position reconstruction is the correct assignment of the crystal coordinates, which are used in the position reconstruction algorithm. Usually, the crystal centre coordinates are used for this purpose. Since the PROTO60 represents, as indicated in Fig. 3.1, a cutout of the cylindrical Barrel EMC, crystals are arranged along a curved surface. Therefore, a natural way to define the PROTO60 coordinate system would be cylinder or angular coordinates, with all crystals covering roughly the same solid angle. However, as an essential condition for an application of angular coordinates during a test experiment, the centre point, to which all longitudinal crystal axis are pointing has to be known and defined precisely. In case of PROTO60, crystals are not visible from the outside due to thermal insulation. Only the axis, which divides the PROTO60 into four matrices of 15 crystals each, located at the boundaries of crystals 20, 21, 28 and 29, is marked at the outside. As described above, during experiment PROTO60 was aligned in a way that this axis is congruent with the beam direction. Another point interfering with the use of an angular coordinate system is the fact that the positioning table is shifting in vertical and horizontal direction, exclusively. Finally, each silicon tracker naturally provides Cartesian coordinates for a traversing charged particle. Thus, a Cartesian coordinate system also for PROTO60 is a sensible compromise. Since the represented solid angle is relatively small, the tilting angle of adjacent crystals differs only slightly. Hence, it is possible to approximate the front faces of a small matrix of crystals as a plane. The central axis and therefore the beam direction was chosen as z-axis, horizontal right and vertical upward direction defined as positive x and y direction, respectively. The origin of the coordinate system then is located in the upper right or left corner of the crystals 28 and 29. By choosing these crystals, which are close to the origin, as impact point of the positron beam and thus as subdetectors with the highest energy deposition, systematic uncertainties due to the flat plane approximation are suppressed.

Orientation and placement of the mentioned projection plane were performed with the help of a PROTO60 CAD model, originally used for its construction and assembly. As crystal coordinates (x_i, y_i) for usage in the position reconstruction algorithm, the centre of area of the crystal front face projection on the plane was used. To obtain these, the four vectors describing the orientation of the side edges were derived from the CAD model for each crystal. Afterwards, the corresponding four points of intersection with the projection plane were calculated, enabling in a last step the determination of the centre of area. In Fig. 3.8, the front face projections along with the corresponding centres of area for the 25 crystals closest to the centre of the electromagnetic shower are drawn, as implemented into the analysis software. The information provided by

(a)

(b)

(c)

(d)
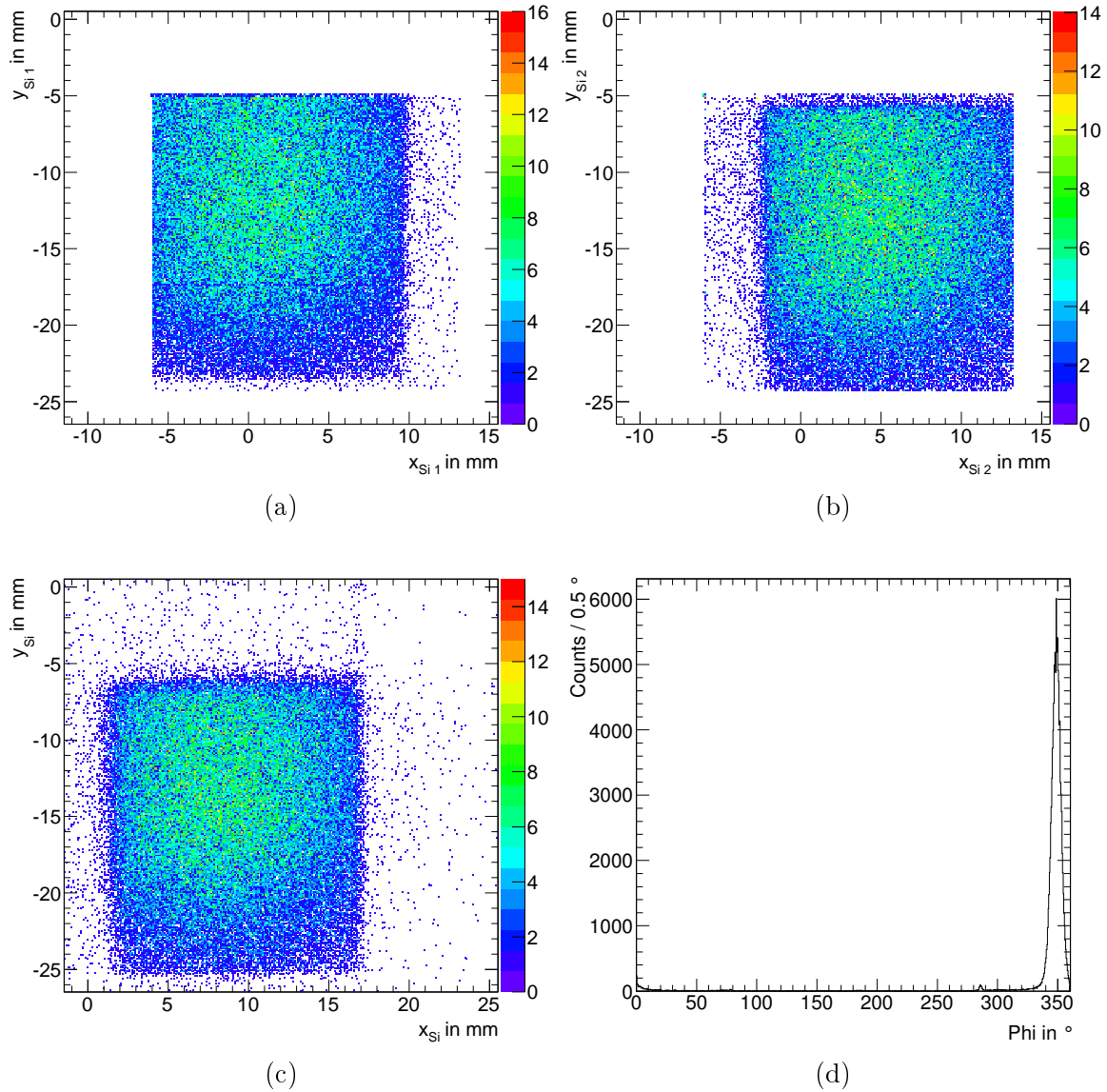
Figure 3.9: Beam spots during run 1 as measured by Si-tracker 1 (a) and Si-tracker 2 (b), respectively. In addition the position extrapolated to the PROTO60 front face is shown (c), which serves as reference position during analysis. For these pictures, the absolute calibration was performed as described in Sec. 3.4.3. In addition, the φ deviation of the particle trajectory, with respect to the symmetry axis of the tracking station is shown (c).

the tracking station consisted of two points (x_{Si1}, y_{Si1}) and (x_{Si2}, y_{Si2}), measured by the double sided Si-strip detectors, in $\Delta z = 758\,\mathrm{mm}$ distance to each other. From these two points, the straight charged particle trajectory was determined. The intersection point of this trajectory with the PROTO60 projection plane (x_{Si}, y_{Si}) is used as reference position throughout analysis. Fig. 3.9 shows the reconstructed and extrapolated beam spots for run 1. The tilting of the particle trajectory with respect to the tracker symmetry axis is expressed by polar angle ϑ and azimuthal angle φ. The distribution of the latter is displayed in Fig. 3.9d and shows a peak around $350\,°$, effectively meaning that the beam is pointing slightly to the lower right. However, the average θ is about $0.3\,°$, which is of the order of the inclination angle variations of the crystal surfaces due to their arrangement.

Intrinsically, values for x_{Si} and y_{Si} are positive and ranging from zero up to a few tens of millimetres. To obtain the absolute position in the PROTO60 coordinate system, as presented above, those have to be calibrated properly. This is performed separately for both applied reconstruction techniques, as described in the following.

3.4.2 S-Curve Correction Technique

Position Calibration

In order to compare the information on incident position provided by the tracking station with the position reconstructed with PROTO60 information, both have to be shifted to share the same point of origin. Therefore, as a first step, the reference position x_{Si} is plotted versus the position x_{lin}. The latter is calculated with the centre of gravity algorithm displayed in Eq. 3.1 and linear energy weighting, i.e. the weight is given by $w_i = E_i$. The resulting distribution[2] is then divided into slices of $0.5\,\mathrm{mm}$ along the x_{lin}-axis. Afterwards, each slice is projected onto the x_{Si}-axis and fitted with a Gaussian distribution. The mean value extracted from these fits is displayed in Fig. 3.10a and Fig. 3.10b, for run 1 and run 2, respectively. The resulting correlation of reconstructed position x_{lin} and uncalibrated reference position x_i shows the expected S-shape with regard to the ideal linear correlation, marked with a solid line. Moreover, its point of inflexion, normally located at the crystal centre, is shifted, reflecting the shift of the coordinate systems of tracking and PROTO60. To gain a quantitative measure of both, S-curve shift and shape, a fit of the S-curve was performed. For this purpose, Eq. 3.2 was slightly modified, resulting in Eq. 3.8.

$$x_{Si} = x'_{Si} + b\arcsinh\left(\frac{x_{lin} - x'_{lin}}{\Delta}\sinh\frac{\Delta}{b}\right).\tag{3.8}$$

---

[2]In contrast to the conventional S-curve plot, axes are interchanged to enable direct fitting with Eq. 3.8.

(a) Run 1.

(b) Run 2.
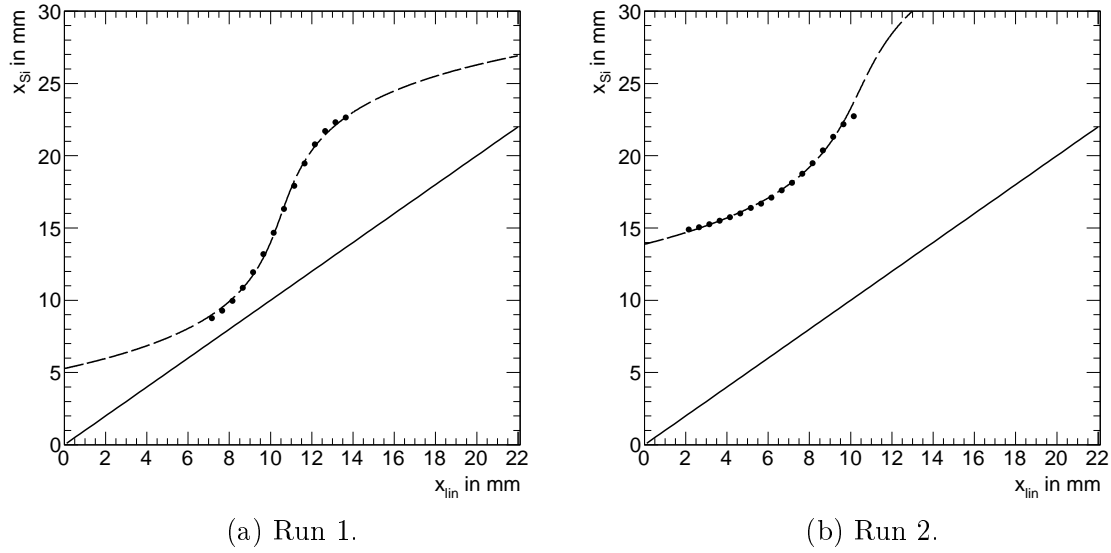
Figure 3.10: Fits to the raw x-direction S-curves obtained with linear weighting. For comparison, an ideal linear correlation is marked with a solid line.

(a) Run 1.

(b) Run 2.
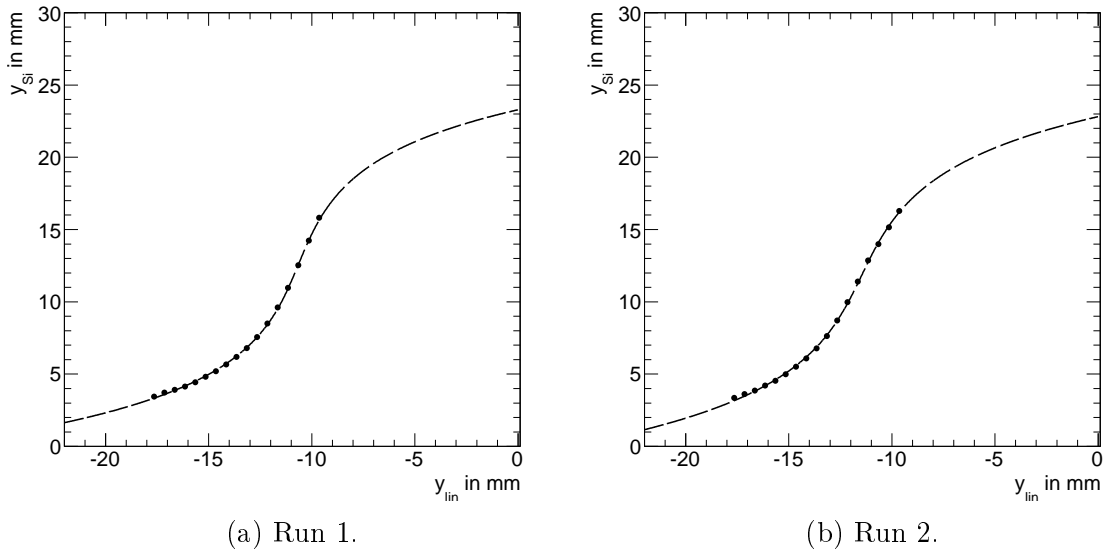
Figure 3.11: Fits to the raw y-direction S-curves obtained with linear weighting.

RUN	COOR-DINATE	PARA-METER	VALUE IN mm		
1	x	b	3.31	$\pm$	0.22
		x'_{Si}	15.95	$\pm$	0.71
		x'_{lin}	10.52	$\pm$	0.31
	y	b	3.47	$\pm$	0.27
		y'_{Si}	12.63	$\pm$	0.50
		y'_{lin}	-10.64	$\pm$	0.25
2	x	b	4.01	$\pm$	1.21
		x'_{Si}	24.46	$\pm$	0.69
		x'_{lin}	10.53	$\pm$	0.56
	y	b	3.78	$\pm$	0.30
		y'_{Si}	11.88	$\pm$	0.60
		y'_{lin}	-11.45	$\pm$	0.32
$\Delta = 10.74\,\mathrm{mm}$ for all Fits					

Table 3.3: Parameters obtained from fit of Eq. 3.8 to the uncalibrated S-curves shown in Fig. 3.10 and Fig. 3.11.

In this case, the reference position is represented by x_{Si}, while x'_{Si} is a fit parameter describing the curve's shift in x_{Si} direction, while parameter x'_{lin} stands for the shift in x_{lin} direction. The purpose of parameter b remains unchanged. However, the constant Δ was set to a value of 10.74 mm, which is the mean halfwidth of a type 6 crystal front face. A plot of the fit functions can be found in Fig. 3.10, while the extracted parameters are collected in Tab. 3.3. For the reasons stated in Sec. 3.4.1, the absolute calibration was performed by shifting the tracking coordinate system by a constant value to be congruent with the PROTO60 coordinate system. This shift $\Delta x'$ is given by the difference of the fit parameters x'_{Si} and x'_{lin} (see Eq. 3.9) and has to be performed separately for each run, since the relative position of tracking and prototype was changed:

$$\Delta x' = x'_{Si} - x'_{lin}. \tag{3.9}$$

The procedure described for x-direction was performed in an analogue way for y-direction. The corresponding curves including the drawn fit function for both runs can be found in Fig. 3.11. The extracted fit parameters are displayed in Tab. 3.3, too.

Procedure

After compensation of the absolute position shift with the described calibration procedure, still a clear non linear correlation of reconstructed position x_{lin} to reference position x_{Si} could be observed. These correlations, the so called S-curves, are displayed in Fig. 3.12 for x-direction, while Fig. 3.13 shows the S-Curves for y-direction. For comparison, a dashed line marks a linear correlation with slope one. To correct for the apparent strong bias towards the crystal's centre, a variant of Eq. 3.2 was chosen, expressed in Eq. 3.10.

$$x_{corr} = x_c + b \operatorname{arcsinh} \left(\frac{x_{lin} - x_c}{\Delta} \sinh \frac{\Delta}{b} \right). \tag{3.10}$$

Now the corrected reconstructed position x_{corr} replaces the tracking position and x_c represents the coordinate of the centre of the crystal with the highest energy deposition. Inside its borders the incident position must be located, if the linear centre of gravity algorithm is used. Because of this, x_c at the same time defines the point of inflexion of the S-curve. Setting again $\Delta = 10.74\,\mathrm{mm}$ as the constant crystal half-width, the parameter b extracted from the fits performed during the calibration procedure could be also used for correction. To have a universal correction of the reconstructed position, valid for both, x- and y-direction, it was decided to use the mean of both values obtained for run 1 (see Tab. 3.3), amounting to $\bar{b} = 3.8\,\mathrm{mm}$. Reason for this decision is on the one hand the fact that for run 2, in x-direction only a dataset covering less than half a crystal size is available (see Fig. 3.10a) and accordingly the fit error for b is large. On the other hand, the y- direction S-curve, shown in Fig. 3.13b, splits into two branches, which also makes determination of b less reliable. The origin of this split, also observed with the logarithmic weighting technique, will be discussed below. An application of Eq. 3.10 with the described parameters, yields corrected position correlations, which show a more linear behaviour. These are displayed in Fig. 3.14 and Fig. 3.15 for x- and y-direction, respectively. For both directions, the corrected position response shows a superior uniformity, which is in most cases close to the ideal, again marked with a dashed line. Despite this fact, some small irregularities can be observed, especially at the crystal junctions, most likely originating from the distinction of cases necessary during the correction process, when picking the crystal centre coordinate x_c. Especially if the energy deposited in the neighbouring crystals is nearly equally large and the photon entered at positions where the S-curve slope is highest, this can lead to the small kinks observed in in Fig. 3.14b, 3.15a and 3.15b. Furthermore it has to be considered that the used constant crystal front halfwidth Δ is only the mean value, while the real crystal width in x-direction is subject to variations of the order of $0.5\,\mathrm{mm}$ in dependence of the photon's incident y_{Si} and vice versa. Moreover, the longitudinal centre of gravity of the electromagnetic shower initiated by a $15\,\mathrm{GeV}$ positron beam, according to Tab. 1.2, is located in approximately $7\,\mathrm{cm}$

(a) Run 1.   (b) Run 2.
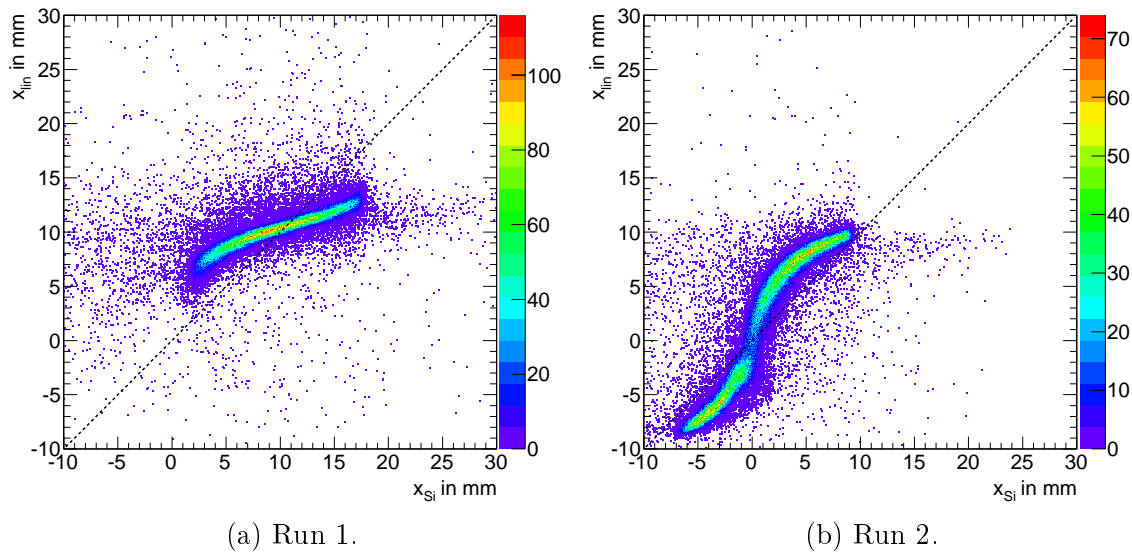
Figure 3.12: Non-linear position correlation (S-curve) in x-direction for both runs, obtained with linear weighting. The dashed line corresponds to a linear correlation.

(a) Run 1.   (b) Run 2.
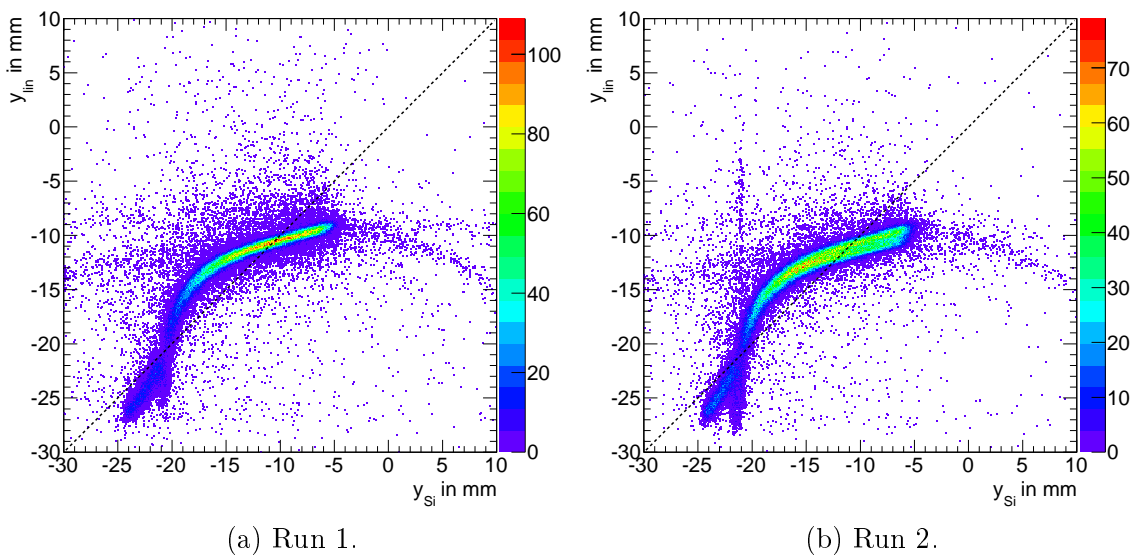
Figure 3.13: Non-linear position correlation (S-curve) in y-direction for both runs, obtained with linear weighting. The dashed line corresponds to a linear correlation.

(a) Run 1.

(b) Run 2.
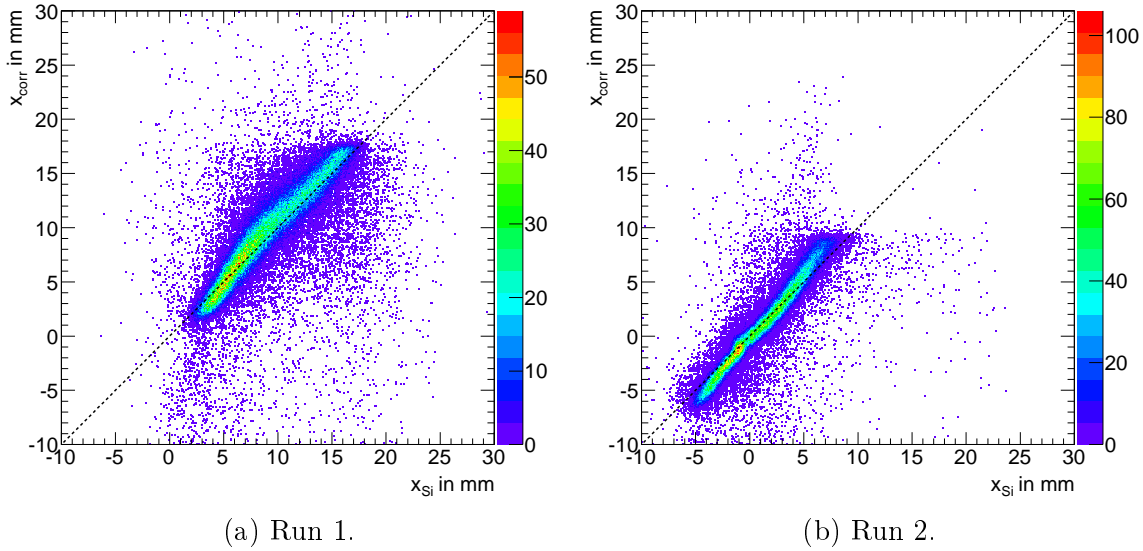
Figure 3.14: Corrected position correlation (S-curve) in x-direction for both runs, obtained with linear weighting. The dashed line corresponds to a linear correlation.

($\approx 8X_0$) depth. Therefore, a larger effective Δ in combination with the more natural angular coordinate system, could further improve linearity. Despite these small irregularities, the results concerning position response deviations and resolution are quite satisfactory, as will be presented in Sec. 3.4.4.

3.4.3 Logarithmic Weighting Technique

Weighting Parameter Determination

Main motivation for the application of the logarithmic weighting, introduced in Eq.3.3, is an intrinsic linearity of the position response. First and essential step is the determination of the weighting parameter W_0. For this purpose, based on experiences with earlier tests, the position reconstruction was performed with different weighting parameter values ranging from $3.0 \leq W_0 \leq 7.0$. The resulting mean position deviation of the reconstructed position x_{log} (y_{log}) from the reference position x_{Si} (y_{Si}) in dependence of W_0 for run 1 is shown in Fig. 3.16a. In addition, Fig. 3.16b displays the width σ_x (σ_y) of this distribution, representing the position resolution, also in dependence of the used weighting parameter value. As indicated by the shaded areas, for values lower than 3.7 in x-direction the resulting $x_{Si} - x_{log}$ distribution is a strongly

(a) Run 1.

(b) Run 2.
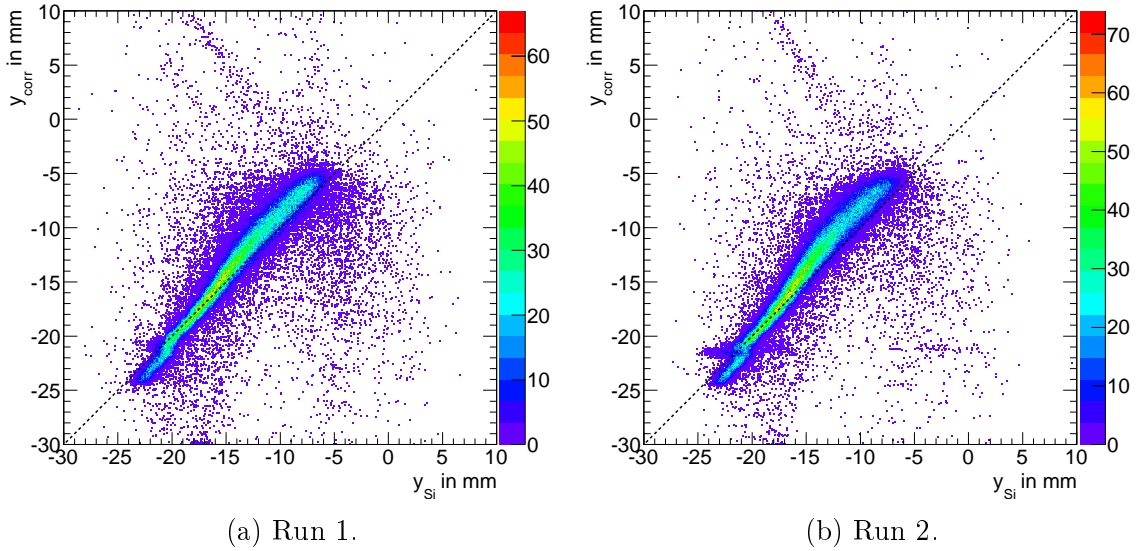
Figure 3.15: Corrected position correlation (S-curve) in y-direction for both runs, obtained with linear weighting. The dashed line corresponds to a linear correlation.

distorted Gaussian. Hence the resulting mean values and width, extracted by a Gaussian fit, deliver no reliable position information. The same holds true for the $y_{Si} - y_{log}$ distribution, if W_0 is lower than 4.1. For larger W_0 however, the distortion vanishes and distributions are symmetric Gaussians. As marked with a dashed line, the value of $W_0 = 4.8$ was chosen for further position reconstruction purposes, since it delivers the most narrow distributions for both, $x_{Si} - x_{log}$ and $y_{Si} - y_{log}$ distribution, while at the same time a negligible variation of the distribution's mean is observed if varying W_0.

Further Aspects

It has to be noted that in case of Fig. 3.16, absolute calibration of the position was already performed, for reasons of better comparability of $x-$ and $y-$ direction. Because of the expected linear response due to the logarithmic weighting technique, this absolute calibration though purely consists of a constant shift of the uncalibrated mean position provided by the tracking station. This shift Δx (Δy) has to be chosen to amount to the values provided in Tab. 3.4, effectively resulting in the mean position deviation in case of $W_0 = 4.8$ to be equal to zero for both performed runs. It has to be stressed that the distributions' width σ_x (σ_y), i.e. the position resolution, is wholly unaffected by the application of this shift. Correlations of reconstructed and

(a)   (b)
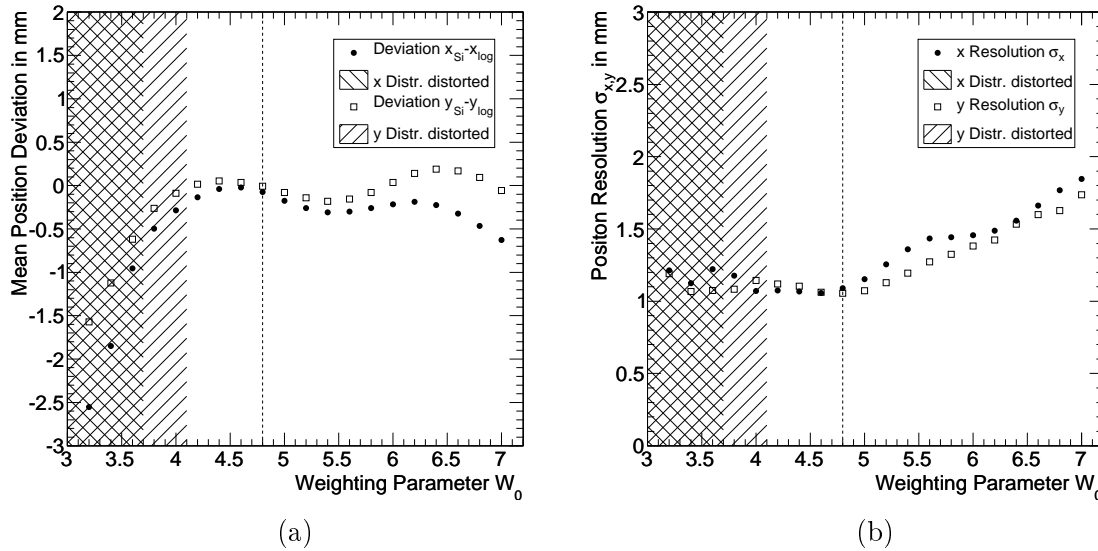
Figure 3.16: Deviation of the reconstructed positions x_{log}, y_{log} from the tracked positions x_{Si}, y_{Si} (a) and position resolution σ_x, σ_y (b) in dependence of the weighting parameter W_0. The shaded areas mark the regions, where the obtained position distributions are distorted. The weighting parameter value $W_0 = 4.8$, henceforth used for position reconstruction, is marked with a dashed line.

RUN	COOR-DINATE	VALUE IN mm
1	Δx	-5.994
	Δy	-24.215
2	Δx	-14.213
	Δy	-24.783
	$W_0 = 4.8$	

Table 3.4: Absolute position shifts applied for calibration of the absolute position values provided by the tracking station to the PROTO60 coordinate system in case of logarithmic weighting with $W_0 = 4.8$.

(a) Run 1.   (b) Run 2.
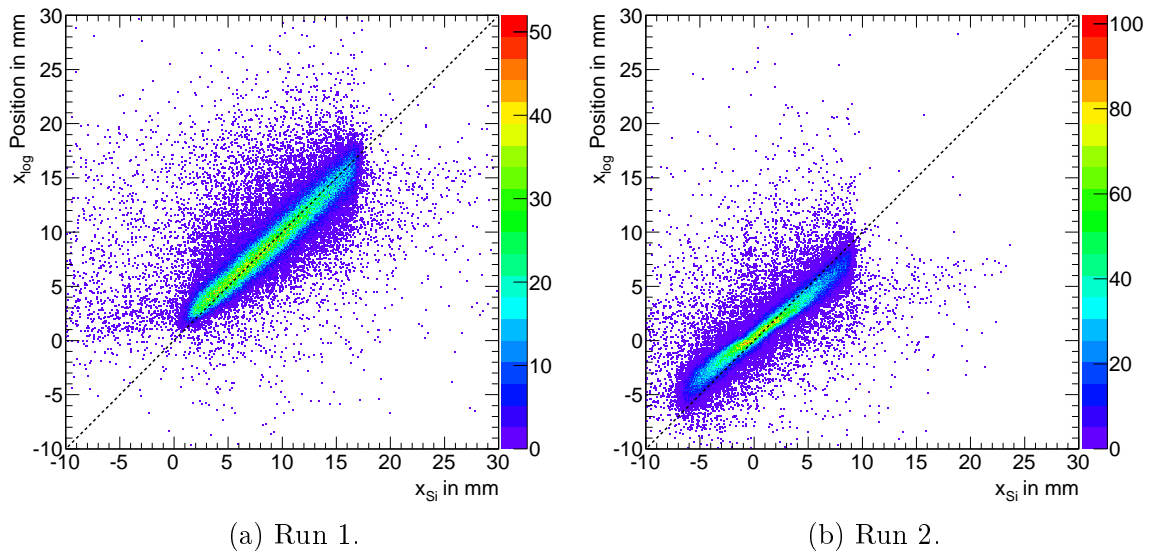
Figure 3.17: Position correlations in x-direction for both runs obtained with logarithmic weighting. The dashed line corresponds to a linear correlation of reference position x_{Si} and reconstructed position x_{log}.

(a) Run 1.   (b) Run 2.
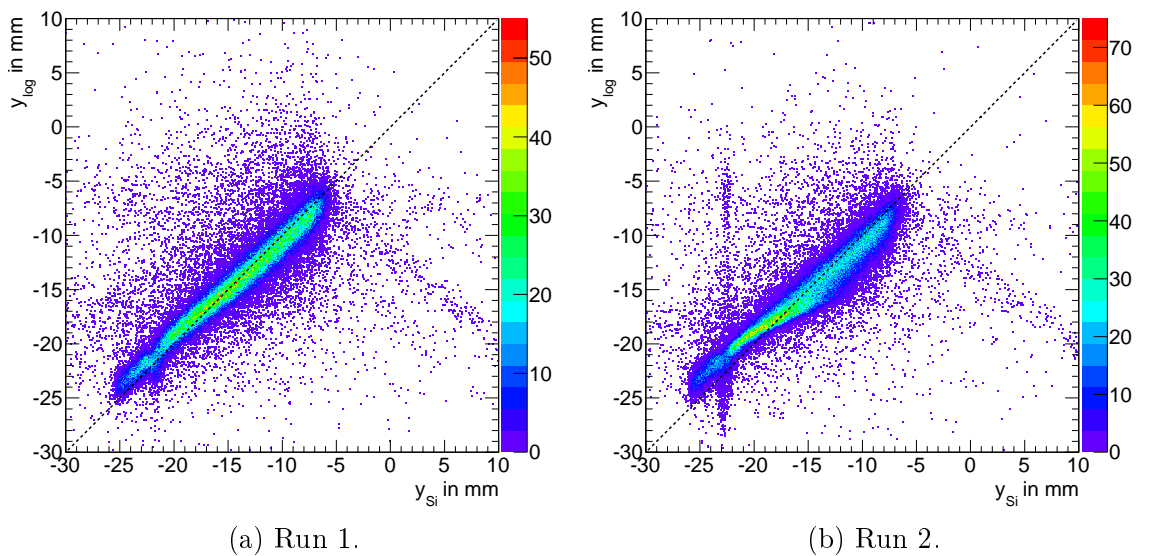
Figure 3.18: Position correlations in y-direction for both runs obtained with logarithmic weighting. The dashed line corresponds to a linear correlation of reference position y_{Si} and reconstructed position y_{log}.

126

reference position, obtained directly without application of further corrections, can be found in Fig. 3.17 and Fig. 3.18 for x-direction and y-direction, respectively. In case of run 1, a uniform linear correlation is observed for both coordinates, whereas in case of run 2 some minor distortions are visible. There for y-direction again a slight split into two branches is visible, as already seen in the correlation obtained with the S-curve correction technique. For a further investigation of this effect, the deviation of y_{log} from y_{Si} is plotted versus y_{Si} in Fig. 3.19c. Here the split is more pronounced. Its origin gets clearer if one investigates the same distribution under the condition that the largest energy deposition either was located in crystal 28 or in crystal 29. These distributions are displayed in Fig. 3.19a and Fig. 3.19b. With application of this cut, one of the branches disappears. This behaviour can be explained by the different location of the crystal centres and most likely more influential, their borders. Consequently, Fig. 3.19a and Fig. 3.19b depict different sections of the corresponding crystal. Thus, remaining bias inflicted by the crystal centre or borders has a different impact, showing as two separate branches in the overall spectrum represented by Fig. 3.19c. Despite the fact that no sophisticated correction was applied, other than the tuning of parameter W_0, the logarithmic weighting technique delivers satisfactory linearity and resolution over the whole region covered by the experiment, as will be presented in the following section.

3.4.4 Results

Overall Response

To allow for a direct comparison of the results obtained with both position reconstruction techniques, the relevant spectra were treated in a similar way. For determination of the overall position response during each of the two runs, where the beam centre was either located at the centre of crystal 28 (run 1) or at the junction between crystal 28 and crystal 29 (run 2), the deviation of the reconstructed position from the reference position was histogrammed. The resulting distributions are depicted in Fig. 3.20 and Fig. 3.21 for the S-curve correction technique and the logarithmic weighting technique, respectively. A Gaussian is fitted to each distribution to extract mean position deviation and position resolution. The obtained parameters for both techniques are collected in Tab. 3.5. The errors of these values, as given by the fitting routine, were below 0.01 mm in all cases and have therefore been omitted from the table for the sake of clarity. Regarding the mean position deviation, one observes that the logarithmic weighting technique shows values close to zero, while for the S-Curve correction technique, variations around zero up to approximately 1 mm are present. This can be attributed to the more complex procedure of calibration of the absolute position value. However, regarding the position resolution in case of run one, where the 15 GeV positron beam centre was located near the centre of crystal 28, both techniques achieve
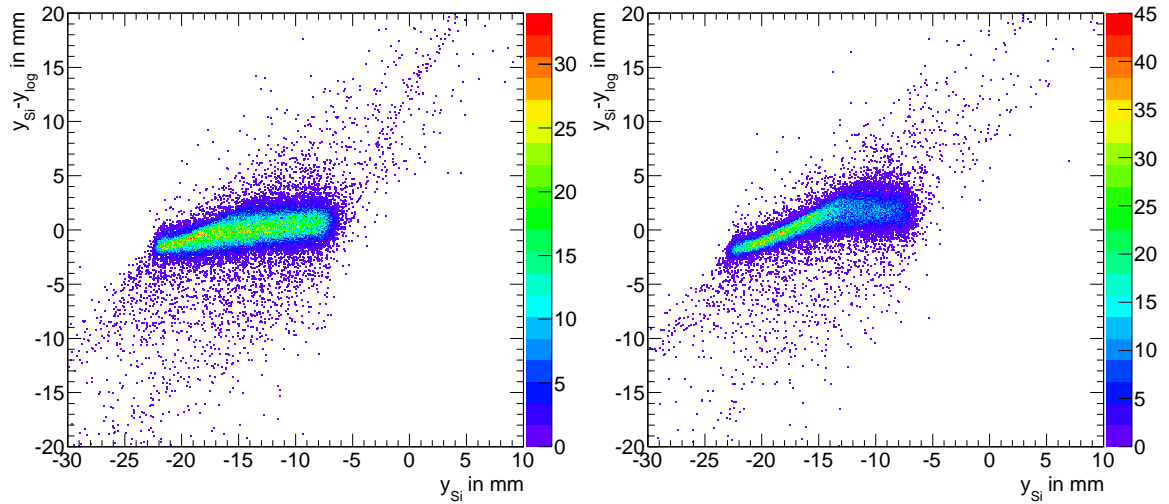
(a) Cut on largest energy deposition in crystal 28.

(b) Cut on largest energy deposition in crystal 29.
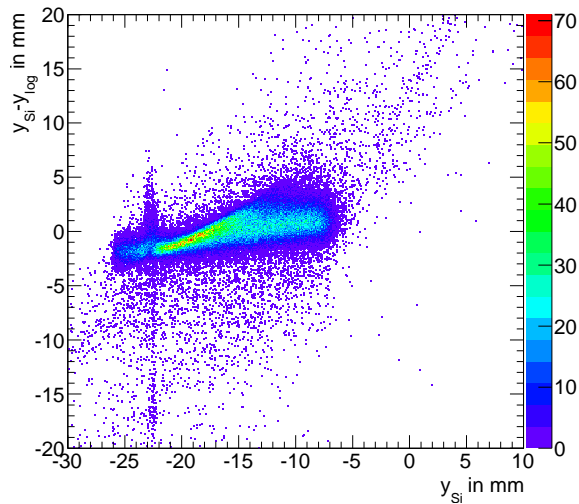
(c) No Cut.

Figure 3.19: Position deviation $y_{Si} - y_{log}$ in dependence of the reference position y_{Si} for three different conditions. Apparently, the two branches in (c) belong to the different cases of maximum energy deposition either inside crystal 28 or crystal 29, whose centre coordinates and borders are at different heights y.
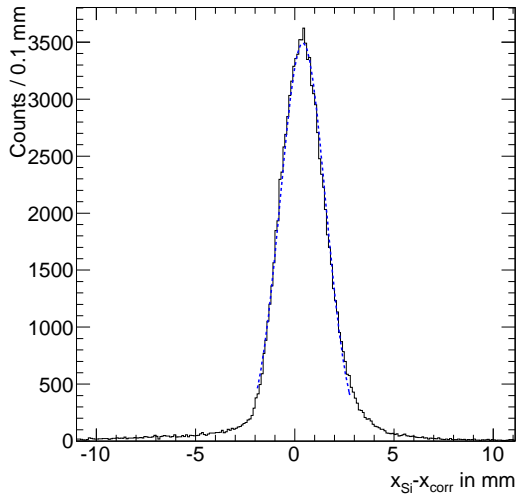
(a) Run 1.
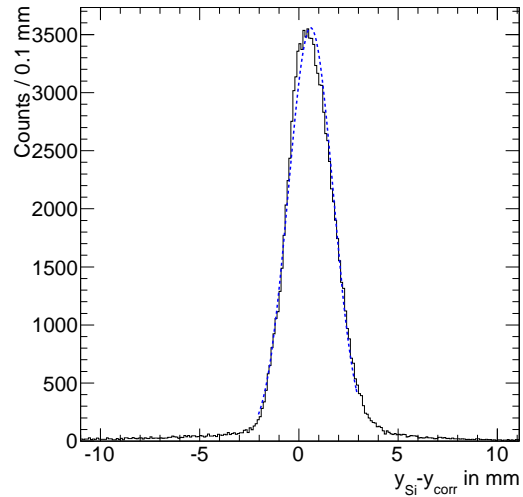
(b) Run 1.
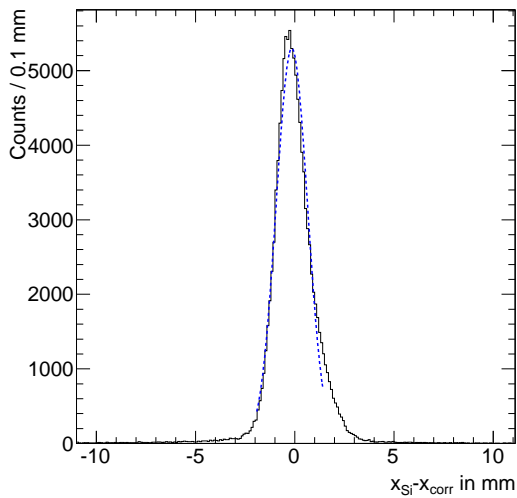
(c) Run 2.
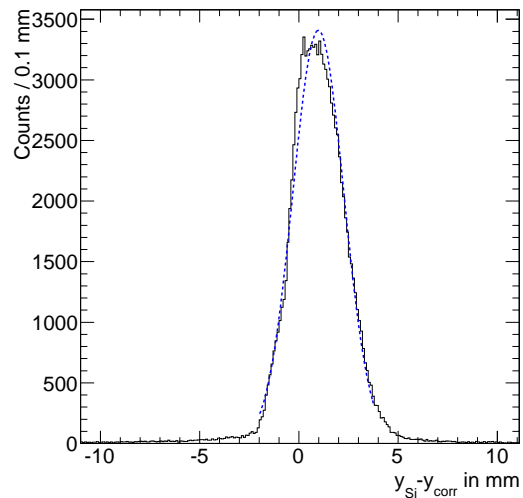
(d) Run 2.

Figure 3.20: Overall position deviation distributions obtained with the S-curve correction technique. Mean and position resolution were determined by a Gaussian fit to the distributions (dashed blue line). The extracted parameters are collected in Tab. 3.5.
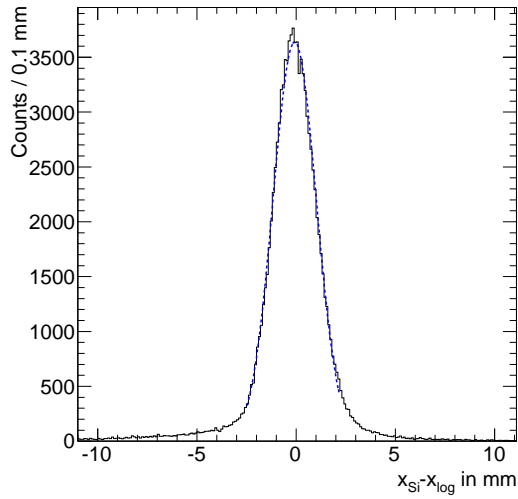
(a) Run 1.
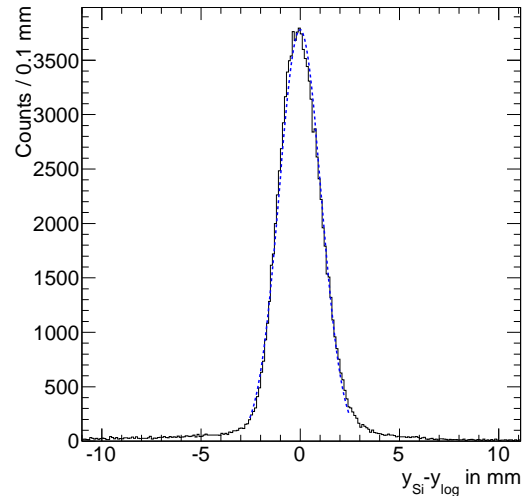
(b) Run 1.
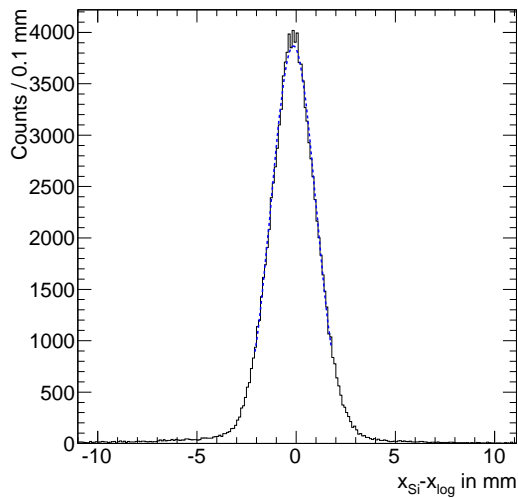
(c) Run 2.
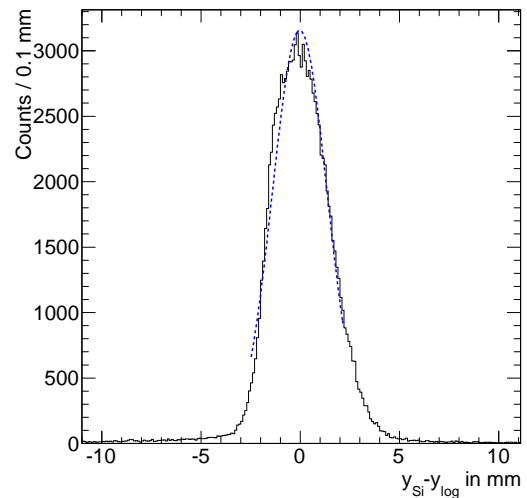
(d) Run 2.

Figure 3.21: Overall position deviation distributions obtained with the logarithmic weighting technique. Mean and position resolution were determined by a Gaussian fit to the distributions(dashed blue line). The extracted parameters are collected in Tab. 3.5.

15 GeV Positron Beam				
RUN	CORRECTED LINEAR WEIGHTING			
	$\langle x_{Si} - x_{corr} \rangle$	σ_x	$\langle y_{Si} - y_{corr} \rangle$	σ_y
1	0.41	1.14	0.60	1.13
2	−0.15	0.79	0.98	1.29
	LOGARITHMIC WEIGHTING			
	$\langle x_{Si} - x_{log} \rangle$	σ_x	$\langle y_{Si} - y_{log} \rangle$	σ_y
1	−0.08	1.09	−0.01	1.05
2	−0.14	1.13	−0.03	1.38
	All values in mm			

Table 3.5: Overview of overall mean position deviation and position resolution for both reconstruction techniques, extracted by Gaussian fits to the distributions shown in Fig. 3.20 and Fig. 3.21.

a comparable value for both, x- and y-direction, of about $\sigma_x \approx \sigma_y \approx 1.1\,\text{mm}$. In case of positioning of the beam centre at the junction between crystal 28 and crystal 29, i.e. run 2, the x_{corr} resolution achieved with the S-curve correction technique, improves even further to $\sigma_x \approx 0.8\,\text{mm}$. In case of logarithmic weighting, no significant change of the overall resolution is observed. However, the overall y-position resolution obtained for run 2 is about $0.2 - 0.3\,\text{mm}$ worse than the result achieved for run 1. This is most likely caused by the observed split in the position correlations (see Fig. 3.15b and Fig. 3.18b), whose origin has been discussed in the previous section.

Position Dependent Response

Also the position dependence of the response for both applied reconstruction techniques was evaluated with similar procedures. Whereas the overall position deviation distributions were obtained over the complete range of available reference positions, to investigate the position dependence of each technique's position response, the deviation from the reference position $x_{Si} - x_{corr}$ ($x_{Si} - x_{log}$), was divided into slices of $0.5\,\text{mm}$ along x_{Si}. The resulting distribution for each slice in x_{Si} was then fitted by a Gaussian distribution. The extracted fit parameters, namely mean deviation and position resolution plotted versus the position of the centre of the chosen slice in x_{Si} are depicted in Fig. 3.22 for both reconstruction techniques. Data from each of the runs is included, as marked in the corresponding legend. For better orientation, crystal borders are marked with narrow shaded areas.

(a)

(b)

(c)

(d)
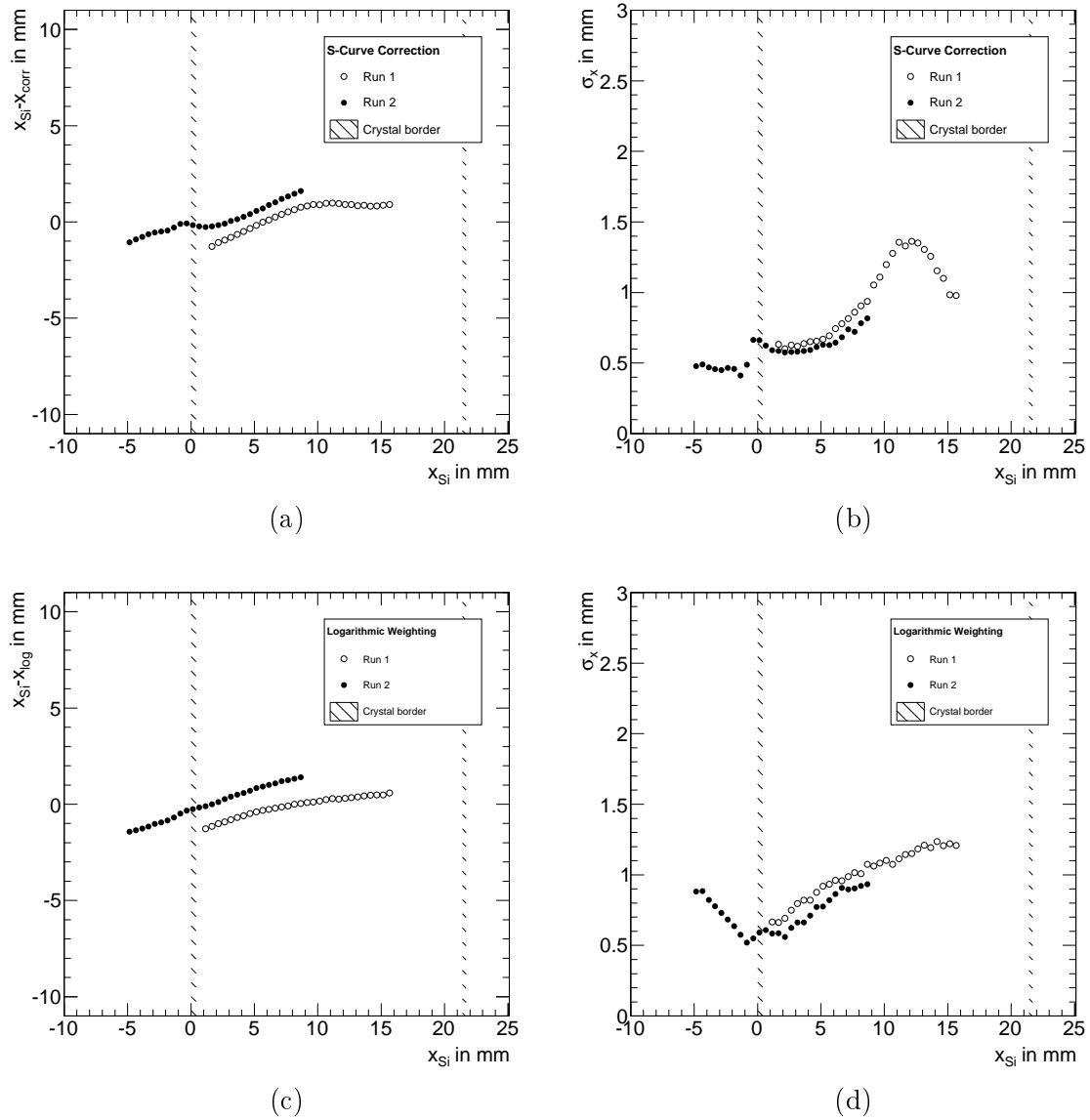
Figure 3.22: Dependence of x-position deviation and position resolution on the incident position obtained with the S-curve correction technique (a-b) and logarithmic weighting technique (c-d). Crystal borders are indicated by shaded areas.

Inspecting first the linearity of the x-position response (see Fig. 3.22a and Fig. 3.22c), for both techniques, two peculiarities are recognisable. On the one hand, a shift of the order of $1\,\text{mm}$ between the data attributed to the different runs is visible, reflecting the uncertainty in the calibration of the absolute position value. In both cases, it was performed with regard to the centre of the position distributions in the separate runs, which indeed show a similar deviation close to zero. On the other hand, either position deviation is not completely independent of the incident position x_{Si}, hinting at a remaining bias in the reconstructed position. Both reconstruction techniques show the same behaviour though, implicating a possible relation to the complex PROTO60 geometry and the limitations imbued by the projection plane approximation. Nevertheless, the extent of these variations is comparable with the overall position resolution. Regarding the position dependence of the resolution, with which the x-position can be reconstructed in PROTO60, S-curve correction technique and logarithmic weighting both deliver best resolutions of down to $\sigma_x = 0.5\,\text{mm}$, if the incident positron enters at the crystal borders, as shown in Fig. 3.22b and Fig. 3.22d, respectively. In this case, the energy deposited by the electromagnetic shower is more equally distributed inside the matrix, and bias due to disproportionately high weight of a single crystal is avoided. Consequently, worst resolution is achieved near the crystal centre, where S-curve correction delivers $\sigma_x \approx 1.4\,\text{mm}$, while the upper limit with logarithmic weighting is a resolution of $\sigma_x \approx 1.3\,\text{mm}$. Also the resolution curve gradient near the crystal centre is slightly less for the latter technique and artefacts at the crystal junction region appear dampened, making the x-position determination by logarithmic weighting slightly more uniform.

A completely analogous procedure was performed for y-direction. The corresponding spectra are displayed in Fig. 3.23. Here, regarding the linearity of the y-response, depicted in Fig. 3.23a and 3.23c, the shift observed between the curves attributed to different runs is less pronounced than the case in x-direction. This is understandable, since the nominal y-position of the beam was not varied between the two performed runs. Nevertheless, also here a remaining bias can be observed, which is more strongly pronounced for run 2, where the shower is distributed over a larger number of crystals. Since the approximations made in the coordinate system are less accurate for the outermost crystals of the matrix, this supports the assumption that the aforementioned remaining bias indeed is caused by them. Furthermore, the small fluctuation caused by the crystal border is located at different x_{Si}, which can be explained by the different height, at which the borders are located in the two runs (see also Fig. 3.8). Also the y-resolution achieved with the S-curve (see Fig. 3.23b) is worst at the crystal centre, where it amounts to $\sigma_y \approx 1.3\,\text{mm}$, while it improves down to a value of $\sigma_y \approx 0.5\,\text{mm}$ at the crystal borders. The resolution curve shape is comparable for both runs. However, for run two, the maximum resolution variation observed is slightly larger. In addition, a fluctuation at the crystal junction region is visible, which can be explained by high probability for shower leakage effects due to the conjuncture of four crystal corners, not

(a)

(b)

(c)

(d)
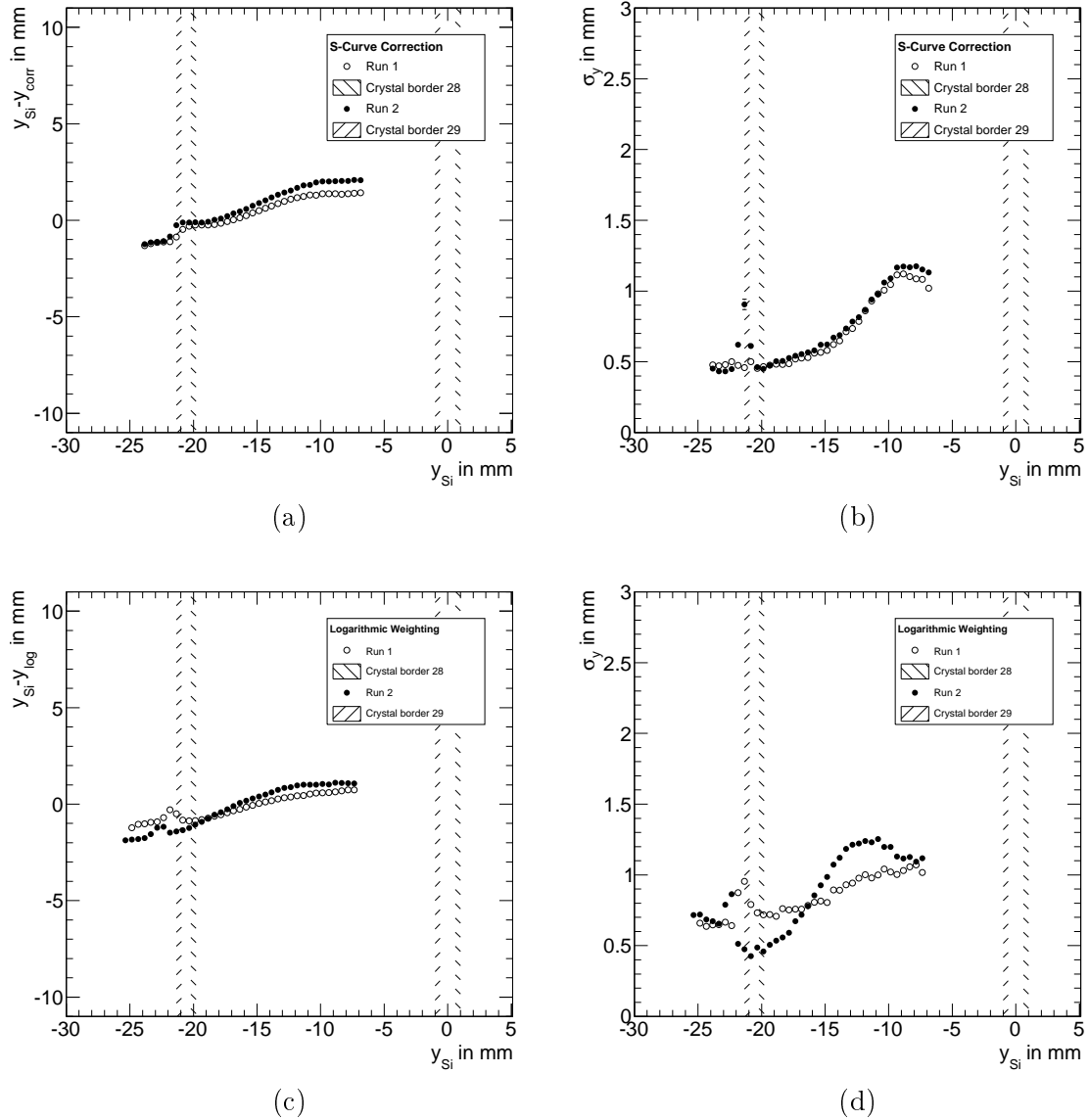
Figure 3.23: Dependence of y-position deviation and position resolution on the incident position obtained with the S-curve correction technique (a-b) and logarithmic weighting technique (c-d). The borders of crystal 28 and crystal 29, which are located at different heights y, are indicated by shaded areas.

present in case of run one. That this geometrical difference has an considerable effect can also be observed in Fig. 3.23d, which shows the y-position resolution obtained with the logarithmic weighting technique. Here the resolution achieved for run 1 shows significantly less variation between the crystal centre resolution of $\sigma_y \approx 1.1\,\text{mm}$ and the crystal border resolution amounting to $\sigma_y \approx 0.7\,\text{mm}$, than the case for run 2. There, similar values as for S-curve correction technique are observed. This dampening of the variations in the run 1 response may be a result of the crystal staggering, which helps to avoid energy leakage at the junction of crystal 28 and its lower neighbour, crystal 36. Nevertheless, there are still fluctuations of the resolution curve in the crystal border regime.

3.5 Position Dependence of the Energy Resolution

With availability of an independent position information provided by the tracking station, an investigation of position dependence of the energy resolution achievable with PROTO60 was possible. A typical line shape of the reconstructed energy, as depicted in Fig. 3.24a, shows a tailing to lower energies, which is more strongly pronounced if the incident particle initiating the electromagnetic shower enters the detector at positions close to the crystal border. Therefore, to extract the appropriate cluster energy and energy resolution, a fitting function is necessary which accommodates for this tailing adequately. Consensus throughout the $\overline{\text{P}}\text{ANDA}$ collaboration to obtain a comparable energy response is the usage of the Novosibirsk function, as expressed in Eq. 3.11:

$$f(E) = A e^{-\frac{\ln\,[1-\Lambda\tau(E-E_0)]^2}{2\tau^2}+\tau^2}, \tag{3.11}$$

$$\Lambda = \frac{\sinh\,(\tau\sqrt{\ln 4})}{\sigma\tau\sqrt{\ln 4}}. \tag{3.12}$$

Beside amplitude A, peak position E_0 and width σ it includes an additional parameter τ describing the tailing. Furthermore it has the advantage that, despite the asymmetry, the FWHM of the function is related to σ by $\sigma = \frac{\text{FWHM}}{2.35}$, as is the case with a Gaussian distribution. To obtain a reasonable compromise between a sufficiently large number of events available for parameter extraction and a precise localisation of the incident particle position, the beam size was restricted to a circular area with 4 mm diameter. This was achieved by accepting only events, where the reference position provided by the tracking station was within a radius $r = \sqrt{x_{Si}^2 + y_{Si}^2}$ of 2 mm. As indicated in Fig. 3.25, starting at the centre of crystal 28, the beam centre was moved in steps of 1 mm distance towards the crystal border. This procedure was performed in x- and y-direction, respectively. Cluster energy peak and relative energy resolution $\frac{\sigma}{E}$ extracted from a Novosibirsk fit to the corresponding line shape

(a)   (b)
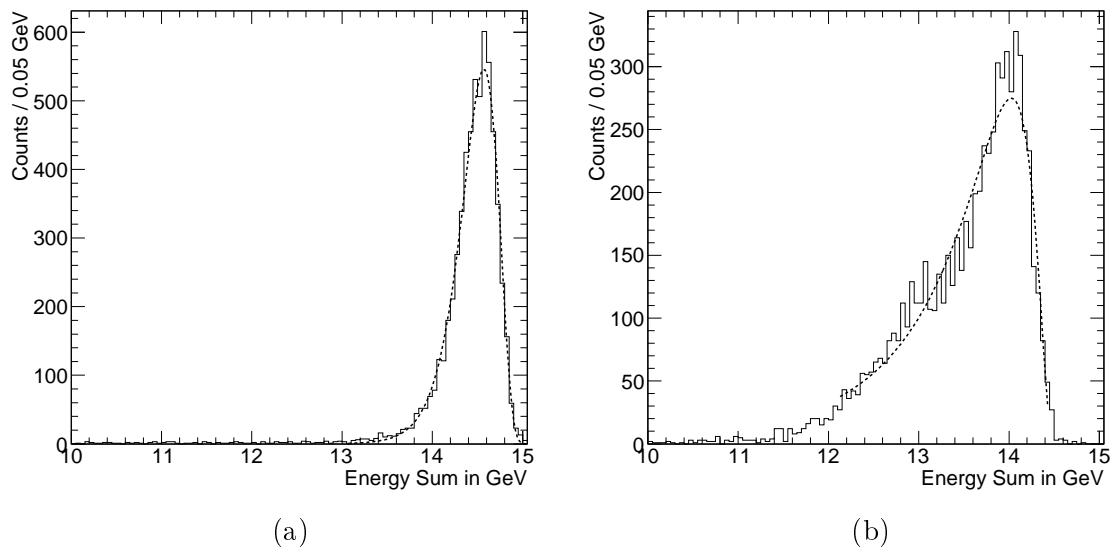
Figure 3.24: Typical line shape of the reconstructed cluster energy for a 15 GeV positron beam located either at the centre of crystal 28 (a) or at its border. In addition, the Novosibirsk function fit to extract cluster energy and resolution is drawn with a dashed line.
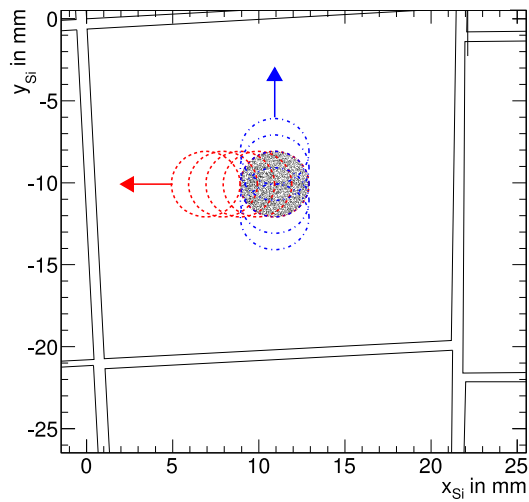
Figure 3.25: Restriction of the beam size to 4 mm diameter achieved by a cut on the reference position (x_{Si}, y_{Si}) provided by the tracking station. Beginning at the centre of crystal 28, the beam centre was successively shifted in steps of 1 mm to the crystal borders, either in x- or y-direction.

in dependence of the deviation of the beam centre to the crystal centre are displayed in Fig. 3.26. During determination of the cluster energy, the single crystal energy threshold was set to $1\,\mathrm{MeV}$. In case of the spectra concerning x-deviation, namely Fig. 3.26a and 3.26b, data from two runs was used to increase the range of available beam centre positions. The observed step between the reconstructed energy between the points belonging to either run, is most likely caused by a slightly different angle of inclination of the incoming particles with respect to the PROTO60 symmetry axis due to movement of the crystal matrix. Otherwise, the energy response is uniform and no significant x-position dependence of the reconstructed peak energy is observed. In contrast to the observation made while inspecting position resolution, the energy resolution is best if the incident positron enters the detector at the crystal centre. In this case, energy containment is nearly complete and an excellent relative energy resolution of $\frac{\sigma}{E} = 1.43 \pm 0.02\,\%$ is achieved. However, at the crystal border, where the energy containment is reduced due to energy leakage at the crystal junctions, the resolution is deteriorated up to a value of $\frac{\sigma}{E} = 3.15 \pm 0.06\,\%$. Also for deviations in y, the peak energy extracted for different beam centre positions is uniform (see Fig. 3.26c). In case of the extracted resolution, a picture comparable to the x-deviation scenario is observed, with the same resolution achieved at the centre of the crystal. However, the deterioration of the resolution on the crystal border region is less, amounting only to $\frac{\sigma}{E} = 2.39 \pm 0.08\,\%$. This effect is most likely a consequence of PROTO60's adjustment relatively to the beam direction. As described in Sec. 3.4.1, beam direction and symmetry axis of PROTO60 were congruent. Thus, particles entering at incident position (0,0) theoretically are able to traverse the prototype facing only a minimum amount of material budget, since they are passing in between adjacent crystals. If only one of both coordinates is equal to zero, corresponding to a x deviation of around $-11\,\mathrm{mm}$, still a high amount of leakage can be expected at the crystal gap. This manifests in the significant resolution deterioration observed in Fig. 3.26b. Because in case of Fig. 3.26d the crystal border is located at a position, where both coordinates are different from zero, beam direction and crystal axis orientation are not parallel. Furthermore, crystals are staggered in y-direction. Thus, the passage of positrons through the gaps in between crystals is avoided and energy leakage effects are reduced. This results in the smaller deterioration of the energy resolution observed for y-deviation from the crystal centre.

(a)

(b)

(c)

(d)
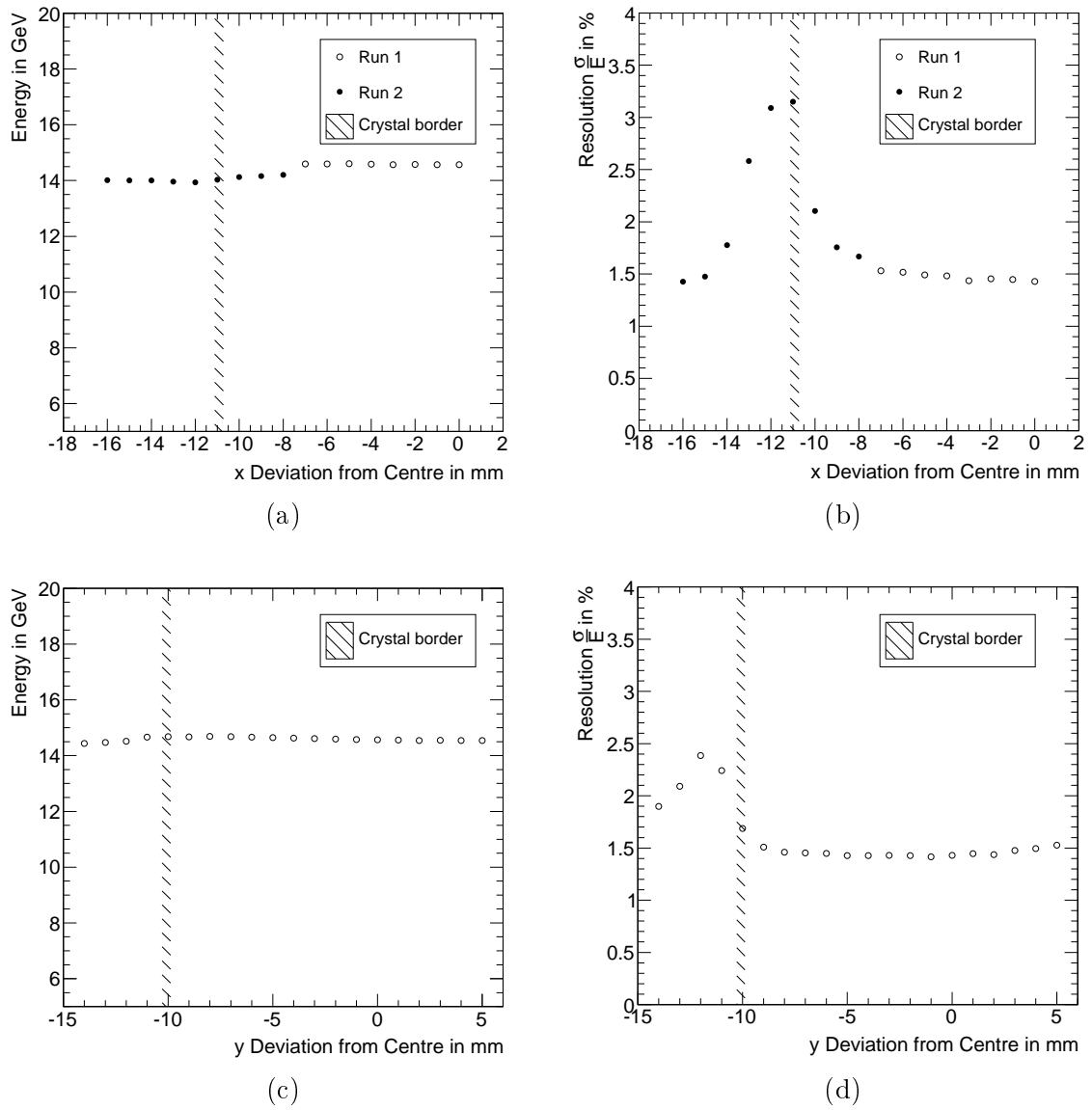
Figure 3.26: Dependence of cluster peak energy and relative energy resolution resolution in dependence of the deviation from the crystal centre. For cluster energy determination, a single crystal threshold of $1\,\mathrm{MeV}$ was used.

Chapter 4

Discussion and Outlook

Reflecting the two main topics investigated within the scope of this work, the following chapter is segmented into two main sections. Sec. 4.1 is covering LY NUFs and entailing position dependencies of the energy response to different particle species, while Sec. 4.2 focuses on position reconstruction and position dependencies in the response of a matrix comprised of sixty individual detectors, namely the $\overline{\text{P}}$ANDA Barrel EMC prototype PROTO60.

4.1 Light Collection NUFs

Related to the fact that the PWO crystals comprising Barrel EMC and FEC are of tapered geometry, the measured LY is depending on the distance of the location of energy deposition to the photo sensor, as indicated schematically in Fig. 2.1. Such effects have already been observed in case of lead tungstate crystals used in the CMS-ECAL. Within the scope of this work, this so called LY NUF has been investigated for PWO-II crystals with $\overline{\text{P}}$ANDA geometry with the help of SLitrani simulations, as well as dedicated experimental setups. Measurements of non-uniform response to minimum ionising cosmic rays, i.e. muons, low energetic 511 keV γ-rays originating from a ^{22}Na-source and 80 MeV protons were successfully performed. In addition, investigations regarding a possible uniformisation procedure were carried out. In the following, the obtained results of simulation and experiments will be discussed successively.

4.1.1 NUF Characterisation

Comparison of Simulation and Experimental Results

First experimental evidence of this so called LY NUFs in case of PWO-II crystals with $\overline{\text{P}}$ANDA geometry, could be observed in the LY measurements performed during

QC, as described briefly in Sec. 2.3.1. A detailed description of the QC procedure can also be found in [34]. The obtained shift of the measured absolute mean LY for an individual geometry, displayed in Fig. 2.23, is correlated to the mean tapering angle μ, as defined in Eq. 2.2. However, to attain an elaborate understanding of this correlation, depicted in Fig. 2.24d, the SLitrani simulation package (see [27, 28]), dedicated for studies of light propagation in anisotropic and birefringent media like PWO, was used. The simulation setup represented closely to the experimental situation present in the precision setup and the implementation of the corresponding optical parameters was based on experimental evidence, as explained in Sec. 2.2.1. As an outcome, the LY dependence on the distance to the photo sensor shown in Fig. 2.15a was obtained. For each geometry type, the NUF can be parametrised by a second order polynomial. The parameter a extracted from fit, which represents the constant term and describes the absolute LY at zero distance from the photo sensor, is roughly the same for each geometry type. In case of the untapered EC-R geometry, a LY equal to a is observed over the complete crystal length. Thus all information on the NUF is included in the parameter Π, combining the higher order parameters b and c of the second order polynomial. Indeed for simulation a linear correlation of the NUF parameter Π and mean tapering angle μ has been observed. Another comparison of a crystal's NUF is achieved by regarding the response normalised to the position closest to the photo sensor. Since the shape is known to be a monotonically increasing curve, the maximum normalised LY R_{LY} at the crystal front represents a criteria for its level of NUF. Especially for comparison to experimental data, where additionally influences due to quality variations have to be taken into account, the maximum relative LY R_{LY} proves to be a more simple and robust indicator, although less sophisticated than the fit method. The measurements performed with the so called precision setup (see Sec. 2.3.2) aimed at an experimental characterisation and comparison of the position dependent response to both, minimum ionising comic rays and low energetic γ-rays. The results obtained at a temperature of $-25\,°\mathrm{C}$, are shown in absolute values in Fig. 2.33 and 2.34a, for minimum ionising muons and $511\,\mathrm{keV}$ photons, respectively. In agreement with simulation, the observed NUF is scaling with the degree of tapering and the curve shape can be described adequately with a second order polynomial. The exact values of the fit parameters though, as well as the deduced parameter Π, are deviating from the simulated values. If regarding the R_{LY} values for each type, consistently lower values than the case in simulation are obtained. For type 1 for instance, the experimentally obtained R_{LY} amounts to roughly 1.6, while simulations yield a value of approximately 2.1 (compare Fig. 2.34b and Fig. 2.15b). The fact that the NUF appears to be damped in experiment compared to simulation, is mainly related to two properties of the PWO-II crystals, which are not included in simulation. First, as indicated by the photograph in Fig. 4.1a, there are chamfers at the crystal edges. Their specified roughness of about $\lesssim 0.5\,\mu\mathrm{m}$ is significantly higher than the roughness of the crystal faces. Due to the introduction of this additional small surfaces with different inclination and larger roughness, which on

<div align="center">(a)   (b)</div>
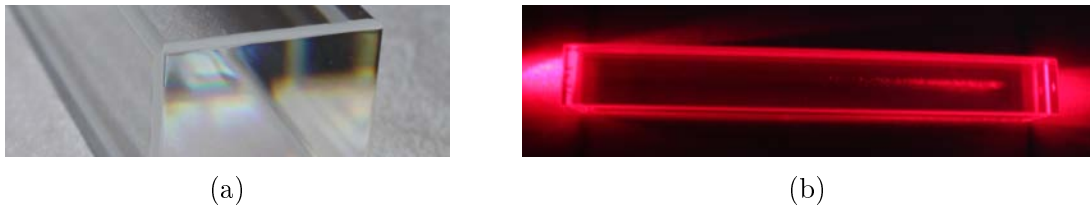
Figure 4.1: Additional aspects influencing light propagation inside a crystal. Shown are the chamfers at the crystal edges (a) and an example for macro defects in the crystal structure, visualised by scattered light originating from a laser pointer (b). Both aspects lead to a reduction of the NUF in comparison to simulations.

average represent approximately $5\,\%$ of the crystal surface, a more diffusive reflection pattern can be expected. In turn this leads to a reduction of totally reflected light and thus a reduction of the NUF. Secondly, macro-defects inside the crystal, which are related to the growing process, lead to additional elastic scattering of the scintillation light. That these macro defects, depending on the individual crystal quality, indeed can significantly influence light propagation through a crystal, is shown exemplary in Fig. 4.1b. Here, red light originating from a laser pointer is shining longitudinally through a crystal of EC-R geometry. In the right half of the crystal volume light is scattered partly outside the crystal by the mentioned defects, making them visible to the eye. Also this effect can only lead to a reduction of the measured NUF, since the initial emission angle of the scintillation photon is diffused. Despite the described discrepancies in the observed maximum NUF, the performed SLitrani simulations deliver a satisfactory description of the curve shape and are an important tool to evaluate the NUF to be expected for geometry types not measured. Another important aspect studied within the SLitrani simulations is the distribution of the generated scintillation light over the crystal rear face, where the photo sensor is located. For the two extreme cases of type 1 and EC-R geometry, consistently a homogeneous distribution of the scintillation light over the complete end face is observed, if the energy deposition is located at distances from the photo sensor larger than one third of the crystal length. This is in particular important, because most of the crystals of the EMC will be read out by LAAPDs, which do not cover the complete crystal rear face. In addition, the two LAAPDs are not placed symmetrically with respect to the centre of area. However, the centre of gravity of the electromagnetic shower is, according to Tab. 1.2, located in the front half of a crystal even at the highest expected energies. Hence, based on the simulation results, a homogeneous illumination of the readout face is also guaranteed during operation in the EMC and the LAAPD readout should not be affected. Nevertheless, to exclude possible inhomogeneities due to the influence of the mentioned chamfers, an experimental validation would be beneficial.

Response to Different Particles

The measurements performed with the precision setup allowed for the first time a direct comparison of position dependent response to cosmic muons and 511 keV photons. Fig. 2.36 summarizes the normalised response at $-25\,°C$ to both particle species for the two extreme cases of type 1 and type EC-R geometry. Within the uncertainties, the same curve shape and maximum relative LY R_{LY} are observed for both, although the individual mechanism of energy deposition as well as the distribution of scintillation light are different. Furthermore, also the mean energy deposition in case of the cosmic ray curve is roughly a factor 50 larger than in the photon case. As a conclusion, it can be stated that the observed NUF is independent of mechanism and amount of energy deposition. However, in the case of cosmic muons, it has to be stressed that if no pathlength correction is applied, the obtained response is indeed nearly uniform. Then the intrinsically lower response near the photo sensor is compensated NUF is outweighed by the higher amount of energy deposited due to the higher crystal thickness and the entailing higher MIP pathlength. In turn, the opposite holds true at the crystal front. Despite normalised uncorrected response for type 1 and type EC-R are therefore comparable, the average absolute response measured for type 1 is larger, as displayed in Fig. 2.33. Since a pre-calibration with cosmic muons is foreseen for the complete EMC and was already applied to measurements with prototypes, e.g. PROTO60, knowledge of the described behaviour is essential for a correct calibration procedure. Details on the calibration procedures regarding PROTO60, including influences of the NUF, can be found in [42]. Also the response measurements to 80 MeV protons, which were performed at room temperature for type 1 and 6 crystals, deliver results comparable to the precision setup measurements, regardless of the use of one single or two LAAPDs. This is another indication that a crystal's NUF is unaffected by the amount of energy deposited, as well as the exact mechanism. Also a change of the position of the photo sensors relatively to the side, where the proton beam impinged, achieved by a rotation of the crystal, shows no significant influence on the obtained NUF at larger distances to the photo sensor. At distances below approximately 5 cm though, if regarding a single LAAPD, small fluctuations can be observed. This observation can be regarded as a confirmation of the above mentioned simulation result, stating a homogeneous illumination of the rear face for distances above one third of a crystal length.

Comparison to Other Experiments

Within the $\overline{P}$ANDA collaboration, additional experiments regarding LY NUFs of pre-production crystals for the EMC, with a setup deploying 511 keV photons have been performed in parallel. The results, which are described in [44] and [45] for measurements at $5°$ and $-25°$ temperature, respectively, show a comparable normalised re-

sponse as the results achieved within the scope of this work. Deviations in the absolute LY can be explained on the one hand by the different temperature and the usage of a VM2000 instead of a Teflon wrapping. On the other hand, the coupling in case of the precision setup is known to be worse as the case with the high rate setup (see Sec. 2.3.2 for detailed explanation), where similar absolute values have been achieved. Comparing the NUFs observed for PWO-II of $\overline{P}$ANDA geometry to the results obtained by the CMS-ECAL collaboration for previous PWO generations, some differences become apparent. In case of the 23 cm long CMS crystals a distinction of front and rear NUF is performed, as described in [46]. The reason for this lies in the different shape observed in LY dependence on the distance to the photo sensor. For a typical CMS crystal, the LY shows a minimum located near to the half length of a crystal. Moreover, if regarding crystals from early production lots, a completely reversed curve shape can be observed, with the LY maximum located near the photo sensor [47]. On the contrary, for final CMS production quality, a shape comparable to the NUF curve obtained with $\overline{P}$ANDA crystals are obtained. This behaviour can be explained by the interplay of absorption and focussing effect inside the lead tungstate crystals. As an example, Fig. 4.2 shows a plot of the NUF parametrisation determined for a type 6 $\overline{P}$ANDA crystal, taken from Tab. 2.7. For demonstration purposes, the minimum LY at zero distance to the photo sensor has been set to a higher value of $a = 37\,\mathrm{MeV}$ in comparison to the measurement. In addition, Fig. 4.2 depicts the resulting NUF curves if an additional absorption with an absorption coefficient of $2.66 \cdot 10^{-3}\,\frac{1}{\mathrm{cm}}$, $2.66 \cdot 10^{-2}\,\frac{1}{\mathrm{cm}}$ or $1.33 \cdot 10^{-1}\,\frac{1}{\mathrm{cm}}$, associated with the final, intermediate and worst crystal quality, is included. This is achieved by multiplication with the overall transmission including total reflections and absorption according to Eq. 2.21. The corresponding response including solely this absorption effects and an assumed uniform LY, i.e. no focussing effect, are plotted in addition (coloured dashed lines). Two main conclusions can be drawn from Fig. 4.2: The first is that the discrepancies in the NUF curve shape are related to the higher absorption present in case of CMS, which becomes even more pronounced because of the 3 cm larger crystal length. Apparently, comparable NUF could be obtained in case of $\overline{P}$ANDA crystals, if absorption inside the crystal is increased. Secondly, it can be recognised that, if absorption is increased only slightly, NUF curve shape is hardly changed, but an decrease of the maximum relative deviation can be observed. This is in agreement with the considerations that in comparison to simulation, additional absorption or light scattering results in a damped NUF. Another implication of Fig. 4.2 is that also additional absorption induced by radiation can affect the NUF distinctly. An experimental investigation of these effects in conjunction with monitoring tests could help to guarantee the long-time stability and linearity of the EMC's energy response.
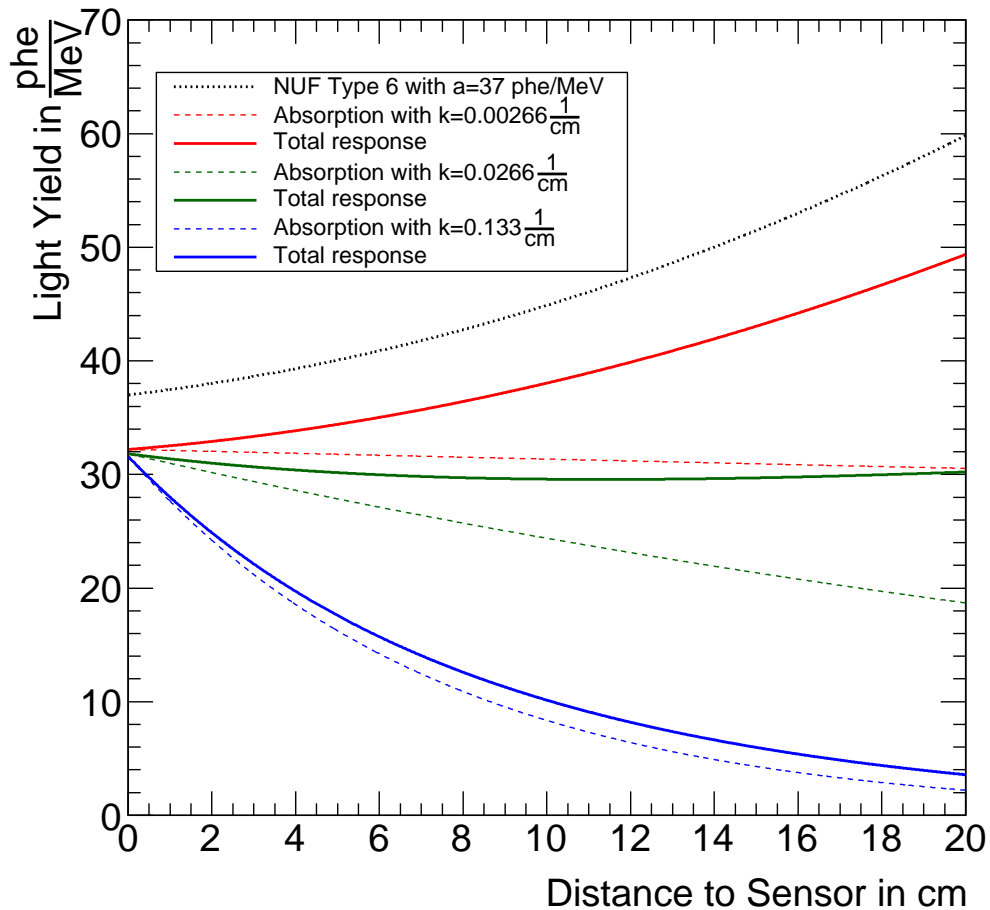
Figure 4.2: NUF parametrisation for a type 6 crystal of $\overline{P}$ANDA geometry taken from Tab. 2.7. The influence of distinct levels of additional absorption, representing different generations of PWO crystal quality, as observed during crystal production for the CMS-ECAL, is calculated according to Eq. 2.21 and plotted (coloured dashed lines). In addition, the obtained total response resulting from the combination of absorption and type 6 NUF curve is shown.

4.1.2 Light Yield Uniformisation

Because of the comparatively long time required for a measurement cycle with the precision setup, another setup, featuring a more compact design enabling more efficient cooling and operating at higher rates, was developed. The measurement series performed with this so called high rate setup investigated uniformisation methods by either wrapping or crystal surface modification. In parallel, uniformisation methods using deposits on the crystal surface, e.g. white paint, were performed by other members of the $\overline{\text{P}}$ANDA collaboration, as described in [45]. A comparison of the effect of different homogeneous wrappings on a crystal's NUF is presented in Fig. 2.39a. No effect on the NUF curve beside a constant shift was observed, regardless whether specular (VM2000) or diffusive wrapping (Teflon) is applied. Even when applying no wrapping at all, the NUF curve shape is unaffected. Furthermore, it is observed that indeed half of the light generated in the crystal is propagated to the photo sensor via internal reflection. This is a clear indication, that the NUF is mainly a consequence of the high amount of total internal reflection. Consistently, also the experiments performed with partial wrapping cutouts or modifications, as indicated in Fig. 2.40 showed no significant change in the NUF curve shape. An alternative approach pursued with tapered non-$\overline{\text{P}}$ANDA geometry crystals, originally foreseen for the proposed Photon Ball at ANKECOSY, included partial and complete roughing of one crystal surface. The roughness achieved with manual emery polishing was determined via AFM measurements to vary between $0.1\,\mu\text{m} \leq R_a \leq 0.6\,\mu\text{m}$. This is a factor 5 to 30 larger roughness than the maximum R_a specified for the $\overline{\text{P}}$ANDA crystals. A comparative measurement of the same crystals before and after emery polishing was performed. The results for absolute and normalised position dependent response are depicted in Fig. 2.45a and Fig. 2.45b, respectively. Best uniformisation was achieved by roughing of the rear third of one crystal side face. This procedure has been proven to half the relative LY deviation at the crystal front, while conserving the same absolute LY at the position closest to the PMT. However, it has to be considered that, although the investigated crystal's geometrical shape roughly resembles the $\overline{\text{P}}$ANDA geometry, they are only $12\,\text{cm}$ long. Thus especially the exact influence of the roughing procedure on $\overline{\text{P}}$ANDA crystals could be different. Nevertheless, as an overall conclusion concerning the investigated uniformisation methods, one can state, that wrapping modifications only are able to influence the absolute amount of light collected, while by roughing of one crystal side face a reduction of the NUF is achieved, in the best case conserving the minimum amount of light collected. Also in case of the CMS-ECAL, wrapping modifications and deposits on the crystal surface did not culminate in satisfactory results [46]. Because of this, uniformisation was achieved by lapping of one complete side face, as described by the authors of [47]. Derived from these experiences and the experimental results achieved in this work can be the fact that, compared to the non-modified case, uniformisation is always connected with a reduced overall LY. Thus, in

case of $\overline{P}$ANDA the response of the untapered EC-R type crystal has to be regarded as the best case which can be achieved by an uniformisation procedure applied to a crystal of tapered geometry.

4.1.3 Impact on Crystal Matrix Response

Based on the observations in the previous section, the impact of the LY NUF on the response of the Barrel EMC prototype PROTO60 and the possible benefits of a LY uniformisation can be evaluated. For this purpose, a GEANT4[1]. simulation with a model based on the PROTO60 CAD model was performed. The original energy deposition inside a crystal at a given distance to the LAAPD is weighted with the measured LY NUF obtained for a type 6 crystal with 80 MeV protons (see Fig. 2.46c). In addition, statistical fluctuations based on the number of produced electron-hole pairs and LAAPD characteristics are included. Fig. 4.3 shows the relative cluster energy resolution at a threshold corresponding to 0.75 MeV by this simulation with and without integration of the measured NUF. Moreover, the resolution parametrisation deduced from PROTO60 test experiments, taken from [42], is depicted. Apparently, in case of PROTO60 the NUF leads to a significant deterioration of the energy resolution for energies above a few hundred MeV compared to the simulation excluding NUFs. Thus, the NUF leads to a limitation of the energy resolution achievable with PROTO60 at higher energies, as indicated by the good agreement of the curve shapes of experimental parametrisation and simulation in this regime. The small constant shift can be attributed to the less idealised experimental situation, including beam alignment and profile, variations in crystal quality and calibration effects.

Despite the conclusion that an ideal uniformisation would certainly have an beneficial influence on the achievable PROTO60 energy resolution at higher energies, for a transfer of these observations to the complete $\overline{P}$ANDA Barrel EMC, several facts have to be taken into account. First, it has to be considered that the crystals comprising PROTO60 are of geometry type six and therefore represent an intermediate level of tapering and NUF. Hence, the effects observed in Fig. 4.3 are expected to be more pronounced in case of geometries with stronger tapering, i.e. types 1-5. The opposite holds true for the less or untapered geometries, namely types 7-11, EC and EC-R. Secondly, one has to contemplate their arrangement within the EMC, as displayed schematically in Fig. 3.1. As is recognisable, the least tapered types are located at low polar angles ϑ, while the most strongly tapered and most non-uniform type 1 is located in the region around $\vartheta \approx 90°$. For larger polar angles, the level of tapering and therefore NUF of the crystals is again decreasing. Regarding the single crystal energy differential rate spectrum for the $\overline{P}$ANDA Barrel EMC, shown in Fig. 4.4, one recognises that, due to fixed target kinematics, at a polar angle of $90°$ a maximum

---

[1]`http://geant4.web.cern.ch/geant4/`; see also [48]
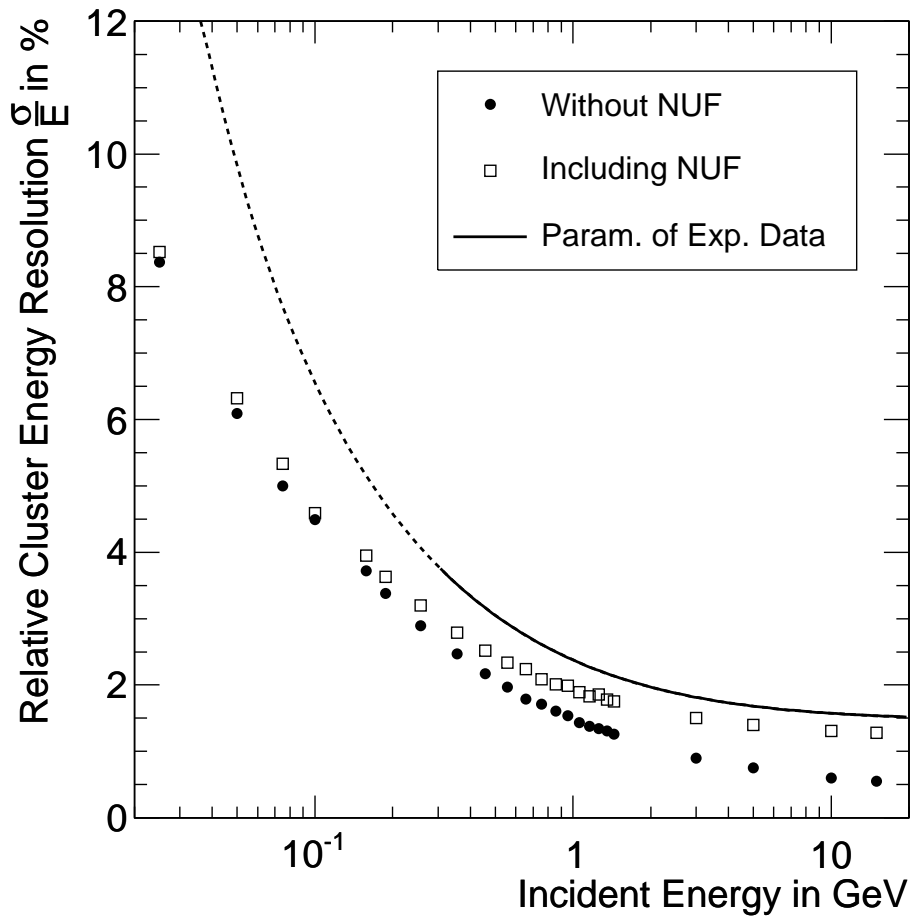
Figure 4.3: Simulations performed with GEANT4 on the influence of the NUF on the PROTO60 energy response. Shown is the relative energy resolution without and including a non-uniform energy response with a maximum relative deviation of 1.23 at 20 cm distance to the photo sensor. In addition, the parametrisation of the experimental data obtained with PROTO60, taken from [42], is drawn with a solid line. The dashed line represents an extrapolation to lower energies, not covered by the experimental data.
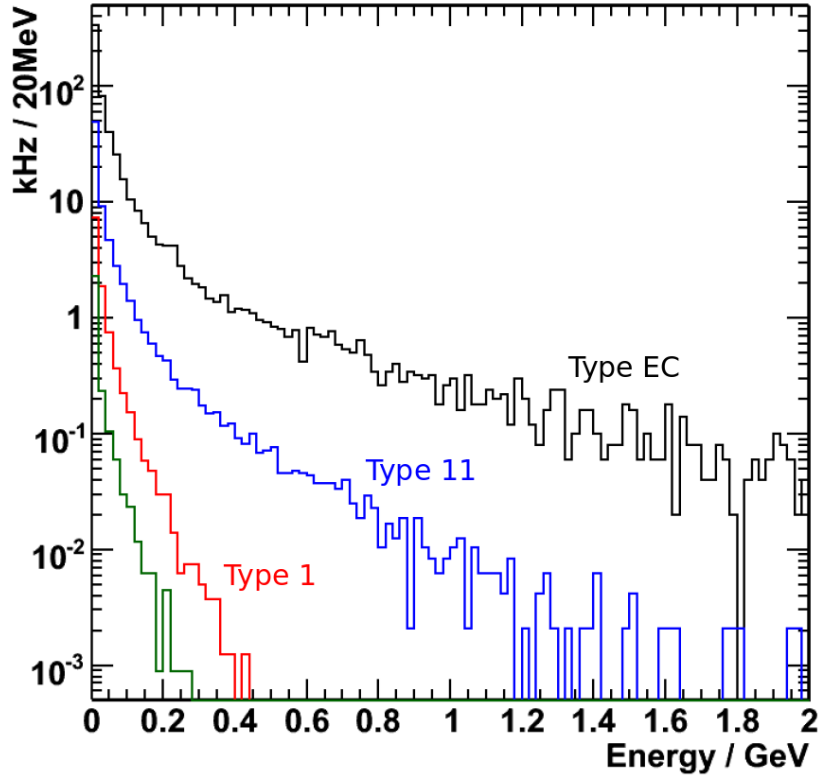
Figure 4.4: Single crystal energy differential rate spectrum expected for the PANDA EMC at $15 \frac{GeV}{c}$ incident beam momentum, in case of polar angles amounting to $5°$ (black), $25°$ (blue), $90°$ (red) and $135°$ (green)[21]. In addition, the crystal geometry types located at these angles are marked.

deposited energy of $0.5\,GeV$ is possible. Given the experience that the central crystal of a cluster contains roughly $70\,\%$ of the complete cluster energy, this value corresponds to an incident energy of approximately $0.7\,GeV$. As a consequence, the crystals with the highest NUF actually are not exposed to such high energies that a significant resolution improvement would be gained by an LY uniformisation. Furthermore, even at $\vartheta = 25°$, representing the region of the barrel's forward border, single crystal energy depositions are below $2\,GeV$. Additionally, the crystals facing these higher energy depositions possess a lower NUF. Also in this case, it is questionable whether even an ideal uniformisation would significantly improve the achievable resolution. Especially, if taking into account a LY degradation, inherent to the investigated uniformisation procedures, the resolution gain in the high energy regime would be outweighed by an resolution deterioration at lower incident energies. However, this is where, according to Fig. 4.4, the highest rates are expected. Based on this arguments, a light yield uniformisation via the presented methods is not recommendable for the $\overline{P}ANDA$ Barrel EMC. Nevertheless, further investigations concerning this issue are planned to be

performed with the next generation barrel prototype PROTO120. As indicated in Fig. 3.1, it will be comprised of the three most non-uniform crystal geometry types and therefore can be expected to provide a final experimental evaluation of the impact of LY NUFs on the Barrel EMC energy response.

4.2 Position Reconstruction with PROTO60

4.2.1 Position Resolution

The position response of the $\overline{P}$ANDA Barrel EMC prototype PROTO60 has already been studied with energy tagged photons in the energy regime ranging from $0.15\,\text{GeV}$ to $1.5\,\text{GeV}$. However, at the highest energies expected in the $\overline{P}$ANDA EMC, no measurement of the position response had been performed. Furthermore, each determination of the position resolution with incident photons, can only be regarded as an upper limit, since no independent tracking of individual photons can be performed. Therefore the achieved results, published in [25], represent a convolution of beam profile and intrinsic detector resolution. In the scope of this work, for the first time, a measurement of the position response to high energy leptons, i.e. positrons of $15\,\frac{\text{GeV}}{c}$ momentum, was performed with PROTO60 at CERN SPS. An independent information on the incident positron, with precision superior to the resolution expected for PROTO60, was provided by the Bonn Tracking Station. During analysis position reconstruction was performed with two distinct reconstruction techniques, both based on a centre of gravity algorithm, as expressed in Eq. 3.1. Application of a simple linear weighting proportionate to the energy deposited inside the individual crystal delivers a non-linear position response (S-curve). This correlation was parametrised and afterwards corrected for the strong bias to the crystals centre, as described in detail in Sec. 3.4.2. The obtained corrected position information (see Figs. 3.14 and 3.15) shows satisfactory linearity, however with slight fluctuations at the junctions between crystals. In a complementary approach, the position was reconstructed with logarithmic weighting of the energy fraction deposited inside a single detector segment with respect to the total cluster energy. The appropriate weighting parameter value was determined to $W_0 = 4.8$, which is in agreement with the value previously obtained for the low energy regime. With the chosen W_0, the logarithmic weighting technique delivers a uniform position response without the need for further corrections (see Fig. 3.17 and 3.18). An overview of the obtained overall resolutions is collected in Tab. 3.5. With the positron beam centred in the centre of a crystal, both techniques yield comparable results in both, x- and y- direction, of $\sigma_{x,y} \approx 1.1\,\text{mm}$. If the beam centre is located at a crystal junction however the overall x-resolution shows an improved value of $\sigma_x \approx 0.8\,\text{mm}$, while the value obtained with logarithmic weighting is hardly

changed. For y-direction however, both techniques show similar behaviour and resolution is deteriorated by $\sim 0.2\,\mathrm{mm}$. Furthermore, both reconstruction techniques deliver consistent results concerning the measured position dependence of the spatial resolution, displayed in Fig. 3.20 and Fig. 3.21. An upper limit of the resolution of $\sigma_{x,y}^{max} = 1.4\,\mathrm{mm}$ is observed if the incident positron enters at the crystal centre. In return, improvements down to $\sigma_{x,y}^{min} = 0.5\,\mathrm{mm}$ are obtained if the particle impinges near the crystal border. An overview of the achieved overall resolution, as well as the obtained lower and upper limit of the position resolution are given in Tab. 4.2. In addition, the resolution relatively to the mean width $2\Delta^2$ of the front face of a crystal with type 6 geometry is shown. Although error in determination of the position resolution by a Gaussian fit was generally below $0.02\,\mathrm{mm}$, a reasonable error estimation, taking into account the strip pitch of $0.05\,\mathrm{mm}$ in the Si-tracker providing the reference position and systematic uncertainties, e.g. as introduced by approximations made during implementation of the crystal coordinates into the reconstruction algorithm (as described in Sec. 3.8), yields a maximum uncertainty $\Delta\sigma_{x,y}$ of $0.1\,\mathrm{mm}$.

Since in the final $\overline{\mathrm{P}}\mathrm{ANDA}$ EMC the use of an angular coordinate system is foreseen, a direct comparison of the achieved resolution to the requirements stated in the technical design report [21] is not applicable. Tab. 4.1 summarises the required spatial resolution σ_{ϑ} for the individual EMC subsections. In addition, these values are set in relation to the angle equivalent covered by a single crystal. Apparently, the strongest requirement to the resolution amounting to $7.5\,\%$ of the complete angle covered by the crystal, is set for the barrel, while for FEC and BEC values of $10.0\,\%$ and $12.5\,\%$, respectively, are required. Setting, in an analogue way, the measured resolution at $15\,\mathrm{GeV}$ incident energy in relation to the crystal front face dimensions, yields value of $\frac{\sigma_{x,y}}{2\Delta} = 5.3\,\%$ (see Tab. 4.2). The obtained resolution, including the determined upper limit measured at the crystal centre, is superior to the specified resolutions in case of all three subsections. Although the measured position resolutions can be regarded as an excellent high energy limit, it has to be considered that for Barrel EMC and BEC, the maximum energies expected are lower than $15\,\mathrm{GeV}$ (see Tab. 4.1). However, the obtained resolution at $15\,\mathrm{GeV}$ is far better than the value obtained by extrapolation of energy dependence parametrisation derived from the low energy regime measurements of the PROTO60 position response to photons, elaborated in detail in [49]. This parametrisation for the upper limit position resolution is expressed as $\sigma_{det\otimes beam}(E/\mathrm{GeV}) = 3.4\,\mathrm{mm} \oplus \frac{2.6\,\mathrm{mm}}{\sqrt{E/\mathrm{GeV}}}$, and known to include also the photon beam profile. Despite the fact that an extrapolation over such a large energy range generally is prone to uncertainties, one can make the statement, that the large constant contribution, which by far exceeds the measured resolution at $15\,\mathrm{GeV}$, is not caused by the detector resolution but rather to be attributed to the influence of the photon beam width. Indeed, if comparing to other test beam experiments performed with matrices

---

[2]Δ represents the crystal front face halfwidth as applied in the S-curve correction technique.

DETECTOR SUBSECTION	POLAR ANGLE RANGE	MAXIMUM ENERGY	SPECIFICATION		
			Single crystal ϑ equiv.	Spatial resolution σ_ϑ	Rel. resolution $\frac{\sigma_\vartheta}{\vartheta}$
Forward Endcap	$5° \leq \vartheta < 22°$	$14.6\,\text{GeV}$	$1°$	$0.1°$	$10.0\,\%$
Barrel EMC	$22° \leq \vartheta < 140°$	$7.3\,\text{GeV}$	$4°$	$0.3°$	$7.5\,\%$
Backward Endcap	$140° \leq \vartheta$	$0.7\,\text{GeV}$	$4°$	$0.5°$	$12.5\,\%$

Table 4.1: Overview of the specified spatial resolution for each of the EMC subsections, taken from [21]. In addition, the maximum deposited energy and the spatial resolution relatively to the angle covered by a single crystal is calculated, enabling a better comparison to the obtained experimental results.

EXPERIMENT AT $15\,\text{GeV}$		
Spatial resolution	Value	Rel. Resolution $\frac{\sigma}{2\Delta}$
$\langle \sigma_{x,y} \rangle$	$1.1\,\text{mm}$	$5.3\,\%$
$\sigma_{x,y}^{min}$	$0.5\,\text{mm}$	$2.3\,\%$
$\sigma_{x,y}^{max}$	$1.4\,\text{mm}$	$6.5\,\%$

Table 4.2: Overview of the overall spatial resolution $\langle \sigma_{x,y} \rangle$ for both, x- and y-direction, obtained for incident $15\,\text{GeV}$ positron beam. In addition, the upper ($\sigma_{x,y}^{max}$) and lower ($\sigma_{x,y}^{min}$) resolution limit, obtained at crystal centre and border, respectively, are given. For comparability to the specifications given in Tab. 4.1, the resolution relatively to the crystal front face mean width 2Δ is given.

comprised of lead tungstate crystals with comparable size, one recognizes that the energy dependent term of the parametrisation amounts to similar values. The authors of [50] for instance report a spatial resolution of $\sigma_x = 0.17\,\text{mm} \oplus \frac{2.8\,\text{mm}}{\sqrt{E/\text{GeV}}}$ for incident electrons of $1-45\,\text{GeV}$ energy impinging a 5×5 array of straight crystals operated at room temperature. In the regime from $0.2-1.0\,\text{GeV}$ incident electron energy, a resolution of $\sigma_y = 0.4\,\text{mm} \oplus \frac{2.6\,\text{mm}}{\sqrt{E/\text{GeV}}}$ is achieved by the authors of [51] with a 3×3 matrix. Both used a linear weighted centre of gravity algorithm and performed an afterwards correction of the S-curve. Another experiment, applying logarithmic weighting for position reconstruction of an 4×4-matrix obtained a comparable resolution as achieved in this work, of $1.14\,\text{mm}$, although at twice as high incident electron energy of $30\,\text{GeV}$. Based on this observations and the experimental evidence at $15\,\text{GeV}$ one can conclude that also for the lower energies expected in the Barrel EMC, the position resolution is significantly better than indicated by the upper limit parametrisation obtained in previous experiments, i.e. the constant contribution is $< 1\,\text{mm}$. Since both investigated reconstruction algorithms yield similar results, the logarithmic weighting technique is preferable for application in the Barrel EMC, because of the large number of different crystal types. Whereas application of the S-curve correction technique would require an exact measurement of the non-linearity for each of the eleven geometry types, the logarithmic weighting technique is expected to deliver an intrinsically linear response, especially if an angular coordinate system is used. However, considering the extremely low energies expected in the BEC and the inherently small cluster sizes, also the logarithmic weighting is prone to non-linearities. Therefore, for the BEC, comprised completely out the rectangular EC-R geometry crystals, the S-curve correction technique represents an excellent alternative. Further improvements to the achieved resolution can be expected, if an angular coordinate system, fitting the arrangement of the crystals inside the barrel, is used. For this purpose, the next generation prototype for the Barrel EMC, which will be comprised of 12×10 crystals of three different geometry types, will feature a suspension and markers dedicated for adjustment to the off-point, in which all crystals are arranged. With this prototype also position reconstruction with clusters including different crystal geometries can be investigated. Furthermore, the introduction of a slight dependence of the used weighting parameter can have a beneficial influence on the achievable position resolution, as indicated in [52].

4.2.2 Energy Resolution Position Dependence

Detailed studies of energy calibration and the overall energy resolution achievable with PROTO60 is discussed in detail in [42]. Given the availability of a precise information on the incident position of the $15\,\text{GeV}$ positrons, a measurement of the energy resolution obtained for a beam of restricted size was performed at different beam centre

positions. A well defined circular beam spot of $4\,\mathrm{mm}$ diameter was selected using the tracking information and moved in steps of $1\,\mathrm{mm}$ from the crystal centre to the crystal border. The energy information is extracted from the line shape by fit of a Novosibirsk function taking into account the typical low energetic tails (see Fig. 3.24). For movement in both, x- and y-direction, the best relative energy resolution, amounting to $\frac{\sigma}{E} = (1.43 \pm 0.02)\,\%$, is obtained if beam centre and crystal centre are identical (compare Fig. 3.26). If the beam centre is located near the crystal border, a deterioration of the energy resolution up to $(3.15 \pm 0.06)\,\%$ for movement in x- and up to $(2.39 \pm 0.08)\,\%$ for movement in y-direction, is observed. Despite this resolution drop, the extracted peak energy is independent of the beam centre location. To correct for the measured cluster energy resolution deterioration, in principle a parametrisation of the measured energy can be used. An elegant alternative is the so called $\ln\left(\frac{E_2}{E_1}\right)$-technique, described in [53], which does not require additional information besides the energy deposition within the crystals. This method is in use by the CMS-ECAL and has been proven to achieve a significant improvement of the overall resolution if applied to PROTO60, as elaborated in [34].

Acronyms

$\overline{\text{P}}$**ANDA** AntiProton ANnihilation at Darmstadt. XV, 1–9, 11–15, 17, 19, 33, 34, 38–40, 43, 55, 57, 60, 71, 74, 75, 81, 92, 94, 98, 100, 103, 104, 106, 111, 135, 139, 142–146, 148–150

ACCOS Automatic Crystal quality COntrol System. 71, 72, 74

ADC Analogue to Digital Converter. X, 80, 84, 109

AFM Atomic Force Microscope. 96, 98, 145

AGOR Accelerateur Groningen-ORsay. 99

ANKE Apparatus for Studies of Nucleon and Kaon Ejectiles. 94, 145

APD Avalanche Photo Diode. 26, 100, 112

APFEL ASIC for $\overline{\text{P}}$ANDA Front End Electronics. 39

APPA Atomic, Plasma Physics and Applications. 5

ASIC Application Specific Integrated Circuit. 40

BEC Backward EndCap. 34, 37, 39, 150, 152

BGO Bismuthe Germanate. 75, 76, 82, 83, 85

BTCP Bogoroditsk Techno Chemical Plant. 71

CAD Computer Aided Design. 14, 38, 75, 88, 90, 116, 146

CAMAC Computer Automated Measurement And Control. 80

CBM Compressed Baryonic Matter. 5

CERN European laboratory for particle physics. 2, 4, 46, 71, 72, 74, 106–108, 110, 111, 149

CFD Constant Fraction Discriminator. 80, 81, 112

CFT Constant Fraction Timing algorithm. 112, 113

CMS Compact Muon Solenoid. VIII, 2, 4, 33, 34, 143

CMS-ECAL Electromagnetic CALorimeter of the CMS experiment. 34, 39, 55, 57, 71, 139, 143–145, 153

COSY COoler SYnchrotron. 94, 145

CPU Central Processing Unit. 109, 110

DAQ Data AcQuisition. 33, 40, 41, 105, 108, 109

DC3145 Dow Corning 3145 RTV. 57

DIRC Detection of Internally Reflected Cherenkov light. XI, 19, 20

ECL Emitter Coupled Logic. 80, 81

EMC Electromagnetic Calorimeter. XV, 2–4, 11, 13, 21, 33, 34, 36, 37, 39–41, 43, 45, 57, 58, 60, 62, 68, 71, 78, 84, 94, 100, 104–106, 111, 116, 139, 141–143, 146, 148–152

FAIR Facility for Antiproton and Ion Research. XI, 1, 3, 5, 6

FEC Forward EndCap. 34, 37, 40, 139, 150

FPGA Field Programmable Gate Array. 40, 41, 111

FRS Forward Range System. 13

FWHM Full Width Half Maximum. 33, 135

FZ Jülich Forschungszentrum Jülich. 94

GEM Gas Electron Multiplier. 19

GSI GSI Helmholtzzentrum für Schwerionenforschung GmbH. 5, 6

HESR High Energy Storage Ring. 5–8, 11, 33

JLU Gießen Justus-Liebig-Universität Gießen. 56, 71, 72, 74, 78, 86

KVI Kernfysisch Versneller Instituut Groningen. 99

LAAPD Large Area Avalanche PhotoDiode. 37–40, 57, 68, 100, 101, 105, 106, 109, 111, 114, 141, 142, 146

LEAR Low Energy Antiproton Ring. 9

LNP Low Power Low Noise charge Preamplifier. 40, 100, 105, 106, 109, 111, 112

LY Light Yield. XV, 43, 71–74, 78, 81, 83, 86–88, 92, 94, 98, 102, 139, 140, 142, 143, 145, 146, 148, 149

MA Moving Average algorithm. 111–113

MDT Mini Drift Tube. 13, 21

MF Muon Filter. 21

MIP Minimum Ionising Particle. 23, 26, 35, 86, 114, 142

MUO MUOn Detection System. 13, 21

MVD Micro Vertex Detector. 16–18, 106

MWD Moving Window Deconvolution algorithm. 111–113

MWPC Multi Wire Proportional Chamber. 19

Mylar Brand name of biaxially-oriented polyethylene terephthalate (boPET) foil. 17

NAS Network Access Storage. 109, 110

NIM Nuclear Instrumentation Module. 80, 81, 110

NUF Non-UniFormity. XV, 44, 45, 52, 63, 64, 71, 74, 75, 78, 81, 84, 86–88, 90, 92, 93, 98–100, 102, 139–146, 148, 149

NuSTAR Nuclear Structure, Astrophysics and Reactions. 5

PID Particle Identification. 11

PMT PhotoMultiplier Tube. 26, 37, 43, 53, 57, 59, 62, 64, 65, 67–71, 75–78, 85–88, 92, 93, 98, 99, 108, 145

PTFE Polytetrafluoroethylene. 78, 79

PVC PolyVinyl Chloride. 104

PWO Lead Tungstate. 33, 52, 55, 81, 84, 139, 140, 143, 144

PWO-II Second generation lead tungstate. 34, 43, 53, 55–58, 67, 71, 78, 81–83, 86, 88, 90, 91, 94, 104, 105, 139, 140, 143

QC Quality Control. 56, 71, 78, 81, 86, 140

QCD Quantum-Chromo-Dynamics. 7, 9–11

QDC Charge integrating ADC. 80, 81, 83, 91

QE Quantum Efficiency. 59

RICH Ring Imaging CHerenkov. 13, 19

RMS Root Mean Square. 60, 96, 111

RS Range System. 21

SADC Sampling Analogue to Digital Converter. 40, 100, 109–111, 113

SIS100 SchwerIonenSynchrotron 100. 5

SIS18 SchwerIonenSynchrotron 18. 5

SLitrani Super LITRANI. 3, 44, 52, 54, 55, 58, 139–141

SPS Super Proton Synchrotron. 2, 4, 106–108, 110, 111, 149

STT Straw Tube Tracker. 17

TCP/IP Transmission Control Protocol / Internet Protocol. 109, 110

TDC Time to Digital Converter. 80, 81, 83, 91

UNILAC UNIversal Linear ACcelerator. 5

VM2000 VM2000 enhanced specular reflector film. 58, 78, 79, 92, 100, 106, 143

VME Versa Module Eurocard. 80, 109, 110

VPTT Vacuum Photo Tetrode. 37, 39, 40, 57

List of Figures

List of Tables

Bibliography

[1] U. Wiedner, "Future prospects for hadron physics at PANDA," *Progress in Particle and Nuclear Physics* **66** no. 3, (2011) 477 – 518. http://www.sciencedirect.com/science/article/pii/S0146641011000822.

[2] **Particle Data Group** Collaboration, J. Beringer *et al.*, "Review of particle physics," *Phys. Rev. D* **86** (Jul, 2012) 010001. http://link.aps.org/doi/10.1103/PhysRevD.86.010001.

[3] F. E. Close and A. Kirk, "The mixing of the f0(1370), f0(1500) and f0(1710) and the search for the scalar glueball," *Physics Letters B* **483** no. 4, (2000) 345 – 352. http://www.sciencedirect.com/science/article/pii/S0370269300006237.

[4] V. Mathieu, N. Kochelev, and V. Vento, "The physics of glueballs," *Int.J.Mod.Phys* **E18** no. 483, (2009) 1–49, arXiv:0810.4453 [hep-ph].

[5] C. J. Morningstar and M. Peardon, "Glueball spectrum from an anisotropic lattice study," *Phys. Rev. D* **60** (Jul, 1999) 034509. http://link.aps.org/doi/10.1103/PhysRevD.60.034509.

[6] A. P. Szczepaniak and E. S. Swanson, "The low-lying glueball spectrum," *Physics Letters B* **577** no. 1-2, (2003) 61–66, arXiv:hep-ph/0308268. http://www.sciencedirect.com/science/article/pii/S037026930301551X.

[7] V. Mathieu, F. Buisseret, and C. Semay, "Gluons in glueballs: Spin or helicity?," *Phys. Rev. D* **77** (Jun, 2008) 114022, arXiv:0802.0088 [hep-ph]. http://link.aps.org/doi/10.1103/PhysRevD.77.114022.

[8] A. Kaidalov and P. Volkovitsky, ""binary reactions in $\bar{p}p$ collisions at intermediate energies"," *Zeitschrift für Physik C Particles and Fields* **63** (1994) 517–524. http://dx.doi.org/10.1007/BF01580332.

[9] G. Atoian *et al.*, "Test Beam Study of the Kopio Shashlyk Calorimeter Prototype," in *Calorimetry in Particle Physics*, C. Cecchi, P. Cenci, P. Lubrano, and M. Pepe, eds., pp. 55–60. Feb., 2005.

[10] **PANDA** Collaboration, "Technical Design Report for the: PANDA Micro Vertex Detector," (2012) , arXiv:1207.6581v2 [physics.ins-det].

[11] **PANDA** Collaboration, "Technical Design Report for the: PANDA Straw Tube Tracker," (2012) , `arXiv:1205.5441v2 [physics.ins-det]`.

[12] **PANDA** Collaboration, "PANDA experiment website." `http://www-panda.gsi.de/framework/det_iframe.php?section=Tracking`.

[13] Amsler, C. et al. (Particle Data Group) *Physics Letters B* **667** no. 1, (2008) .

[14] W. R. Leo, *Techniques for Nuclear and Particle Physics Experiments.* Springer, 2 ed., Februar, 1994.

[15] B. Rossi, *High Energy Particles.* Prentice-Hall, Inc., 1952.

[16] N. Akchurin *et al.*, "Contributions of cherenkov light to the signals from lead tungstate crystals," *Nuclear Instruments and Methods in Physics Research Section A: Accelerators, Spectrometers, Detectors and Associated Equipment* **582** no. 2, (2007) 474 − 483. `http://www.sciencedirect.com/science/article/pii/S0168900207018785`.

[17] M. Berger *et al.*, "XCOM: Photo Cross Sections Database." `http://www.nist.gov/pml/data/xcom/index.cfm`.

[18] C. Leroy and P. G. Rancoita, *Principles of radiation interaction in matter and detection; 2nd ed.* World Scientific, Singapore, 2009.

[19] H. Koch *et al.*, "Proposal: meson spectroscopy at LEAR with a 4 π neutral and charged detector," Tech. Rep. CERN-PSCC-85-56. PSCC-P-90, CERN, Geneva, 1985.

[20] G. Akopdjanov *et al.*, "Determination of photon coordinates in a hodoscope cherenkov spectrometer," *Nuclear Instruments and Methods* **140** no. 3, (1977) 441 − 445. `http://www.sciencedirect.com/science/article/pii/0029554X77903585`.

[21] **PANDA** Collaboration, "Technical Design Report for: PANDA Electromagnetic Calorimeter (EMC)," 2008.

[22] **CMS** Collaboration, "Measurement of the Muon Stopping Power in Lead Tungstate," (2012) , `arXiv:0911.5397v2 [physics.ins-det]`.

[23] S. Baccaro *et al.*, "Ordinary and extraordinary complex refractive index of the lead tungstate (PbWO4) crystal," *Nuclear Instruments and Methods in Physics Research Section A: Accelerators, Spectrometers, Detectors and Associated Equipment* **385** no. 2, (1997) 209 − 214. `http://www.sciencedirect.com/science/article/pii/S0168900296010169`.

[24] **Particle Data Group** Collaboration, "Atomic and nuclear properties of materials for more than 300 materials."
`http://pdg.lbl.gov/2012/AtomicNuclearProperties/`.

[25] M. Kavatsyuk *et al.*, "Performance of the prototype of the electromagnetic calorimeter for PANDA," *Nuclear Instruments and Methods in Physics Research Section A: Accelerators, Spectrometers, Detectors and Associated Equipment* **648** no. 1, (2011) 77 – 91.
`http://www.sciencedirect.com/science/article/pii/S0168900211011600`.

[26] W. Erni, "Basel LNP, a discrete Preamplifier for VPT/T (and APD) readout, model SP883d, Preliminary Version."
`http://jazz.physik.unibas.ch/panda/uploads/2012-07-24--11-45-10_`
`SP883d_Datasheet_Manual_PreampV0.6.4.pdf`.

[27] F.-X. Gentit, "SLitrani Simulation Package." `http://gentitfx.fr/SLitrani/`.

[28] F.-X. Gentit, "Optics in Anisotropic Media."
`http://gentitfx.fr/litrani/birefringence/Physics_behind.pdf`.

[29] R. Brun and F. Rademakers, "Root - an object oriented data analysis framework," *Nuclear Instruments and Methods in Physics Research Section A: Accelerators, Spectrometers, Detectors and Associated Equipment* **389** no. 1-2, (1997) 81–86.
`http://www.sciencedirect.com/science/article/pii/S016890029700048X`.

[30] V. I. Dormenev, *Lead Tungstate Scintillation Crystals for the Electromagnetic Calorimeter of the PANDA Experiment.* PhD thesis, Institute for Nuclear Problems, Belrussian State University, Minsk, 2008.

[31] Hamamatsu Photonics K.K., "Photomultiplier Tubes R1828-01, R2059 (Datasheet)," 2010. `http://www.hamamatsu.com/resources/pdf/etd/`
`R1828-01_R2059_TPMH1259E04.pdf`.

[32] A. Dbeyssi *et al.*, "Tests of optical glues for the PANDA electromagnetic calorimeter," *Nuclear Instruments and Methods in Physics Research Section A: Accelerators, Spectrometers, Detectors and Associated Equipment* **722** no. 0, (2013) 82 – 86.
`http://www.sciencedirect.com/science/article/pii/S0168900213004786`.

[33] E. Auffray *et al.*, "Performance of ACCOS, an Automatic Crystal quality Control System for the PWO crystals of the CMS calorimeter ," *Nuclear Instruments and Methods in Physics Research Section A: Accelerators, Spectrometers, Detectors and Associated Equipment* **456** no. 3, (2001) 325 – 341.
`http://www.sciencedirect.com/science/article/pii/S0168900200006653`.

[34] T. Eißner, *The new PWO Crystal Generation and Concepts for the Performance Optimisation of the PANDA EMC*. PhD thesis, Justus Liebig Universität Gießen, 2013.

[35] , "Thermal expansion coefficients of the elements (data page)," 2013. http://en.wikipedia.org/wiki/Thermal_expansion_coefficients_of_the_elements_(data_page).

[36] R. Novotny, W. Doring, M. Hoek, M. Buescher, V. Hejny, *et al.*, "The PHOTON BALL at COSY,".

[37] University of Groningen, "AGOR-faciliteit," 2012. http://www.rug.nl/kvi/facilities/agor/.

[38] G. Akopdjanov *et al.*, "Determination of photon coordinates in a hodoscope cherenkov spectrometer," *Nuclear Instruments and Methods* **140** no. 3, (1977) 441 – 445. http://www.sciencedirect.com/science/article/B73DN-471XFCS-Y6/2/c6e753227616aaff934c48cf7b327fad.

[39] T. C. Awes *et al.*, "A simple method of shower localization and identification in laterally segmented calorimeters," *Nuclear Instruments and Methods in Physics Research Section A: Accelerators, Spectrometers, Detectors and Associated Equipment* **311** no. 1-2, (1992) 130 – 138. http://www.sciencedirect.com/science/article/B6TJM-473M9VK-GN/2/a5f46fe40b805e3df4573a38fcc584dc.

[40] European Organisation for Nuclear Research (CERN), "CERN web page," 2011. http://public.web.cern.ch/public/en/research/AccelComplex-en.html.

[41] S. Bianco, M. Becker, K.-T. Brinkmann, R. Kliemt, K. Koop, R. Schnell, T. Würschig, and H.-G. Zaunick, "Measurements with a Si-strip telescope," in *PoS(RD11)025*. 2011.

[42] M. Moritz, *Measurements and improvements of the response of the PANDA-EMC prototype PROTO 60 to high energetic particles and photons in accelerator experiments*. PhD thesis, Justus Liebig Universität Gießen, 2013.

[43] M. Kavatsyuk, E. Guliyev, P. J. J. Lemmens, H. Lohner, T. P. Poelman, and G. Tambave, "Feature-extraction algorithms for the panda electromagnetic calorimeter," in *Nuclear Science Symposium Conference Record (NSS/MIC), 2009 IEEE*, pp. 210–213. 2009.

[44] M. Marteinsdóttir, "Light Yield Non-uniformity in PWO Scintillators," Master's thesis, Stockholm University, 2009.

[45] O. Lundberg, "Measures to Improve the Light Yield Uniformity of Tapered PWO Scintillator Crystals," Master's thesis, Stockholm University, 2011.

[46] D. Britton, M. Ryan, and X. Qu, "Light collection uniformity of lead tungstate crystals for the CMS electromagnetic calorimeter," *Nuclear Instruments and Methods in Physics Research Section A: Accelerators, Spectrometers, Detectors and Associated Equipment* **540** no. 2-3, (2005) 273 – 284.

[47] E. Auffray, F. Cavallari, M. Lebeau, P. Lecoq, M. Schneegans, and P. Sempere-Roldan, "Crystal conditioning for high-energy physics detectors," *Nuclear Instruments and Methods in Physics Research Section A: Accelerators, Spectrometers, Detectors and Associated Equipment* **486** no. 1-2, (2002) 22 – 34. http://www.sciencedirect.com/science/article/pii/S0168900202006708. <ce:title>Proceedings of the 6th International Conference on Inorganic Scin tillators and their Use in Scientific and Industrial Applications</ce:title>.

[48] S. Agostinelli *et al.*, "Geant4–a simulation toolkit," *Nuclear Instruments and Methods in Physics Research Section A: Accelerators, Spectrometers, Detectors and Associated Equipment* **506** no. 3, (2003) 250 – 303. http://www.sciencedirect.com/science/article/B6TJM-48TJFY8-5/2/ 23ea98096ce11c1be446850c04cfa498.

[49] D. Bremer, "Reconstruction of Electromagnetic Showers and Determination of the Position Resolution of a Prototype for the PANDA Electromagnetic Calorimeter," Master's thesis, Justus Liebig Universität Gießen, 2010.

[50] V. A. Batarin *et al.*, "Precision measurement of energy and position resolutions of the BTeV electromagnetic calorimeter prototype," *Nuclear Instruments and Methods in Physics Research Section A: Accelerators, Spectrometers, Detectors and Associated Equipment* **510** no. 3, (2003) 248 – 261. http://www.sciencedirect.com/science/article/B6TJM-48YVM7S-B/2/ 8fb0beaa593db9b3ebd59cdc78759a98.

[51] H. Shimizu *et al.*, "Performance of a PbWO4 crystal calorimeter for 0.2-1.0 GeV electrons," *Nuclear Instruments and Methods in Physics Research Section A: Accelerators, Spectrometers, Detectors and Associated Equipment* **447** no. 3, (2000) 467 – 475. http://www.sciencedirect.com/science/article/ B6TJM-40GHR4P-G/2/ec990f0d9029ee5dbe5bea9cb4c725d4.

[52] H. Moeini *et al.*, "Design studies of the pwo end-cap calorimeter for panda," arXiv:1306.2819 [ins-det]. http://http://arxiv.org/abs/1306.2819.

[53] J. Descamps and P. Jarry, "Periodic position dependence of the energy measured in the CMS electromagnetic calorimeter,". CERN-CMS-NOTE-2006-045.

Acknowledgements

Erklärung der Urheberschaft

Ich erkläre: Ich habe die vorgelegte Dissertation selbständig und ohne unerlaubte fremde Hilfe und nur mit den Hilfen angefertigt, die ich in der Dissertation angegeben habe.

Alle Textstellen, die wörtlich oder sinngemäß aus veröffentlichten Schriften entnommen sind, und alle Angaben, die auf mündlichen Auskünften beruhen, sind als solche kenntlich gemacht.

Bei den von mir durchgeführten und in der Dissertation erwähnten Untersuchungen habe ich die Grundsätze guter wissenschaftlicher Praxis, wie sie in der "Satzung der Justus-Liebig-Universität Gießen zur Sicherung guter wissenschaftlicher Praxis" niedergelegt sind, eingehalten.

Daniel Andreas Bremer

Gießen, im November 2013